Proceeding of 14th meeting on

Research Astronomy

Institute for Advanced Studies in Basic Sciences

May 13-14, 2010

Zanjan, Iran

Scientific Organizing Committee (SOC):

Y. Sobouti

H. Haghi

K. Karami

S. Rahvar

S. Nasiri

Publication's office, IASBS, Zanjan
May, 2010

14th Meeting on Research Astronomy

May 13-14, 2010, IASBS, Zanjan, Iran

Foreword

The 14th Meeting on Research Astronomy was held on May 13-14, 2010, under the chairmanship of Professor Yousef Sobouti, the president of Institute for Advanced Studies in Basic Sciences (IASBS). The scientific committee also included S. Nasiri (Zanjan University), H. Haghi (IASBS), K. Karami (Kurdistan University), and S. Rahvar (Sharif University).

The structure of the 14th Meeting on Research Astronomy included oral and poster presentations and addressed different topics in Astrophysics and Cosmology such as: Alternative gravities, solar physics, galaxy group, cosmic rays, binary stars, accretion disk, dark energy, microlensing, dense stellar system …

About 120 Participants from all over Iran attended this meeting and contributed to its success not only through their talks and/or posters but by taking an active part in discussions.

Many colleagues and members of our Institute have helped us in many ways. In particular, webpage and electronic registration systems designed by Dr A. Ghods and Mr Mahmoud Shirazi and the secretary of meeting, Mrs S. Mihanparast.

Special thank goes to vice president of our institute Dr H. Khalesifard, for the financial support and providing us the facilities of IASBS for holding the 14th Meeting on Research Astronomy.

Hosein Haghi
May 2010

Proceeding of 14th meeting on research astronomy

Table of Contents

The r-modes-Alfvén waves coupling in magnetic rotating stars

S. Abbassi[1,2] and M. Rieutord[3]
[1] *School of Physics, Damghan University of Basic Sciences, Damghan, P.O.Box 36715-364, Iran*
[2] *School of Astronomy, Institude for Studies in Theocratical Physics and Mathematics, 19395-5531, Tehran, Iran*
[3] *Laboratoire d'Astrophysique de Toulouse-Tarbes, Universit de Toulouse, CNRS, 14 avenue E. Belin, 31400 Toulouse, France*

We carry out numerical and mathematical investigations of shear Alfvn waves inside of a rotating spherical shell filled with an incompressible conducting fluid (with finite conductivity), and bathed in a strong dipolar magnetic field. In particular, we are interested in studying inertial r-mode instability in rapidly rotating neutron stars. We considered the magneto-viscous Ekman layers at the core-crust interface and discussed the resulting damping mechanism for r-mode oscillations.
PACS numbers: 05.10.-a ,05.10.Gg, 98.70.Vc

I. INTRODUCTION

Numerous astrophysical systems exhibit a pulsating behavior that can be significantly influenced by both magnetic field and rotation. The rapidly oscillating Ap (roAp) stars, the magnetic white dwarf stars and neutron stars as well as planetary cores fall into the above category. In neutron stars, however, possible astrophysical implications of r-modes instability have motivated extensive investigations of this mode during the past few years. r-modes belong to the class of inertial modes that arise in rotating fluids due to the Coriolis force. It has been shown that these modes easily couple to gravitational radiation and become unstable, allowing the neutron stars to lose their angular momentum. The foregoing instability may however be weakened or even suppressed by all the dissipative mechanisms which couple to an r-mode oscillations. Much work has thus been devoted to the analysis of the various mechanisms which may damp r-modes. Until now, the Ekman layer which forms below the crust of a neutron star, has been recognized as the most important source of dissipation.

However, it is well-known that the magnetic field is an important component of a neutron star. It is therefore clear that fluid flows may be seriously influenced by this field and that other channels of dissipation for the r-mode instability may exist through this component. Much work was devoted to investigate the modifications induced by a magnetic field on these kind of modes.

The aim of the present paper is to explore furthermore the channels of dissipation for the unstable m=2 r-mode of a rotating neutron star, when a dipolar magnetic field perturbs the flow. Indeed, a possibility that has not been considered by previous studies, is the fact that an unstable r-mode of a spherical layer, might develop internal shear layers thanks to the magnetic field action. Since fluid layers of different natures are expected thanks to phase transitions of nuclear matter, the existence of internal shear layers are also very likely as we shall see.

Rotating fluid layers bathed by a magnetic field are however not specific to neutron stars. They are also found in planetary core, like in the Earth's core. Thus, in order to make the following study of more general interest, we shall consider a very simplified model of neutron star, neglecting relativistic or superconducting effects. We thus extend the results of to the case where a dipolar magnetic field perturb the fluid flow (in the limit of very large magnetic Prandtl numbers).

II. THE MODEL

We consider a rotating star modeled as an infinitely electrically conducting core surrounded by a spherical layer of fluid. The ratio of the inner core radius to the outer radius R is η. The kinematic viscosity and magnetic diffusivity of the fluid are respectively ν and ν_m.

The star is rotating with uniform angular frequency $\mathbf{\Omega} = \Omega \mathbf{e}_z$ along the z-axis. The core is supposed to be the source of a permanent axisymmetric magnetic dipole covering the whole layer. The symmetry axis of the magnetic field is along the z-axis. Note that such a partition of the star is necessary in order to avoid the problem of the definition of the magnetic field in the core of the star, the dipole field being singular at the center. The fluid in the layer is taken to be incompressible; we thus eliminate phenomena related to compressibility such as p-modes (rapid and slow magnetic waves, when a magnetic field is applied). Classical MHD approximations are used, that is fluid particles have sizes far greater than the typical Debye length of the plasma and all the motions are assumed to be non-relativistic, so that the electric displacement can be neglected in Ampre's law.

A. Equations of motion

The shell is bathed by an axisymmetric dipolar magnetic field:

$$\mathbf{B}_0 = B_p \cdot R^3 \left(\frac{\cos\theta}{r^3}\mathbf{e}_r + \frac{\sin\theta}{2r^3}\mathbf{e}_\theta \right), \tag{1}$$

where $(\mathbf{e}_r, \mathbf{e}_\theta, \mathbf{e}_\varphi)$ are spherical coordinate unit vectors. B_p is the amplitude of the magnetic field at the surface of the star.

The equations of motion for an incompressible rotating plasma can be written as

$$\frac{\partial \mathbf{v}}{\partial t} + \mathbf{v}\cdot\nabla\mathbf{v} + 2\boldsymbol{\Omega}\times\mathbf{v} =$$
$$-\nabla p/\rho - \nabla\Phi_{\text{eff}} + \frac{1}{4\pi\rho}(\nabla\times\mathbf{B})\times\mathbf{B} + \nu\Delta\mathbf{v}, \tag{2a}$$
$$\frac{\partial \mathbf{B}}{\partial t} = \nabla\times(\mathbf{v}\times\mathbf{B}) + \nu_m\Delta\mathbf{B} \tag{2b}$$
$$\nabla\cdot\mathbf{B} = 0, \tag{2c}$$
$$\nabla\cdot\mathbf{v} = 0, \tag{2d}$$

where $\Phi_{\text{eff}} = \Phi - \Omega^2 r^2 \sin^2\theta/2$ is the effective gravito-rotational potential. Here $\mathbf{v}$ is the velocity field, $\mathbf{B}$ is the total magnetic field (dipole field plus perturbation), and $\nu_m = c^2/(4\pi\sigma)$ where σ is the plasma's electrical conductivity and c is the speed of light.

A non-dimensional form of the previous equations can be obtained by introducing the parameters

$$V_{\text{A}} = B_p/\sqrt{4\pi\rho}, \qquad V_\Omega = 2\Omega R, \qquad \text{Le} = \text{V}_\text{A}/\text{V}_\Omega,$$

$$E = \nu/(RV_\Omega), \qquad E_m = \nu_m/(RV_\Omega),$$

where V_{A} is the Alfvn speed, V_Ω is rotational speed, E is the Ekman number and E_m the magnetic Ekman number. For simplicity, we will refer to these numbers simply as "diffusivity numbers". As shown by its definition, this number measures the ratio of the Alven speed to the rotation speed.

By linearizing magneto-hydrodynamic equations to the kinetic $\mathbf{v}$ and magnetic $\mathbf{b}$ perturbations, one can study infinitesimal perturbations from the equilibrium. We assume these perturbations have a time dependence of the form $\text{e}^{\lambda t}$, where $\lambda = \tau + i\omega$ (τ is the damping rate, ω the pulsation and $i^2 = -1$), and we use the following non-dimensional variables:

$$\begin{aligned} \mathbf{v} &\rightarrow V_\Omega \mathbf{v}(\mathbf{r})e^{\lambda t}, \\ \mathbf{B} &\rightarrow B_p\mathbf{B}(\mathbf{r}) + B_p\mathbf{b}(\mathbf{r})e^{\lambda t}, \\ \rho &\rightarrow \rho_o, \end{aligned} \tag{4}$$

where $\mathbf{v}(\mathbf{r})$ and $\mathbf{b}(\mathbf{r})$ are now first order non-dimensional quantities. Therefore, Eqs. (2) reduce to the following set of equations:

$$\lambda\nabla\times\mathbf{u} + \nabla\times(\mathbf{e}_z\times\mathbf{u}) =$$
$$\text{Le}^2\nabla\times((\nabla\times\mathbf{b})\times\mathbf{B}) + \text{E}\nabla\times\Delta\mathbf{u}, \tag{5a}$$
$$\lambda\mathbf{b} = \nabla\times(\mathbf{u}\times\mathbf{B}) + E_m\Delta\mathbf{b}, \tag{5b}$$
$$\nabla\cdot\mathbf{u} = 0, \tag{5c}$$
$$\nabla\cdot\mathbf{b} = 0, \tag{5d}$$

where $\mathbf{B}$ denotes the permanent dipolar magnetic field and we used $\nabla\times\mathbf{B} = 0$. Here we take the curl of momentum equation in order to eliminate pressure term.

B. Boundary conditions

Six boundary conditions are required in order to solve Eqs. (5) uniquely. On the inner boundary $r = \eta R$ ($\eta < 1$), the magnetic field perturbations have only tangent components because the core is assumed to be infinitely conducting. On the surface $r = R$, the total magnetic field vector matches the external field which is dipolar potential, as there are no currents in the external vacuum. Note that on both boundaries surface currents can occur. As for the velocity field, we may either use stress-free or no-slip boundadry conditions.

As for the magnetic field, different conditions apply for the inner and outer boundaries. On the interior, the perturbation to the electric field is perpendicular to the conducting core, and the perturbation to the magnetic field is tangent. This gives the following three equations:

$$b_r = 0, \tag{6a}$$
$$\frac{E_m}{r}\frac{\partial}{\partial r}(rb_\theta) = -u_\theta B_r, \tag{6b}$$
$$\frac{E_m}{r}\frac{\partial}{\partial r}(rb_\varphi) = -u_\varphi B_r. \tag{6c}$$

The magnetic field perturbations outside the star ($r > R$) are derived from a potential that does not diverge towards infinity:

$$\mathbf{b}_{\text{ext}} = \nabla\phi, \tag{7}$$

The boundary conditions at the surface of the star just the continuity of the magnetic field there. These conditions are easily expressed after expansion of the fields in spherical harmonics (see appendix).

Eq. (5), together with boundary conditions, defines a generalized eigenvalue problem, where λ is the eigenvalue and $(\mathbf{v}, \mathbf{b})$ is the eigenvector which can be computed numerically.

where A and B are differential operators with respect to the r variable only. The eigenvector associated with λ can be written as

$$\mathbf{x}_{\lambda m}(r) = \left| \begin{array}{l} \vdots \\ u_m^\ell(r) \\ c_m^\ell(r) \\ w_m^{\ell+1}(r) \\ a_m^{\ell+1}(r) \\ \vdots \end{array} \right. \quad (8)$$

where ℓ is running from m to ∞.

C. The case of neutron stars

In neutron stars, typical values for the various physical quantities are

$$B_p \sim 10^{12}\ \mathrm{G}, \quad \rho \sim 10^{14}\ \mathrm{gcm}^{-3}, \quad R \sim\ 10\mathrm{km}, \quad (9a)$$
$$\Omega = 2\pi\nu_s \sim 1900\ \mathrm{rad\ s}^{-1} \quad (9b)$$
$$\sigma \sim 4.7 \times 10^{27}\ \mathrm{s}^{-1}, \quad \nu \sim 3.2 \times 10^3 \mathrm{cm}^2\ \mathrm{s}^{-1}, \quad (9c)$$
$$\nu_m \sim 1.5 \times 10^{-8} \mathrm{cm}^2\ \mathrm{s}^{-1}. \quad (9d)$$

Here, the values for σ and ν are given for temperature $T \sim 10^8$ K. Therefore, $V_\mathrm{A} \sim 2.8 \times 10^4$ cm s^{-1}, $V_\Omega \sim 3.8 \times 10^9$ cm s^{-1}, Le $\sim 7.5 \times 10^{-6}$, $E \sim 8.4 \times 10^{-13}$, and $E_m \sim 4 \times 10^{-24}$. We note that the magnetic Prandtl number $\nu/\nu_m = E/E_m \sim 10^{11}$ is extremely large. This means that the diffusion of magnetic perturbations is a negligible source of dissipation. As consequence, we may simplify the set of equations by setting $E_m = 0$. In this case the magnetic perturbation is readily given by the fluid flow, namely

$$\vec{b} = \lambda^{-1} \nabla \times (\vec{u} \times \vec{B})$$

Hence, the set of equations reduce to

$$\lambda \nabla \times \mathbf{u} + \nabla \times (\mathbf{e}_z \times \mathbf{u}) =$$
$$\mathrm{Le}^2 \nabla \times \Big[(\nabla \times \nabla \times (\vec{\mathrm{u}} \times \vec{\mathrm{B}})) \times \mathbf{B} \Big] + \mathrm{E} \nabla \times \Delta \mathbf{v}, \quad (10a)$$
$$\nabla \cdot \mathbf{v} = 0, \quad (10b)$$
$$(10b)$$

This system is completed by boundary conditions on the velocity solely. Indeed the magnetic field is completely frozen in the fluid and the magnetic perturbations just represent the oscillations of the dipole field lines. Interestingly, boundary conditions on the magnetic field show that if $E_m = 0$ then $v_\theta = v_\varphi = 0$. This means that on the inner core boundary no slip boundary conditions apply. This is natural since the core is assumed at rest and no motion of the field lines is authorized there.

The small value of the Lehnert number suggest that the coupling between the r-modes and the magnetic field is quite weak. We readily see from the simplified perturbations equations that the influence of Lorentz force will be noticeable compared to the viscous one, if Le $\geq \sqrt{\mathrm{E}}$. Noting that the Lorentz operator and the viscous operator are both of second order, we observe that no length scale comes into this inequality. This means that it is valid both in the Ekman boundary layers and in the bulk of the layer. From the numbers that characterize neutron stars we see that inequality is met, which means that the magnetic field influence the flow more than the viscosity and possibly change the instability of the r-modes. A more detailed calculation is now necessary to assess the effect. It cannot be excluded a priori that some non dimensional factors renders this effect negligible. Therefore, we now turn to a numerical study of this problem.

III. SPHERICAL HARMONIC PROJECTION

To solve the eigenvalue problem expressed by Eq. (5), we project the set of equations on the spherical harmonics. We expand the perturbed velocity and magnetic fields into poloidal and toroidal components:

$$\mathbf{v} = \sum_{\ell=0}^{\infty} \sum_{m=-\ell}^{\ell} u_m^\ell(r) \mathbf{R}_\ell^m + v_m^\ell(r) \mathbf{S}_\ell^m + w_m^\ell(r) \mathbf{T}_\ell^m, \quad (11a)$$
$$\mathbf{b} = \sum_{\ell=0}^{\infty} \sum_{m=-\ell}^{\ell} a_m^\ell(r) \mathbf{R}_\ell^m + b_m^\ell(r) \mathbf{S}_\ell^m + c_m^\ell(r) \mathbf{T}_\ell^m, \quad (11b)$$

where the radial functions $\{u_m^\ell, v_m^\ell\}$ ($\{a_m^\ell, b_m^\ell\}$) and $\{w_m^\ell\}$ ($\{c_m^\ell\}$) are the poloidal and toroidal parts of the velocity (magnetic) fields, respectively. $\mathbf{R}_\ell^m$, $\mathbf{S}_\ell^m$, and $\mathbf{T}_\ell^m$ are the vectorial spherical harmonics

$$\mathbf{R}_\ell^m = Y_\ell^m \mathbf{e}_r, \quad \mathbf{S}_\ell^m = r \nabla Y_\ell^m, \quad \mathbf{T}_\ell^m = r \nabla \times \mathbf{R}_\ell^m. \quad (12)$$

The harmonic decomposition of Eqs., (6a) and (7) is given in appendix.

Equation (5) reduces to an eigenvalue problem

$$\mathrm{A}\mathbf{x} = \lambda \mathrm{B}\mathbf{x}, \quad (13)$$

where A and B are differential operators with respect to the r variable only.

Equation (5) reduces to an eigenvalue problem

$$\mathrm{A}\mathbf{x} = \lambda \mathrm{B}\mathbf{x}, \quad (14)$$

where A and B are differential operators with respect to the r variable only.

A. Numerical aspects

We just recall here that the equations governing the radial functions $u^\ell_m, v^\ell_m, w^\ell_m, a^\ell_m, b^\ell_m, c^\ell_m$ are discretized using the Gauss-Lobatto grid and the resulting eigenvalue problem is solved either with a QZ method or with the Arnoldi-Chebyshev algorithm according to whether we solve for the complete spectrum or a few eigenvalues.

IV. R-MODES-ALFVÉN WAVES COUPLING

R-modes are a subclass of inertial modes which are purely toroidal. In the case of a non-magnetic and inviscid incompressible fluid, exact analytical solutions exist [?,] and the associated velocity field can be written as

$$\mathbf{v} = [\ell(\ell+1)]^{-1/2}\alpha R\Omega(r/R)^\ell \mathbf{T}^\ell_\ell, \tag{15}$$

where α is an arbitrary constant. The mode's frequency in the frame corotating with the fluid is given by

$$\omega = -2\Omega/(m+1). \tag{16}$$

Here, we shall focus on the r-mode, with $m = 2$ which is the most unstable when coupled to gravitational radiation.

A. Damping rate versus Lehnert number

Since we assumed an infinite magnetic Prandtl number, we noted that the boundary conditions on the inner core boundary are of no-slip type. This means that for Le $\ll \sqrt{\mathrm{E}}$ the damping rate follows the law derived in Rieutord 2003, namely

$$\tau = -\frac{35}{2^{7/2}}\frac{1+\eta^6}{1-\eta^7}\mathcal{I}_2\sqrt{E}, \quad \text{with} \quad \mathcal{I}_2 \simeq 0.804$$

If $\eta = 0.35$, $\tau = -2.494\sqrt{E}$.

In Fig1 we have plotted the damping rate with a set of given Ekman number. When $\epsilon(Le)$ is zero the damping rate dose vary with Ekman number linearly as we expect. But with adding the coupling coefficient the behavior of the damping rate will decouple with linear behavior. For big coupling coefficient, the damping rate is independent on the Ekman number.

In Fig2 we have plotted the damping rate with coupling coefficient Le. It will show the above behavior. We should explain why $|\tau|$ first decreases. In the weak field limit we see that the characteristics are curved, why ?

Final questions: can we define Le$_\mathrm{c}$? a critical Lehnert number, for instance such that $\tau = 2\tau(\mathrm{Le} = 0)$, beyond

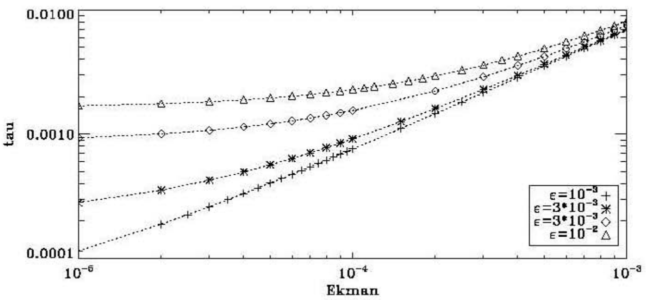

FIG. 1. The behaviour of damping rate with Ekman number.

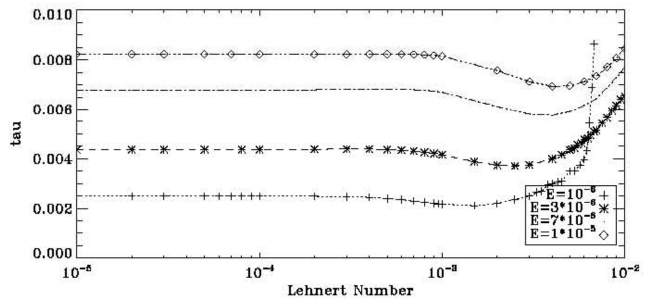

FIG. 2. The behaviour of damping rate with Lenhart number.

which the magnetic fully controls the damping. If a good definition of Le$_\mathrm{c}$ exists, then obviously Le$_\mathrm{c} \equiv$ Le$_\mathrm{c}$(E) and most probably Le$_\mathrm{c} = \alpha\sqrt{\mathrm{E}}$. The interesting point is then what's the value of α. If $\alpha \gg 1$ then no hope that the B-field pertubs damping, on the contrary $\alpha \ll 1$, B-field is essential. Other point, how does α depends on η.

Other small question: how does the boundary layer change when Le increases? is it what has been predicted by Mendell et al ?

Acknowledgements We wish to thank ...

[1] Rieutord M., ApJ, 2001, 557, 493.
[2] Rieutord M. 1991, Geophys. Astrophys. Fluid Dyn., 59, 185
[3] Rincon F. & Rieutord M. 2003, A&A, 398, 663
[4] Biront D., Goossens M., Cousens A., & Mestel, L. 1982, MNRAS, 201, 61
[5] Abramowitz M. & Stegun I. A., eds. 1972, Handbook of Mathematical Functions (New York: Dover)
[6] Bigot L. & Dziembowski, W. A. 2002, A&A, 391, 235

PROBING THE TIME VARIABILITY OF BROAD ABSORPTION LINE SYSTEMS

A. Aghaee[1,2], R. Srianand[3] and P. Petitjean[4]
[1] *Department of Physics, University of Sistan and Baluchestan, Zahedan 98135-674, Iran*
[2] *School of Astronomy, Institute for Research in Fundamental Sciences (IPM), P. O. Box 19395-5531, Tehran, Iran*
[3] *IUCAA, Post Bag 4, Ganeshkhind, Pune 411 007, India*
[4] *Institut d'Astrophysique de Paris, Université Paris 06 & CNRS, UMR7095, 98bis Bd Arago, 75014 Paris, France*

Clues on the nature and origin of high velocity quasar outflows are important for our understanding of the dynamics of gas in the central regions of Active Galactic Nuclei (AGNs) as well as the metal enrichment of the Inter Galactic Medium (IGM). Line radiation pressure has often been suggested to be an important process in driving these outflows. However, no convincing evidence has been given so far: line-locking is still controversial and no clear case of accelerating/decelerating clouds has been seen. Continuous monitoring of these sources is important for understanding of (a) the nature and origin of the flow, (b) the contribution of drag forces (or confining medium) and/or (c) the dynamical evolution of the outflow and the Broad Line Region (BLR). In particular, detailed investigations of variability of Low Ionization Broad Absorption Line (LBAL) quasars (QSOs) is an unexplored territory. We have observed some of these objects that will be analyzed.

PACS numbers: 05.10.-a ,05.10.Gg, 98.70.Vc

I. INTRODUCTION

Associated absorption systems (with $z_{\rm abs} \simeq z_{\rm em}$) seen in the spectra of high-z QSOs can be classified as: (i) Broad absorption systems (or BALs) with widths $\Delta v \sim$ a few 1000 km s^{-1}; (ii) mini-BALs with $\Delta v \sim$ a few 100 km s^{-1} and (iii) Narrow associated systems (or NALs) with $\Delta v \sim$ a few 10 km s^{-1}. Although low-ionization species such as Mg II and Fe II are seen in a few cases (see e.g. [1]), the BALs are characterized by the presence of very highly ionized gas. The column density ratios N(OVI)/N(HI), N(NV)/N(HI) and N(CIV)/N(HI) are much larger than unity indicative of metallicities of the order or larger than solar. BALs and mini-BALs are associated with the central regions of the QSO, which need not be the case for NALs with $z_{\rm abs} \sim z_{\rm em}$. However, the shape of the lines and the ionization state of the gas make it easy to differentiate the systems arising in ejected gas and those arising from gas belonging to the host-galaxy or even to members of a galaxy cluster surrounding the QSO. It has been shown that the gas ejected by AGNs has high metallicity, ($Z \geq Z_{\odot}$), high values of ionization parameter and the corresponding clouds have dimensions so small that they often cover the continuum and broad line region only partially (e.g. [2]; [3]). In a few cases absorption due to excited fine-structure transitions have been detected. The derived particle density, based on the fine-structure excitation, is large ($n > 1000$ cm^{-3}). In addition, a few lines have been shown to vary and signatures of radiative acceleration (line-locking) have been claimed (e.g. [4], [5], [6], [7]).

II. ABSORPTION LINE VARIABILITY

The residual flux in the bottom of the associated absorption lines toward most of the AGNs show variability. The simplest explanation for variability is a change in the ionizing conditions of the absorbing gas. In that case the variability time-scale is directly related to the recombination time-scale. Thus the observed variability in the residual flux can be used to constrain the particle density if it correlates with changes in the ionizing continuum. However it is known that, due to complex density and velocity fields in the BLR, the covering factor (f_c) one estimates from the absorption is the fraction of photons occulted by the absorbing cloud. It is not necessarily the same as the fractional area covered by the cloud. Thus dynamical effects like, changes in the BLR structure, motion of the absorbing clouds across our line of sight and finite light travel time in the BLR can produce variability in the absorption lines (see [8]) without being triggered by a continuum variability (see Fig. 1). Luckily, although difficult, it is possible to distinguish between these alternatives from observation of the variability of several absorption doublets of different ionization levels, mostly CIV$\lambda\lambda$1548,1550, NV$\lambda\lambda$1238,1242 and OVI$\lambda\lambda$1031,1037.

III. DYNAMICAL EVOLUTION OF THE BLR

The structure and dynamical evolution of the BLR in nearby Seyfert galaxies are probed by reverberation mapping techniques ([9]). Using the transfer function obtained from the time series data of continuum and emission line fluxes one can decipher the physical conditions in the BLR. Even though emission line profile variations

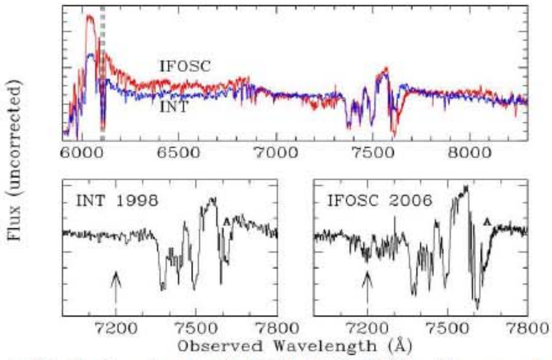

FIG. 1. Spectrum of APM 0827+5255. Top panel shows our IFOSC spectrum observed on Jan 18, 2006 together with the INT spectrum observed on Feb 27, 1998. Lower panels show the C IV BAL observed during the two epochs. Our IFOSC spectrum shows the presence of a new C IV absorption component (marked with an arrow). Features marked with A are atmospheric absorption.

follow continuum variations over a period of days, it has been noticed that long period variations in the profiles are not due to ionization changes but rather to dynamical changes of a clumpy BLR (see [10]). The dynamical time-scale of BLR material crossing the BLR is of the order of one to few years in these objects. Indeed the cloud crossing time across the region occulted by the absorbing gas will be $\sqrt{f_c}$ time that for crossing the BLR. Thus the characteristic timescales are small. As reverberation mapping studies of high-z QSOs are difficult, due to small observed continuum variability, one has to rely on some other indirect techniques to study the structure of the BLR. One can use differential amplification seen between continuum and emission lines in few closely spaced gravitationally lensed QSOs (see [11]). However, there is only one clear case where this technique is applicable. Thus probing the BLR dynamics through the variability of the covering factor in the associated absorption system is a unique alternative that has not been explored so far.

IV. RADIATIVE ACCELERATION

It has been suggested for long that the momentum transfered through resonance absorption lines could play an important role in driving out flows from QSOs as it does in the case of O star winds ([12], [13]).

A possible way to reveal line-driven acceleration is the presence of absorption features with velocity separation similar to doublet and/or multiplet splittings (a consequence of the so-called line-locking effect). Such a structure in absorption is achieved when there is a reduction in the line flux that drives the far away gas element due to absorption produced by the gas closer to the QSO ([14]). The gas from different elements of the flow must therefore cover the same region of the background source. As discussed above the gas producing intrinsic absorption is known to cover the background source only partially. Thus, to achieve line-locking in the case of QSOs, the flow must be somehow collimated. This may be the reason why tentative evidences for line-locking ([15], [5], [6], [16]) as well as double through (the so-called Ly α ghost) seen in the mean profile of BALs ([17] [18], [13]) are not completely convincing. For the first time, Srianand *et al.* have observed a very clear example of collimated radiation-driven flow that shows line-locking (in Q 1511+090; [19]). However, there is not a single case of detection of acceleration/deceleration of the absorbing gas as predicted by radiative acceleration models (eg. [20]). Thus systematic monitoring of a well chosen set of BAL QSOs will be important to understand the nature, origin and the influence of these outflows.

V. OBSERVATIONS AND PERSPECTIVES

We observed some SDSS BAL QSOs using the 2-m telescope at IUCAA Girawali Observatory (IGO) in India. The observations have been carried out from 2009/12/15 to 2009/12/17. Long-slit spectra covering the wavelength range 3300 - 8300 Åwere obtained using the GR1, GR7, and GR8 grisms of the IUCAA Faint Object Spectrograph (IFOSC) and a slit width of 1.5 arcsec. IFOSC employs an EEV 2Kx2K, thinned, back-illuminated CCD with 13.5μm pixels. The spatial sampling scale at the detector is 44μm per arcsecond giving a field of view of about 10.5 arcminutes on the side. Data reduction and analysis of these data will be done in the near future.

[1] Wampler E. J., Chugai N. N., and Petitjean P., 1995, ApJ, 443, 586.
[2] Petitjean P. *et al.*, 1994, A&A, 291, 29.
[3] Hamann T., 1997, ApJS, 109, 279.
[4] Petitjean P. & Srianand R., 1999, A&A, 345, 73.
[5] Srianand R., 2000, ApJ, 528, 617.
[6] Srianand R. & Petitjean P., 2000, A&A, 357, 414.
[7] Srianand R. & Petitjean P., 2001, A&A 373, 816.
[8] Srianand R. & Shankaranarayanan S., 1999, ApJ, 518, 672.
[9] Peterson B. M., 1993, PASP, 105, 247.
[10] Wanders I. & Peterson B. M., 1996, ApJ, 466, 174.
[11] Narasimha D. & Srianand R., 2000, BASI, 28, 395.
[12] Castor J. I., Abbott D. C. & Klein R. I., 1975, ApJ, 195, 157.
[13] Arav N., Li Z. Y., & Begelman M. C., 1994, ApJ, 432, 62.
[14] Scargle J. D., 1973, ApJ, 179, 705.
[15] Foltz C. B. *et al.*, 1987, ApJ, 317,450.
[16] Vilkovsikiji E. Y. & Irwin M. J., 2001, MNRAS, 321,4.

[17] Weymann R. J. *et al.*, 1991, ApJ, 373,23.
[18] Korista K. T. *et al.*, 1993, ApJS, 88, 357.
[19] Srianand R. *et al.*, 2002, MNRAS, 336, 753.
[20] Murray N. *et al.*, 1995, ApJ, 441,498.

Study of ambipolar diffusion in filamentary clouds by Adomian decomposition method

Ali-Reza Khesali, Mohsen Nejad-Asghar, Nahid Bahmani
Department of Physics, University of Mazandaran, Babolsar, Iran

The decomposition method for studying the evolution of an isothermal prolate magnetized molecular core has been implemented. By assuming a declining density profile for initial value, the diffusion of the magnetic field and its drift velocity are calculated. The results show that diffusion of the magnetic field near the cylinder axis is more occurred relative to its intermediate and external regions. On the other hand, the inner plasma particles move toward the axis of the cylinder while the intermediate and outer ion particles move outwards. This feature, which causes decreasing of the density in the inner region of the cloud and increasing of it in the intermediate area, may be responsible to explain the formation of small scale condensations in the intermediate region of a collapsing molecular cloud.
PACS numbers: 98.38.Dq, 02.60.Jh, 02.60.Lj

I. INTRODUCTION

Molecular clouds are regions of relatively dense interstellar gas and dust that can shield their contents against the destructive ambient ultraviolet (UV) radiation field. In such a cold, protected environment the predominant form of matter, atomic hydrogen, preferentially associates into molecular hydrogen. Substructure within these clouds is a complex pattern of filaments, sheets, bubbles, irregular clumps, and cores. Many people have calculated the collapse and fragmentation of cores. [1] [2] Magnetic fields are important many astrophysical situations. They may control the dynamics of the interstellar medium from small scales to very large scales. They may play a vital role in the evolution of interstellar clouds and, therefore, in the onset of protostar formation. [3] Magnetic fields thread all interstellar space and act upon ions and electrons.

In a molecular cloud, where the fractional ionization is very low, neutral particles only rarely encounter charged particles, and so are not well-coupled. Thus, the interstellar magnetic field can drag the ions through the neutral gas which is known as ambipolar diffusion process.Mestel suggested that the magnetic field could be removed from the cloud core by ambipolar diffusion, in which neutral gas drifts under the influence of gravity through ionized material tied to the magnetic fields [4]. Stodólkiewicz found solutions for the equilibrium structure of an isothermal cylinder, for a fluid where the ratio of gas pressure to magnetic pressure is constant [5]. Hennebelle explored a set of self-similar solutions for a rotating, magnetized cylindrical filament that may undergo collapse in the axial direction, in addition to radial collapse [6]. Numerically, the problem of ambipolar diffusion in self-gravitating infinite cylinders has been challenged at length in some papers for example by [7]–[8]. One-dimensional similarity solutions for a collapsing, homogeneous, infinitely long cylinder that is subject to ambipolar diffusion was investigated by Fröhlich [9]. The goal of this paper is to solve the equations of the collapsing isothermal cylinder by decomposition method, including magnetic and ambipolar diffusion effects.

II. BASIC EQUATIONS

In order to study ambipolar diffusion in a filamentary Molecular cloud, we start by writing the equations of magnetohydrodynamics in cylindrical coordinates (r, φ, z) .We consider axisymmetric and long filaments along z-axis.Thus, all the physical variables depend just on the radial distance r and time t . As for the magnetic field geometry, the axial component B_z of the field is assumed to be dominant. The governing equations are the continuity equation,

The conservation of mass equation,

$$\frac{\partial\rho}{\partial t} + v\frac{\partial\rho}{\partial r} + \frac{\rho}{r}\frac{\partial}{\partial r}(rv) = 0, \tag{1}$$

The momentum equation,

$$\rho\frac{\partial v}{\partial t} + \rho v\frac{\partial v}{\partial r} + \frac{\partial P}{\partial r} + \frac{1}{2\mu}\frac{\partial B^2}{\partial r} + (\rho g) = 0, \tag{2}$$

The Poisson's equation,

$$\frac{1}{r}\frac{\partial(rg)}{\partial r} = 4\pi G\rho, \tag{3}$$

And the induction equation,

$$\frac{\partial B}{\partial t} + v\frac{\partial B}{\partial r} + \frac{B}{r}\frac{\partial(rv)}{\partial r} = \frac{1}{r}\frac{\partial(rBv_d)}{\partial r}, \tag{4}$$

Where v_d is the relative drift between the ions and the neutrals,

$$\mathbf{v_d} = \mathbf{v_i} - \mathbf{v_n} = -\frac{1}{\mu_0\gamma_{\mathbf{ad}}\, C\rho^{3/2}}\mathbf{B}\frac{\partial\mathbf{B}}{\partial\mathbf{r}}\hat{\mathbf{r}}, \tag{5}$$

Where $\mathbf{v_i}$ and $\mathbf{v_n}$ are the ion and neutral velocities, respectively. This relation is obtained by assumption that the Lorantz force and the drag force must vastly dominate other forces that acts on the charged species.γ_{ad} is the collision drag coefficient in molecular cloud that is $3.5 \times 10^{10} m^3 kg^{-1} s^{-1}$. Here we use the canonical expression $\rho_i = \varepsilon \rho^{\frac{1}{2}}$,which $\varepsilon \sim 7.5 \times 10^{-15} kg^{\frac{1}{2}} m^{\frac{3}{2}}$.we also assume an isothermal relation between the gas pressure and the density, $p \propto \rho$. We put the basic equation(1-4) in dimensionless form by using appropriate units for time , magnetic field,velocity,radial distance,mass density, gravitational acceleration.

$$r \to \widetilde{v}\widetilde{t}r, \qquad B \to B\widetilde{B}, \qquad \rho \to \rho\widetilde{\rho},$$

$$t \to t\widetilde{t}, \qquad v \to v\widetilde{v}, \qquad g \to \frac{\widetilde{v}}{\widetilde{t}}g,$$

$$v_d \to \widetilde{v}v_d, \qquad \widetilde{B} \to \widetilde{v}\sqrt{2\mu\widetilde{\rho}}, \qquad \widetilde{t} \to 4\pi G\widetilde{\rho}$$

Now equation(1-4) is continuing;

$$\frac{\partial \rho}{\partial t} = -v\frac{\partial \rho}{\partial r} - \rho\frac{\partial v}{\partial r} - \frac{\rho v}{r}, \tag{6}$$

$$\frac{\partial v}{\partial t} = -v\frac{\partial v}{\partial r} - \frac{1}{\rho}\frac{\partial \rho}{\partial r} - \frac{1}{\rho}\frac{\partial B^2}{\partial r} - g, \tag{7}$$

$$\frac{\partial g}{\partial r} = \rho - \frac{g}{r}, \tag{8}$$

$$\frac{\partial B}{\partial t} = -v\frac{\partial B}{\partial r} - B\frac{\partial v}{\partial r} - \frac{vB}{r} + \frac{\eta_{ad}}{\rho^{\frac{3}{2}}}(B^2\frac{\partial^2 B}{\partial r^2} + 2B(\frac{\partial B}{\partial r})^2 + \frac{B}{r}\frac{\partial B}{\partial r} - \frac{3B^2}{2\rho}\frac{\partial \rho}{\partial r}\frac{\partial B}{\partial r})), \tag{9}$$

Where all quantities are dimensionless and

$$\eta_{ad} = \frac{\widetilde{B}^2\widetilde{t}}{\mu\gamma_{ad}\ \varepsilon\ \widetilde{\rho}^{\ \frac{3}{2}}\ \widetilde{r}^{\ 2}}, \tag{10}$$

III. IMPLEMENTATION OF THE METHOD

The Adomian decomposition method has been widely used with promising results in linear and nonlinear partial differential equation and consists of decomposing the unknown function $u(x, y)$ of any equation into a sum of an infinite number of components defined by the decomposition series

$$u(x, y) = \sum_{n=0}^{\infty} u_n(x, y)$$

Where the components $u_n(x, y), n \geq 0$ are to be determined in a recursive manner [10]. However,the nonlinear term $F(u)$, such as $u^2, u^3, u^4, sinu, e^u$ etc.Can be expressed by infinite series of the so-called Adomian polynomials A_n given in the form

$$F(u) = \sum_{n=0}^{\infty} A_n(u_0, u_1, u_2, ..., u_n)$$

Where the so-called Adomian polynomials A_n can be evaluated for all forms of nonlinearity. The Adomian polynomials A_n for the nonlinear term $F(u)$ can be evaluated by using the following expression

$$A_n = [(\frac{1}{n!})(\frac{d^n}{d\lambda^n})F(u(\lambda))]_{\lambda=0},$$

For solution of equation ,we must have boundary conditions .we obtain recursive relation by using of boundary condition . Boundary Condition are the continue condition,

$$g(0, t) = 0, \quad v(0, t) = 0,$$

$$\rho(0, t) = \frac{1}{(1 + 0.01r^2)^2}, \qquad B(0, t) = \alpha\sqrt{\rho(r, 0)},$$

And For solve the nonlinear partial differential equation (6-9) ,at first we write the equation in an operator form and then the nonlinear terms are replaced by Adomian polynomials A_n, C_n, D_n.

$$L_t\rho = \sum_{n=0}^{\infty} A_n \tag{11}$$

$$L_t v = \sum_{n=0}^{\infty} c_n - g \tag{12}$$

$$L_t g = \rho - \frac{g}{r} \tag{13}$$

$$L_t B = \sum_{n=0}^{\infty} D_n \tag{14}$$

Where L_t and L_t^{-1} is defined by

$$L_t = \frac{\partial}{\partial t}, \qquad L_t^{-1}(.) = \int_0^t (.)dt$$

Applying L_t^{-1} to both sides of (13) and using initial condition and choosing $g_0(r, t) = 0$ we obtain recursive relation;

$$g_{n+1} = L_r^{-1}(\rho_n - \frac{g_n}{r}) \tag{15}$$

Applying the inverse operator L_t^{-1} to both sides of (11),(12).(14) and using the initial condition we find

$$\rho(r, t) = L_t^{-1}(\sum_{n=0}^{\infty} A_n) + \rho(0, t) \tag{16}$$

$$v(r,t) = L_t^{-1}(\sum_{n=0}^{\infty} C_n - g) \tag{17}$$

$$B(r,t) = L_t^{-1}(\sum_{n=0}^{\infty} D_n) + B(0,t) \tag{18}$$

Substituting

$$\rho(r,t) = \sum_{n=0}^{\infty} \rho_n(r,t) \tag{19}$$

$$g(r,t) = \sum_{n=0}^{\infty} g_n(r,t) \tag{20}$$

$$v(r,t) = \sum_{n=0}^{\infty} v_n(r,t) \tag{21}$$

$$B(r,t) = \sum_{n=0}^{\infty} B_n(r,t) \tag{22}$$

We find recursive relation ;

$$\rho_{n+1} = L_t^{-1}(A_n) \tag{23}$$

$$v_{n+1} = L_t^{-1}(C_n - g_n) \tag{24}$$

$$B_{n+1} = L_t^{-1}(D_n) \tag{25}$$

IV. SUMMARY AND CONCLUSION

It is well known that the ambipolar diffusion, the relative motion of plasma and neutral particles, is an important mechanism in the weakly ionized gases. It is rapidity of this ambipolar diffusion which makes the notion of a long filament contracting almost purely in radial direction feasible. Filamentary structures are commonly seen in giant molecular clouds as sites in which star-forming clumps are embedded. Gravitational fragmentation, i.e. the formation of clumps which might eventually evolve into star-forming spheroidal cores, probably needs a longer time span. We have determined the structure of a collapsing magnetized isothermal cylinder by the Adomian's decomposition method. The decomposition method, which has been receiving much attention in recent years in applied mathematics in general, demonstrates fast convergence of the solution and therefore provides several significant advantages. The method attacks the problem in a direct way without using linearization, perturbation or any other restrictive assumption that may change the physical behavior of the model

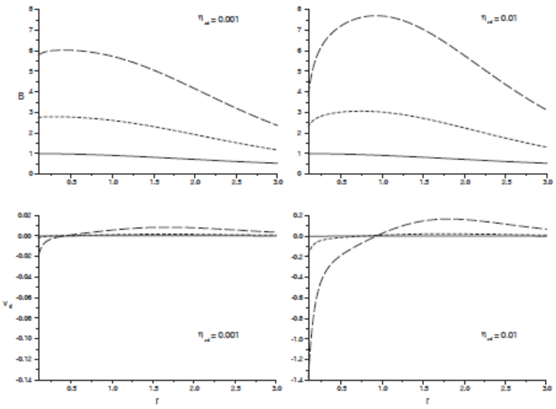

FIG. 1. The evolution of magnetic field and drift velocity in a cylindrical molecular cloud at times $t = 0$ (solid), $t = 3$ (dot), and $t = 5$ (dash), with the coefficient η_{ad} equal to 0.001 and 0.01.

under discussion. Our solutions are related to the case of the observed steeply declining density profile in a filamentary structure. The strength of ambipolar diffusion is measured by the coefficient η_{ad} in Eq(10), which its value is approximately near $0.001 - 0.01$ in a typical molecular cloud. The evolution of magnetic field strength and the drift velocity, for η_{ad} equal to 0.001 and 0.01, are shown in Fig(1). It is worth noting that, as time goes on, the diffusion of the magnetic field near the cylinder axis is more occurred relative to its intermediate and external regions. Therefore, the drift velocity that depends on the gradient of magnetic field, is negative in the vicinity of the cylinder axis, namely, the inner plasma particles are plunging toward the center faster than the neutrals, while the intermediate and outer ion particles are moving in slower than the neutrals also are still plunging in toward the center. The effect of ambipolar diffusion with two typical values of the diffusion parameter η_{ad} is shown in Fig(1). It is clear that increasing the value of diffusion parameter η_{ad} causes to amplify the effect of ambipolar diffusion. The diffusion of the magnetic field near the cylinder axis is more occurred relative to its intermediate and external regions. In Fig (2), we demonstrate the difference of two densities; one proper to considering the ambipolar diffusion and other without it. This difference in the vicinity of the cylinder axis and its intermediate region show that allowing for ambipolar diffusion leads to relative decrease the density in the inner region of the cloud while it will be increase in the intermediate area. In the other words, in the case where ambipolar diffusion is present, the density increases slower in the inner regions while it increases faster in the intermediate area. The neutral gas thus condenses inward a quasihydrostatic state, although perfect equilibrium is generally not reached. When the condensing gas becomes sufficiently centrally concentrated, the innermost regions of

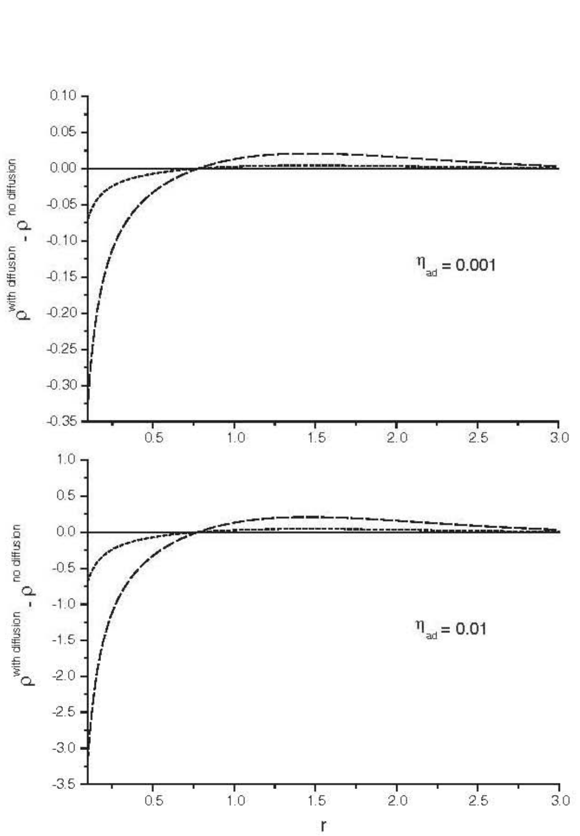

FIG. 2. The evolution of density difference, one proper to considering the ambipolar diffusion and other without it, in a cylindrical molecular cloud at times $t = 0$ (solid), $t = 3$ (dot), and $t = 5$ (dash), with the coefficient η_{ad} equal to 0.001 and 0.01.

the structure begin to collapse dynamically onto a growing protostar. As magnetic fields diffuse outward, gas condenses inward to form a centrally concentrated structure, a process that has been termed the gravomagneto catastrophe [11]. The treatment shows that the resulting inner region of the filament display non-zero, inward drift velocity at the end of the diffusion epoch, in agreement with current observations.

This effect causes to drop off the particles from the inner region of the filament to the intermediate area as depicted in Fig(2). Since the core is collapsing radially, the density should increase in both cases (with and without ambipolar diffusion). Actually, It should increase in the case ambipolar diffusion is present, but in a different way. One of the major conclusions of our study is that the difference of two densities, one proper to considering the ambipolar diffusion and other without it, expresses relative decrease of the density in the inner region of the cloud and increasing of it in the intermediate area. In the case ambipolar diffusion is considered there is a preferred radius (approximately 0.07 pc), which inside this scale the collapse is hindered. This feature may explain the formation of small scale condensations in the intermediate region of a collapsing molecular cloud.

[1] Bonnell, I., Bastien, P., 1992, ApJ, 401, 654.
[2] Boss, A.P., 2009, ApJ, 697, 1940.
[3] Crutcher, R.M., 1999, ApJ, 520, 706.
[4] Mestel, L., Spitzer, L.Jr., 1956, MNRAS, 116, 503.
[5] Stodólkiewicz, J.S., 1963, AcA, 13, 30.
[6] Hennebelle, P., 2003, A&A, 397, 381.
[7] Mouschovias, T.Ch., Morton, S.A., 1991, ApJ, 371, 296.
[8] Mouschovias, T.Ch., Morton, S.A., 1992, ApJ, 390, 144.
[9] Fröhlich, 2005, A&A, 441, 153.
[10] Wazwaz, A.M., 2002, Partial diffrential equations, Swets&Zeitlinger B.V., Lisse
[11] Adams, F.C.,& Shu, F.H., 2007, ApJ, 671, 497.

Cooling of the neutron star and direct URCA process

M. Bigdeli[1], G.H. Bordbar[2] and F. Rabet[1]
[1]*Department of Physics, Zanjan University,P.O.Box 45195-313, Zanjan, Iran*
[2]*Department of Physics, Shiraz University, Shiraz 71454, Iran*

In this paper, we have determined the threshold density for the occurrence of direct URCA process in the neutron star. According to our results, this process occurs at the density about 1.48 fm^{-3}.

PACS numbers: 21.65.-f, 26.60.-c, 64.70.-p

I. INTRODUCTION

Neutron stars are some of the massive objects in the universe. They are burn in the supernova explosions with interior temperatures of order 20-50 MeV. After several minutes, a neutron star enters the neutrino cooling epoch and then it is rapidly cooled via the neutrino emission. The simplest process that can explain the neutrino emission is the direct URCA process [1]. It consists of two reactions as follows,

$$n \rightarrow p + e^- + \bar{\nu}_e$$
$$p + e^- \rightarrow n + \nu_e. \quad (1)$$

The neutrino and antineutrino momenta ($p_\nu \approx k_B T/c$) are smaller than the Fermi momenta, and can be neglected. For the neutron star matter which consists of neutrons, protons and electrons (npe matter), the momentum conservation condition becomes [1],

$$p_{F_p} + p_{F_e} > p_{F_n}. \quad (2)$$

For this system, we also have the charge neutrality condition,

$$\rho_p = \rho_e, \quad (3)$$

where $\rho_i \propto p^3_{F_i}$ is the number density of particle i. According to above equations, the proton fraction, $Y = \frac{\rho_p}{\rho}$ ($\rho = \rho_n + \rho_p$ is the number density of baryons) at the threshold becomes $Y_c = \frac{1}{9}$. If the proton fraction exceeds the threshold, a neutron star will be cooled via the rapid direct URCA process.

In the neutron star matter, the proton fraction depends on the symmetry energy of the nuclear matter [1]. We calculate the nuclear symmetry energy as follows.

II. NUCLEAR SYMMETRY ENERGY

The energy per nucleon of the asymmetrical nuclear matter can be calculated by semi-empirical mass formula as [2,3],

$$E(\rho, \beta) = E(\rho, 0) + E_s(\rho)\beta^2 \quad (4)$$

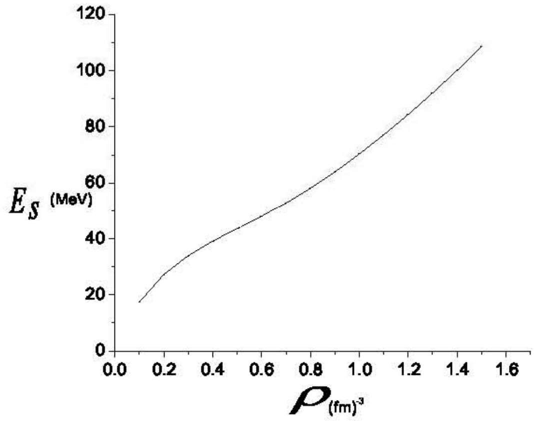

FIG. 1. Nuclear symmetry energy as a function of the baryon density.

where $\beta = (1 - 2Y)$ is the asymmetry parameter. $E_s(\rho)$ is the symmetry energy of the nuclear matter which is given by the following relation,

$$E_s(\rho) = E(\rho, 1) - E(\rho, 0). \quad (5)$$

$E(\rho, 1)$ and $E(\rho, 0)$ are the energy per particle of pure neutron matter and symmetrical nuclear matter respectively. In our calculations, these energies have been determined using the LOCV method [4,5].

According to the beta-equilibrium condition in the neutron star matter, we have

$$\mu_e = \mu_n - \mu_p = 2\frac{\partial E}{\partial \beta}, \quad (6)$$

where μ_i is the chemical potential of particle i. If electrons are assumed to be ultra relativistic, we can get

$$\hbar c(3\pi^2 \rho Y)^{1/3} = 4E_s(\rho)(1 - 2Y). \quad (7)$$

We see that the proton fraction can be calculated from the nuclear symmetry energy.

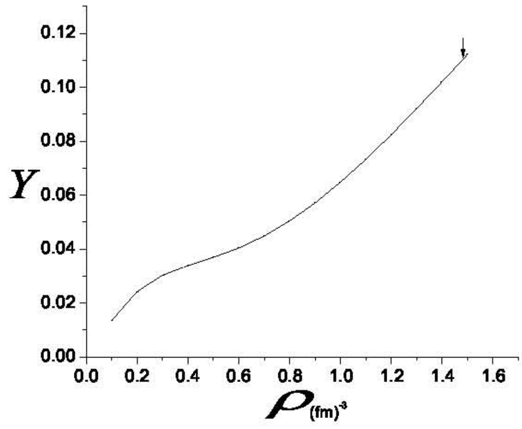

FIG. 2. Proton fraction versus the baryon density.

III. RESULTS AND DISCUSSION

The symmetry energy of nuclear matter has been plotted as a function of the baryon density in Fig. 1. This figure shows that the nuclear symmetry energy is an increasing function of the density.

We have also presented the proton fraction versus the baryon density in Fig. 2. As it can be seen from this figure, the threshold density for the occurrence of the direct URCA process (in which the proton fraction has the value $Y_c = \frac{1}{9}$) is about $\rho_c \approx 1.48\ fm^{-3}$.

[1] S. Shapiro and S. Teukolsky, Black Holes,White Dwarfs and Neutron Stars (Wiley-New York,1983).
[2] G.H. Bordbar and M. Modarres, Phys. Rev. **C 58**, 714 (1998).
[3] G. H. Bordbar and M. Bigdeli, Phys. Rev. **C 77**, 015805 (2008).
[4] G. H. Bordbar and M. Bigdeli, Phys. Rev. **C 75**, 045804 (2007).
[5] G. H. Bordbar and M. Bigdeli, Phys. Rev. **C 76**, 035803 (2007).

Magneto-Acoustic Waves in Solar Spicules

Ebadi, H.[1]
[1] *Department of Astrophysics, Physics Faculty, University of Tabriz, Tabriz, Iran*

The propagation of linear magnetohydrodynamics (MHD) waves in a spicule embedded in the coronal environment is investigated. Fast and slow body waves are presented under spicule conditions but the surface modes are absent. Moreover, slow body waves are overlapped in the spicule conditions. The cut-off value of the fundamental kink mode is c_k and it's phase speed has sharp increase towards long wavelengths. Steady flows change the treatments of propagating waves because of induced Doppler shifts. The flow also induces shifts in cut-off values and phase speeds of the waves. Down flows and out flows have different effects on cut-off values. The present work results suggest that the steady flow should be considered in the wave propagation models of solar spicules.

PACS numbers: 05.10.-a ,05.10.Gg, 98.70.Vc

I. INTRODUCTION

Spicules appear as grass-like, thin and elongated structures in images of the solar lower atmosphere and they are usually observable in chromospheric H_α, D_3 and Ca II H lines. These spiky jets are propelled upwards from the solar surface into the magnetized low atmosphere of the sun. Spicules are carry a mass flux of two order of magnitudes that of a solar wind into the low solar corona [1].
The Dispersion relation for flux tubes which are embedded in a medium with different parameters are derived by Edwin and Roberts [2] in a valuable work. They didn't assume the steady flow in their work. The presence of flows in the solar atmosphere has been discussed for a long time and there are many observational evidences to them. Their effect on the phase speed of magneto-acrostic waves comes arise from the Doppler shift related to them. Data derived from SUMER show a systematic correlation between a density-sensitive emission-line ratio and Doppler shift across the same profiles, which are thought to be caused by steady flows [3]. Recently it is generated to contain the steady flows [4] and they concluded that the effect of steady-state background has to be considered particularly carefully when evaluating observation signatures of MHD waves for diagnostics in the solar atmosphere.
So, the present work will be attempt to drive the same dispersion relation but with a different way as [4] one and the results will be applied to Magneto-Acoustic waves propagation in solar spicules.

II. BASIC EQUATIONS

The linearized MHD equations with steady flow are as follows [4], [5]:

$$\frac{\partial \rho}{\partial t} + (U_0 \cdot \nabla)\rho + \rho_0(\nabla \cdot v) = 0 \quad (1)$$

$$\rho_0 \frac{\partial v}{\partial t} + \rho_0 (U_0 \cdot \nabla) v = -\nabla p + \frac{1}{\mu}((\nabla \times b) \times B_0) \quad (2)$$

$$\frac{\partial b}{\partial t} = \nabla \times (U_0 \times b) + \nabla \times (v \times B_0) \quad (3)$$

$$\frac{\partial p}{\partial t} + (U_0 \cdot \nabla) p - c_0^2 (\frac{\partial \rho}{\partial t} + (U_0 \cdot \nabla)\rho) = 0 \quad (4)$$

if we assume Fourier transform of the perturbations as [6]:

$$v = v(r) e^{i(\omega t + n\theta - kz)} \quad (5)$$

and applying this to the MHD linear equations, we will arrive at the following relation for perturbed velocity:

$$\frac{d}{dr}[\frac{\rho_\alpha(r)(k^2 v_{A\alpha}^2(r) - \Omega_\alpha^2)}{m_\alpha^2 + \frac{n^2}{r^2}} \frac{1}{r}\frac{d}{dr}(r v(r))] - \rho_\alpha(r)(k^2 v_{A\alpha}^2(r) - \Omega_\alpha^2) v(r) = 0 \quad (6)$$

where subscript α=0 indicates the corresponded quantities inside the tube and α=e has the same meaning outside of it. Following these notations, m_α and Ω_α are as follows:

$$m_\alpha^2 = \frac{(k^2 c_\alpha^2 - \Omega_\alpha^2)(k^2 v_{A\alpha}^2 - \Omega_\alpha^2)}{(c_\alpha^2 + v_{A\alpha}^2)(k^2 c_{T\alpha}^2 - \Omega_\alpha^2)}, c_{T\alpha}^2 = \frac{c_\alpha^2 v_{A\alpha}^2}{c_\alpha^2 + v_{A\alpha}^2} \quad (7)$$

$$\Omega_\alpha = \omega + U_\alpha k \quad (8)$$

Here c_α and $v_{A\alpha}$ are the sound and Alfven waves respectively and ρ_α is mass density and U_α is corresponded to steady flow.
Continuity of the radial velocity component v(r) and the total pressure across the cylinder boundary r=a then yields the required dispersion relation:

$$\rho_e(\Omega_e^2 - k^2 v_{Ae}^2) m_0 \frac{I_n'(m_0 a)}{I_n(m_0 a)} = \rho_0(\Omega_0^2 - k^2 v_{A0}^2) m_e \frac{K_n'(m_e a)}{K_n(m_e a)} \quad (9)$$

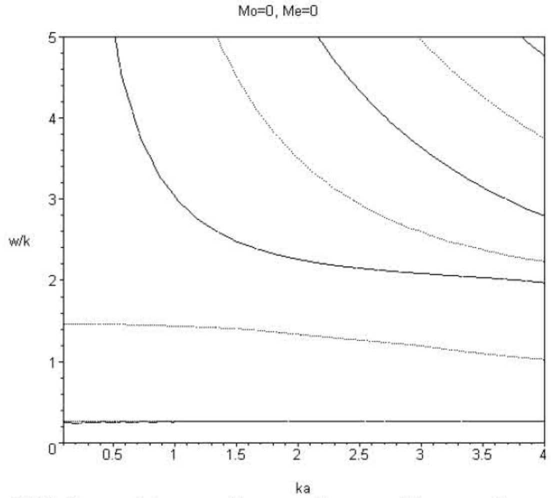

FIG. 1. caption caption caption caption caption caption caption caption caption caption caption caption.

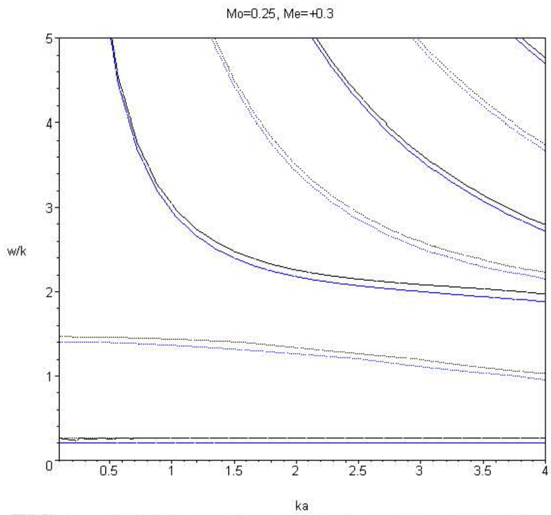

FIG. 2. caption caption caption caption caption caption caption caption caption caption caption caption.

This dispersion relation describes both surface ($m_0^2 > 0$) and body waves ($m_0^2 < 0$).
Let we define the full length of the spicule to be l=2L, the wavelength of the fundamental standing wave is λ=l and thus the wave number of the fundamental mode is k=$\frac{2\pi}{\lambda}=\frac{\pi}{l}$, while high order harmonics would have wave numbers k=$\frac{N\pi}{l}=\frac{N\pi}{2L}$ where N=1,2,... .

III. RESULTS AND DISCUSSION

In FIG. 1 we plot the phase speed variations under spicule and it's environment (coronal) conditions, i.e., $V_{A0} = 100\frac{km}{s}$, $V_{Ae} = 750\frac{km}{s}$, $c_0 = 25\frac{km}{s}$, $c_e = 115\frac{km}{s}$ and $\frac{\rho_0}{\rho_e} = \frac{1}{50}$. So, $c_k = 144\frac{km}{s}$, $c_T = 24\frac{km}{s}$ and $c_{Te} = 114\frac{km}{s}$ are calculated.
As it is clear from FIG. 1, in spicule conditions only fast and slow body waves are appeared and surface waves are absent. Because in spicule conditions $c_0 \simeq c_T$, so the slow body waves are overlapped. The fundamental kink mode cut-off value is c_k and it has sharp increase on long wavelengths limit which was expected.
In FIG. 2 we plotted the same but with steady flow taking into account. It is appear that the cut-off values and phase speeds are shifted because of flow. The steady flow caused the profiles to Doppler shifted and as result the frequencies of the waves to be changed.

IV. CONCLUSION

FIG. 1 illustrates the behavior of waves under coronal conditions, i.e. $V_{Ae}, V_{Ao} > c_e, c_e$. In such circumstances there are no longer any surface modes but two classes of body waves can occur. Of particular interest are the fast modes which arise only if $V_{Ae} > V_{Ao}$. Thus for coronal atmosphere fast body modes occur only if $\rho_0 > \rho_e$.
The cut-off values of the fast and slow body migrate due to the flow. they migrate to higher values of ka when the flow increases in the positive direction of z (FIG. 2) and decreases to the lower values for flows in the negative direction.
Finally, we conclude here that there is one main difference in the behavior of the waves in a magnetic cylinder in the presence of background flow: the phase speed of the first harmonic of the fast kink mode is Doppler shifted due to the flow.

[1] Zaqarashvili T. V. *et al.*, 2009, SSRv, 149, 355.
[2] Edwin R. M. *et al.*, 1983, SoPh, 88, 179.
[3] Judge P. G. *et al.*, 1998, ApJ, 502, 981.
[4] Terra-Homem M. *et al.*, 2003, SoPh, 217, 199.
[5] Aschwanden R. M., 2007, SoPh, 88, 179.
[6] Ajabshirizadeh A. *et al.*, 2009, ApSS, 319, 31.

Simulation of Maser Emission From Planetary Nebula Using the Monte Carlo Method

Mohsen Nejad-Asghar, Ali-Reza Khesali, and Mahjoobeh Elyasi
Department of Physics, University of Mazandaran, Babolsar, Iran

Maser emission can be observed in different regions of interstellar medium, such as planetary nebulae (PNe). In this research, radiation transfer and required condition for production of maser in PNe have been considered using the Monte Carlo method. For this purpose, a one-dimensional cloud layer have been used and the rate of maser generators have been considered in a parametric manner. Simulations show that with increasing the maser generators in the PNe, the intensity of the maser radiation is linearly increased. Slope of this line indicates a relation between intensity of produced maser and the total radiation of the PNe. Finally, the fraction of maser generators in some PNes have been determined by comparison of the relative intensity of masers with the observation results.

I. INTRODUCTION

More stars that passes through asymptotic giant branch (AGB) and reach the pre-PNe stage shows exhibits of maser emission from molecules OH and H_2O. After passing the red giant stage, gravity contracts the central star and as a result the star enters in to the PNe phase. In this phase, the gas around the central star is ionized and maser generators will disappear. We know that the water maser remains just for several decades, while hydroxide masers, which exist in PNe envelope, can survive for more than 1000 years (see, e.g., [1–3]).

Population inversion processes, which are amplified by pump, are the most important mechanism known to produce the maser in the interstellar medium. The question is that can we find a relation between maser generators and the observed relative intensity of radiation? We want to determine the fraction of maser generators by this relationship. For this purpose, we attend to the observations and measurements of H_2O and OH masers of three PNes: K3-35, Vy2-2 and IC4997. de Gregorio-Monsalvo et al. reported the water masers of 27 PNe using the VLA observations [3]. Their report shows that the flux density of water masers in K3-35 PNe and IC4997 are approximately equal to 2.9Jy and 0.5Jy, respectively. Also, they measured the flux density of H_2O maser from Vy2-2. Their results show that the flux density of water maser from this PNe is less than 0.014Jy. For the flux density of OH masers, we use the data of [1,2], which give the mean value 38.5mJy for Vy2-2 and the mean value 56.8mJy for K3-35. These mean values have obtained from different frequencies of hydroxide molecule radiation. Also, there has not been reported any maser radiation of OH molecules from IC4997. For the flux density in non-maser radiation, here we use the measurements of IRAS which was reported by [4] and [5]. According to these reports, we have 44.2Jy, 22.7Jy and 9.9Jy for flux density of non-maser radiation of Vy2-2, K3-35 and IC4997, respectively.

We use the radiative transfer equation to study the transmission of radiation through a gaseous cloud. If a system contains symmetry and homogeneity in its opacity source, radiative transfer problem can analytically be solved. But, in astrophysical systems such as PNes which do not have symmetric and homogeneous environment, radiation transfer equation should be solved by the simulation methods. In this way, we use the Monte Carlo method to solve the radiation transfer problem in multi-level and non-LTE systems as outlined by [6]. Also, we use this method to study the generation of masers in PNes [7]. In section 2, we describe the Monte Carlo method for radiation transfer. The simulation of maser generation in one dimensional layer is presented in section 3, and we find a relation between relative intensity of maser radiation and their generators. In section 4, we determine the fraction of maser generators of water and hydroxide in the three PNes: Vy2-2, K3-35 and IC4997 as the conclusion.

II. MONTE CARLO METHOD FOR RADIATION TRANSFER

In Monte Carlo method, we have dealing with propagation of photon packages and their interaction with matter within a medium. First, we should know the effect of matter on propagation of photons. We consider a homogeneous medium which is filled by absorbers and scatters with number density n and cross section σ. The radiation field intensity I_ν is defined as the beam's energy per unit time in the frequency range $d\nu$ that passes through surface area within a solid angle. The equation of radiation transfer as the beam passes through the medium is

$$\frac{dI_\nu}{dl} = -n\sigma I_\nu + j_\nu \qquad (1)$$

where j_ν is the emissivity.

The probability that a photon interacts within an infinitesimal length dl is $n\sigma dl$. If we divide a length L of medium using N segments of length dl, the probability of no interaction is $(1 - n\sigma\ L/N)^N$. If N is sufficiently large, then this probability can be written as $1 - n\sigma L \simeq \exp(-\tau)$ where $\tau = \int_0^L n\sigma\ dl$ is the optical depth in the line of sight L. Therefore, the probability that an interaction dose occur is $1- e^{-\tau} = n\sigma L$. When a photon interacts with the medium, one of two cases may happen: absorption or scattering. If a photon absorbed, we do not consider it and a new photon will propagate from the source. Thus, an absorbed photon do not have portion in output flux. On the other hand, scattered photon travels in a new direction that is determined by the angular phase function $P(\cos\theta)$ where θ is the scattering angle. The isotropic scattering angular phase function is $P(\cos\theta) = 1/2$.

Now, after expression of these initial concepts, we study the radiation transfer in a one dimensional layer of gas. We assume that the photons are radiated from the source and their flux in any direction of emission is isotropic. For transmission of photon in the cloud, a uniform random number $0 \leq \xi \leq 1$ is generated, and the polar and azimuth angels are produced by $\mu = \cos\theta = 2\xi - 1$ and $\phi = 2\pi\xi$, respectively. The initial positions of photons have been considered at the origin and their motions are directed in the unit vector

$$n_x = \sin\theta\cos\phi, n_y = \sin\theta\sin\phi, n_z = \cos\theta. \tag{2}$$

For one dimensional layer, the component z is only considered and we assume $z_{max} = 1$. The maximum optical depth of this layer is $\tau_{max} = n\sigma\ z_{max} = n\sigma$. The mean free path of the photon is given by $l_{mfp} = \tau/\tau_{max}$ where $\tau = -\ln\xi$. The photon's new position is determined by

$$\begin{aligned} X_{new} &= X_{old} + l_{mfp}\sin\theta\cos\phi, \\ Y_{new} &= Y_{old} + l_{mfp}\sin\theta\sin\phi, \\ Z_{new} &= Z_{old} + l_{mfp}\cos\theta. \end{aligned} \tag{3}$$

The passage of a beam in the medium with thickness z_{max} and the scattered direction θ after passing a layer with thickness dl are shown in Fig. 1. At this new position, the photon may be absorbed, scattered or escape from the cloud (i.e., $z > z_{max}$ or $z < 0$). We just consider the pure isotropic scattering, which the photons are scattered uniformly into 4π steradian. The new direction randomly produced by uniform sampling of ϕ and μ in the range $(0, 2\pi)$ and $(-1, 1)$, respectively. We repeat this procedure until photon exits from the cloud.

III. SIMULATION OF MASER PRODUCTION IN PNE

We consider a gaseous cloud which includes the generators of maser. In transmission of photons through

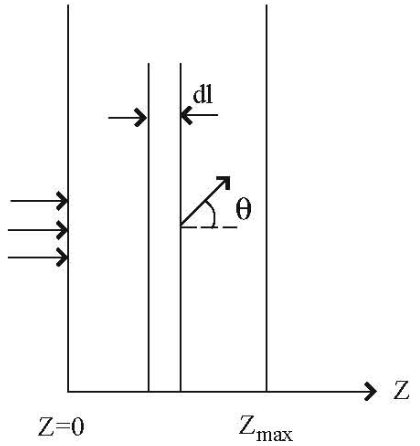

FIG. 1. The passage of radiation beam through the one dimensional layer. θ is the scattering angel.

this gas, they may encounter with maser generators. As shown in Fig. 2, a cloud with thickness L is considered, and n photons is sending into it. In angle bin θ_i, the number of outgoing photons is n_i and the number of produced maser photons is n'_i. This simulation has been done in a one-dimensional case and we ignore the magnetic field of the central star. Also, only it is considered the scattering of photons and ignored their absorption.

We use the radiative transfer equation (1) to study the passage of radiation in the gaseous cloud. Because the PNe is ionized, its spontaneous emission is negligible, and therefore we ignore emissivity j_ν in the radiation transfer equation. Thus, we write the equation of radiation transfer as follows

$$\frac{dI}{dl} = -n\sigma\ I + n_m\sigma_m\ I \tag{4}$$

where σ_m is the collision cross-section of maser generators and n_m is their number density. The first term in right hand side of equation (4) shows decay of radiation caused by opacity, while the second term indicates amplification of radiation caused by maser generators. Since the necessary condition to produce maser in environment is population inversion [7], the second term is appeared with a positive sing. Solving the equation of radiation transfer (4), we have

$$I = I_0\ e^{-\int_0^L n\sigma\ dl}\ e^{+\int_0^L n_m\sigma_m\ dl} = I_0\ e^{-\tau}\ e^{+\tau_m} \tag{5}$$

where I_0 is the initial radiation intensity and $\tau_m = n_m\sigma_m\ L$ is the reverse of maser optical depth. Defining $\alpha = n_m/n$ as relative abundance of maser generators, and $\beta = \sigma_m/\sigma$ as relative cross-sections, the reverse of optical depth of maser can be written as $\tau_m = \alpha\beta\tau$. In fact, α and β are free parameters in the model in which

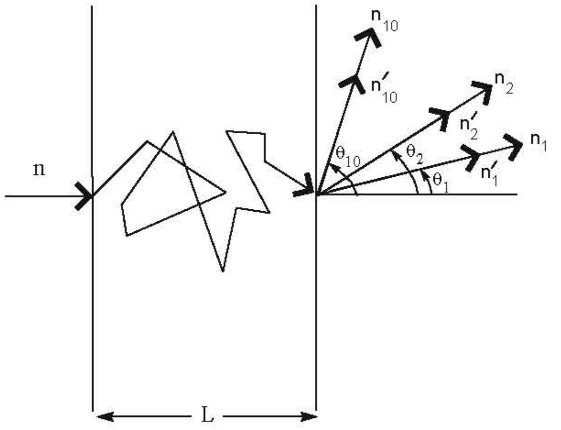

FIG. 2. Transmission of n photons through the one dimensional gaseous cloud and their scattering which lead to exiting in angel bins θ_1, θ_2, ..., θ_{10}. Number of photons in each angle bin is shown by $n_1 - n_{10}$ and the number of produced masers are given by $n'_1 - n'_{10}$.

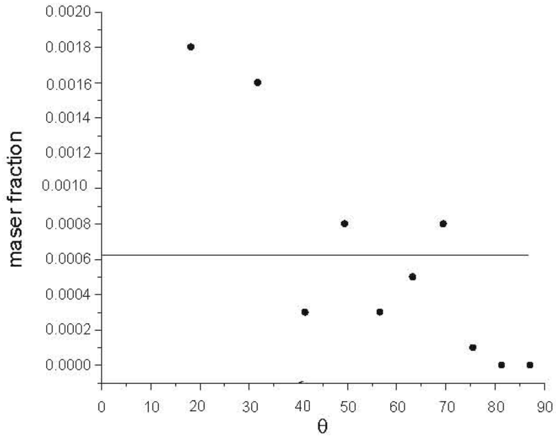

FIG. 3. Maser fraction at outgoing angle from the layer of PNe with $\alpha = 10^{-6}$. The solid line is the mean value of maser fraction at different outgoing angles.

they are appeared in the form of multiple, thus, without missing the generality of the problem, we choose $\beta = 1$ and debate about the value of α.

The reverse of optical depth of maser indicates the probability that a photon encounters to a maser generator. On the other word, choosing a value for τ_m is a necessary condition for producing maser. In this way, according to the exponential relation between intensity and reverse of optical depth of maser, we create a random number for τ_m that is in a logarithmic function deviate. If this random number is smaller than maximum value $\tau_{mmax} = \alpha\tau$, then, photon will encounter to a maser generator and there is possibility to produce coherent photon with preliminary photon. These coherent photons lead to the maser radiation.

We define maser fraction as the percent of produced masers to non-maser radiated photons at each angle bin

$$\text{maser fraction} \equiv \left(\frac{n'_i}{n_i}\right) \times 100, \qquad (6)$$

which is shown in Fig. 3 for a layer of PNe with $\alpha = 10^{-6}$. The average of maser fraction is also depicted in this figure with a straight solid line. The mean maser fraction, for different values of abundance α in the range of $10^{-7} - 10^{-5}$, is shown in Fig. 4.

IV. SUMMARY AND CONCLUSION

The problem of radiation transfer and production of maser in the inhomogeneous astrophysical systems are such as PNe, cannot be analytically solved. Thus, we used the Monte Carlo method for simulation of maser

PNe	IC4997	K3-35	Vy2-2
I_m(Jy) for H_2O	0.5	2.9	< 0.014
I_m(mJy) for OH	-	56.8	38.5
I_{PNe}(Jy)	9.9	22.7	44.2
$\alpha_{H_2O} \times 10^{-5}$	0.9	2.2	< 0.005
$\alpha_{OH} \times 10^{-7}$	-	4.4	1.5

TABLE I. The fraction of water and hydroxide maser generators in three PNes.

producing. A linear relationship between average fraction of produced masers and relative abundance of maser generators α is obtained as follows:

$$\frac{I_m}{I_{PNe}} = (0.56 \pm 0.004)\left(\frac{\alpha}{10^{-4}}\right) \qquad (7)$$

where I_m indicates the intensity of maser radiation and I_{PNe} is the intensity of non-maser radiation. Using obtained linear equation (7) and observation results, we obtain the fraction of water and hydroxide maser generators in three PNes: Vy2-2, K3-35 and IC4997, with I_{PNe} = 44.2, 22.7 and 9.9Jy, respectively. The results are given in Table I. In this way, we can use the linear relation (7) for other PNes to obtain adequate information for the fraction of maser generators.

[1] Desmurs J.F., Baudry A., Sivagnanam P., Henkel C., 2002, A&A, 394, 975.

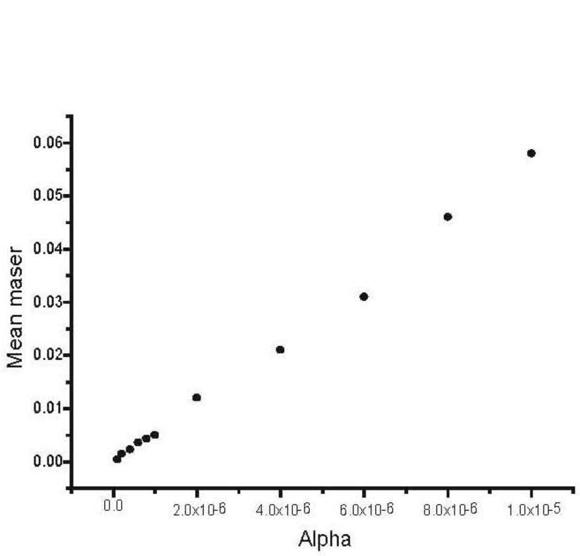

FIG. 4. The average of maser fraction in different values of abundance α of maser generators.

[2] Gomez Y., Miranda L.F., Anglada G., Torrelles J.M., 2003, IAUS, 209, 263.
[3] de Gregorio-Monsalvo I., Gomez Y., Anglada G., Cesaroni R., Miranda L.F., Gomez J.F., Torrelles J.M., 2004, ApJ, 601, 921.
[4] Pottasch S.R., Baud B., Beintema D., Emerson J., Habing H.J., Harris S., Houck J., Jennings R., Marsden P., 1984, A&A, 138, 10.
[5] Akito T., Shinichi T., 1998, AJ, 115,1989.
[6] Bernes C., 1979, Astr.Astrophys, 73, 67.
[7] Spaans M., van Langevedle J.H., 1992, MNRAS, 258, 159.

Effects of Mass -Transfer Rate on Superhump Phenomenon

K. Faghei[1], R. Speith[2], and S. E. Arena [2]
[1] *School of Physics, Damghan University of Basic Sciences, Damghan, Iran*
kfaghei@dubs.ac.ir
[2] *Institute for Astronomy and Astrophysics, Tuebingen University, Tuebingen, Germany*

Abstract

We studied two-dimensional smoothed particle hydrodynamics (SPH) simulation of SU UMa stars during superoutburst for consideration of mass-transfer rate effects on superhump phenomenon. Obtained result are qualitatively consistent with results of grid-based numerical scheme.

I. INTRODUCTION

A. SU UMa stars

SU UMa stars belongs to the dwarf nova class of catalysmic variables (Cvs). Like all CVs, SU UMa stars are semi-detached binary systems consisting of a white dwarf and a low mass, main sequence star. The secondary fills its Roche lobe, and a stream of gas flows from its surface toward the primary through the inner lagrangian point.

SU UMa stars exhibit bimodal distribution of outbursts. Normal outbursts have an amplitude of ≈ 3 magnitude and last from one to four days. Superoutbursts are ≈ 1 magnitude brighter and last aout two weeks. Furthermore, about one day after the rise to supermaximum superhumps show up. Superhumps are an additional variation of the brightness with an amplitude about 30 percent and a period P_{SH} that is a few percent longer than the orbital period P_{Orb} of the system. The period excess $\triangle P = (P_{SH} - P_{Orb})/P_{Orb}$ is specific for each system and ranges from aout 0.8 up to 8 percent.

Both outburst types are disc phenomena. The outburst mechanism is understood in principle but many details are unclear and none of the existing models can explain.

B. The outburst mechanisms

1. Normal outbursts

Normal Outbursts occur because of a thermal instability of the disc. The material in the disc, mostly hydrogen, can be either in a cold and neutral or in a hot and ionized state. So for a given value of the surface density Σ, the temperature of the disc can be double valued, and accordingly so can the local mass-transfer rate and the viscosity. This dependence of the temperature on Σ, known as the 'S-curve', was suggested by Meyer & Meyer-Hofmeister (1983).

Once the critical surface density has been reached anywhere in the disc a heating wave starts running through the disc, transferring the whole disc into the higher state (outbursts). During the outburst the local mass-transfer rate is enhanced. The outburst is stopped by propagation of a cooling front, re-transforming the disc into the lower state . The cooling front develops at the outer edge of the disc when the surface density drops below the second critical value.

2. Superoutbursts

Superoutbursts follow a different mechanism. They are driven by a combination of a thermal and a tidal instability of the disc (see Whitehurst 1988). The model expleins why superoutbursts are seen only in systems with extreme mass ratio $q = M_2/M_1 \leq 0.25$.

During normal outbursts the disc size grows because of the enhanced viscosity. In systems with $q \leq 0.25$ the disc is able to grow to a size where a tidal instability is excited in its outer region, and the whole disc becomes eccentric and starts to process rapidly in the corotating frame. The tidal influence of the secondary on the disc and hence the viscous dissipation is largest when the bulk of eccentric disc passes the secondary, leading to the 'superhumps' in the light curve.

C. Outline

Recently Kley et al. (2008) considered effects of mass transfer rate in close binary systems by grid-based scheme. They presented that mass transfer rate did not any important effect on an eccentric disc. In this paper we try to reproduce Kley et al. (2008) simulation by smoothed particle hydrodynamics method to consider accuracy of their results. In Section 2 we describe the hydrodynamic model and discuss about obtained results. Results will be summarized in Section 3.

II. SPH SIMULATIONS OF A PRECESSING ACCRETION DISC

A. Smoothed Particle Hydrodynamics

Smoothed particle hydrodynamics (SPH) was introduced by Lucy (1977) and Gingold & Monaghan (1977). It is a gridless Lagrangian particle method for the solution of the hydrodynamics equations. Instead of solving the equations on a grid, the fluid is modelled by small interacting packets of matter that move along with the flow and carry mass and momentum. Hydrodynamic variables such as density, pressure and temperature are assigned to each particle. The values of these quantities are determined by the interactions with the neighbour particles.

SPH is especially suited for the simulation of accretion discs because SPH can handle large density contrasts, open boundries are easily implemented, and SPH possesses an adaptive resolution both by the variation of the interaction range of each particle and also by the particle mass. So it is possible to resolve the most interesting regions very fine. Readers in the basic principles of SPH find detailed reviews of the SPH method in Benz (1990) or Monghan (1992).

B. Turbulent viscosity

It is well known from the theory of stationary accretion discs that the ordinary molecular viscosity is too small by many orders of magnitude in order to account for the required dissipation and angular momentum transfer (see Frank et al. 1992). Since the Reynolds number in this case greatly exceeds the critical value for onset of turbulence in laboratory experiments it is usually assumed that the disc is in a state of fully developed turbulence. Such a flow can be described by an effective viscosity

$$\nu \rightarrow \nu_{eff} = \nu_{mol} + \nu_{turb} \approx \nu_{turb} \tag{1}$$

where $\nu_{turb} \approx l_{turb} v_{turb}$ is given by the size l_{turb} and the turnover velocity v_{turb} of the largest turbulent cells (see Lanndau & Lifshitz 1991). The length l_{turb} is limited by the disc height H whereas it is reasonable to assume that v_{turb} cannot exceed the sound speed c_s. Taking the relation $H \sim c_s r/v_\varphi$from the theory of stationary discs with the Keplerian velocity $v_\varphi = \sqrt{GM/r}$ we obtain*

$$\nu_{turb} \sim Hc_s \sim c_s^2 \frac{r}{v_\varphi} \sim 10^{15} cm^2 s^{-1} \sim 2 \times 10^{-7} R_\odot^2 s^{-1} \tag{2}$$

which gives an order of magnitude estimate for the turbulent viscosity in the disc. For our simulations we use a constant viscosity throughout ($\nu = \nu_{turb} = constant$) which is a free model parameter. It turns out that generally lower values of ν than the estimate (2) have to be used in order to match the observed properties of the superhump phenomenon.

C. Simulations

1. Preliminary remarks

The simulations are two-dimensional, i.e., for the pressure, the density, etc., we use values which are integrated over the height of the disc. Because of the missing vertical structure we cannot include radiation transport in the simulations. Instead, we assume that heat produced by viscous interaction is radiated away instantaneously from both sides of the disc.

2. Boundary conditions

The accretion disc is limited by the surface of the WD. In reality a boundary layer may develop between WD and the inner edge of the disc. The physics of this boundary layer is not well understood. It is also possible that the inner edge of the disc has evaporated and no boundary layer exists. In the simulations particles which get closer to WD than a certain minimum disstance are simply removed from the calculations.

3. Procedure of the simulations

We use the parameters of well-known binary system, OY Car. The data are taken from CV catalogue by Ritter & Kolb (1994). We made four simulations for different mass-transfer rate, from $10^{-11} M_\odot yr^{-1}$ to $10^{-8} M_\odot yr^{-1}$. In these simulations we choose a kinematic viscosity of $3 \times 10^{-8} R_\odot^2 s^{-1}$.

The simulations are started with an empty disc. Then particles are fed into the Roche lobe of the primary via the inner Lagrangian point. An accretion disc starts to develop. After about 100 orbital periods the disc becomes eccentric and starts to precess, provided the mass ratio is sufficiently large (see Fig 1).

One the disc precesses superhumps can show up. A Fourier transformation of the resulting light curve yields the superhump period.

In the simulations the viscosity is taken as constant. This means that the disc is always in the hot state and no information about the rise to supermaximum can be obtained. However, the behavior of the disc during superoutburst cab be studied well with these simulations.

---

*Values typical for an accretion disc are $c_s \approx 3 \times 10^6 cms^{-1}, r = 10^{10} cm$ and $v_\varphi = 10^8 cms^{-1}$ Frank et al. 1992

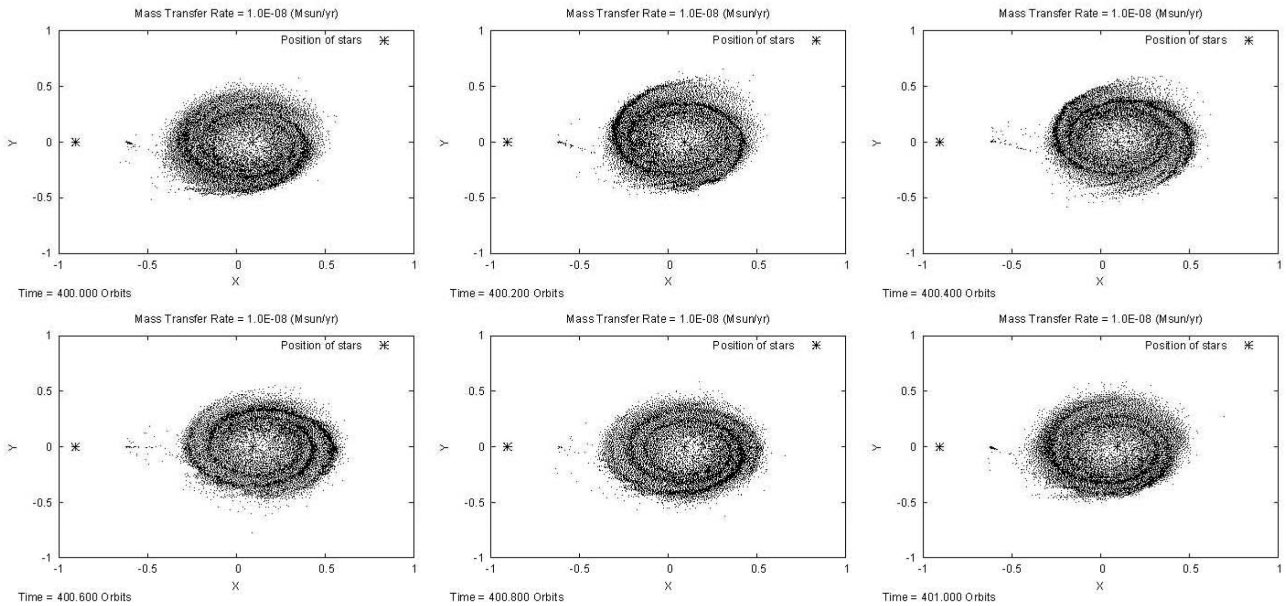

FIG. 1. A simulation of OY Car. After about 100 orbital periods an eccentric, precessing disc develops. Here precession of the disc during one orbital period of the system can be seen.

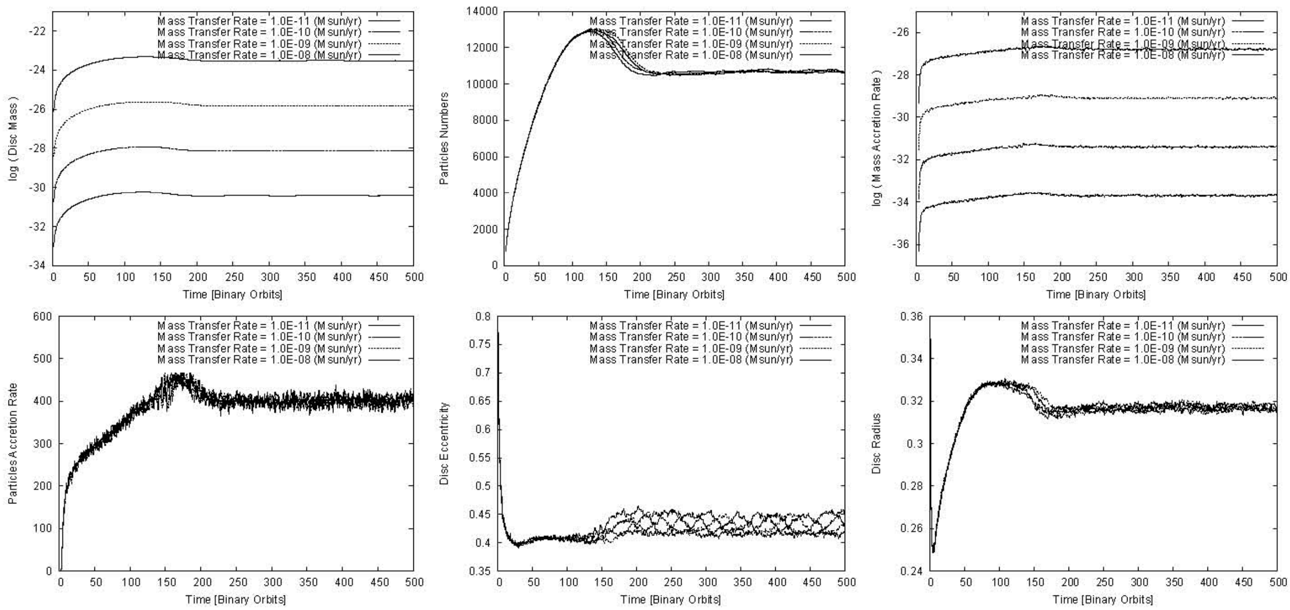

FIG. 2. Physical quantities of disc as function of time for models including mass inflow through the L_1 point with different mass-transfer rate

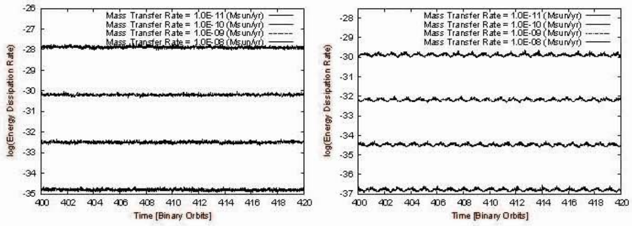

FIG. 3. The source of superhump: in the left curves all particle are considered., in the right curves only those particles that are close to the scondary. Figures show that the superhumps is generated mainly by part of the disc closest to the secondary star. This is because in this region the tidal stress from secondary on the distored disc is largest. The system parameters used here are those of OY Car.

D. Results

The whitehurst model for superoutbursts predicts eccentric precessing discs for mass ratios of $q \leq 0.25$. We performed simulations with mass ratio $q = 0.1$. The runs were continued until either the discs started to precess or an equilibrium between inserted and accreted particles occured (see Fig. 2). The simulated accretion discs show exactly the same behaviour as predicted by theory.

The simulations show that the particles number and particles accretion rate on WD are similar for different mass-transfer rate, but by increasing mass transfer rate, mass accretion rate and disc mass increase by factor of adding mass-transfer rate, because the particle mass is determined by the mass-transfer rate and the number of injected particles per orbital period. So changes in the mass-transfer rate with fixed particle injection rate will alter the particle mass accordingly. Also, Fig. 2 shows that the eccentricity and the radius of disc approximately are same for different mass-transfer rate.

In Fig. 3 the light curve of a simulation of OY Car is shown. In the left curves the dissipation of all particles is included, in the right only particles with a minimum distances 0.3 to WD are considered. From Fig. 3 one can see that innermost parts of the disc do not contribute to the superhump, in fact, only the parts of the outer disc that are next to the secondary star are responsible for the superhump.

III. SUMMARY

We develop a two-dimesional SPH code in countinue to previous studies by other authors, includes the full viscous shear tensor according to the Navier-Stokes equation. This SPH code was used study the superoutburst behavior of SU UMa stars.

Simulated accretion discs becomes eccentric and start to precess in systems with a mass ratio of lower than 0.25, as predicted by theory. The influence of the mass-transfer rate from secondary on the superhump period was studied. In the locally isothermal disc models with constant kinematic viscosity, independence of dynamics of the flow, and in particular the final values of eccentricity and disc radius in a quasi-steady state means that the results are independent of the magnitude of the inflow rate! that is qualitatively consistent with obtained result by grid-base scheme (Kley et al. 2008). In future we want to consider a more realistic disc model that includes suitable radiation and energy transport mechanism and allows for the possibility of time-dependent outbursts.

Acknowledgements Very fruitful discussions with Wilhelm Kley is gratefully acknowledged. Also KF acknowledges the use of the supercomputing facilities at Institute for Astronomy and Astrophysics of Tuebingen University (IAAT).

[1] Frank J, King A., Raine D., 1992, Accretion power in astrophysics, Cambridge Univ. Press, Cambridge
[2] Gingold R. A., Monaghan J. J., 1977, MNRAS, 181,375
[3] Kley, W., Papaloizou, J. C. B., Ogilvie, G. I., 2008, A&A., 487, 671K
[4] Lucy L. B., 1977, AJ, 82, 1013
[5] Meyer F., Meyer-Hofmeister E., 1983, A&A, 132,143
[6] Monaghan J.J., 1992, ARA&A, 30, 543
[7] Ritter H., Kolb U., 1994, in Lewin W. H. G., van Paradijs, van den Heuvel E. D. J., eds, X-ray Binaries. Cambridge Univ. Press, Cambridge
[8] Whitehurst R., 1988, MNRAS, 232, 35

Hydrodynamical Wind on a Magnetized ADAF With Thermal Conduction

S. Abbassi[1,2] J. Ghanbari[3] and M. Ghasemnezhad [3]
[1] *School of Physics, Damghan University of Basic Sciences, Damghan, P.O.Box 36715-364, Iran*
[2] *School of Astronomy, Institude for Studies in Theocratical Physics and Mathematics, 19395-5531, Tehran, Iran*
[3] *Department of Physics, School of Sciences, Ferdowsi University of Mashhad, Mashhad, 91775-1436, Iran*

We examine the effects of a hydrodynamical wind on the advection dominated accretion flows with thermal conduction in the presence of a toroidal magnetic field under a self-similar treatment. The disk gas is assumed to be isothermal. For a steady state structure of such accretion flows a set of self similar solutions are presented. The mass-accretion rate $\dot{M}$ decrease with radius r as $\dot{M} \propto r^{s+\frac{1}{2}}$, where s is an arbitrary constant. We show that existence of wind will lead to enhance of accretion velocity. The cooling effects of outflows or winds is noticeable and should be taken into account for calculating energy spectrum of ADAFs. Increasing of the effect of wind decrease the temperature of disk, because of energy flux which are taking away by the winds.

PACS numbers: 05.10.-a ,05.10.Gg, 98.70.Vc

I. INTRODUCTION

Accretions onto compact object are the most energetic process in the universe. It is believed that many astrophysical objects are powered by mass accretion on to black holes. The standard geometrically thin, optically thick accretion disk model can successfully explain must of observational features in active galactic nuclei (AGN) and X-ray binaries.

Accretion disks are an important ingredient in our current understanding of many astrophysical systems on all scales. Examples of presumed disks accretors include Young stars, compact objects in close binary system, active galactic nuclei(AGN) and quasars (QSOs). There is also evidence that the process of mass accretion via a disk is often and perhaps always associated with mass loss from the disk in the form of a wind or a jet.

Mass loss appears to be a common phenomenon among astrophysical accretion disk system. These mass-loss mechanisms are observed in microquasars, Young stellar objet and even from brown dwarfs. An outflow emanating from an accretion disk can act as a sink for mass, angular momentum and energy and can therefore alter the dissipation rates and effective temperature across the disk (Knigge 1999). The accretion flows lose their mass by the winds as they flow into the central object. As a result of mass loss,the accretion rate,$\dot{M}$, is no langer constant in radiuse r. It is often expressed as $\dot{M} \propto r^s$ with s being constant of order unity.

Astrophysical jets and outflows emanating from accretion disks have been extensively investigated by many researcher. various driving sources are proposed, including thermal, radiative and magnetic ones. Traditionally the name of jet depends on its driving force. In this study we will flow the hydrodynamical (thermal) wind which have been discussed by many authors.

Accretion disk models have been extensively studied during the past three decades (see Kato et al 1998 for a review). Besides the traditional standard disk by shakura and sunayev (1973), there is new-type disks,such as advection-dominated accretion flows(ADAF) or radiative inefficient acretion flows (RIAF) for a very small mass-accretion disks (Narayan & Yi 1994)and supercritical accretion disk or so-called slim disk, for a very large mass-accretion rate (Abramowicz et al 1998). ADAFs with winds or outflows have been studied extensively during recent years, but thermal conduction has been neglected in all these ADAFs solutions with winds and toroidal magnetic field. Shadmehri(2008) studied hot accretion with outflows and thermal conduction.He showed that thermal conduction opposes the rotational velocity, but increase the temperature. In advected dominated inflow-outflow solutions (ADIOS) it is assumed that the mass flow rate has a power low dependence on radius with the power low index s, treated as a parameter.

Kitabatake , fukue & Matsumato (2002) studied supercritical accretion disk with winds, though angular momentum loss of the disk, because of the winds,has been neglected.In this paper, we present self-similar solutions for ADAF with thermal conduction and a toroidal magnetic field in the presence of outflows or winds. In section 2,we present assumptions, basic equations. Self-similar solutions are investigated in section 3. The aim of this work is to consider possibility that winds in the presence of thermal conduction and a toroidal magnetic field which has been largely neglected before, could affected the global properties of the hot accretion flows substantially. In section4 we show the result and give discussions of the results.

II. THE BASIC EQUATIONS

We investigate the effect of mass outflow by the wind and mass accretion rate by viscosity simultaneously. We consider an accretion disk that is axi-symmetric and geometrically thin. ($\frac{\partial}{\partial\phi} = \frac{\partial}{\partial t} = 0$) and geometrically thin $\frac{H}{R} < 1$. In cylindrical coordinates (r, φ, z), we vertically integrate the flow equations, also we suppose that all flow variables are only a function of r. We ignore the relativistic effect and we use Newtonian gravity. We adopt α-prescription for viscosity of rotating gas. For magnetic field we considered a toroidal configuration.

The equation of continuity gives

$$\frac{\partial}{\partial r}(r\Sigma v_r) + \frac{1}{2\pi}\frac{\partial \dot{M}_w}{\partial r} = 0 \tag{1}$$

where v_r is the accretion velocity ($v_r < 0$) and $\Sigma = 2\rho H$ is the surface density at a cylindrical radius r. The mass loss rate by outflow/wind is represented by $\dot{M}_w$. So

$$\dot{M}_w(r) = \int 4\pi r' \dot{m}_w(r') dr'$$

where $\dot{m}_w(r)$ is mass loss rate per unit area from each disk face. On the other hand we can rewrite the continuity equation:

$$\frac{1}{r}\frac{\partial}{\partial r}(r\Sigma v_r) = 2\dot{\rho} H \tag{2}$$

where $\dot{\rho}$ the mass loss rate per unit volume, H is the disk half-thickness.

The equation of motion in the radial direction is:

$$v_r \frac{\partial v_r}{\partial r} = \frac{v_\varphi^2}{r} - \frac{GM_*}{r^2} - \frac{1}{\Sigma}\frac{d}{dr}(\Sigma c_s^2) - \frac{c_A^2}{r} - \frac{1}{2\Sigma}\frac{d}{dr}(\Sigma c_A^2) \tag{3}$$

where v_φ, c_s and c_A are the rotational velocity of gas disk, sound and Alfven velocities of the fluid respectively. Sound speed are defined as $c_s^2 = \frac{p_{gas}}{\rho}$, p_{gas} being the gas pressure and Alfven velocity is defined as $c_A^2 = \frac{B_\varphi^2}{4\pi\rho} = \frac{2p_{mag}}{\rho}$, where p_{mag} being the magnetic pressure.

The integrated angular momentum equation over z gives: (e.g., Shadmehri 2008)

$$r\Sigma v_r \frac{d}{dr}(r v_\varphi) = \frac{d}{dr}(r^3 \nu \Sigma \frac{d\Omega}{dr}) - \frac{\Omega (lr)^2}{2\pi}\frac{d\dot{M}_w}{dr} \tag{4}$$

where the last term of right hand side represents angular momentum carried by the outflowing material. Here, $l = 0$ corresponds to a non-rotating wind and $l = 1$ to outflowing material that carries away the specific angular momentum(Knigge 1999). Also ν is kinematic viscosity coefficient and we assume:

$$\nu = \alpha c_s H \tag{5}$$

where α is a constant less than unity. By integrating over z of the hydrostatic balance ,we have:

$$\frac{GM}{r^3}H^2 = c_s^2[1 + \frac{1}{2}(\frac{c_A}{c_s})^2] = (1+\beta)c_s^2 \tag{6}$$

where $\beta = \frac{P_{mag}}{P_{gas}} = \frac{1}{2}(\frac{c_A}{c_s})^2$ which indicates the important of magnetic field pressure compared to gas pressure. We will show the dynamical properties of the disk for different values of β. Now we can write the energy equation considering cooling and heating processes in an ADAF. We assume the generated energy due to viscous dissipation and the heat conducted into the volume is concerned are balanced by the advection cooling and energy loss of outflow. Thus,

$$\frac{\Sigma v_r}{\gamma - 1}\frac{dc_s^2}{dr} - 2H v_r c_s^2 \frac{d\rho}{dr} = \frac{f\alpha\Sigma c_s^2}{\Omega_k} r^2 (\frac{d\Omega}{dr})^2 - \frac{2H}{r}\frac{d}{dr}(rF_s) - \frac{1}{2}\eta \dot{m}_w(r) v_k^2(r) \tag{7}$$

where the second term on right hand side represents energy transfer due to the thermal conduction and $F_s = 5\Phi_s \rho c_s^3$ is the saturated conduction flux (Cowie & Makee 1977). Dimensionless coefficient Φ_s is less than unity. Also, the last term on right hand side of energy equation is the energy loss due to wind or outflow (Knigge 1999). Depending on the energy loss mechanism, dimensionless parameter η may change. In our case we consider it as a free parameter of our models so that larger η corresponds to more energy extraction from disk because of the outflows (Knigge 1999). Finally since we consider the toroidal component for the global magnetic field of central stars, the induction equation with field scape can be written as:

$$\frac{d}{dr}(V_r B_\varphi) = \dot{B}_\varphi \tag{8}$$

where $\dot{B}_\varphi$ is the field scaping/creating rate due to magneti instability or dynamo effect.

III. SELF-SIMILAR SOLUTIONS

Self-similar solution can not be able to describe the global behavior of the solutions, because in this method there are not any boundary conditions which have been taken into account. However as long as we are not interested in the solutions near the boundaries, such solution describe correctly, true and useful asymptotically behavior of the flow in the intermediate areas.

We assume that the physical properties are self-similar in the radial direction. In the self-similar model the velocities are assumed to be expressed as follows:

$$v_r(r) = -c_1 \alpha v_k(r) \tag{9}$$

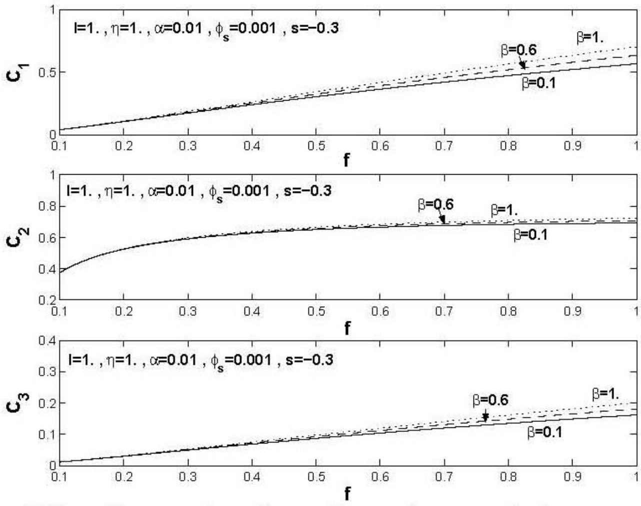

FIG. 1. Numerical coefficient C_is as a function of advection parameter f for several values of β, magnetic field strength. All of this figures was set up for $s = -0.3$, $\alpha = 0.01$, $\phi = 0.001$ and $l = \eta = 1$.

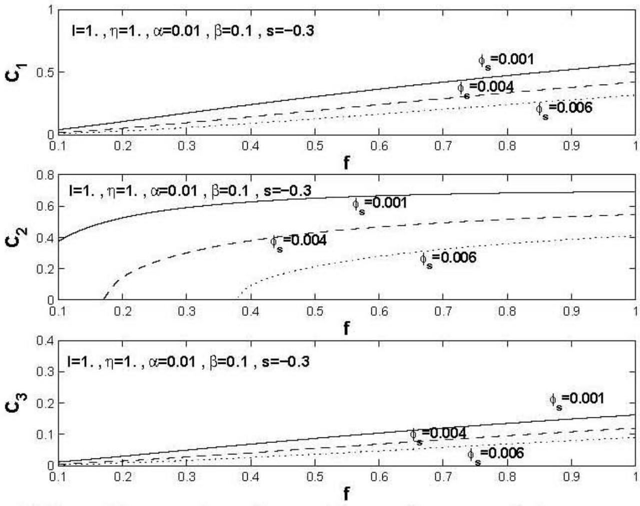

FIG. 2. Numerical coefficient C_is as a function of advection parameter f for several values of ϕ_s, thermal conduction parameter. All of this figures was set up for $s = -0.3$, $\alpha = 0.01$, $\beta = 0.1$ and $l = \eta = 1$.

$$v_\varphi(r) = c_2 v_k(r) \tag{10}$$

$$c_s^2(r) = c_3 v_k^2(r) \tag{11}$$

$$c_A^2(r) = \frac{B_\varphi^2(r)}{4\pi\rho(r)} = 2\beta c_3 v_k^2(r) \tag{12}$$

where

$$v_k(r) = \sqrt{\frac{GM}{r}} \tag{13}$$

and constant c_1,c_2 and c_3 are determined later. From the hydrostatic equation, we obtain the disk half-thickness H as:

$$\frac{H}{r} = \sqrt{c_3(1+\beta)} = \tan\sigma \tag{14}$$

Hence, a supercritical disk with winds also has a conical surface,whose opening (half-thickness) angle is σ.

Assuming the surface density Σ to be in the form of:

$$\Sigma = \Sigma_0 r^s \tag{15}$$

Note that the value of s should be determined iteratively for consistency. Then we assume that the power law index of the density ρ in the radial direction is constant regardless of z. Hence we set $\rho \propto r^{s-1}$

$$\dot{\rho} = \dot{\rho}_0 r^{s-\frac{5}{2}} \tag{16}$$

$$\dot{B}_\varphi = \dot{B}_0 r^{\frac{s-5}{2}} \tag{17}$$

$$\dot{M}_w = \dot{M}_0 r^{s+\frac{1}{2}} \tag{18}$$

$$\dot{m}_w = \dot{m}_0 r^{s-\frac{3}{2}} \tag{19}$$

It should be noted that, for a self-similar disk without any wind mass loss, the suffix s is $s = -\frac{1}{2}$.

By substituting the above self-similar solutions in to the dynamical equations of the system, we obtain the following system of dimensionless equations, to be solved for c_1,c_2 and c_3:

$$\dot{\rho}_0 = -(s+\frac{1}{2})\frac{c_1\alpha\Sigma_0)}{2}\sqrt{\frac{GM_*}{(1+\beta)C_3}} \tag{20}$$

$$H = \sqrt{(1+\beta)c_3}r \tag{21}$$

$$-\frac{1}{2}c_1^2\alpha^2 = c_2^2 - 1 - [s-1+\beta(s+1)]c_3 \tag{22}$$

$$c_1 = 3(s+1)c_3 + (s+\frac{1}{2})l^2\dot{m} \tag{23}$$

$$(\frac{1}{\gamma-1} - \frac{1}{2})c_1c_3 = \frac{9}{4}fc_3c_2^2 - \frac{5\Phi_s}{\alpha}(s-\frac{1}{2})c_3^{\frac{3}{2}} - \frac{1}{8}\eta\dot{m} \tag{24}$$

$$\dot{m} = 2c_1 \tag{25}$$

where $\dot{m} = \frac{\dot{M}_0 w}{\pi\alpha\Sigma_0\sqrt{GM}}$ is the nondimensional mass accretion rate. After algebraic manipulations, we obtain a forth order algebraic equation for c_1:

$$D^2c_1^4 + 2DBc_1^3 + (B^2 + 2D(E-1))c_1^2 +$$

$$(2B(E-1)-A^2)c_1+(E-1)^2=0 \tag{26}$$

Where

$$D=\frac{1}{2}\alpha^2 \tag{27}$$

$$B=\frac{4}{9f}(\frac{1}{\gamma-1}-\frac{1}{2})-[s-1+\beta(s+1)][\frac{1-2(s+\frac{1}{2})l^2}{3(s+1)}] \tag{28}$$

$$A=\frac{20\Phi_s}{9f\alpha}(s-\frac{1}{2})[\frac{1-2(s+\frac{1}{2})l^2}{3(s+1)}]^{\frac{1}{2}} \tag{29}$$

$$E=\frac{\eta}{3}\frac{(s+1)}{(1-2(s+\frac{1}{2})l^2)} \tag{30}$$

Abbassi et al. (2006) have solved these equations when $s=-\frac{1}{2}$, because they did not have any wind or mass-loss in their model. This algebraic equation shows that the variable c_1 which determines the behaviour of radial velocity depends only on the α, Φ_s, β, f, s and η. Other flow's quantity such as c_2 and c_3 can be obtained easily from c_1:

$$c_2^2=\frac{4c_1}{9f}[\frac{1}{\gamma-1}-\frac{1}{2}]$$

$$+\frac{20\Phi_s}{f\alpha}(s-\frac{1}{2})[\frac{1-2(s+\frac{1}{2})l^2}{3(s+1)}]^{\frac{1}{2}}c_1^{\frac{1}{2}}+\frac{\eta}{3}(\frac{s+1}{1-2(s+\frac{1}{2})l^2}) \tag{31}$$

$$c_3=c_1(\frac{1-2(s+\frac{1}{2})l^2}{3(s+1)}) \tag{32}$$

We can solve this simple equations numerically and clearly just physical solution can be interpreted. Without wind thermal conduction and magnetic field, $s=l=\eta=\phi_s=\beta=0$, these equations and their similarity solutions reduce to the standard ADAFs solution (Narayan Yi 1994). Also without wind reduce to Abbassi et al. 2008. Now we can analysis behavior of the solutions.

IV. GENERAL PROPERTIES OF ACCRETION FLOWS

In the pervious sections we have introduced solutions of advection type accretion flow with winds in the presence of thermal conduction bathed in a toroidal magnetic field. In this section we will discuss the general properties accretion flow and we will investigate possible effect

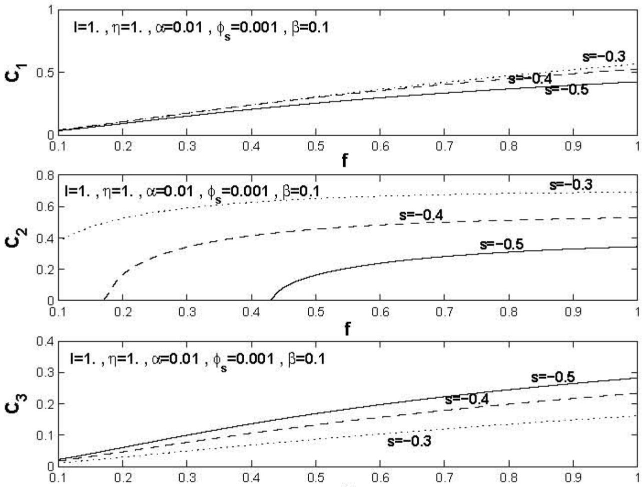

FIG. 3. Numerical coefficient C_is as a function of advection parameter f for several values of s, wind parameter. All of this figures was set up for $\phi_s=0.001$, $\alpha=0.01$, $\beta=0.1$ and $l=\eta=1$.

of wind, thermal conduction and magnetic field on the physical quantities of accretion flow.

Using the self-similar solution we will estimate the mass-accretion rate as:

$$\dot{M}=-2\pi r\Sigma v_r=2\pi\Sigma_0 c_1\alpha\sqrt{GM}r^{s+1/2}$$

$$=\dot{M}_{out}(\frac{r}{r_{out}})^{s+1/2} \tag{33}$$

where r_{out} is the disks outer radius and $\dot{M}_{out}$ is mass-accretion rate there. In the case of accretion disk with now wind, $s=-1/2$ the accretion rate is independent to the radius, while for those with wind, $s>-1/2$, the accretion rate decrease with radius as we expect. Because winds start from various radii, the mass loss rate is not constant but depends on radius. As a results, some part of accretion materials are not concentrated at the center, but is dilated over a wide space. According to wind mass loss, the accretion rate decreases with radius as we expected.

With a simple calculation we will se that a significant amount of accretion materials flung away via the wind and mass loss. Only $1-10\%$ of M_{out} is ultimately accreted onto the central accretor. Using the above expression for accretion rate we have:

$$\frac{\dot{M}_{in}}{\dot{M}_{out}}\sim(\frac{r_{in}}{r_{out}})^{s+1/2}$$

if we estimate $r_{in}\sim10^{-3}r_{out}$ we finally have for $s=1/2$:

$$\frac{\dot{M}_{in}}{\dot{M}_{out}}\sim10^{-3}$$

We show the temperature of the present self-similar ADAFs disks with toridal magnetic field and outflow. In the optically thin case, where the gas pressure is dominated, we can adopt the Ideal gas law to estimate the effective temperature as

$$\frac{R}{\bar{\mu}}T = c_S^2 = \frac{GM}{r} \tag{34}$$

where T is the gas temperature, R gas constant and $\bar{\mu}$ the mean molecular weight. If we use $(GM = r_g c)$, where r_g and c are the Schwartzshild radius and light speed respectively, the temperature gradient is expected as:

$$T = c_3 \frac{c^2/2}{R/\bar{\mu}} \frac{r_g}{r} \tag{35}$$

which means that $T \propto \frac{c_3}{r}$. This has similar form (radial dependency) with non magnetic case, but coefficient c_3 implicitly depends on magnetic field β, outflow effect s, advection f and the effect of thermal conduction ϕ.

In the optically thick case radiation pressure is dominated. In this case sound speed is related to radiation pressure. We can write the average flux F as:

$$F = \sigma T_c^4 = \frac{3c}{8H}\Pi = \frac{3}{8}c\Sigma_0\sqrt{\frac{c_3}{1+\beta}}GMr^{s-2} \tag{36}$$

where $\Pi = \Sigma c_s^2$ is the height-integrated pressure, T_c disk central temperature and σ the Stefan-Boltzman constant. The optical thickness of the disk in the vertical direction is:

$$\tau = \frac{1}{2}\kappa\Sigma = \frac{1}{2}\kappa\Sigma_0 r^s,$$

where κ is the electron-scattering opacity. So we can calculate the effective flux and effective temperature of the disk surface as:

$$\sigma T_{eff}^4 = \frac{\sigma T_c^4}{\tau} = \frac{3c}{4\kappa}\sqrt{\frac{c_3}{1+\beta}}\frac{GM}{r^2} = \frac{3}{4}\sqrt{\frac{c_3}{1+\beta}}\frac{L_E}{4\pi r^2}, \tag{37}$$

$$T_{eff} = \left(\frac{3L_E}{16\pi\sigma}\sqrt{\frac{c_3}{1+\beta}}\right)^{1/4} r^{-1/2} \tag{38}$$

where $L_E = 4\pi c\frac{GM}{\kappa}$ is the Eddington Luminosity of Central object. If we integrate these equation radially we have the disk luminosity as:

$$L_{disk} = \frac{3}{4}\sqrt{\frac{c_3}{1+\beta}}L_E \ln\frac{r_{out}}{r_{in}}, \tag{39}$$

As this equation shows, disk luminosity was affected by magnetic field explicitly by β but it would be affected by outflow, thermal conduction and viscosity through the c_3 implicitly.

It should be emphasis that the Luminosity and effective temperature of the disk, L_{disk} and T_{eff},are not affected by the mass loss by outflow (there are not any s dependencies). But wind would effect on the radiative appearance of the disk through the c_3 in these formulas, implicitly. The average flux decrease all over the disk when we have mass loss outflow compare with the case of no mass loss. The Surface density and there fore optical depth decrease for the mass loss case. So we can see the deep inside of the disk.

---

[1] Abbassi S., Ghanbari J., Najjar S.,2008, MNRAS, 388, 663
[2] Abbassi S., Ghanbari J., Salehi F., 2006, A&A, 460, 357A
[3] Ghanbari J.,Salehi F., Abbassi S.,2007,MNRAS, 381, 159
[4] Abramowicz M.A., Chen X., Kato S., Lasota J.P., Regev O., 1995, ApJ, 438, L37
[5] Cowie L. L., Mckee C.F., 1977, ApJ, 275, 641
[6] Hameury J.M.,Lasota J.P., Maclintock J. E.,Narayan R., 1997, ApJ, 489, 234
[7] Honma F., 1996, PASJ, 48, 77
[8] Ichimaru S. 1977, ApJ, 214, 840
[9] Johanson B.M., Quataert E., 2007, ApJ, 660, 1273J
[10] Kaburaki, O. 2000, ApJ, 531, 210
[11] Lasota J. P., Kato S., Fukue J., 1996
[12] Mahadevan R.,Quataert E., 1997, ApJ, 490, 605
[13] Manmoto T. et.al, 2000, APJ, 52, 127
[14] Mihalas D.,Mihalas B.W., 1984, Foundation of Radiation Hydrodynamics. Oxford Univ. Press, New York
[15] Narayan R., & Yi, I. 1994, ApJ, 428, L13
[16] Narayan R., & Yi, I. 1995a, ApJ, 444, 238
[17] Narayan R., & Yi, I. 1995b, ApJ, 452, 710
[18] Narayan R., Maclintock J.E., Yi I., 1996, ApJ, 457, 821
[19] Narayan R., Igumenshchev I.V., Abramowicz M.A., 2000, ApJ, 539, 798
[20] Shadmehri M., 2004, A&A, 424, 379
[21] Shadmehri M., 2008, AP&SS, 317, 201S
[22] Shakura N. I., & Sunyaev R.A. 1973, A&A, 24, 337
[23] Shapiro S., Lightman A.P., Eardley D.M., 1976, ApJ, 204, 187
[24] Tanaka T., Menou K., 2006, APJ, 649, 345

Statistical Properties of Umbral Dots

H. Hamedivafa
Department of Physics, Faculty of Science, Imam Khomeini International University, Qazvin 34149-16818, Islamic Republic of Iran

The statistical properties of area and brightness of umbral dots, formed in a sunspot umbra observed on 18 June 2004, [9], were studied using an improved method of image segmentation and feature tracking algorithm, [3]. Central (Peripheral) umbral dots have a typical size around 0.16 (0.17) arcsec with a Gaussian distribution. The distribution of umbral dots' brightness shows a multi-population distribution. The brightness of the central umbral dots does not exceed $0.7I_{phot}$. In most cases, umbral dots' area reaches its maximum after their brightness reaches. It seems that the time-averaged brightness of umbral dots varies periodically with birth time of umbral dots.

I. INTRODUCTION

A sunspot umbra appears dark due to its low temperature as compared to the quiet sun (photosphere). This darkness is due to (not completely) suppression of convective energy transport by the strong magnetic field of the sunspot. On the other hand, sunspot umbra shows a variety of fine-structures. Umbral dots (UDs), small bright points, are one of these. Two theoretical models of sunspot magnetic structure, *monolithic* and *cluster*, have been proposed to explain the umbral fine structures. It seems that both magnetoconvection (reduced convective energy transport in the monolithic model, [7], and intrusion of field-free hot plasma (in cluster model, [4,12], as well as (along with) radiation must explain the observed (low) brightness of a sunspot umbra. In this paper, some statistical properties of UDs as well as some new findings about systematic long-term variations of UDs' intensity are reported.

II. DATA SET

The time series of images (red broad-band, 602.0 ± 1.3 nm) used here has previously been acquired and corrected by Sobotka & Puschman, [9], and taken from a large leading sunspot on 18 June 2004 (NOAA 10634) with the 1-m Swedish Solar Telescope, [6], at La Palma, Canary Islands. The best image of this time series has been show in Fig.1.

The spatial resolution of the observation is about 0.14 arcsec ($\approx$100 km). The pixel size of the CCD camera used to take frames is equivalent to 0.0405 arcsec. This data set contains 350 frames of 500$\times$500 pixels. The average time interval between the frames is 20 s. Some results about the kinematics and evolution of the fine structures in this sunspot have previously published, [9–11].

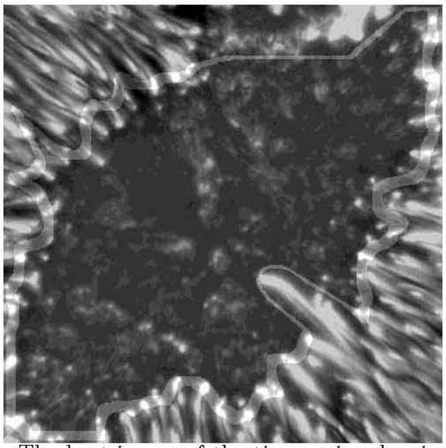

FIG. 1. The best image of the time series showing the fine structures of the sunspot and the defined border of the umbra.

III. FEATURE TRACKING AND IMAGE SEGMENTATION

The formation of UDs and the temporal changes of their physical quantities (size, intensity and position) are studied using an improved feature tracking algorithm. This tracking algorithm firstly developed by Sobotka *et al.*, [8], that has recently been improved by Hamedivafa, [3]. This improved algorithm helps us to distinguish between (unresolved) features (e.g. UDs) that split into two or more parts (UDs), (unresolved) features merge with their adjacent features, features do not experience split/merge during their lifetime. Therefore, this algorithm can record the *true* area and the *true* lifetime of resolved (non-split/merge) UDs formed on an umbra as well as their *true* birth time (frame). For a complete discussion, refer to [3].

A fixed umbral region was defined, using a time-averaged image at an empirical isointensity level after a wide boxcar smoothing. To sign the peripheral UDs (mostly moving into the umbra), a narrow lane at the border of the umbra was defined (see Fig.1). UDs crossing this lane are signed as peripheral UDs.

This feature tracking uses segmented images. To make a segmented image, UDs are isolated from their background using the low-noise curvature determination algorithm developed by Hamedivafa, [3]. This method of image segmentation defines the edge of a UD by finding the inflection point of the intensity profile. This procedure, clearly tends to yield smaller area than the *real* one (all pixels brighter than the background) for UDs. To eliminate the miss-features and reject the very dim-pixels isolated on the segmented images, a variable threshold brightness was applied.

All bright features with a lifetime equal or longer than 3 frames (60 s) and a time-averaged area larger than 10 pixels (equivalent to an effective diameter of 0.14 arcsec, the spatial resolution of the observation) are considered as UDs.

By applying the feature tracking to the time series of the segmented images, the evolution of 483 centrally resolved UDs (were not the results of split or merging and did not spilt or merge), containing 6420 individual UDs on all frames, were registered. It must be mentioned that the majority (96.2%) of all (12740) observed UDs split or merged with other UDs, or are the results of split/merge. Also, 996 UDs (7.8% of all) were not the results of split or merging (having a well-defined birth frame) but experienced split or merging (not having a well-defined death frame as well as lifetime). I leave the discussion about split or merging of UDs to another opportunity.

Also, the feature tracking recorded a sample of peripherally resolved UDs containing 164 UDs (2952 individual UDs). It is important to pay attention to the considerations noticed by Hamedivafa, [3]: usually, the defined umbral area (boundary) is smaller than the real one. This causes registering of wrong area and lifetime for most of peripheral UDs. Therefore, if we want to study UDs' area/lifetime it is necessary to exclude these UDs. But, for a comparison, in some cases (see Sect.IV), I'll take them into account.

IV. AREA AND BRIGHTNESS OF UMBRAL DOTS

Fig.2 shows histogram of areas of centrally and peripherally individual (resolved) UDs, separately. Two Gaussian functions are fitted the points. As Hamedivafa, [3] and Hamedivafa, [2] noticed, it is clear that the distributions of UDs' areas (not diameters) are Gaussian, here, with peaks at 0.019 arcsec^2 (equivalent to an effective diameter of 0.16 arcsec) for central UDs and at 0.023 arcsec^2 (equivalent to an effective diameter of 0.17 arcsec) for peripheral UDs. This result is similar to that published by Sobotka & Puschman, [11]. It must be noticed that the typically identified size of UDs depends, irrespective of the size and the age of the umbra, on the spatial resolution of the observation, the pixel size of the CCD camera used to record images and UDs' locations as well as on the method of image segmentation, [1]. As mentioned before, the used algorithm here registers smaller size than the real one for UDs.

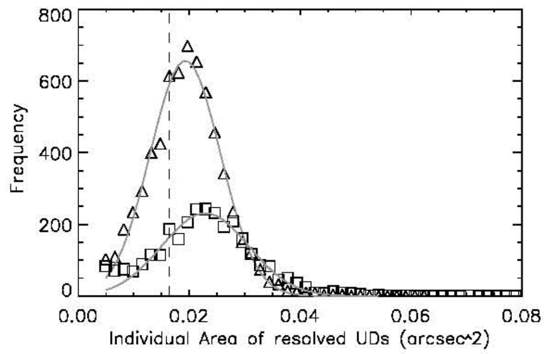

FIG. 2. The histograms of areas of centrally (triangles) and peripherally (squares) individually resolved UDs. The superposed histograms are Gaussian fits. The vertically dashed-line shows the spatial resolution of the observation.

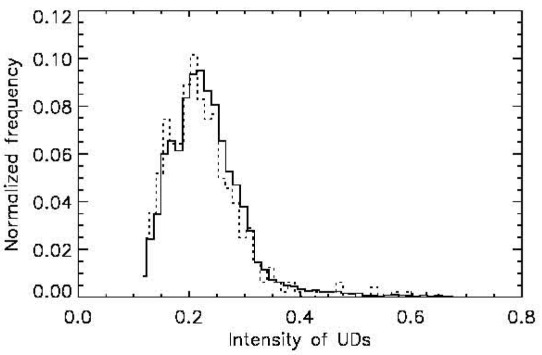

FIG. 3. The histograms of peak intensities (solid line) of all centrally individual UDs and of their time-averaged peak intensities (dotted line).

The histogram of peak intensities of all centrally individual UDs is displayed in Fig.3 (solid line). Fig.3, also, shows the histogram of the time-averaged peak intensities (I_{avg}) of these UDs (dotted line). These histograms are the same and show a multi population of UDs' intensities as reported by Sobotka *et al.*, [8], and Hamedivafa, [3]. The peak intensities of most centrally UDs are around $0.2 I_{phot}$ and do not exceed $0.7 I_{phot}$ (I_{phot}: spatially averaged intensity of the photosphere around the sunspot).

UD's brightness and their area do not show any cor-

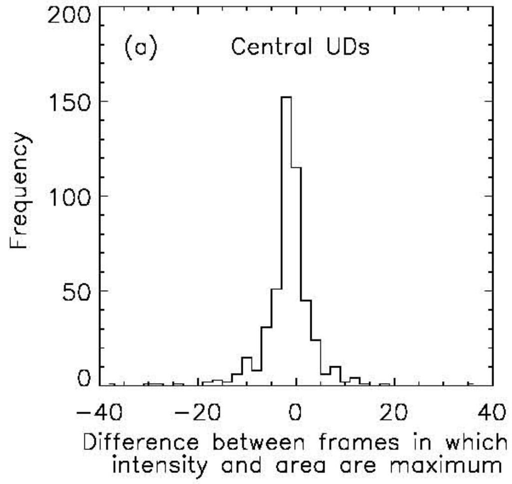

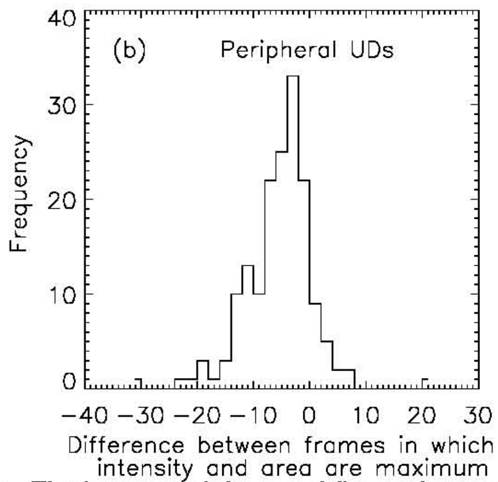

FIG. 4. The frequency of the time difference between the instant of the maximum of peak intensity and the instant of the maximum of area for each centrally (a) and peripherally (b) UDs.

relations, [3,5]. These two (observational) findings are in contrast to the results of Bharti *et al.*, [1]. They found that the simulated UDs, [7], do not have a typical size, and the UDs' area is correlated to the UDs' brightness.

To study the dependence of UDs' brightness on their area, the time difference between the instant of the maximum of peak intensity and the instant of the maximum of area for each UD was calculated. Fig.4 depicts the frequency of these time differences for centrally and peripherally resolved UDs, separately. Although we do not know the true birth frame of peripheral UDs these time differences are meaningful, if UDs' area and brightness reach their maximum after entering of UDs into the umbral region. The peak position of the two histograms (at a negative value) says that intensity of the most peripheral

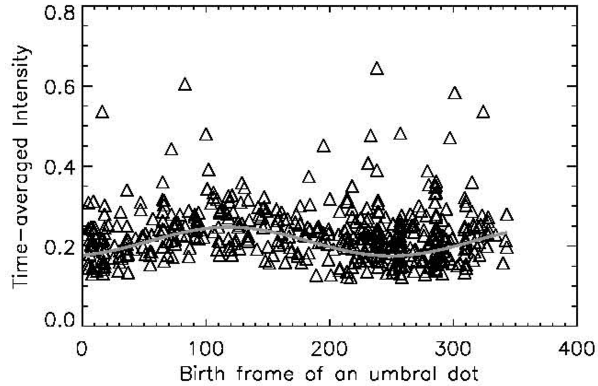

FIG. 5. Time-averaged peak intensities of all central UDs versus of their birth frame.

as well as central UDs often (82% and 73%, respectively) reaches its maximum sooner (statistically averaged, 110 s and 32 s, respectively) or at the same time, than their area reaches.

Fig.5 shows that I_{avg} has a systematic relation with time (the UD's birth frame). It seems that this systematic relation is a periodic behavior with a period of about 260 frames ($\approx$ 85 min). The gray solid-line shows an interpolated line using the average of the values on the y-axis at each time (frame). The time-averaged areas of UDs do not show any considerable dependence on time.

V. CONCLUSION

In recent years, Schüssler & Vögler, [7], simulated magnetoconvection in a sunspot umbra in which convective energy is transported by narrow upflow plumes. These simulated bright structures in intensity images are similar to UDs. Bharti *et al.*, [1], studied some statistical properties of these simulated UDs. They found that the UDs do not have a typical size, and larger umbral dots tend to be brighter and live longer. However, the present study as well as recently previous studies, [8,3,13], give observational evidences that UDs have a typical size, and their brightness does not show any directly proportional behavior. The present study provide an observational evidence that, in most cases, UD's area reaches its maximum after the UD acquire its maximum brightness. This finding may seem obvious. However, the time difference between these two maximum is longer for peripheral UDs (110 s) than that for central UDs (32 s). Therefore, this can shed light on the understanding the thermal and magnetic structure of UDs and those of their diffuse background. Also, the observed periodic relation of I_{avg} as a function of UD's birth time can help us to comprehend how UDs are formed as a result of magnetic structure and flow pattern beneath a sunspot umbra.

Acknowledgements I would like to thank M. Sobotka for his kind assistance in providing me with his most valuable observational data. The SST is operated by the Royal Swedish Academy of Sciences in the Spanish Observatorio del Roque de los Muchachos of the Instituto de Astrofísica de Canarias.

[1] Bharti L., Beeck B., Schssler M., 2010, A&A 510, 12.
[2] Hamedivafa H., 2006, The 10th Meeting of Research Astronomy, Proceedings (Zanjan: IASBS), 44.
[3] Hamedivafa H., 2008, Solar Phys. 250, 17.
[4] Parker E. N., 1979, ApJ 234, 333.
[5] Riethmüller T. L., *et al.*, 2008, A&A 492, 233.
[6] Scharmer G. B., *et al.*: 2003, in S. Keil and S. Avakyan (eds.), Innovative Telescopes and Instrumentation for Solar Astrophysics, Proc. SPIE, 4853, 341.
[7] Schüssler M., Vögler A., 2006, ApJ 641, L73.
[8] Sobotka M., Brandt P. N., Simon G. W., 1997, A&A 328, 682.
[9] Sobotka M., Puschmann K. G.: 2007, in F. Kneer, K. G. Puschmann, and A. D. Wittmann (eds.), Modern Solar Facilities - Advanced Solar Science, Universitätsverlag Göttingen, 205.
[10] Sobotka M., Puschmann K. G., Hamedivafa H., 2008, Centr. Eur. Astrophys. Bull. 32, 125.
[11] Sobotka M., Puschmann K. G., 2009, A&A 504, 575.
[12] Spruit H. C., Scharmer G. B., 2006, A&A 447, 343.
[13] Watanabe H., Kitai R., Ichimoto K., 2009, ApJ 702, 1048.

A Model of Modified Newtonian Gravity for Planetary Motions

R. Hashemi, R. Saffari
Department of Physics, The University of Guilan, 41335-1914, Rasht, Iran

In this paper we test a model of modified Newtonian potential that obtained from weak field approximation solution of $f(R)$ gravity theory which can be used as effective potential in Solar system scale. In particular we are going to examine impact of modifications on Solar system dynamics. We apply a perturbative approach to compare $f(R)$ induced secular precession of the longitude of pericentre ϖ of a test particle with the latest determination of corrections to the usual perihelion precession. Then we constraint our model parameters, b and n by comparing with observational data sets. Our results show that this model creditable in Solar system scale.
PACS numbers: 04.50.kd, 96, 04.80.Cc

I. INTRODUCTION

Observations seem to question General Relativistic model of gravitational interactions on large scale structures. The data coming from rotation curves of spiral galaxies can not be explained without dark matter, light curves of type Ia supernovae and cosmic microwave background radiation experiments, firmly state that our universe is undergoing an accelerated expansion phase that can not be explained within GR unless the existence of dark energy. But the problem one has to face with dark energy and dark matter is understanding their nature. In order to explain observations, another possibility is modified $f(R)$ gravity models [1] and [2]. Historically, the first attempts to find deviations from the Newtonian inverse square law of gravitation were performed to explain the anomalous secular precession of mercury's perihelion discovered by Le verrier (1859). Hall (1894) noted that he could account for mercury's precession if the law of gravity, instead of falling off as $1/r^2$, actually falls of as $1/r^k$ with $k = 2.00000016$. However, such an idea was not found to be very appealing, since it conflicts with basic conservation laws, Gauss's law, unless one also postulates a correspondingly modified metric for space. It was recently realized that deviations from the Newton's inverse square law could provide windows into new physics [4]. Indeed in the modern framework of the challenge of unifying gravity with the other three fundamental forces of nature possible new phenomena could show up as deviations from the inverse-square law of gravitation. In general they would occur at sub millimeter length scales, but sometimes also at astronomical or even cosmological distances. For review of the many theoretical speculations about deviations from the inverse-square law see [5]. In the low energy limit, the gravitational potential generated by a point like source may be Written as:

$$\Phi(r) = \frac{-GM}{r} + br^{n+1}, \tag{1}$$

Where G is the Newtonian gravitational constant, M is the mass of central body, n and b are the model's parameters. because of dimension of potential we multiply b with c^2/r_0^{n+1} The problem that worth to be addressed is: There are three parameters to be constrained. While n, b control the shape of the correction term, the parameter r_0 controls the scale where deviations from the Newtonian potential sets in. all of the parameters have to be determined by comparison with observations at solar system. We will use the EPM 2004 ephemerides by Pitjeva, and the observational data from perihelion precession of mercury and deflection of light to obtain our model parameters. We will show that solar system tests are, in fact, able to tell us something important about ranges $r_0 < 10^{14}$.

II. THE EFFECT OF THIS MODEL ON THE PERIHELIA AND DETERMINE N

Let us, work out the orbital effects induced by Eq. (1), treated as a small perturbation of the Newtonian monopole term, on the planetary motions of solar system planets [3]. In view of a direct comparison with the latest estimated extra rates of the longitude of perihelion ϖ, we will consider the secular precession of such an element. For a radial perturbing acceleration , the gauss equation for the variation of ϖ can be written as

$$\frac{d\varpi}{dt} = -\frac{\sqrt{1-e^2}}{\alpha a e} A_r \cos f, \tag{2}$$

Where $\alpha = \sqrt{GM/a^3}$ is the Keplerian mean motion, a is the planets semi major axis, e is the eccentricity and f is the true anomaly. In order to obtain the secular rate of ϖ, Eq. (1) must, first, be evaluated upon the unperturbed Keplerian ellipse,given by

$$r = a(1 - e\cos E), \tag{3}$$

In terms of the eccentric anomaly E; then, it must be inserted into the right-hand side of Eq. (2) and, finally, the integral over a complete orbital revolution must be performed. The following formulas will be used

$$\cos f = \frac{\cos E - e}{1 - e\cos E}, \tag{4}$$

$$dt = \frac{1 - e\cos E}{\alpha}\, dE, \tag{5}$$

See [6]. The extra acceleration becomes

$$A_r = bc^2(n+1)(\frac{r}{r_0})^n, \tag{6}$$

It is possible to obtain

$$< \dot{\varpi} >= (n+1)c^2 b \frac{1}{r_0^{n+1}} \frac{\sqrt{(1-e^2)a^n}}{\sqrt{GM}}, \tag{7}$$

Pitjeva has recently estimated corrections $< \dot{\varpi} >$ to the secular rates of the longitudes of perihelia of the planets of solar system. See table(I) Here we will not use one perihelion at a time for each planet. Indeed let us consider a pair of planets A and B and take the ratio of their estimated extra-rates of perihelia: if Eq. (7) is responsible for them, then the quantity

$$\Gamma_{AB} = |\frac{\dot{\varpi}_A}{\dot{\varpi}_B} - (\frac{a_A}{a_B})^n|, \tag{8}$$

must be compatible with zero, within the errors, [7]. We use this method to determine n: by taking the variance of Γ_{AB} and minimizing it for the various planets, we obtain $n = 4.88$ and the minimum variance becomes $\sigma = 0.178$. With this value for n we decrease differences between theoretical values and observational data. In order to define our potential we need to determine b. then we obtain it in the next section.

III. CLASSICAL TESTS OF GENERAL RELATIVITY AND APPOINTING VALUE FOR B

Because of the perturbations by the existence of all the other planes, the force experienced by any planet does not very exactly as inverse-square. The perihelion of mercury shows the largest effect. We next indicate the way the advance of the perihelion can be calculated from modified equation of motion. To perform this calculation we use the universal gravitational law for $F(r)$

$$\ddot{u} + u = -\frac{m}{l^2 u^2} F(\frac{1}{u}), \tag{9}$$

The quantity u is therefore the reciprocal of distance between m and M. see [8]. The modification of the gravitational force law is

$$\ddot{u} + u - \frac{1}{\chi} + \delta\ u^-(n+2) = 0, \tag{10}$$

Where $1/\chi = mk/l^2$ and $\delta = (n+1)mb/l^2$ Eq.(10) is nonlinear and we use a successive approximation procedure to obtain a solution. We choose the first solution to be the solution of Eq. (10)

$$u_1 = \frac{1}{\chi}(1 + e\cos\theta), \tag{11}$$

If we substitute this expression into the right hand side of Eq. (10) we find

$$\ddot{u} + u = \frac{1}{\chi} + \delta\ [1/\chi(1 + e\cos\theta)]^{-(n+2)}, \tag{12}$$

With expansion of second term of right hand side of Eq. (12) we obtain

$$u_{seqular} = \frac{1}{\chi}(1 + e\cos(\theta - \frac{n+2}{2}\delta\ \chi^{n+3}\theta), \tag{13}$$

We have chosen to measure θ from the position of perihelion at $t = 0$, successive appearances at perihelion result when the argument of the cosine term in $u_{seqular}$ increases to 2π, 4π,... but an increases of the argument by 2π requires that

$$2\pi = \theta(1 - \frac{n+2}{2}\ \delta\ \chi^{n+3}), \tag{14}$$

$$\theta = 2\pi(1 + \frac{n+2}{2}\ \delta\ \chi^{n+3}), \tag{15}$$

$$\Delta = \pi(n+2)\ \delta\ \chi^{n+3}, \tag{16}$$

Therefore the effect of our model for potential in the force law is to displace the perihelion in each revolution by an amount Eq. (16) that is the apsides rotate slowly in space.If we refer to the definitions of χ and δ we find

$$\Delta = \frac{\pi bc^2(n+1)(n+2)M\ m}{l^2\ r_0^{n+1}}(\frac{l^2}{m\ k})^{n+3}, \tag{17}$$

We can write $k = GMm$ and $l^2 = mka(1 - e^2)$. To obtain b from Eq. (17) we use the observational data of table (II), and put the value of Δ. In previous section we obtain the value of n. then we can calculate b for the various radiuses. The results of these calculations are in table (III). As we see this modified model is creditable only at $r_0 \leq 10^{14}$.

IV. RESULTS AND DISCUSSION

In this paper we put on the test the hypothesis that modifications of the Newtonian inverse-square law, parameterized in terms of our model, can occur in astronomical scales by using the corrections to the Newtonian-Einsteinian secular rates of the perihelia of mercury phenomenologically estimated, in the least-square sense, with the EPM 2004 ephemerides by Pitjeva. by taking their ratio we found that the parameter n. and, with comparing the observational praecession of mercury with induced precession of our model, we could obtain b for various radiuses.

	Mercury	Earth
$\Delta\dot{\varpi}(arcs/cy)$	-0.000036±.005	-0.0002±.00004
$a(AU)$	0.387	1
e	0.205	0.016
$P(yr)$	0.24	1

TABLE I. observational data for planets

planet	Precession(arcs/century)
Mercury	43.11±.11
Earth	5±1.2

TABLE II. Precessional rates for the perihelion

r_0	b
Solar system radius	$19 \times 10^{-5.48}$
Schwarzschild radius of Sun	$1.06 \times 10^{-66.16}$
Milky Way radius	33×10^{36}

TABLE III. calculation results for value of b

V. CONCLUSION

In this work we have studied the secular precession of the pericenture of a test particle in motion around a central mass M whose Newtonian gravitational potential exhibits a correction which is to the form of Eq. (1). Comparing with latest value of observations, we obtain our model parameters, $n = 4.88$ and it gives the small value for b in Solar System scale. We have considered that these modifications have to be small, which is in compatibility with well known tests of GR and as a consequence we have treated them as perturbations. Here we have showed that, $f(R)$ theories provide cosmologically viable models that could be used to explain precession of perihelion without need for dark matter. Finally we propose to calculate numerical value of model parameters, from other tests of GR such as deflection of light.

[1] Saffari R. and Rahvar S., 2008, Phys. Rev. D 77, 104028,
[2] Saffari R. and Rahvar S., 2009, Mod. Phys. Lett A 24, 305,
[3] Hashemi R. and Saffari R., 2009, *Proceeding of 2nd Astronomy and Astrophysics Conference*, Shahid Chamran University of Ahvaz,
[4] Fujii Y., 1991, Int. J. Mod. Phys. A, 6(20), 3505,
[5] Adelberger E. *et al.*, 2003, Ann. Rev. Nucl. Part. Sci, 53, 77,
[6] Roy A. E., 2005, *Orbital Motion*, IoP,
[7] Pitjeva E. V., 2005, SolarSys. Res., 39(3), 176,
[8] Thornton S. T. and Marion J., 2004, *Classical Dynamics of Particles and Systems*, TLARC.

Formation of Maser in The Interstellar Medium by Wiggling Relativistic Free-Electrons

Mohsen Nejad-Asghar, Ali-Reza Khesali, and Azar Khosravi
Department of Physics, University of Mazandaran, Babolsar, Iran

We present a suitable mechanism for production of observed masers in the star forming regions. The numerical simulations show that total electric potential of a system of charged grains in the molecular clouds can be negative, thus may be formed in a semi-crystallized cluster. The released relativistic free-electrons from the jets in the star forming regions can pass through these clusters of grains to wiggle and radiate the long wavelength radiation in the order millimeter. This mechanism can be used to justify the generation of the masers in the non-molecular wavelengths which have been observed in the star forming regions.

PACS numbers: 98.38.Er, 98.38.Bn, 98.38.Dq

I. INTRODUCTION

Maser is an interesting phenomena which has been ubiquitously observed in the interstellar medium. A common observed maser from the interstellar medium is OH maser at 1670, 1612 and 1665MHz lines that almost can be found at star forming regions [1]. There is also detected 1.35cm line of H_2O maser with OH maser in the W49. In molecular cloud NGC6334F, the 1.25cm line of NH_3 maser has been observed in addition to OH and H_2O masers [2]. Also, with OH maser at 6035MHz, there has been observed methanol maser at 6.6, 107 and 19.9GHz in massive and moderate star forming regions [3]. The vibrational excited emissions of SiO at transition $J = 1 - 0$, and a 7mm continuum emission which is according to the free-free emission from compact-HII and ultra compact-HII regions, has been observed in three very luminous regions: Orion-KL, W51N and SgrB2 [4].

Almost many observed maser emission lines can be justified by molecular collisions and radiative pumping, which is according to the inversion population in radiative levels [5]. The mechanism of molecular collisional and radiative pumping is unable to justify all observed maser lines. For example, the observed $5_{12} \rightarrow 4_{22}$ (923μm) and $10_{29} \rightarrow 9_{36}$ (934μm) are rather unusual in that the upper states dose not lie along the rotational backbone of H_2O [2]. Another example is the SiO emission which displays anomalies in some rotational lines [6]. In study of the methanol maser at 6668MHz, Lyubchenko and Valtts suggested an unknown factor that may act to give additional amplification of this line [7]. In addition, the excited state OH maser at 4765MHz is another example of anomaly since the emission at 4750MHz from the same level is thermal. Thus, this maser emission can not be justified by normal pumping mechanisms [8].

The detailed processes giving maser line radiation in space which are from many recent detailed studies, with high spatial and velocity resolution and with polarization measurements, are not well understood. Holmlid proposed an improved maser mechanism based on amplifi tion of the original molecular line emission by stimulat emission in Rydberg matters [9]. In this paper,we try propose another mechanism for generation of maser some wavelengths. This mechanism is according to t generation of free-electron lasers in laboratories, whicl known as the wiggler method.

The essential idea of the wiggler method is that a re tivistic free-electron is caused to move transversely to general forward motion by static and periodic electric magnetic fields [10]. The associated acceleration leads the free-free radiation, which if their contributions be herent, the superposed radiation detected by an obser is a laser (or maser). Mirzanejhad and Bahadory p sented the ability of the crystallized dusty plasma a micro-structure wiggler field to induce transverse regu motions to a relativistic free-electron [11] . In this id the micro-cluster of dusty plasma can act as a wigg filed to produce free-electron laser.

We know that the grains in the interstellar medi have been charged negatively or positively by photoel tric and collision processes, respectively (e.g., [12]). this research, we study the necessary conditions for f mation of clusters of the charged grains in the molecu clouds. According to the existence of jets in the s forming regions and relativistic motion of the revea free electrons from them [13,14], the cluster of grains n may be considered as wiggler field. In section 2, we inv tigate the necessary conditions for formation of cluster grains in the interstellar medium. In section 3, the w gler method is presented and generation of masers passing a free electron from these clusters of grains studied. Finally, section 4 is devoted to summary a conclusions.

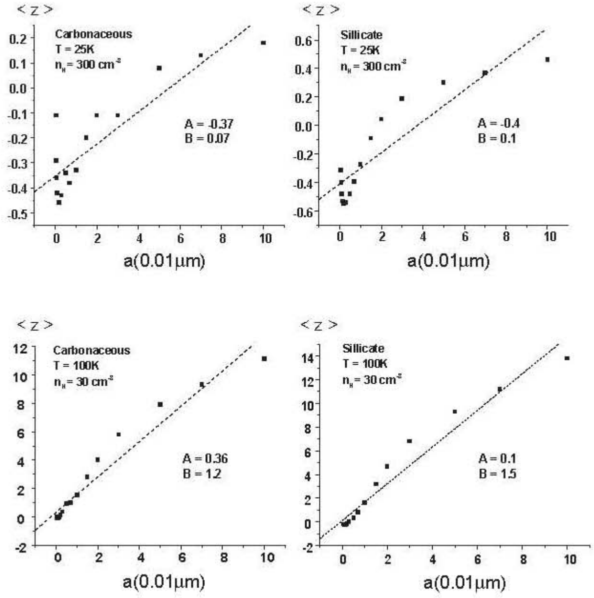

FIG. 1. The mean charge for carbonaceous and silicate grains at different sizes are shown. The dash lines show the linear fit to the points. The intercept and slope of each line are also shown in the figures.

II. CLUSTERING OF INTERSTELLAR GRAINS

It is possible for grains to become positively charged by photoelectric process, and to become negatively charged by collision processes (e.g., [15]). Here, we use the results given in the figures 29 and 30 of [12], which show the mean charge of carbonaceous and silicate grains for different sizes at interstellar medium. The charge of grains have been shown by $q =< z > e$ where e is the electron charge and $< z >$ is a positive or negative real number. The average charge of grains at different sizes which is obtained from the Figs. 29 and 30 of [12] are depicted in Fig. 1. As we can see from this figure, a linear relation between points can be approximated. Here, we approximately use a linear relation between the mean of grain charge $< z >$ and its size a as $< z >= A + Ba$, where the parameters A and B are the intercept and slope of line, respectively. The intercept and slope of each line are also shown in the Fig. 1. According to this figure, the intercept and slope are physically in the range of $-0.4 < A < 0.4$ and $0.06 < B < 1.5$, respectively. The diagrams of the Fig. 1 show that the small grains have negative charges while the larger ones are positively charged. This phenomena may be explained by the idea that the photoelectric effect is usually more important for larger grains, while for small ones, the collision processes are more significant.

Here, we inquiry suitable values for the parameters A and B in the aforementioned physical ranges so that the

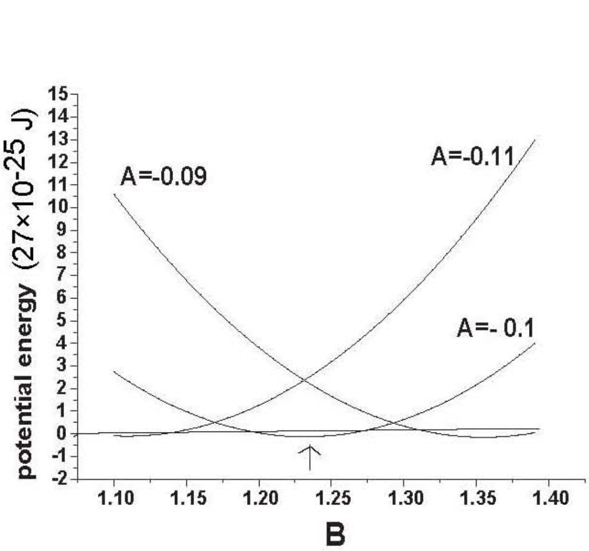

FIG. 2. Total electric potential energy for different para eters A and B.

charged grains may become a stable cluster. For this p pose, we simulate a system of charged grains to find th total electric potential energy. We know that the m density of particles in a typical molecular clouds is in t order of 3.5×10^{-20}g.cm^{-3} and the mean mass of a typi grain is approximately 5.8×10^{-19}g. Since the mass ra of grains to gas is approximately 0.01 [2], we obtain a t ical number density of grains equal to 6×10^{-4}cm^{-3} wh will be used in our simulations. In addition, distributi function of grain sizes is given by $n(a) \propto a^{-3.5}$ [16]. this way, we simulate the system of charged grains w number density and size distribution function in three mensional space using Mont-Carlo method. For differe coefficients A and B, the total electric potential ene are shown in Fig. 2. This is clear that a system of charg particles with negative total electric potential energy stable and will not diffuse. Thus, we see from Fig. 2 t there may be suitable values of the parameters A and in the satisfactory physical range which leads to form tion the cluster of grains. For example, an appropri choice for the parameters A and B may be $A = -0.1$ a $B = 1.24$.

III. WIGGLER MECHANISM AND MASER PRODUCTION

One kind of laser (maser) which is remarkably unl with common lasers (masers) is free electron laser (mas [17–19]. The wiggler motion of a relativistic free-electr which periodically moves transversely to its general f ward motion is the essential idea for free electron la (maser). This wiggler motion can be generated by sta

FIG. 3. Interference of produced waves in the passage of relativistic free-electrons near the cluster of grains.

and periodic electric or magnetic fields in space [10]. In addition, clusters of charged particles may produce the wiggler motion [11]. In this case, the free-electron periodically moves transversely to its general forward motion, and the associated acceleration lead to the emitted radiation.

Now, we consider how the produced electromagnetic waves from wiggler motion of free-electron, can coherently be amplified to generate laser (maser). We suppose that the produced electromagnetic waves are in forward direction with velocity c. The coherent condition is that after passing a wiggler period, the produced wave must be forwarded as a right multiple of wavelength. The cluster of grains and formation of laser (maser) are schematically shown in the Fig. 3. If $V_{\|}$ be parallel component of electron velocity in direction of the electromagnetic wave, the coherent condition can be expressed as follows:

$$(c - V_{\|})t = n\lambda_s \tag{1}$$

where λ_s is the electromagnetic wavelength, n is an integer number, and $t = \lambda_w / V_{\|}$ is the time for electron to travel the distance among charged grains λ_w. The coherent condition (1) can be rewritten as

$$(1 - 1/\beta_{\|})\lambda_w = n\lambda_s \tag{2}$$

where $\beta_{\|} = V_{\|}/c$. If the numerator in the left hand side of equation (2) is estimated as $(1 - \beta_{\|}) \simeq (1 - \beta_{\|})/2$ and the denominator is set as $\beta_{\|} = 1$, we obtain the coherent condition as follows:

$$\lambda_s \simeq \frac{\lambda_w / n}{\gamma_{\|}^2} \tag{3}$$

where $\gamma_{\|} \equiv (1 - \beta_{\|})^{-1/2}$.

Now, we consider the emitted radiation from relativistic free electrons, which are released from jets, and pass through the cluster of charged grains. In the previous section, we found that he size of grain clusters are large and distances between charged grains are in the order of millimeter/centimeter. A relativistic electron that passes among these clusters can radiate under electrostatic field of each charged grain, if its distance from the grain is not larger than b_{max}, which its value is not exact but can be approximated by $V_{\|}/\omega$ where $\omega = 2\pi c/\lambda_s$. Different experiments by computer simulations show that the cluster of grains are approximately in a semi-crystallized form so that the distances between grains can be integer multiple

wavelength (millimeter)	abundance (intensity)%
0.48	0.81
0.95	0.41
1.43	0.25
1.90	0.2
2.38	0.16

TABLE I. The percent of abundance of wiggler free-electron masers.

of each other. Thus, the relativistic electrons in passage of these clusters can radiate the coherent waves that their wavelengths are in the order of millimeter/centimeter, which are called maser. In Table I, we express the percent of abundance of photons which are coherent and can form masers at different wavelengths. Of course, we have not considered the maser photons with abundance less than 0.1%.

IV. SUMMARY AND CONCLUSION

In this paper, a liner relation between the mean charge of grains $< z >$ and their sizes a is assumed as $< z >= A + Ba$ where A and B are intercept and slope, respectively. Systems of grains with size distribution $n(a) \propto a^{-3.5}$ and number density $6 \times 10^{-4}\text{cm}^{-3}$ are simulated, and the total electric potential for different parameters A and B are shown in Fig. 2. Suitable values of the parameters A and B are found that lead to negative value of the total electric potential which cause to stable semi-crystallized cluster of grains in molecular clouds. Then, the radiation of released relativistic free-electrons from jets, in passage through these clusters, are considered. According to the coherent condition of wiggler free-electron mechanism, the wavelength and the percent of abundance of produced masers are given in Table I.

As a remarkable result of this research, we note on the wavelength 950μm with abundance 0.41%. Since there are some errors in our simulations, we can say that the observed wavelengths of masers at 923 and 934μm lines, which could not be explained by the pumping mechanism, may be justified by the wiggler free-electron mechanism. Of course, the wiggler mechanism, which is presented in this paper, suggests the existence of masers in other wavelengths that may be discovered by suitable observations in the further.

[1] Caswell J.L, 1999, MNRAS, 308, 683.

[2] Stahler S.W., Palla F., *The Formation of Stars*, 2004, WILEY-VCH Verlag GmbH & Co.KGaA, Weinheim, chap. 14.
[3] Ellingsen S.P., Cragg D.M., Lovell J.E.J., Sobolev A.M.,Ramsdale P.D., Godfry P.D., 2004, MNRAS, 345, 401.
[4] Zapata L.A., Menten K., Beuther H., 2009, ApJ, 691, 332.
[5] Moran J.M., in *Frontiers of Astrophysics*, 1978, Ed. E.H. Avrett (Cambridge: Harvard University Press).
[6] Pardo J.R., Cernicharo J., Gonzalz-Alfonose E., Bujarrabal V., 1998, A&A , 329, 219.
[7] Lyubchenko Y., Valtts I.E., 2002, A&AT, 21, 63.
[8] Szymczak M., Kus A.J., Hrynek G., 2000, MNRAS, 312, 211.
[9] Holmlid L., 2006, Ap&SS, 305, 91.
[10] Jackson J.D. , *Classical Electerodynamics*, 1999, 3rd Edition, John Wiley&Sons, NewYork, p. 683.
[11] Mirzanejhad S., Bahadory B., 2007, PhPl, 14d3101M.
[12] Draine B.T., in *The Cold Universe*, 2004, Saas-Fee. Advanced course32, Springer-Verlag, Ed. A.W. Blain, F. Combes, B.T. Draine, D. Pfenniger and Y. Revaz, p. 213.
[13] Achterberg A., 1987, in Astrophysical Jets and Their Engines, Proceedings of the NATO Advanced Study Institute, Erice, Italy, 223
[14] Wang D.-Y., Ma Y., 2000, IAUS, 195, 439
[15] Tielens A.G.G.M., *The Physics and Chemistery of the Interstellar Medium*, 2005, Cambridge University Press, p. 135.
[16] Whittet D.C.B., *Dust in the Galactic Environment*, 2003, IOP Publication Ltd., p. 106.
[17] Milonni p., Eberly j., *Lasers*, 1988, Wiley&Sons, NewYork.
[18] Neil G., Merminga L., 2002, Rev. Mod. Phys, 74, 3.
[19] George B., Rybicki L., Alan P., *Radiative Processes in Astrophysics*, 2004, Wiley-VCH Verlag GmbH&CO-KGaA.

THE THERMAL AND MAGNETIC STRUCTURE OF PERIPHERAL UMBRAL DOTS

M. Rahmani and H. Hamedivafa
Department of Physics, Faculty of Science, Imam Khomeini International University, Qazvin 34149-16818, Islamic Republic of Iran

This work aims to constrain the thermal and magnetic structure from peripheral umbral dots using high-resolution spectropolarimetry. The full Stokes spectra recorded by the spectropolarimeter on Hinode of umbral dots in a sunspot umbra close to the disk center are analyzed. The height dependence of the temperature, magnetic field vector, magnetic inclination, and line-of-sight velocity across umbral dots are obtained from an inversion of the Stokes vectors of the two Fe I lines at 630.2 nm by running the SIR code. For this peripheral umbral dot a horizontal cut was identified. Then the results of the different plasma parameters versus pixels in three optical depths 1, 0.1, 0.01 were analyzed here. No difference is found at higher altitudes ($-3 \leq \log(\tau_{500}) \leq -2$) between the studied umbral dot and the diffuse umbral background. Below that level, the difference rapidly increases, so that at the continuum formation level ($\log(\tau_{500}) = 0$) we find a temperature enhancement of about 1050 K, a magnetic field weakening of 700 G, and upflows of 1.2 km s^{-1}.

I. INTRODUCTION

The sunspot is one of the most important structures in the solar photosphere. Physics of sunspots is a fascinating field of research in solar astronomy. The sunspot umbra is populated with small bright dot-like features, named umbral dots (UDs). The study of umbral dots is essential for understanding the energy transport in sunspots, since UDs are considered to be a manifestation of the convection. Two different models have been proposed for formation of umbral dots. In Parker's sunspot model, [7] , the region below the visible surface of the umbra is made up of individual flux tubes embedded in a field-free plasma. At the visible surface, the upper flaring part of the magnetic field is composed by combination of these flux tubes into a single flux tube, so, a spot forms. Choudhuri, [2], in the basis of Parker's model considered the field free hot gas plumes between the bundles of thin magnetic flux tubes. He showed that the plumes have a tapering shape with a certain apex.

The monolitic sunspot model considers a sunspot as the aggregation of uniform vertically thin columns, and UDs as a natural result of the overstable oscillatory convection. The monolitic model predicts smaller field strength, upflows in the center of UDs in addition to downflows at their boundaries, and a cusp-like structure. Resent Three-dimensional simulation of magnetoconvection that has done by Schüssler & Vögler [10], shows the convective cells that penetrated from below the umbral surface and appear like umbral dots. Observations show that magnetic field in umbral dots is weaker than their surroundings, whereas their temperature is more than the surroundings umbra.

Different amounts of magnetic field reduction in UDs have been reported. The lowest magnetic field was found by Beckers & Schröter, [1], reaching 10% of magnetic field in the surrounding umbra having opposite polarity. Kneer , [4], found that UDs exhibit upflows of 3 km s^{-1} and a 50% weaker magnetic field compared to the nearby umbra, whereas Lites *et al.*, [5] and Tritschler & Schmidt, [13], reported little field weakening. Pahlke & Wiehr, [6] reported 20% magnetic field reduction in hot component compared to the nearby umbra. Riethmüller *et al.*, [8] found from observations of 30 peripheral UDs and 21 central UDs that, at the continuum formation level, the magnetic field is 510 G and 480 G, respectively, weaker than in the umbra and is more inclined in peripheral UDs Than in central UDs. They observed significant upflows of 800 ms^{-1} in peripheral UDs, while central UDs did not show any important line-of-sight velocity signature. Sobotka & Jurĉák, [11] found that peripheral UDs are hotter than the surrounding umbra by 400 K in the low photosphere and by 180 K in the high photosphere. This means that peripheral UDs may be located higher in the atmosphere than central UDs. This assumption is also supported by the fact that magnetic field in peripheral UDs is reduced typically by 200 G with respect to the surrounding umbra in the low photosphere, i.e. , twice more than in central UDs. They found that the magnetic field in peripheral UDs is, on average, 6° (in low photosphere) more horizontal than in their surroundings. Significant upflows of 420 ms^{-1} on average are observed in the low photosphere, but they are missing in the high photosphere.

II. OBSERVATIONS AND DATA REDUCTION

The data employed here were taken by the spectropolarimeter of the solar optical telescope onboard Hinode

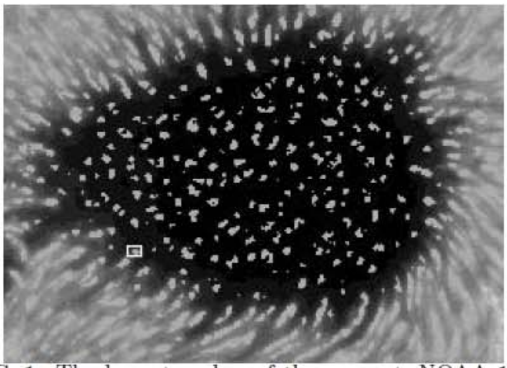

FIG. 1. The largest umbra of the sunspot, NOAA 10926, are observed by the Hinode SOT/SP on 11 December 2006. UDs were highlighted.

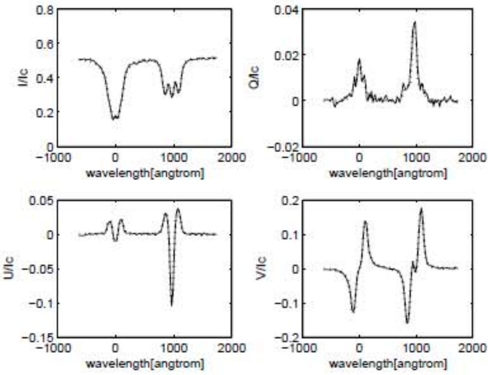

FIG. 2. Stokes I, Q, U and V profiles from the center of the UD. The solid lines are the observed, and the dotted lines are the best fit profiles.

from 14:17 to 14:55 UT on 11 December 2006. The spatial resolution should be close to the diffraction limit of the telescope, 0.32 arcsec ($\approx$ 230 km). At this time sunspot was located at a heliocentric angle 8°, very close to disk center. The picture of this sunspot has been shown in Fig.1. The Full Stokes spectra in the Fe I lines at 6301.5 Å(g=1.67) and 6302.5 Å(g=2.5) were selected. The observations covered the spectral range from 6300.89 Åto 6303.26 Å, with a sampling of 21 m Å$pixel^{-1}$. The spectropolarimeter was operated in its normal map mode. The sampling along the slit was 0.16 arcsec and the slit-scan sampling was 0.147 arcsec . The integration time per slit position was 4.8 s and the time interval between the two slit was 5.1 s.

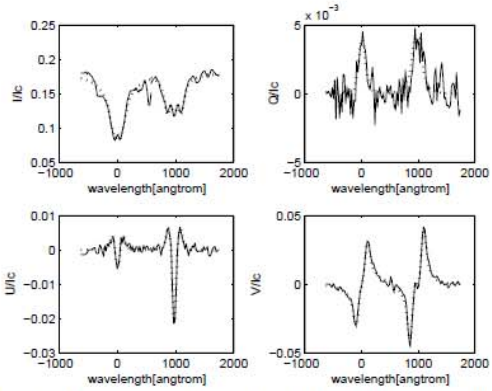

FIG. 3. The same as Fig.2, but for the diffused background.

III. DATA ANALYSIS

To obtain atmospheric stratifications of temperature (T), magnetic field strength (B), magnetic inclination (γ), and line-of-sight velocity (V_{LOS}) we use the inversion code SIR described by Ruiz Cobo & del Toro Iniesta, [9]. It is a one-dimensional inversion code working under the assumption of local thermodynamic equilibrium (LTE) and hydrostatic equilibrium. This code compute synthetic Stokes profiles of selected spectral lines and synthetic model atmospheres. Starting with an initial guess model, the synthetic profiles were iteratively fitted to the observed data using response functions (RFs), and the merit function, χ^2, is minimized.

IV. INVERSION RESULTS

We analyzed a peripheral UD, which was identified by applying the low-noise curvature determination algorithm described by Hamedivafa, [3]. For this UD the location of its core was identified, a horizontal cut was made through it, reaching to the neighboring diffuse background (DB), in both sides. The profiles of full Stokes spectra from all pixels along this cut were inverted. This UD has been marked in Fig.1 and was chosen because of its high brightness, leading to particularly small error bars. A comparison of the measured profiles with the best-fit profiles resulted from the inversion can be seen in Fig.2 for the brightest pixel (center) of the UD, and in Fig.3 for the DB (selected as the location of the lowest continuum intensity). The Stokes spectra can be fitted remarkably well.

The stratifications of the retrieved atmospheric parameters T, V_{LOS}, B and γ both in the center of the UD and in the DB are plotted in Fig.4. In the upper photosphere ($\log(\tau_{500}) = -2$), we find a less significant difference between UD and DB (400 K). In the middle photosphere ($\log(\tau_{500}) = -1$) and lower photosphere ($\log(\tau_{500}) = 0$), the UD temperature is higher than the DB temperature, consistent with the intensity

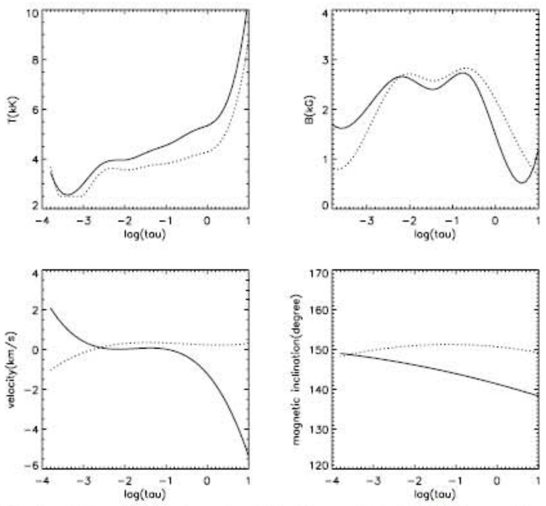

FIG. 4. Atmospheric stratification obtained from the inversion code at the location of the UD's center (solid lines) and of diffuse background near the UD (dotted lines).

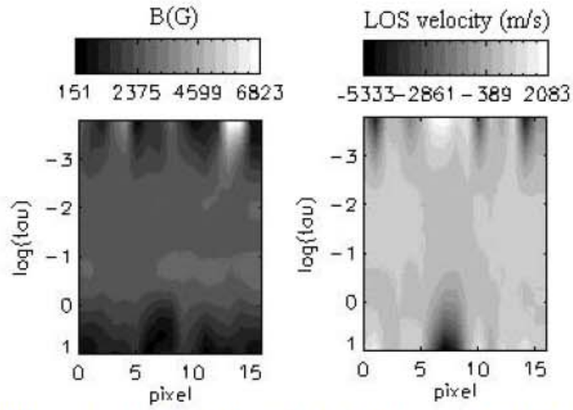

FIG. 5. Vertical cut through the UD marked in Figure 1 in a horizontal direction along 16 pixels. Colors of the left panel indicate magnetic field strength. The right panel shows line-of-sight velocity. Negative velocities are upflows.

enhancement of the UD in the continuum map. The line-of-sight velocity (which is identical to the vertical velocity due to the small heliocentric angle of the sunspot) exhibits strong upflows (negative values) in the UD center at deep layers, whereas this flows in the DB at all of the optical depths ($\log(\tau_{500}) < -2.5$) are downward and very small (≈ 200 m s-1). The magnetic field strength of the UD and DB is almost the same for the heights $-3 \leq \log(\tau_{500}) \leq -1$ and changes between 2400 G and 2600 G. Below $\log(\tau_{500}) = -1$ the field strength of the UD and DB decreases strongly with depth, while magnetic field is weaker than that in DB.

The vertical cuts of magnetic field strength and line-of-sight velocity through 16 pixels for this UD shown in Fig.1 are shown in Fig.5. As we can see in Fig.5 at deep layers ($\log(\tau_{500}) = 0$) the field strength is much weaker than the DB, and strong line-of-sight velocity is observed in the center of the UD (the 8th pixel) only at layers near optical depth unity.

Fig.6 shows the diagrams of T, B, line-of-sight velocity and γ for this UD along the 16-pixels horizontal cut at three optical depths 1, 0.1, 0.01. In Fig.6 we see that the temperature in the center (the 8th pixel) has the maximum amount and decreases in both sides towards the umbral background (DB). Magnetic strength in the center of the UD with respect to the DB is weaker. In optical depth unity magnetic strength in the UD center is 35% weaker than the DB. A strong upflow velocity in the center of the UD is observed (1.2 km s-1), whereas in the DB a small downflow exists. At higher layers ($\tau_{500} = 0.1, \tau_{500} = 0.01$) this upflow vanishes. The magnetic field is 10° more inclined in the UD than that in the DB (around the UD). In Fig.6 we see that when we close to the upper layers ($\tau_{500} = 1$ to $\tau_{500} = 0.1$) magnetic inclination in the center of the UD is 5° more inclined than that in DB but the inclination is more vertical than that in the deeper layers, Also inclination in the upper photospheric layers is the same as that in the DB but is more vertical than that in the deeper layers. A more horizontal magnetic field above the hot region (UD) with weaker magnetic fields means that the magnetic field lines are closed above that region (UD).

V. CONCLUSION

We analyzed a peripheral UD using Hinode Spectropolarimetric data of a sunspot very close to disk center using the SIR code. The inverted Stokes profiles of the Fe I lines at 630.2 nm were done. We determined the photospheric stratifications of temperature, magnetic field strength, magnetic inclination, and line-of-sight velocity for that UD.

Vertical cuts through UDs provide a remarkable confirmation of the results of MHD simulations of Schüssler & Vögler, [10]. Fig.5 looks remarkably like Fig.2 of [10]: both show that UDs differ from their surroundings mainly in the lowest visible layers, where the temperature is enhanced and the magnetic field is weakend. We found a temperature enhancement of about 1050 K and a magnetic field reduction of about 700 G (at optical depth unity). In addition this peripheral UD displays upflow velocity of about 1.2 km s^{-1}, again in good agreement with the simulations. Socas-Navaro *et al.*, [12], reported 10° more inclined magnetic fields in peripheral UDs. Riethmüller *et al.*, [8], found an inclination increase of 4° for peripheral UDs. Sobotka & Jurĉák, [11], measured 6°

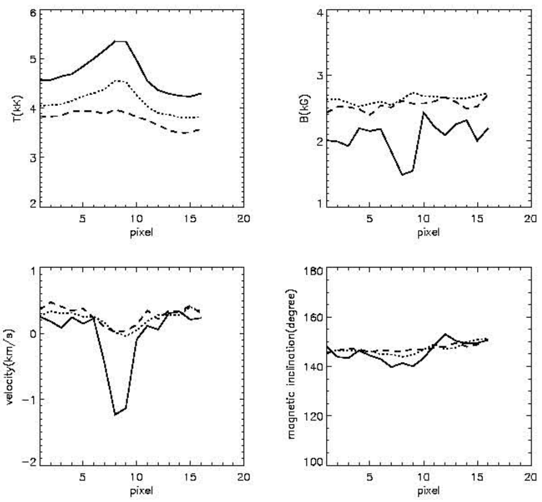

FIG. 6. Diagrams of Temperature, magnetic field strength, LOS velocity and magnetic inclination in a horizontal direction along 16 pixels for the UD marked in figure 1. Solid-lines, dotted-lines and dashed-lines related to optical depths 1, 0.1 and 0.01 respectively.

more inclind magnetic fields in peripheral UDs in deep layers. These results are qualitatively confirmed by this work. In Fig.6, there is clear evidence for a localized decrease in UD field strength in the low photosphere, co-located with an upflow that extends to higher photosphere and a weak downflow around the UD. Fig.6 looks like Fig.4 of [10].

There are also some differences between our results and those of Schüssler & Vögler. They reported dark lanes in the UDs, but in this UD, no dark lanes observed. More inclined magnetic fields in deeper layers can be interpreted in terms of the strong DB fields expanding with height and closing over the UD, as proposed by Socas-Navaro *et al.*.

Acknowledgements This work has been carried out by the help of observed data at the NAOJ Hinode Science Center. Hinode is a Japanese mission developed and launched by ISAS/JAXA, with NAOJ as domestic partner and NASA and STFC (UK) as international partners. It is operated by these agencies in cooperation with ESA and NSC (Norway).

[1] Beckers J. M. and Schröter E.H., 1968, Sol. Phys. 4, 303.
[2] Choudhuri A.R. 1986, APJ 302, 809.
[3] Hamedivafa H., 2008, Sol. Phys. 250, 17.
[4] Kneer F., 1973, Sol. Phys. 28, 361.
[5] Lites B. W., *et al.* 1991, APJ 373,683.
[6] Pahlke K. D., Wiehr E., 1990, A&A 228, 246.
[7] Parker E. N., 1979, APJ 234, 333.
[8] Riethmüller T. L., *et al.*, 2008, A&A 492, 233.
[9] Ruiz Cobo B., and del Toro Iniesta J. c., 1992, APJ 398, 375.
[10] Schüssler M., Vögler A., 2006, ApJ 641, L73.
[11] Sobotka M., and Jurĉák J., 2009, APJ 694, 1080.
[12] Socas-Navaro H., *et al.*, 2004, A&A, 321, 643.
[13] Tritschler A., and Schmidt W., 1997, A&A, 321, 643.

Atmospheric effects on extensive air showers observed with the surface detector of the Alborz Observatory

Shahriari, Mahdi [1] and Khakian Ghomi, Mahdi [1]
[1] *Amirkabir University of Technology, Tehran, Iran*

Atmospheric parameters, such as pressure (P), temperature (T) and density ($\rho \sim P/T$), affect the development of extensive air showers initiated by energetic cosmic rays. [1] We have studied the impact of atmospheric variations on extensive air showers by means of the surface detector of the Alborz Observatory. The rate of events shows the influence of these parameters. We are observing the behaviour can be explained by a model including correlation function between the recording rate of data and atmospheric parameters.

I. INTRODUCTION

High-energy cosmic rays (CRs) are measured by recording the extensive air showers (EAS) of secondary particles they produce in the atmosphere. As the atmosphere is the medium in which the shower evolves, its state affects the lateral and longitudinal development of the shower. [1]

For example an increase (or decrease) of the ground P corresponds to an increased (or decreased) amount of matter traversed by the shower particles; this affects the stage of the longitudinal development of the shower when it reaches the ground. Also the water-Cherenkov detectors are sensitive to both the electromagnetic component and the muonic component of the EAS, which are influenced to a different extent by atmospheric effects. These in turn influence the signal measured in the detectors. [1]

The properties of the primary CR, e.g., energy, mass and arrival direction, have to be inferred from EAS, which can be sampled by an array of detectors at ground level. Therefore the study and understanding of the effects of atmospheric variations on EAS in general, and on a specific detector in particular, is very important for the comprehension of the detector performances and for the correct interpretation of EAS measurements. [1]

We have studied the atmospheric effects on EAS by means of the surface detector (SD) of the Alborz Observatory, Tehran, Iran .

According to the hypothesis that arrival of primary CRs and thus recording of EASs is a random phenomena, first we survey our data that if represents such an events or not. Then, we study the effects of temperature and pressure parameters of atmosphere on the rate of recorded events in 30 minutes intervals.

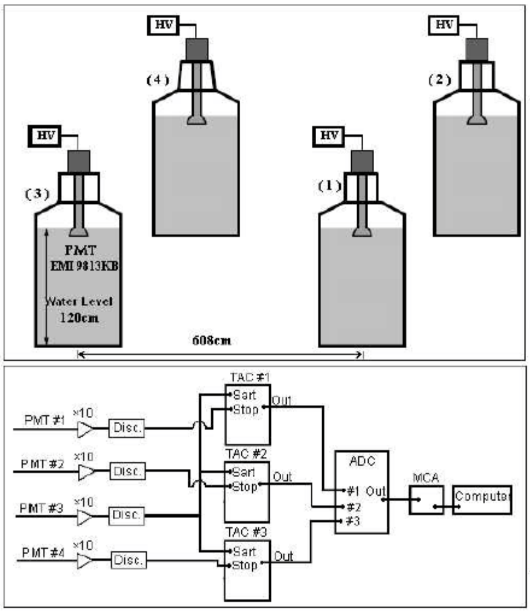

FIG. 1. Schematic view of water Cherenkov detectors as a square array, and the electronic circuit.

II. FIRST STAGE, DATA ANALYSIS

Four Water Cherenkov Detectors (WCDs) used to detect the photons and the charged particles of the EASs from 50TeV up to 5PeV. The array arranged in a square with side 608cm as shown in Fig.1, on the roof of the Physics Department at Sharif University of Technology in Tehran($35.43°N, 51.20°E, 1200ma.s.l = 890g.cm^{-2}$). [2]

The SD trigger condition, based on a 4-station coincidence. According to the electronic circuit, the signal produced by secondary particles of an EAS leads to the 3 time lags between the output signals of PMTs (3,1), (3,2), and (3,4) that are read out as parameters 1 to 3. So by this procedure an event is logged. [2].

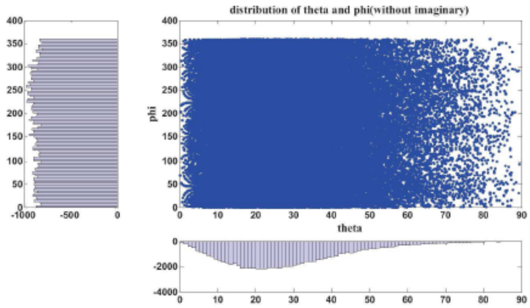

FIG. 2. Distribution of θ and ϕ for real showers detected.

A. Calculation of the arrival direction of an air shower

In our analysis, it's assumed that the front surface of an air shower disk is approximately a plane perpendicular to the direction of the primary cosmic ray. Let a unit vector $\hat{n}$ represent the incident direction of the air shower, which in xyz coordinate system is:

$$\hat{n} = sin(\theta)cos(\phi)\hat{i} + sin(\theta)sin(\phi)\hat{j} + cos(\theta)\hat{k} \qquad (1)$$

where, θ and ϕ are zenith and azimuth angles, respectively. If we measure T_{12}, T_{13} and T_{14} from four Detectors, we can determine the arrival direction, $\hat{n}(\theta, \phi)$, by least square fitting method. In this calculations we see imaginary value for θ of some events that represents no specific plane, we omited these events. Distribution of θ and ϕ of real showers is shown in Fig.2, The results is as follow:

Time duration of experiment: 1175.5 hours,
Date of experiment: 07/10/01 to 07/11/30,
Total NOs. of detected events: 85625,
NOs. of real showers: 79892,
Maximum of θ: 86.8942°,
Minimum of θ: 2.6086°,
Maximum of ϕ: 344.9456°,
Minimum of ϕ: 15, 1362°,

B. Distribution of the number and time-spacing of events

Here we investigate the time difference between events detection. It can be shown if the number of events in a fixed time period has a Poisson distribution, the time difference between consecutive events has exponential distribution, and the time difference between time zero and the time of mth event detection has Gamma distribution, With the below properties: [3]

For Poisson distribution:
$e^{(-\lambda)} * \lambda^x/x!$
$mean(x) = \lambda$
$variance(x) = \lambda$

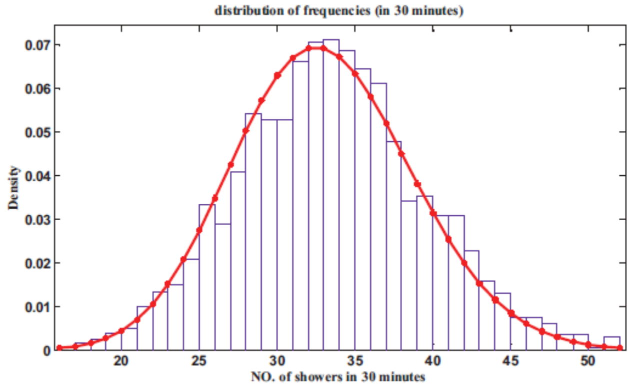

FIG. 3. Distribution of the number of events in 30 minutes periods in time duration of experiment and a fit of Poisson distribution function on it.

For exponential distribution:
$a * \exp(-b{*}x)$
$mean(x) = 1/b$
$variance(x) = 1/(b^2)$
For Gamma distribution:
$b^m/(m-1)! * \exp(-b{*}x)$
$mean(x) = m/b$
$variance(x) = m/(b^2)$

Distribution of the number of events in 30 minutes along the experiment time and it's Poisson fitting is shown in Fig.3, and the results is inserted in table1.

For time-spacing distribution between two consecutive events, with exponential distribution function (1st degree Gamma distribution function) fitting and for time difference between three, four and five consecutive events, with two, three and four degree Gamma distribution function fitting, shown in Fig.4, we obtained information inserted in table1.

III. RESULTS OF FIRST STAGE

With attention to attained results at previous scene, it is confirmed that our Cherenkov detector data is random phenomena descriptive, and data recording technique did not change the nature of data.

IV. SECOND STAGE, ATMOSPHERIC EFFECTS INVESTIGATION

In Fig.5, frequency of real showers for 30 minutes intervals is shown. The results is as follow:

Number of 30 minutes intervals: 2352
Mean of events in intervals: 32.9817

results from fitting	results from data
Poisson fit: Mean: 33.0174 Variance: 33.0174 Parameter Estimate: lambda 33.0174	mean = 33.0174 Variance = 35.6269
Gamma fit:	
$m = 1 : a * \exp(-b*x)$ $a = 1.687e + 004$ $b = 0.01888$ $1/b = 52.966$ $1/(b^2) = 2805.4$	mean = 52.9704 Variance = 2800.1298
$m = 2 : a*x* \exp(-b*x)$ $a = 396$ $b = 0.01886$ $2/b = 106.04$ $2/b^2 = 5622.7$	mean = 105.9404 Variance = 5647.2994
$m = 3 : a*x^2 * \exp(-b*x)$ $a = 4.161$ $b = 0.01891$ $3/b = 158.65$ $3/b^2 = 8389.5$	mean = 158.9108 Variance =8467.7265
$m = 4 : a*x^3 * \exp(-b*x)$ $a = 0.02966$ $b = 0.01889$ $4/b = 211.7522$ $4/b^2 = 1.1210e + 004$	mean = 211.882 Variance = 11277.7183

TABLE I. Results obtained from fitting on different parameters distribution and results from data for comparison between them to sure about our data.

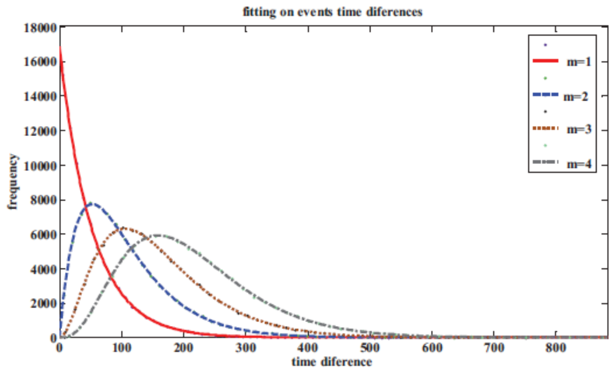

FIG. 4. Distribution of events time-spacing.

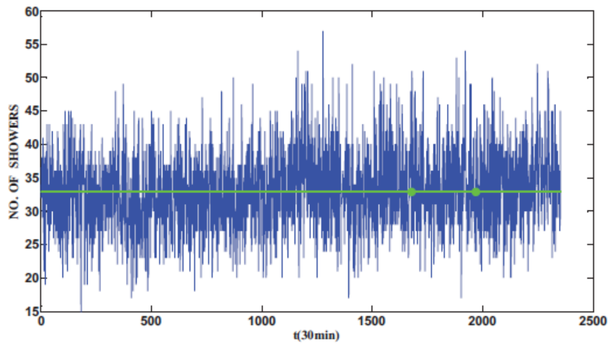

FIG. 5. Frequency of real showers in 30 minutes intervals of experiment time duration with the mean value (line).

Standard deviation of events: 5.9737

After this, the temperature and pressure of each half hours of experiment time is caught from meteorologic data from Mehrabad airport. Distribution of temperature and pressure of the experiment date is shown in Fig.6, the results is as follow :

Maximum of temperature: $29°C$,
Minimum of temperature: $2°C$,
Mean of temperature: $16.2682°C$,
Standard deviation of temperature: 5.012,
Maximum of pressure: $891.1mb$,
Minimum of pressure: $875.4mb$,
Mean of pressure: $884.6675mb$,
Standard deviation of pressure: 3.2945,

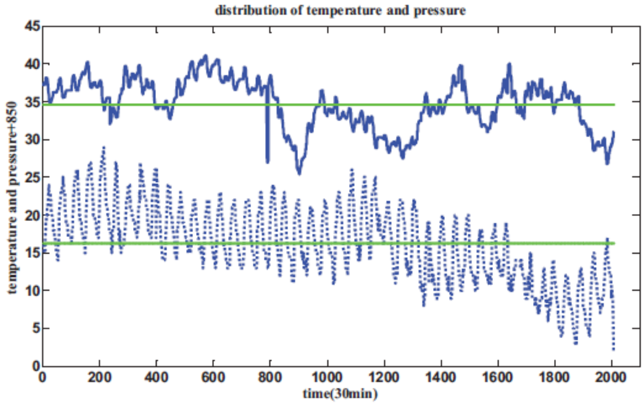

FIG. 6. Distribution of temperature (dashed line) and pressure (continuous line) in each half hour of experiment time with the mean values (line).

V. INVESTIGATION OF CORRELATION FUNCTION BETWEEN TEMPERATURE, PRESSURE AND FREQUENCY

At the end, the Correlation Coefficients matrix of the linear correlation between temperature, pressure and frequency is calculated. The above three parameters are mean of parameters in 30 minutes period of all days of experiment. The result matrix is as follow:

$$\begin{bmatrix} 1.0000 & -0.2410 & -0.0539 \\ -0.2410 & 1.0000 & 0.2363 \\ -0.0539 & 0.2363 & 1.0000 \end{bmatrix} \tag{2}$$

Here,component(i,j) is the Correlation Coefficient between column i and column j of the data, that temperature, pressure and frequency is 1st, 2nd and 3rd column respectively.

VI. CONCLUSION

According to the first stage results we found out that our data is a suitable data for other analysis about the manner of EASs, such as 2nd stage that we studied to some extent the effect of atmospheric variations (P, T) on extensive air showers using about 80 000 events collected by the surface detector of the Alborz Observatory from 07/10/01 to 07/11/30. We observed a significant modulation of the rate of the events with the atmospheric variables.

Correlation coefficient matrix shows a slight correlation between temperature, pressure and rate parameters.

We will study more accurately these effects, also with more data from scintillator and Cherenkov detectors to

[1] J. Abraham, *et al.*, 2009, Atmospheric effects on extensive air showers observed with the surface detector of the Pierre Auger observatory.
[2] F. Sheidaei, *et al.*, 2007, A Study on anisotropy of cosmic ray distribution with a small array of water cherenkov detectors.
[3] *Introduction to theory of statistics*, Alexander M.Mood, Franklin A.Graybill, Duane C.Bose.

Modified Newton's law and Friedman Equations from entropic force

Ahmad Sheykhi *
Department of Physics, Shahid Bahonar University, P.O. Box 76175, Kerman, Iran
Research Institute for Astronomy and Astrophysics of Maragha (RIAAM), Maragha, Iran

By employing the modified entropy-area relation, motivated from the loop quantum gravity, we derive corrections to Newton's law of gravitation as well as modified Friedman equations by adopting the viewpoint that gravity can be emerged as an entropic force.

It was first pointed out by Jacobson [1] that the hyperbolic second order partial differential Einstein equation has a predisposition to the first law of thermodynamics. This profound connection between the first law of thermodynamics and the gravitational field equations has been extensively observed in various gravity theories [2, 3]. Recently the study on the connection between thermodynamics and gravity has been generalized to the cosmological situations [4–9], where it was shown that the differential form of the Friedmann equation on the apparent horizon in the FRW universe can be rewritten in the form of the first law of thermodynamics. The extension of this connection has also been carried out in the braneworld cosmology [10, 11]. The deep connection between the gravitational equation describing the gravity in the bulk and the first law of thermodynamics on the apparent horizon reflects some deep ideas of holography. Although Jacobson's derivation is logically clear and theoretically sound, the statistical mechanical origin of the thermodynamic nature of general relativity remains obscure.

Recently, Verlinde [12] has put forward an idea similar in spirit to Jacobson's thermodynamic derivation of the Einstein equations, where it is argued that Newton's law of gravitation can be understood as an entropic force caused by information changes when a material body moves away from the holographic screen. Quantitatively, when a test particle or excitation moves apart from the holographic screen, the magnitude of the entropic force on this body has the form

$$F\triangle x = T\triangle S, \tag{1}$$

where $\triangle x$ is the displacement of the particle from the holographic screen, while T and $\triangle S$ are the temperature and the entropy change on the screen, respectively. Verlinde's derivation of Newton's law of gravitation at the very least offers a strong analogy with a well understood statistical mechanism. Therefore, this derivation opens a new window to understand gravity from the first principles. The study on the entropic force has raised a lot of enthusiasm recently (see [13–16] and references therein).

It is important to note that in Verlinde discussion, the black hole entropy S plays a crucial role in the derivation of Newton's law of gravitation. Indeed, the derivation of Newton's law of gravity depends on the entropy-area relationship $S = A/4\ell_p^2$ of black holes in Einsteins gravity, where $A = 4\pi R^2$ represents the area of the horizon and $\ell_p^2 = G\hbar/c^3$ is the Planck length. However, this definition can be modified from the inclusion of quantum effects, motivated from the loop quantum gravity (LQG). The quantum corrections provided to the entropy-area relationship leads to the curvature correction in the Einstein-Hilbert action and vice versa [17, 18]. The corrected entropy takes the form [19]

$$S = \frac{A}{4\ell_p^2} - \beta \ln\frac{A}{4\ell_p^2} + \gamma\frac{\ell_p^2}{A} + \text{const}, \tag{2}$$

where β and γ are dimensionless constants of order unity. The exact values of these constants are not yet determined and still an open issue in loop quantum cosmology. These corrections arise in the black hole entropy in LQG due to thermal equilibrium fluctuations and quantum fluctuations [20]. Taking the corrected entropy-area relation (2) into account, we will derive the corrections to the Newton's law of gravitation as well as the modified Friedman equations. We rewrite Eq. (2) in the following form

$$S = \frac{A}{4\ell_p^2} + s(A), \tag{3}$$

where $s(A)$ stands for the correction terms in the entropy expression. We adopt the viewpoint of [12]. Suppose we have two masses one a test mass and the other considered as the source with respective masses m and M. Centered around the source mass M, is a spherically symmetric surface $\mathcal{S}$ which will be defined with certain properties that will be made explicit later. To derive the entropic law, the surface $\mathcal{S}$ is between the test mass and the source mass, but the test mass is assumed to be very close to the surface as compared to its reduced Compton wavelength $\lambda_m = \frac{\hbar}{mc}$. When a test mass m is a distance $\triangle x = \eta\lambda_m$ away from the surface $\mathcal{S}$, the entropy of the surface changes by one fundamental unit $\triangle S$ fixed by the discrete spectrum of the area of the surface via the relation

$$\triangle S = \frac{\partial S}{\partial A}\triangle A = \left(\frac{1}{4\ell_p^2} + \frac{\partial s(A)}{\partial A}\right)\triangle A. \tag{4}$$

The energy of the surface $\mathcal{S}$ is identified with the relativistic rest mass of the source mass:

$$E = Mc^2. \tag{5}$$

*sheykhi@mail.uk.ac.ir

On the surface $\mathcal{S}$, there live a set of "bytes" of information that scale proportional to the area of the surface so that

$$A = QN, \tag{6}$$

where N represents the number of bytes and Q is a fundamental constant which should be specified later. Assuming the temperature on the surface is T, and then according to the equipartition law of energy [21], the total energy on the surface is

$$E = \frac{1}{2} N k_B T. \tag{7}$$

Finally, we assume that the force on the particle follows from the generic form of the entropic force governed by the thermodynamic equation of state

$$F = T \frac{\triangle S}{\triangle x}, \tag{8}$$

where $\triangle S$ is one fundamental unit of entropy when $|\triangle x| = \eta \lambda_m$, and the entropy gradient points radially from the outside of the surface to inside. Note that N is the number of bytes and thus $\triangle N = 1$, hence from (6) we have $\triangle A = Q$. Now, we are in a position to derive the entropic-corrected Newton's law of gravity. Combining Eqs. (4)- (8), we easily obtain

$$F = -\frac{Mm}{R^2} \left(\frac{Qc^3}{2\pi k_B \hbar \eta} \right) \left[\frac{1}{4\ell_p^2} + \frac{\partial s}{\partial A} \right]_{A=4\pi R^2}, \tag{9}$$

This is nothing but the Newton's law of gravitation to the first order provided we define $Q = 8\pi k_B \eta \ell_p^4$. Thus we reach

$$F = -\frac{GMm}{R^2} \left[1 + 4\ell_p^2 \frac{\partial s}{\partial A} \right]_{A=4\pi R^2}, \tag{10}$$

Finally, using Eq. (2) we obtain the modified Newton's law of gravitation as

$$F = -\frac{GMm}{R^2} \left[1 - \frac{\beta}{\pi} \frac{\ell_p^2}{R^2} - \frac{\gamma}{4\pi^2} \frac{\ell_p^4}{R^4} \right], \tag{11}$$

Thus, with the correction in the entropy expression, we see that the Newton's law will modified accordingly. As we mentioned, these corrections are well motivated from bottom-up quantum gravity theories. The log correction to the area-entropy relation appears to have an almost universal status, having been derived from multiple different approaches to the calculation of entropy from counting microscopic states in different quantum gravity models. Since the last two terms in Eq. (11) can be comparable to the first term only when R is very small, the corrections make sense only at the very small distances. When R becomes large, the entropy-corrected Newton's law reduces to the usual Newton's law of gravitation.

Let us compare our result with that obtained in [15]. The first correction term originates from the log correction in Eq. (17) of [15] is similar to ones we obtained in Eq. (11), however, it seems that the second correction term in Eq. (17) of [15] is not reasonable. Physically, the effect of the correction terms on the quantity should be less than the uncorrected quantity. Similarly, the contribution of the first correction term in the physical quantity (force here) should be more from the second term and so on. For all above reasons, we think the second correction term in Eq. (17) of [15] is not correct, and the corrected form is that presented in our note. The origin of this difference is due to the fact that the second (volume) correction term to the entropy expression in [15] is not indeed a correction term, although it was argued by [15] that this term is also emerged in a model for the microscopic degrees comprising the black hole entropy in LQG [23]. Let us stress here that although in the literature there is doubt about the second correction term in entropy-corrected relation, however, it is widely believed [19] that the next quantum correction term to black hole entropy have the form ℓ_p^2/A, which leads to the resonable correction terms to Newton's law of gravitation (11) as we have shown in the present work and will lead to corrected modified Friedmann equation as we will see later.

Next, we extend our discussion to the cosmological setup. Assuming the background spacetime to be spatially homogeneous and isotropic which is given by the Friedmann-Robertson-Walker (FRW) metric

$$ds^2 = h_{\mu\nu} dx^\mu dx^\nu + R^2 (d\theta^2 + \sin^2\theta d\phi^2), \tag{12}$$

where $R = a(t)r$, $x^0 = t, x^1 = r$, the two dimensional metric $h_{\mu\nu}$=diag $(-1, a^2/(1-kr^2))$. Here k denotes the curvature of space with $k = 0, 1, -1$ corresponding to open, flat, and closed universes, respectively. The dynamical apparent horizon, a marginally trapped surface with vanishing expansion, is determined by the relation $h^{\mu\nu}\partial_\mu R \partial_\nu R = 0$. A simple calculation gives the apparent horizon radius for the FRW universe

$$R = ar = \frac{1}{\sqrt{H^2 + k/a^2}}. \tag{13}$$

We also assume the matter source in the FRW universe is a perfect fluid with stress-energy tensor

$$T_{\mu\nu} = (\rho + p) u_\mu u_\nu + p g_{\mu\nu}. \tag{14}$$

Due to the pressure, the total mass $M = \rho V$ in the region enclosed by the boundary $\mathcal{S}$ is no longer conserved, the change in the total mass is equal to the work made by the pressure $dM = -pdV$, which leads to the well-known continuity equation

$$\dot{\rho} + 3H(\rho + p) = 0, \tag{15}$$

where $H = \dot{a}/a$ is the Hubble parameter. It is instructive to first derive the dynamical equation for Newtonian cosmology. Consider a compact spatial region V with a compact boundary $\mathcal{S}$, which is a sphere with physical radius $R = a(t)r$. Note that here r is a dimensionless quantity which remains constant for any cosmological object partaking in free cosmic expansion. Combining the second law of Newton for the test particle m near the surface, with gravitational force (11) we get

$$F = m\ddot{R} = m\ddot{a}r = -\frac{GMm}{R^2}\left[1 - \frac{\beta}{\pi}\frac{\ell_p^2}{R^2} - \frac{\gamma}{4\pi^2}\frac{\ell_p^4}{R^4}\right], \tag{16}$$

We also assume $\rho = M/V$ is the energy density of the matter inside the the volume $V = \frac{4}{3}\pi a^3 r^3$. Thus, Eq. (16) can be rewritten as

$$\frac{\ddot{a}}{a} = -\frac{4\pi G}{3}\rho\left[1 - \frac{\beta}{\pi}\frac{\ell_p^2}{R^2} - \frac{\gamma}{4\pi^2}\frac{\ell_p^4}{R^4}\right], \tag{17}$$

This is nothing but the entropy-corrected dynamical equation for Newtonian cosmology. The main difference between this equation and the standard dynamical equation for Newtonian cosmology is that the correction terms now depends explicitly on the radius R. However, we can remove this confusion. Assuming that for Newtonian cosmology the spacetime is Minkowskian with $k = 0$, then we get $R = 1/H$, and we can rewrite Eq. (17) in the form

$$\frac{\ddot{a}}{a} = -\frac{4\pi G}{3}\rho\left[1 - \frac{\beta\ell_p^2}{\pi}\left(\frac{\dot{a}}{a}\right)^2 - \frac{\gamma\ell_p^4}{4\pi^4}\left(\frac{\dot{a}}{a}\right)^4\right]. \tag{18}$$

It was argued in [13] that for deriving the Friedmann equations of FRW universe in general relativity, the quantity that produces the acceleration is the active gravitational mass $\mathcal{M}$ [22], rather than the total mass M in the spatial region V. With the entropic corrections terms, the active gravitational mass $\mathcal{M}$ will also modified as well. On one side, from Eq. (17) with replacing M with $\mathcal{M}$ we have

$$\mathcal{M} = -\frac{\ddot{a}a^2}{G}r^3\left[1 - \frac{\beta}{\pi}\frac{\ell_p^2}{R^2} - \frac{\gamma}{4\pi^2}\frac{\ell_p^4}{R^4}\right]^{-1}. \tag{19}$$

On the other side, the active gravitational mass is defined as [13]

$$\mathcal{M} = 2\int_V dV\left(T_{\mu\nu} - \frac{1}{2}Tg_{\mu\nu}\right)u^\mu u^\nu. \tag{20}$$

A simple calculation leads

$$\mathcal{M} = (\rho + 3p)\frac{4\pi}{3}a^3 r^3. \tag{21}$$

Equating Eqs. (19) and (21) we find

$$\frac{\ddot{a}}{a} = -\frac{4\pi G}{3}(\rho + 3p)\left[1 - \frac{\beta}{\pi}\frac{\ell_p^2}{R^2} - \frac{\gamma}{4\pi^2}\frac{\ell_p^4}{R^4}\right]. \tag{22}$$

This is the modified acceleration equation for the dynamical evolution of the FRW universe. Multiplying $\dot{a}a$ on both sides of Eq. (22), and using the continuity equation (15), after integrating we find

$$H^2 + \frac{k}{a^2} = \frac{8\pi G}{3}\rho\left[1 - \frac{\beta}{\pi}\frac{\ell_p^2}{\rho R^2}\int\frac{d(\rho a^2)}{a^2} - \frac{\gamma}{4\pi^2}\frac{a^2\ell_p^4}{\rho R^4}\int\frac{d(\rho a^2)}{a^4}\right]. \tag{23}$$

Now, in order to calculate the integrations in the correction terms we need to find $\rho = \rho(a)$. Assume the equation of state parameter $w = p/\rho$ is a constant, the continuity equation (15) can be integrated immediately to give

$$\rho = \rho_0 a^{-3(1+w)}, \tag{24}$$

where ρ_0, an integration constant, is the present value of the energy density. Inserting relation (24) in Eq. (23), after integration, we obtain

$$H^2 + \frac{k}{a^2} = \frac{8\pi G}{3}\rho\left[1 - \frac{\beta(1+3w)}{3\pi(1+w)}\frac{\ell_p^2}{R^2} - \frac{\gamma(1+3w)}{4\pi^2(5+3w)}\frac{\ell_p^4}{R^4}\right]. \tag{25}$$

Using Eq. (13) we can further rewrite the above equation as

$$\left(H^2 + \frac{k}{a^2}\right)\left[1 - \frac{\beta\ell_p^2(1+3w)}{3\pi(1+w)}\left(H^2 + \frac{k}{a^2}\right) - \frac{\gamma\ell_p^4(1+3w)}{4\pi^2(5+3w)}\left(H^2 + \frac{k}{a^2}\right)^2\right]^{-1} = \frac{8\pi G}{3}\rho. \tag{26}$$

If β and γ are viewed as small quantities, then the above equation can be expanded up to the linear order of β and γ. The result is

$$\left(H^2 + \frac{k}{a^2}\right) + \frac{\beta\ell_p^2(1+3w)}{3\pi(1+w)}\left(H^2 + \frac{k}{a^2}\right)^2 + \frac{\gamma\ell_p^4(1+3w)}{4\pi^2(5+3w)}\left(H^2 + \frac{k}{a^2}\right)^3 = \frac{8\pi G}{3}\rho, \tag{27}$$

which is in complete agreement with the result of [8] (see also [9]). In this way we derive the entropy-corrected Friedmann equation of FRW universe by considering gravity as an entropic force caused by changes in the information associated with the positions of material bodies. In the absence of the correction terms ($\beta = 0 = \gamma$), one recovers the well-known Friedmann equation in standard cosmology. Since the last two terms in Eq. (25) can be comparable to the first term only when a is very small, the corrections make sense only at early stage of the universe where $a \to 0$. When the universe becomes large, the entropy-corrected Friedmann equation reduces to the standard Friedman equation.

In summary, we have shown that with the entropy corrections to the area-relation of the black hole entropy, the Newton's law of gravitation and the Friedmann equations will be modified accordingly. These corrections are motivated from the LQG which is one of the promising theories of quantum gravity. We derived the correction terms to the Newton's law of gravity as well as modified Friedmann equations of the FRW universe starting from the holographic principle and the equipartition law of energy by using Verlinde's argument that gravity appears as an entropic force. In particular, we have found that an apparently universal log correction to the area-entropy, yields deviations from Newton's law and Friedman equations that are identical in form to those obtained from perturbative quantum gravity. This at once sheds light on the reason for the universality of the log correction and provides a strong consistency check on Verlinde's model.

Acknowledgments

I am grateful to Prof. B. Wang and Prof. R.G. Cai for helpful discussions and reading the manuscript. This work has been supported by Research Institute for Astronomy and Astrophysics of Maragha.

[1] T. Jacobson, Phys. Rev. Lett. **75**, 1260 (1995).
[2] C. Eling, R. Guedens, and T. Jacobson, Phys. Rev. Lett. **96**, 121301 (2006).
[3] T. Padmanabhan, Phys. Rept. **406** (2005) 49;
T. Padmanabhan, Rept. Prog. Phys. 73 (2010) 046901.
[4] M. Akbar and R. G. Cai, Phys. Rev. D **75**, 084003 (2007).
[5] R. G. Cai and L. M. Cao, Phys.Rev. D **75**, 064008 (2007).
[6] R. G. Cai and S. P. Kim, JHEP **0502**, 050 (2005).
[7] B. Wang, E. Abdalla and R. K. Su, Phys.Lett. B **503**, 394 (2001);
B. Wang, E. Abdalla and R. K. Su, Mod. Phys. Lett. A **17**, 23 (2002);
R. G. Cai and Y. S. Myung, Phys. Rev. D **67**, 124021 (2003);
R. G. Cai and L. M. Cao, Nucl. Phys. B **785** (2007) 135.
[8] R. G. Cai, L. M. Cao and Y. P. Hu, JHEP 0808 (2008) 090.
[9] S. Nojiri and S. D. Odintsov, hep-th/0506212;
S. Nojiri and S. D. Odintsov, hep-th70506212;
A. Sheykhi, B. Wang, submitted to EPJC.
[10] A. Sheykhi, B. Wang and R. G. Cai, Nucl. Phys. B **779** (2007)1.
[11] A. Sheykhi, B. Wang and R. G. Cai, Phys. Rev. D **76** (2007) 023515;
A. Sheykhi, B. Wang, Phys. Lett. B 678 (2009) 434;
A. Sheykhi, Class. Quantum Grav. 27 (2010) 025007.
[12] E. P. Verlinde, arXiv:1001.0785 [hep-th].
[13] R.G. Cai, L. M. Cao and N. Ohta, arXiv:1001.3470.
[14] R.G. Cai, L. M. Cao and N. Ohta, arXiv:1002.113;
Yi Ling, Jian-Pin Wu, arXiv:1001.5324;
Yun Soo Myung, arXiv:1002.0871;
R. Banerjee, B. R. Majhi, arXiv:1003.2312;
S.W. Wei, Y. X. Liu, Y. Q. Wang, arXiv:1001.5238;
Y. X. Liu, Y. Q. Wang, S. W. Wei, arXiv:1002.1062;
R.A. Konoplya, e-Print: arXiv:1002.2818;
[15] L. Modesto, A. Randono, arXiv:1003.1998.
[16] Y.F. Cai, J. Liu, H. Li, arXiv:1003.4526.
[17] T. Zhu and J.R. Ren, Eur. Phys. J. C 62 (2009) 413;
R.G. Cai et al, Class. Quantum Grav 26 (2009) 155018;
D. A. Easson, arXiv: 1003.1528.
[18] M. R. Banerjee, S. K. Modak, JHEP 0905 (2009) 063;
S. K. Modak, Phys. Lett. B 671 (2009) 167;
R. Banerjee, S. Gangopadhyay, S. K. Modak, Phys. Lett. B 686 (2010) 181.
[19] J. Zhang, Phys. Lett. B 668 (2008) 353;
R. Banerjee and B. R. Majhi, Phys. Lett. B 662, 62 (2008);
R. Banerjee and B. R. Majhi, JHEP 0806 (2008) 095;
R. Banerjee, B. R. Majhi and S. Samanta, Phys. Rev. D 77, 124035 (2008);
R. Banerjee, B. R. Majhi, Phys. Lett. B 674 (2009) 218;
B. R. Majhi, Phys. Rev. D 79 (2009) 044005;
S. Nojiri and S. D. Odintsov, Int. J. Mod. Phys. A 16 (2001) 3273;
J. Lidsey et. al., Phys. Lett. B 544 (2002) 337;
[20] C. Rovelli, Phys. Rev. Lett. 77 (1996) 3288;
A. Ashtekar, J. Baez, A. Corichi, and K. Krasnov, Phys. Rev. Lett. 80 (1998) 904.
[21] T. Padmanabhan, Class. Quantum Grav. 21, 4485 (2004);
T. Padmanabhan, arXiv:0912.3165;
T. Padmanabhan, arXiv:1003.5665
[22] T. Padmanabhan, arXiv:1001.3380 [gr-qc].
[23] L. Smolin, arXiv:1001.3668.

A mixture spatial point pattern model for the quasar luminosity function

Amir T. Payandeh Najafabadi[1] and Fatemeh Baniasadi[2]
[1] *Department of Mathematical Sciences, Shahid Beheshti University, G.C. Evin, 1983963113, Tehran, IRAN.*
[2] *Department of Basic Sciences, Payame-noor university branch of Shiraz, Shiraz, Iran.*

Consider the problem of estimating the quasar luminosity function (QLF). Hugeback, A. (2007), Ph.D. dissertation, The University of Chicago, 84 pages; AAT 3273021, considered the QLF as a nonhomogeneous poisson process. Then, she estimated the inhomogeneous intensity of such process using the SDSS data release 3 (DR3). This article follows the Hugeback's (2007) model introduces a mixture model which improves Hugeback's model in several aspects. Namely, the database has been divided into two parts $z \lesssim 2.45$ and $z \geq 3$. Now, by using pseudolikelihood, concept of F function, and along with the residuals diagnostic plots, a mixture model for the QLF has been derived. Such mixture model: **(i)** improves deviance of Hugeback's model and **(ii)** satisfies the residual assumptions while the Hugeback's is violated from such assumptions. Moreover, inhomogeneity of the QLF; existence of interaction effect of redshift and absolute optical magnitude on the QLF have been.

PACS numbers: 95.55.-n, 02.50.-r, 03.75.Hh.

I. INTRODUCTION

The Quasar Luminosity Function (QLF) is the spatial density of quasars per luminosity interval, which observes as a function of M and z. The QLF is also useful for understanding the spatial clustering of quasars and its relation to quasar lifetimes (Martini & Weinberg 2001). The QLF is a statistical measure for joint distribution of quasar in luminosity and redshift. Moveover, the QLF can be employed: **(i)** to predict the number-magnitude relation quasars in assessing the incompleteness of a magnitude-limited survey; **(ii)** to calculate the redshift distribution of bright quasar in establishing their cosmic evolution; **(iii)** to interpret the spatial clustering of quasars in testing the assumption of an isotropic and homogeneous universe; and **(iv)** to estimate the contribution of quasars to the ultraviolet background radiation. Earlier works on the QLF study, conducted by Marshall et al. (1983, 1984) and Marshall (1985), found that: **(i)** there is a strong decline of quasar activity from $z \sim 2$ to the present universe; **(ii)** the model with a single power-law shape, $\Phi(L) \propto L^3$, provided good fits to the observed QLF for $z < 2$ at the bright end. Koo & Kron (1988) and Boyle et al. (1988) found a break in the LF, whenever more faint quasars were discovered. They modeled the shape of the QLF by a double power-law form with a steep bright end and a much flatter faint end. In 1995, Pie considered 1200 quasars over the range of redshift $0 \leq z \leq 4.5$. Then, they modeled the QLF, for such range of redshift, by the Gaussian distribution, which reaches to its maximum at $z \simeq 2.8$. Moreover, they found that the shape of the LF can be well fitted by either a double power law or an exponential $L^{0.25}$ law. Warren et al. (1994), Kennefick et al. (1995), Schmidt et al. (1995), and Fan et al. (2001b), among others, have been explored properties of the QLF for bright quasars, i.e., $z \sim 4$. Moreover, Schmidt et al. (1995) and Fan et al. (2001b) fitted a single power-law, form with an exponential decline in density with redshift, to the QLF. Such model shows that at high redshift, $z < 3$, the shape of the QLF evolves with redshift as well. Boyle et al. (2000) and Croom et al. (2004) used the September 1999 version of 2QZ data contains 6684 observation. To show that, the pure luminosity evolution (PLE) models provide an acceptable fit to the observed redshift of the LF. Also, they shown that the best fit for the LF is obtained by the two-power law function. Wolf et al. (2003) and Richards et al. (2006) are such authors who considered the QLF as a function with form $\Phi = \Phi^* 10^{A_1 \mu}$, where $\mu = M - (-26 + B_1\xi + B_2\xi^{(2)} + B_3\xi^3)$ and $\xi = \ln((1+z)/(1+2.45))$ with free parameters Φ^*, A_1, B_1, B_2, and B_3. In 2007, Hugeback in a quite different setting employed the functional form of the QLF, given by Wolf et al. (2003) and Richards et al. (2006). Using the fact that SDSS only surveys one quarter of the sky, Richards et al. (2006) introduced probability function $\Psi(M, z)$, as a function of redshift z and optical magnitude M, to a quasar with specific M and z locate within the quarter of the sky surveyed.

This article considers the problem of estimating the intensity function of the QLF based upon Data SDSS data release 3, say DR3. Such data includes redshift, i-band magnitude (dereddened) of the 1622 deg$^{(2)}$ quarter of the sky, more detail can be found at: http://www.sdss.org/dr3/. Moreover to increase accuracy and efficiency of fitted model, we decide: **(1)** to remove quasars which have zero (or nearly zero) probability to be quasars in the 1622 deg$^{(2)}$ quarter of the sky from the database; **(2)** to divide DR3 into two categories $z \lesssim 2.45$ and $z \geq 3$, where two critical cut points, 2.45 and 3, obtained from Hugeback (2007). The former probabilities arrived from Richards et al. (2006), while the latter modification is obtained from Marshall's (1985) findings, which state that a fitted model provides better fit whenever data was split into two categories. Now, using the Hugeback's (2007) model for each categories a mixture model has been derived. Such mixture model **(i)** improves deviance of Hugeback (2007)'s model and **(ii)** satisfies the residual assumptions while the Hugeback (2007)'s is violated from such assumptions.

This article developed as the following. Section 2 reviews on some elements in the spatial point patterns. The mixture model specifies and implements against the DR3 data in Section 3. Finally, findings are discussed in Section 4.

II. METHODOLOGY

Spatial point patterns are mathematical models that describe the arrangement of objects that are irregularly or randomly distributed in the plane or in space. The patterns formed by the objects are analyzed in many scientific disciplines; hence a great variety of objects may be considered such as atoms, molecules, biological particles, pores, or stars and galaxies. Spatial point process is perhaps the most developed and beautiful branch of the modern field of spatial statistics; this is perhaps because points are the most elementary of geometrical objects and lead to data structures that are particularly clear and useful. A simple graphical representation of the pattern of objects as a point map is a very useful preliminary step towards understanding its properties: visual inspection provides a qualitative characterization of the type of the pattern even if rather vague terms are used in the initial description (clustered, aggregated, clumped, patchy, regular,inhibited, uniform, even). Analysis is very much concerned with detecting and describing these correlations. Many different aspects of the nature of a specific spatial point pattern may be described using the appropriate statistical methods. The simplest of these is the point intensity, i.e. the average number of objects per unit area or volume, if point density can be considered constant across space. However, characteristics that are more typical of point process statistics describe correlations among the points in the pattern relative to their distances.

Recent decades have seen a strong increase in the development of point process methodology, based on a profound theoretical development and driven by applications from many different fields of science. In addition to the classical fields of application such as astronomy and particle physics extensively apply point process methods. Astrostatistics is an old and classical field of spatial statistics. Astronomers study both spatial random fields in space (the density field, the velocity field and others) and spatial point patterns in two and three-dimensional space.

In the analysis of spatial point patterns, one of the main objectives is often to assess the strength of 'interaction' or dependence between the points. Standard practice in the analysis of point patterns is first to form a non-parametric estimate of the first-order intensity $\lambda(s)$, for $\in R^{(2)}$ then if this is deemed to be uniform, $\lambda(s) \equiv \lambda$, to investigate inter-point interactions by estimating various summary statistics such as the K-function or the empty space distribution function (F-function) and the nearest-neighbor distance distribution function (G-function).

Statistical inference for finite point patterns, which are point patterns with finite number of points within their corresponding bounded sets, can be difficult in places. Baddeley & Turner (2000) provided an extensive treatment of both practical and theoretical aspects of pseudo-likelihood (pl) estimation. They defined pseudolikelihood function as

$$pl(\theta) = \exp\{-\int_B \lambda_\theta(x;\xi)dx\} \prod_{u\in x_B} \lambda_\theta(x \setminus \xi; x),$$

where θ and λ_θ respectively stand for parameters and the Papangelou conditional intensity of a spatial point process; x_B is the restriction of data set; and ξ is a point in x_B. Then, they described a technique to compute maximum pseudolikelihood (mpl) estimates of the parameters of a spatial point process, approximately. The mpl works appropriately for a very wide class of spatial point process models, while the usual maximum likelihood method is intractable for those, more can be found in Baddeley & Turner (2000). A user-friendly implementation of pseudolikelihood estimation is given in the R package Spatstat by Baddeley & Turner (2005).

After fitting a model by estimating its parameters, using the mpl method, validation of fitted model should be examined. It is convenient to study the model's residuals. Baddeley, Turner, Moller, & Hazelton (2005) developed a method to measure fitness of models with respect to their residuals. Moreover, they developed four diagnostic plots, in a panel, to check existence of: spatial trend, dependence on spatial covariant, and interaction between points of the pattern and other effects. Such diagnostic plots, which use to check, visually, model's assumptions, can be drawn by the R package Spatstat. In general, the plots should detect misspecification of true spatial trend, covariant effects, and interpoint interaction in the data by the fitted model. These plots are Mark, Contour, and Two Lurking variable plots, more detail may be found in Baddeley et al. (2005). The fitted values produced by the model are most unlikely to match the values of the data perfectly. The size of the discrepancy between the model and the data is a measure of the inadequacy of the model; a small discrepancy may be tolerable, but a large one will not be. Deviance and Akaic (AIC) are two criteria to measure discrepancy of the model against the data. Finally, the prediction plot can be used to investigate coincidences of the fitted model's trend to observed data's trend.

III. MODEL SPECIFICATION AND RESULTS

A major complicating factor in the estimation of the QLF is that observed quasars were not selected uniformly at random from the population of all detectable quasars in the universe. The selection probabilities for each quasar are dependent on that quasars apparent brightness (m) and its redshift(z) distance from Earth. Richards et al. (2006) calculated observational probability, say $\Psi(\cdot)$, that a quasar with the given redshift and apparent optical magnitude would be included in the data. The observational probabilities are affected by whether a particular quasar is extended or non-extended, and therefore Richards et al. have created two separate tables of the estimated probabilities.

For the purposes of estimating the intensity function of the QLF based upon Data SDSS data release 3, say DR3, which includes redshift, i-band magnitude (dereddened) of the 1622 deg$^{(2)}$ quarter of the sky, more detail can be found at: http://www.sdss.org/dr3/. Moreover to increase accuracy and efficiency of fitted model, we decide: (1) to remove quasars which have zero (or nearly zero) probability to be quasars in the 1622 deg$^{(2)}$ quarter of the sky from the database; (2) to divide DR3 into two categories $z \lesssim 2.45$ and $z \geq 3$, where two critical cut points, 2.45 and 3, obtained from Hugeback (2007). The former probabilities arrived from Richards et al. (2006), while the latter modification is obtained from Marshall's (1985) findings, which state a fitted model provides better fit whenever data was split into two categories. Now, using the Hugeback's (2007) model for each categories (containing 14423 quasars in total) the QLF a nonhomogeneous poisson process, in $M \times z$ space, with an inhomogeneous intensity function $Log_{10}(\Phi_\theta(M;z)) = (\mu^{(1)} + f_1^{(1)}(M;\alpha^{(1)}) + f_2^{(1)}(z;\beta^{(1)}) + f_3^{(1)}(M;z;\gamma^{(1)}))I(z \lesssim 2.45) + (\mu^{(2)} + f_1^{(2)}(M;\alpha^{(2)}) + f_2^{(2)}(z;\beta^{(2)}) + f_3^{(2)}(M;z;\gamma^{(2)}))I(z \geq 3)$, where $\theta = (\mu^{(1)}, \mu^{(2)}, \alpha^{(1)}, \alpha^{(2)}, \beta^{(1)}, \beta^{(2)}, \gamma^{(1)}, \gamma^{(2)})$ are model's parameters which are unknown and be estimated; $f_1^{(l)}(M;\alpha^{(l)}) := \sum_{i=1}^{A^{(l)}} \alpha_i^{(l)}(M - M_0)^i$; $f_2^{(l)}(z;\beta^{(l)}) := \sum_{j=1}^{B^{(l)}} \beta_j^{(l)} \xi_l(z)^j$; $f_3^{(l)}(M;z;\gamma^{(l)}) := \sum_{k=1}^{D^{(l)}} \gamma_k^{(l)} (M - M_0 - \xi_l(z))^{k+1}$; and $\xi_l(z) := log_{10}((1-z)/(1+z_l))$, for $l = 1, 2$; and $A^{(1)}$, $A^{(2)}$, $B^{(2)}$, $B^{(2)}$, $D^{(2)}$, and $D^{(2)}$ are the model complexity levels; and follows Richards et al.'s suggestion two values M_0, z_1, and z_2 are to be -26, 2.45, and 0, respectively. The likelihood function for the nonhomogeneous poisson process is $L(\theta|X) = \exp\{-|\lambda_\theta|\}/N! \prod_{i=1}^{N} \Phi_\theta(M_i; z_i)$, where $|\lambda_\theta| := \int_z \int_M \Phi_\theta(M;z)\gamma(z)dMdz$ and $\gamma(z)dz$ be the infinitesimal volume differential (measured in cubic megaparsecs) of a spherical shell about the Earth at a given redshift z. Unknown model's parameters θ are estimated by using the plm technique, described the above, after fixing model complexity levels $A^{(1)}$, $A^{(2)}$, $B^{(1)}$, $B^{(2)}$, $D^{(1)}$, and $D^{(2)}$. Using the Spatstat package to fit the mixture nonhomogeneous poisson process with the above inhomogeneous intensity function against the DR3 data led to $Log_{10}(\Phi_\theta(M;z)) = (-34.847 + \sum_{i=1}^{4} \alpha_i^{(1)}(M+26)^j + \sum_{j=1}^{6} \beta_j^{(1)}(log_{10}(1+z))^j + \sum_{l=1}^{6} \gamma_i^{(1)} [M + 26 - log_{10}(1+z)]^{l+1})I(z \leq 2.45) + (-157.387 + \sum_{i=1}^{3} \alpha_i^{(2)}(M+26)^j + \sum_{j=1}^{6} \beta_j^{(2)}(log_{10}(1+z))^j + \sum_{l=1}^{3} \gamma_i^{(2)} [M + 26 - log_{10}(1+z)]^{l+1})I(z \geq 3)$, where $\alpha_1^{(1)} = 16.437$, $\alpha_2^{(1)} = -12.149$, $\alpha_3^{(1)} = -1.0257$, $\alpha_4^{(1)} = 0.115$, $\alpha_1^{(2)} = -13.709$, $\alpha_2^{(2)} = -21.589$, $\alpha_3^{(2)} = -2.832$, $\beta_1^{(1)} = 114.945$, $\beta_2^{(1)} = -20.529$, $\beta_3^{(1)} = -245.006$, $\beta_4^{(1)} = 303.084$, $\beta_5^{(1)} = -138.491$, $\beta_6^{(1)} = 18.250$, $\beta_1^{(2)} = 3175.412$, $\beta_2^{(2)} = -25265.79$, $\beta_3^{(2)} = 102210.200$, $\beta_4^{(2)} = -224448.900$, $\beta_5^{(2)} = 253994.200$, $\beta_6^{(2)} = -116029.800$, $\gamma_1^{(1)} = 11.176$, $\gamma_2^{(1)} = 0.845$, $\gamma_3^{(1)} = 0.022$, $\gamma_4^{(1)} = -0.022$, $\gamma_5^{(1)} = -0.008$, $\gamma_6^{(1)} = -0.0004$, $\gamma_1^{(2)} = 8.488$, $\gamma_2^{(2)} = -0.952$, and $\gamma_3^{(2)} = -0.3459$.

one can conclude from the above well fitted model that: (1) for both categories $z \lesssim 2.45$ and $z \geq 3$ a significant effect of interaction between redshift, z, and magnitude, M, on the intensity the QLF can be observed; (2) for lower redshift $z \lesssim 2.45$ the interaction between z and M has more affect the intensity of the QLF. Now, the fitted mixture model can be compared with the Hugeback's (2007) model. The following hypothesis has been made to compare these models, in sense of residuals viewpoint.

$$\begin{aligned} &H_0 : \text{Hugeback's model is an appropriate one} \\ &H_1 : \text{the mixture model is an appropriate one.} \end{aligned} \tag{1}$$

Implementation of the Deviance against DR3 data to test the above hypothesis has been summarized in Tables 1 and 2.

Table 1: Deviance comparison between Hugeback's (say H) and the mixture (say M) models for $z \lesssim 2.45$.

Model	Resid. Df	Resid. Dev	df	Deviance	p-avlue
H	65786	24235.6			
M	65778	22768.3	8	1467.2	0

Table 2: Deviance comparison between Hugeback's (say H) and the mixture (say M) models for $z \geq 3$.

Model	Resid. Df	Resid. Dev	df	Deviance	p-avlue
H	9722	2.371×10^{18}			
M	9717	2432	5	2.3071×10^{18}	0

Zero p-values, of both model, suggests that: the null hypothesis H_0 should be rejected in favor of H_1. Therefore, the mixture model provides a better fit for DR3 data. This finding is also verified by the AIC criteria.

IV. SUMMARY AND DISCUSSION

This article presented a mixture parametric model for quasars as a two-dimensional nonhomogeneous poisson process which allows to introduce two different inhomogeneous intensity for low ($z \precsim 2.45$) and high ($z \geq 3$) redshift and different order terms for effect of redshift, absolute magnitude, and their interaction against of the DR3 data. Appropriateness of the mixture model from several different viewpoints has been explored.

Our findings based upon the mixture model state that: (**i**) The QLF is a nonhomogeneous poisson process; (**ii**) dividing the DR3 data, based upon redshift, into two categorizes provides a more accurate and well fitted model to data; (**iii**) The interaction between redshift, z, and magnitude, M, effect of intensity of the QLF for both low and high redshift; and (**iv**) for low redshift $z \lesssim 2.45$ such interaction between provides more effect on the intensity of the QLF.

The first observation has been verified also by Hugeback (2007), among others. The second finding is also verified by Marshall (1985), who discovered that split of data, based upon redshift, lead to a better fitness. The third result, which verified also by Hugeback (2007), is in contrast to the popular scientific theory proposed by Fan et al. (2001) which states that absolute magnitude and redshift should be treated as separable components in the quasar luminosity function. However, it is important to keep in mind that unknown errors in the K correction function or the estimates of the observational probabilities could have a significant impact on the results of the analysis. We are unable to test for the robustness of the mixture model against these types of errors, and therefore one has to be cautious about making any strong claims as to the true nature of the quasar luminosity function. Our last result, which states different for redshift polynomial order of interaction effect will be changed, may strongly verifies Hugeback's (2007) suggestion to establish a new scientific theories in order to explain the distribution of quasars in our universe has changed over time.

[1] Baddeley, A. & Turner, R. (2000). Practical maximum pseudolikelihood for spatial point patterns. *Australian and New Zealand Journal of statistics*, **42**, 283.

[2] Baddeley, A. & Turner, A. (2005). An R package for analyzing spatial point patterns. *Journal of statistical software*, **12**, 1.

[3] Baddeley, A., Turner, R., Moller, J., & Hazelton, M. (2005). Residual analysis for spatial point processes. *J. R. Statist. Soc. B*, **67**, 617.

[4] Boyle, B., Shank, .T, & Peterson, B. (1988). The evolution of optically selected QSOs. II, *Notices of the Royal Astronomical Society*, **235**, 935.

[5] Boyle, B. et al., (2000). The 2dF QSO Redshift Survey - I. The optical luminosity function of quasi-stellar objects. *Notices of the Royal Astronomical Society*, **317**, 1014.

[6] Croom, S. et al., (2004). The 2dF QSO Redshift Survey - XII. The spectroscopic catalogue and luminosity function. *Monthly Notices of the Royal Astronomical Society*, **349**, 1397.

[7] Fan, X. et al. (2001). High-Redshift Quasars Found in sloan Digital Sky Survey Commissioning Data. IV. *The Astronomical Journal*, **121**, 54.

[8] Fan, X. et al. (2001b) High-Redshift Quasars Found in Sloan Digital Sky Survey Commissioning Data. III. A Color-selected Sample at i* ¡ 20 in the Fall Equatorial Stripe. The Astronomical Journal, **121**, 1.

[9] Hugeback, A., et al. (2007). *Point process models for astronomy: Quasars, coronal mass ejections, and solar flares.*Ph.D. dissertation, The University of Chicago, 84 pages; AAT 3273021.

[10] Kennefick, J. D., Djorgovski, S. G., & deCarvalho, R. R. (1995). The Luminosity Function of z¿4 Quasars from the Second Palomar Sky Survey. *Astronomical Journal*, **110**, 25.

[11] Koo, D. C., & Kron, R. G. (1988). Spectroscopic survey of QSOs to B = 22.5, the luminosity function. *Astrophysical Journal*, **325**, 92.

[12] Marshall, H. L. (1985). The evolution of optically selected quasars with Z less than 2.2 and B less than 20. *Astrophysical Journal*, **299**, 109.

[13] Marshall, H. L. et al. (1984). A complete sample of quasars at B = 19.80. it Astrophysical Journal, Part 1, **283**, 50.

[14] Marshall, H. L. et al. (1983). Analysis of complete quasar samples to obtain parameters of luminosity and evolution functions. *Astrophysical Journal, Part 1*, **269**, 35.

[15] Martini, P. & Weinberg, D. H. (2001). Quasar clustering and the lifetime of Quasars. *Astrophysical Journal, Part 1*, **547**, 12.

[16] Richards, G. T., et al. (2006). The sloan digital sky quasar survey: Quasar luminosity function from data release. *The Astronomical Journal* , **131**, 2766.

[17] Schmidt M., et al. (1995). Spectrscopic CCD Surveys for Quasars at Large Redshift. IV. Evolution of the Luminosity Function from Quasars Detected by Their Lyman-Alpha Emission. *Astronomical Journal*, **110**, 68.

[18] Warren, J. et al. (1994). A wide-field multicolor survey for high-redshift quasars, Z greater than or equal to 2.2. 3: The luminosity function. *Astrophysical Journal*, **421**, 412.

[19] Wolf, et al., (2003). The evolution of faint AGN between z_1 and z_5 from the COMBO-17 survey. *Astronomy & Astrophysics*, **408**, 499.

Cosmic Strings Collision in Cosmological Backgrounds

Hassan Firouzjahi[1], Salomeh Khoeini-Moghaddam[1,2] and Shahram Khosravi[2,3]
[1]*School of Physics, Institute for Research in Fundamental Sciences (IPM), Tehran, Iran*
[2]*Department of Physics, Faculty of Science,Tarbiat Mo'allem university, Tehran, Iran*
[3]*School of Astronomy, Institute for Research in Fundamental Sciences (IPM), Tehran, Iran*

The collisions of cosmic strings loops and the dynamics of junctions formations in expanding backgrounds are studied. The key parameter controlling the dynamics of junctions formation, the cosmic strings zipping and unzipping is the relative size of the loops compared to the Hubble expansion rate at the time of collision. We study analytically and numerically these process for large super-horizon size loops, for small sub-horizon size loops as well as for the loops with radii comparable to the Hubble expansion rate at the time of collision.

I. INTRODUCTION

In models of brane inflation cosmic strings are copiously produced [1,2], . These cosmic superstrings are in the form of fundamental strings (F-strings), D1-branes (D-strings) or the bound states of p F-strings and q D-strings, the (p, q) strings. When two (p, q) cosmic superstrings collide junctions are formed due to charge conservation. Therefore one may consider the junction formation as a novel feature of a network of cosmic superstings which may prove crucial in cosmic superstrings detection in cosmological observations. Networks of cosmic strings with junctions have interesting physical properties, such as the formation of multiple images [3,4] and non-trivial gravitational wave emission [5,6]. However, after the junction is formed it can not grow indefinitely and after some time the junction start to unzip and the colliding loops disentangle and pass by from each other [7]. The junctions' zipping and unzipping are interesting and yet non-trivial dynamical properties. These phenomena becomes more significant in the light of cosmic strings simulation by Urrestilla and Vilenkin [8]. In their model, the cosmic strings are two types of U(1) gauge strings with interactions between them.

Due to the interaction, the strings cannot exchange partners and a bound state will form if the strings are not moving too fast. It was shown that the length and the distribution of the string network are dominated by the original strings and there is a negligible contribution to the string network length and population from the bound states strings.

II. LOOPS COLLISION IN AN EXPANDING UNIVERSE

Here we present the formalism of junction formation for arbitrary cosmic strings colliding in a cosmological background.

Our cosmological background is the standard FRW metric

$$ds^2 = a^2(\tau)(d\tau^2 - d\mathbf{x}^2)\,, \tag{1}$$

where τ is the conformal time related to the cosmic time t via $dt = ad\tau$, $a(\tau)$ is the scale factor and we assume that the background space-time has no spatial curvature. Our cosmological background is either radiation dominated (RD) or matter dominated (MD).

Suppose X_i^μ represents the profile of the i-th cosmic string in the target space-time. As usual, we can go to the temporal gauge where the time on the string world-sheet is the same as the conformal time, $X^0 = \tau$, and $X_i^\mu = (\tau, \mathbf{x}_i)$. Denoting the other coordinate of the world-sheet parametrization by σ, the gauge condition, $\dot{\mathbf{x}}_i \cdot \mathbf{x}'_i = 0$, holds where the $\cdot$ and the prime indicate the derivatives with respect to τ and σ respectively.

After collision, there are four junctions and eight kinks. The formation of the kinks is a manifestation of the fact that the speed of light is finite and parts of the old strings which did not "feel" the formation of junctions evolve as before. In the following we denote the incoming strings by $\mathbf{x}_i$ where $i = 1, 2$ whereas the newly formed strings are denoted by $\mathbf{y}_a$ where $a = 1, 2, 3$. The junctions and the kinks on each string are described by $\sigma_a = s_a(\tau)$ and $\sigma_i = \omega_i(\tau)$ respectively.

The action for the system of two loops in collision is

$$\mathbf{S} = -\sum_J \sum_{i=1}^{2} \mu_i \int d\tau d\sigma_i a^2(\tau) \sqrt{(1 - \dot{\mathbf{y}}_i^2)\, \mathbf{y}_i'^2} \tag{2}$$

$$\theta(\delta_i^J(s_i^J(\tau) - \sigma_i))\, \theta(\delta_i^J(\sigma_i - \omega_i^J(\tau))) \tag{3}$$

$$- \sum_{i=1}^{2} \mu_i \int d\tau d\sigma_i a^2(\tau) \sqrt{(1 - \dot{\mathbf{x}}_i^2)\, \mathbf{x}_i'^2}$$

$$\theta(\delta_i^A(\omega_i^A(\tau) - \sigma_i))\, \theta(\delta_i^B(\omega_i^B(\tau) - \sigma_i)) \tag{4}$$

$$- \sum_{i=1}^{2} \mu_i \int d\tau d\sigma_i a^2(\tau) \sqrt{(1 - \dot{\mathbf{x}}_i^2)\, \mathbf{x}_i'^2}$$

$$\theta(\delta_i^C(\omega_i^C(\tau) - \sigma_i))\, \theta(\delta_i^D(\omega_i^D(\tau) - \sigma_i)) \tag{5}$$

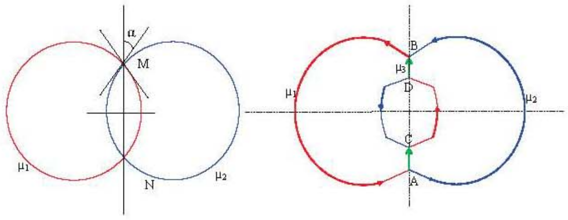

FIG. 1. A schematic view of the loops at the time of collision(left) and after collision (right). The arrows in the right figure indicate the directions in which the coordinateσ_i increases. We use the convention that on aσ_i loop runs counter clockwise. There are four junctions and eight kinks in total.

$$
\begin{aligned}
& - \mu_3 \int d\tau d\sigma_3 a^2(\tau) \sqrt{(1-\dot{\mathbf{y}}_3^2)\,\mathbf{y}_3'^{\,2}} \\
& \qquad \theta(\delta_3^A(s_3^A(\tau)-\sigma_3))\,\theta(\delta_3^C(s_3^C(\tau)-\sigma_3)) \qquad (6)\\
& - \mu_3 \int d\tau d\sigma_3 a^2(\tau) \sqrt{(1-\dot{\mathbf{y}}_3^2)\,\mathbf{y}_3'^{\,2}} \\
& \qquad \theta(\delta_3^B(s_3^B(\tau)-\sigma_3))\,\theta(\delta_3^D(s_3^D(\tau)-\sigma_3)) \qquad (7)\\
& + \sum_J \sum_{a=1}^{3} \int d\tau a^2(\tau)\, \mathbf{f}_a^J \cdot [\mathbf{y}_a(s_a^J(\tau),\tau) - \bar{\mathbf{y}}^J(\tau)] \\
& + \sum_J \sum_{i=1}^{2} \int d\tau a^2(\tau)\, \mathbf{k}_i^J \cdot [\mathbf{x}_i(\omega_i^J(\tau),\tau) - \mathbf{y}_i(\omega_i^J(\tau),\tau)]
\end{aligned}
$$

where J represents the junctions. $\mathbf{f}_a^J$ and $\mathbf{k}_i^J$ are Lagrange multipliers which enforce that at the kinks the newly formed strings and the old strings meet, $\mathbf{x}_i(\omega_i^J(\tau),\tau) = \mathbf{y}_i(\omega_i^J(\tau),\tau)$ and on the junctions the three newly formed strings join together $\mathbf{y}_a(s_a^J(\tau),\tau) = \bar{\mathbf{y}}^J(\tau)$ where $\bar{\mathbf{y}}^J(\tau)$ represents the position of the junction J in target space. δ_i^J is $+1$ if σ increases towards the junction and -1 in the opposite case.Varying the action and solving the equations of motion gives

$$
1 - \delta_1^J \epsilon_1 \dot{s}_1^J = \frac{\bar{\mu} M_1 \hat{c}_{23}}{\mu_1 [M_1\hat{c}_{23} + M_2\hat{c}_{13} + M_3\hat{c}_{12}]}\,, \qquad (8)
$$

where $M_1 \equiv \mu_1^2 - (\mu_2-\mu_3)^2$ with a similar definition for M_2 and M_3. One can also obtains a similar equation for $\dot{s}_{2,3}$ with an appropriate permutation of the indices. This set of equations for $\dot{s}_a^J$ is our starting point to study the evolutions of junctions.

Consider a loop extended in $x-y$ plane moving relativistically in z direction. We choose the following ansatz for the loop configuration

$$
\mathbf{x} = \begin{pmatrix} f(\tau)\cos\frac{\sigma}{R_0} \\ f(\tau)\sin\frac{\sigma}{R_0} \\ z(\tau) \end{pmatrix}\,. \qquad (9)
$$

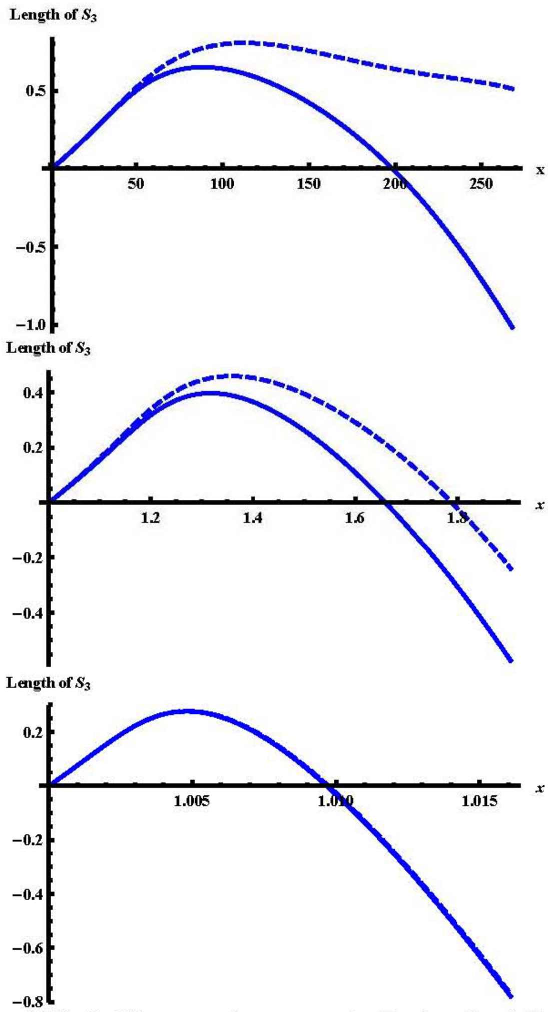

FIG. 2. These graphs represents the length of the newly formed strings.The figures are for super-horizon ,intermediate and sub-horizon size loops respectively. The solid (dashed) curve is for the radiation (matter) dominated background. In the third graph two curves coincide.

In this picture, $R(\tau) \equiv a(\tau)f(\tau)$ is the physical radius of the loop and $R_0 = f(\tau_0)$ represents the size of the loop at the time of collision.

Here the loop center of mass velocity is defined by $v = \dot{z}(\tau)$. For the ease of the numerical investigations, we introduced the dimensionless time variable $x \equiv \tau/\tau_0$ and $F(x) \equiv f(\tau)/\tau_0$. Also the prime here and below represents derivatives with respect to the dimensionless time x.

To be specific, we consider three examples of (a): large super-horizon size loops with $F_1 = 100$, (b): intermediate size loops with $F_1 = 0.5$ and (c): small sub-horizon size loops with $F_1 = 0.01$.

III. CONCLUSION

In this work we have studied the cosmic strings collision in cosmological backgrounds. The motivation for this work was to understand analytically the findings of simulation in [8] where it was found that there were little contributions from the bound states strings in their multiple strings network. One can understand this phenomena as follows. For the junctions to develop upon strings collision, some appropriate initial conditions should be satisfied. These depends on the relative tensions of the colliding strings, the angle of collision and their relative velocities. Yet the more interesting observation is that even when junctions are created, they can not grow indefinitely and the bound state strings start to unzip.

[1] S. Sarangi and S. H. H. Tye, Phys. Lett. B **536**, 185 (2002) [arXiv:hep-th/0204074].
[2] M. Majumdar and A. Christine-Davis, JHEP **0203**, 056 (2002) [arXiv:hep-th/0202148].
[3] B. Shlaer and M. Wyman, Phys. Rev. D **72**, 123504 (2005) [arXiv:hep-th/0509177].
[4] R. Brandenberger, H. Firouzjahi and J. Karouby, Phys. Rev. D **77**, 083502 (2008) [arXiv:0710.1636 [hep-th]]; T. Suyama, Phys. Rev. D **78**, 043532 (2008) [arXiv:0807.4355 [astro-ph]].
[5] R. Brandenberger, H. Firouzjahi, J. Karouby and S. Khosravi, JCAP **0901**, 008 (2009) [arXiv:0810.4521 [hep-th]]; M. G. Jackson and X. Siemens, JHEP **0906**, 089 (2009) [arXiv:0901.0867 [hep-th]]; P. Binetruy, A. Bohe, T. Hertog and D.A. Steer, arXiv:0907.4522.
[6] L. Leblond, B. Shlaer and X. Siemens, arXiv:0903.4686 [astro-ph.CO]. K. Dasgupta, H. Firouzjahi and R. Gwyn, "Lumps in the throat," JHEP **0704**, 093 (2007) [arXiv:hep-th/0702193]; M. Lake, S. Thomas and J. Ward, "String Necklaces and Primordial Black Holes from Type IIB Strings," arXiv:0906.3695 [hep-ph].
[7] H. Firouzjahi, J. Karouby, S. Khosravi and R. Brandenberger, "Zipping and Unzipping of Cosmic String Loops in Collision," Phys. Rev. D **80**, 083508 (2009) [arXiv:0907.4986 [hep-th]].
[8] J. Urrestilla and A. Vilenkin, "Evolution of cosmic superstring networks: a numerical simulation," JHEP **0802**, 037 (2008) [arXiv:0712.1146 [hep-th]].

Noncommutative Braneworld Inflation

Kourosh Nozari[1,2] and Siamak Akhshabi[1]
[1] *Department of Physics,Faculty of Basic Sciences,University of Mazandaran,P.O.Box 47416-95447, Babolsar, Iran*
[2] *Research Institute for Astronomy and Astrophysics of Maragha, P.O.Box 55134-441, Maragha, Iran*

We construct a new noncommutative braneworld inflation within the smeared, coherent state picture of spacetime noncommutativity. This model realizes an inflationary, bouncing solution without recourse to any axillary scalar or vector fields in a Randall-Sundrum II setup. There is no initial singularity and the model has the potential to produce scale invariant spectrum of scalar perturbations. We study also the evolution of perturbations in this noncommutative braneworld setup and we compare our results with recent observations.

PACS numbers: 02.40.Gh , 11.10.Nx, 04.50.-h,98.80.Cq

I. INTRODUCTION

Motivated by string theory and also loop quantum gravity, spacetime fuzziness can be encoded using the relation $[\hat{x}^i, \hat{x}^j] = i\theta^{ij}$ where θ^{ij} is a real, antisymmetric matrix, with the dimension of length squared which determines the fundamental cell discretization of spacetime manifold [1]. As a consequence of this noncommutativity, the notion of point in the spacetime manifold becomes obscure since there is a fundamental uncertainty in measuring the coordinates as $\Delta x^i \Delta x^j \geq \frac{1}{2}|\theta^{ij}|$. This finite resolution of the spacetime points especially affects the cosmological dynamics in the early stages of the universe evolution. Essentially, effects of trans-Planckian physics should be observable in the cosmic microwave background radiation. For this reason, various attempts to construct noncommutative inflationary models have been done by adopting various different approaches [2]. A new approach uses the smeared, coherent state picture of noncommutativity [3]. The key idea in this model is that noncommutativity *smears* the initial singularity and as a result there will be an smooth transition between pre and post big bang eras via an accelerated expansion. It has been shown that noncommutativity eliminates point-like structures in the favor of smeared objects in flat spacetime [4]. The effect of smearing is mathematically implemented as a substitution rule: position Dirac-delta function is replaced everywhere with a Gaussian distribution of minimal width $\sqrt{\theta}$. In this framework, the mass density of a static, spherically symmetric, smeared, particle-like gravitational source can be described as $\rho_\theta(r) = \frac{M}{(2\pi\theta)^{\frac{3}{2}}}\exp(-\frac{r^2}{4\theta})$. The particle mass M, instead of being perfectly localized at a point, is diffused throughout a region of linear size $\sqrt{\theta}$. Based on this novel idea, in this letter we construct a noncommutative braneworld inflation on the RSII setup and we study evolution of cosmological perturbations in this framework.

II. THE MODEL

The Friedmann equation governing the cosmological evolution on the RS II brane is given as follows [5]

$$H^2 = \frac{\Lambda_4}{3} + \left(\frac{8\pi}{3M_4^2}\right)\rho + \left(\frac{4\pi}{3M_5^3}\right)\rho^2 + \frac{\mathcal{E}_0}{a^4}, \tag{1}$$

where M_4 and M_5 are four and five dimensional fundamental scales respectively and Λ_4 is the effective cosmological constant on the brane. We suppose that the initial singularity that leads to RS II geometry afterwards, is smeared due to spacetime noncommutativity. In this respect, the energy density on the brane can be decomposed as $\rho = \rho_0 e^{-|\tau|^2/4\theta} e^{-|\vec{X}|^2/4\theta}$ where $R^2 = \tau^2 + |\vec{X}|^2$ and $\tau = it$ is the Euclidean time. We suppose that the universe enters the RS II geometry immediately after the initial smeared singularity which is a reasonable assumption from a M-theory perspective of the cyclic universe. In the spacetime foliation, from one hypersurface to another, the $\vec{X}$-dependent part of ρ does not change, so it can be included into ρ_0. If we neglect the dark radiation term and also the brane cosmological constant, the Friedmann equation (1) can be rewritten as $H^2 = \frac{8\pi}{3M_4^2}\rho\left[1 + \frac{\rho}{2\lambda}\right]$. In our noncommutative setup, this equation could be rewritten as follows [6]

$$\left(\frac{\dot{a}}{a}\right)^2 = \frac{8\pi}{3M_4^2}\rho_0 e^{-t^2/4\theta}\left[1 + \frac{\rho_0 e^{-t^2/4\theta}}{2\lambda}\right]. \tag{2}$$

This equation can be solved for $a(t)$ to obtain

$$a(t) = \mathcal{H}\Bigg(\left[\frac{1}{4}\,\frac{\rho_0 - 2\sqrt{2\theta}\,\lambda^{3/2}\sqrt{\frac{8\pi}{3M_4^2}}}{\rho_0}\right], \left[\frac{1}{2}\right],$$

$$\frac{1}{8}\,\frac{\sqrt{2}\sqrt{\frac{8\pi}{3M_4^2}}\left[(4\rho_0 + 4\lambda)\theta + t\rho_0\right]^2}{\theta\sqrt{\lambda}\rho_0}\Bigg)$$

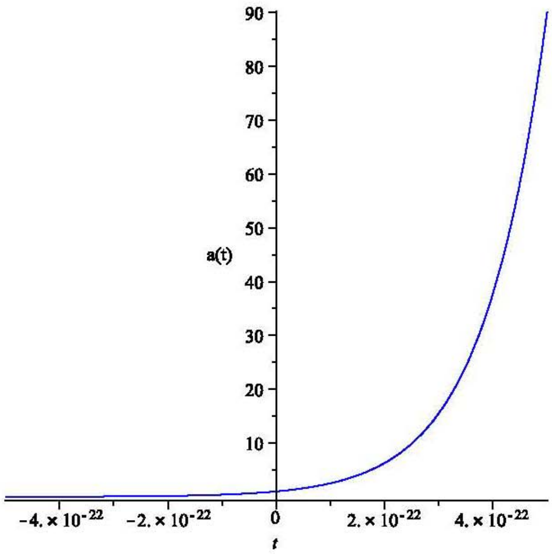

FIG. 1. Evolution of the scale factor in noncommutative Randall-Sundrum II geometry. There is an inflationary era without recourse to any scalar or vector fields. The model avoids also the initial singularity.

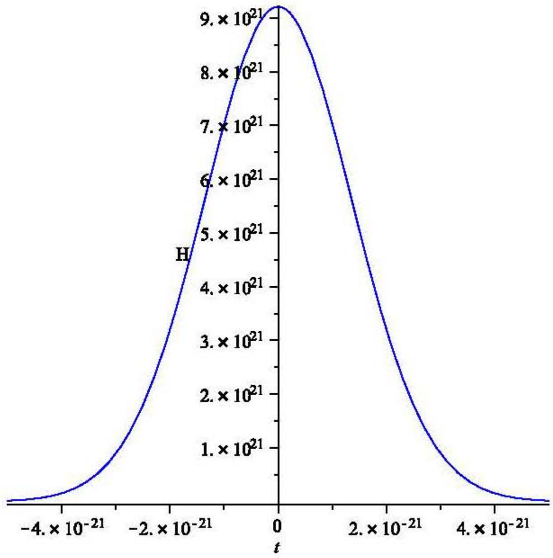

FIG. 2. Evolution of the Hubble parameter in noncommutative Randall-Sundrum II geometry.

$$\times\exp\left\{-\frac{1}{16}\,\frac{[(8\,\rho_0+8\,\lambda)\,\theta+t\rho_0]\,\sqrt{2}\sqrt{\frac{8\pi}{3M_4^2}t}}{\theta\,\sqrt{\lambda}}\right\}+$$

$$[(4\,\rho_0+4\,\lambda)\,\theta+t\rho_0]\times$$

$$\exp\left\{-\frac{1}{16}\,\frac{[(8\,\rho_0+8\,\lambda)\,\theta+t\rho_0]\,\sqrt{2}\sqrt{\frac{8\pi}{3M_4^2}t}}{\theta\,\sqrt{\lambda}}\right\}\times$$

$$\mathcal{H}\Bigg(\left[\frac{1}{4}\,\frac{3\,\rho_0-2\,\sqrt{2}\theta\,\lambda^{3/2}\sqrt{\frac{8\pi}{3M_4^2}}}{\rho_0}\right],\ \left[\frac{3}{2}\right],$$
$$\frac{1}{8}\,\frac{\sqrt{2}\sqrt{\frac{8\pi}{3M_4^2}}\,[(4\,\rho_0+4\,\lambda)\,\theta+t\rho_0]^2}{\theta\,\sqrt{\lambda}\rho_0}\Bigg), \qquad (3)$$

where $\mathcal{H}$ shows the Hypergeometric function of the arguments. Figure 1 shows that this noncommutative model naturally gives an inflation era without consulting to any axillary inflaton field. On the other hand, due to smeared picture adopted in this noncommutative framework, there is no initial singularity in this setup. The number of e-folds in this model is given by

$$N=\int_{t_i}^{t_f}H dt\simeq$$

$$\frac{8}{3}\pi\,\rho_0\left[\sqrt{\pi\theta}\ \mathrm{erf}\Big(\frac{1}{2}\,\frac{t_f}{\sqrt{\theta}}\Big)+\frac{1}{2}\,\sqrt{2\pi\theta}\ \mathrm{erf}\Big(\frac{1}{2}\,\frac{\sqrt{2}t_f}{\sqrt{\theta}}\Big)\lambda^{-1}\right]M_4{}^{-2}$$

$$-\frac{8}{3}\pi\,\rho_0\left[\sqrt{\pi\theta}\ \mathrm{erf}\Big(\frac{1}{2}\,\frac{t_i}{\sqrt{\theta}}\Big)+\frac{1}{2}\,\sqrt{2\pi\theta}\ \mathrm{erf}\Big(\frac{1}{2}\,\frac{\sqrt{2}t_i}{\sqrt{\theta}}\Big)\lambda^{-1}\right]M_4{}^{-2}$$

$$\simeq\frac{8}{3}\,\pi\,\rho_0\left[t-\frac{1}{12}\,\frac{t^3}{\sqrt{\pi}\theta^{\frac{3}{2}}}+\frac{1}{160}\,\frac{t^5}{\sqrt{\pi}\theta^{\frac{5}{2}}}+\right.$$
$$\left.\frac{1}{2}\,\Big(2\,t-\frac{1}{6}\,\frac{\sqrt{2}t^3}{\sqrt{\pi}\theta^{\frac{3}{2}}}+\frac{1}{40}\,\frac{\sqrt{2}t^5}{\sqrt{\pi}\theta^{\frac{5}{2}}}\Big)\lambda^{-1}\right]M_4{}^{-2}. \qquad (4)$$

If ρ_0 is suitably large, we will get sufficient amount of inflation in this scenario. Supported by various observations, a scale invariant spectrum of scalar perturbations should be generated after inflation. We define the slow-roll parameters as $\epsilon\equiv\frac{M_4^2}{4\pi}\left(\frac{H'}{H}\right)^2$, $\eta\equiv\frac{M_4^2}{4\pi}\left(\frac{H''}{H}\right)$. We assume that as usual the scalar spectral index is given by the $n_s-1\simeq-6\epsilon+2\eta$. Figure 3 shows variation of n_s versus the cosmic time. As one can see from this figure, it is possible essentially to have scale invariant scalar spectrum in this model.

III. COSMOLOGICAL PERTURBATIONS

We now suppose that the initial singularity that leads to RS II geometry afterwards, is smeared due to spacetime noncommutativity. In this respect, we set $\rho(t)=\frac{1}{32\pi^2\theta^2}e^{-t^2/4\theta}$. The effective noncommutative pressure in this setup is $p=-\rho+\frac{t}{6\theta}e^{-t^2/8\theta}$ and the equation of state parameter will be [7]

$$\omega=-1+\frac{16}{3}\pi^2\theta\,te^{-t^2/8\theta}. \qquad (5)$$

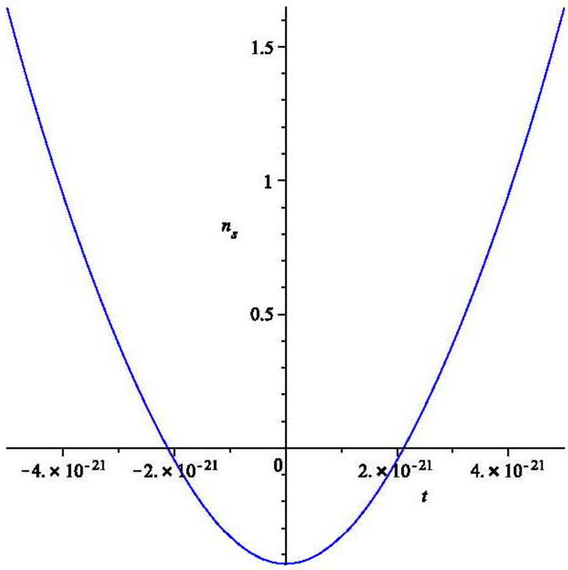

FIG. 3. Variation of the scalar spectral index versus the cosmic time. The spectral index approaches the Harrison-Zel'dovic spectrum at the end of inflation. The parameters used to plot this figure are the same as previous figures. The spectral index is exactly one at $t = \pm 4.021168857\times 10^{-21}$.

Similarly, the speed of sound is

$$c_s^2 = \frac{\dot{p}}{\dot{\rho}} = \frac{-3t - 64\theta^2\pi^2 e^{-t^2/8\theta} + 32\theta\pi^2 t^2 e^{-t^2/8\theta}}{3t}. \quad (6)$$

Now we can find the *effective* equation of state and speed of sound where these effective quantities are essentially related to the dark radiation energy density, ρ^ε. We note that there are constraints from nucleosynthesis on the value of ρ^ε so that $\frac{\rho^\varepsilon}{\rho} \leq 0.03$ at the time of nucleosynthesis [8]. In this respect, we can neglect this contribution to find

$$\omega^{\rm eff} = \frac{1}{192}\,{\rm e}^{-\frac{1}{8}\frac{t^2}{\theta}}$$

$$\left[-192\,\pi^2\theta^2\lambda + 1024\,t{\rm e}^{\frac{-t^2}{8\theta}}\pi^4\theta^3\lambda - 3\,{\rm e}^{\frac{-t^2}{8\theta}} + 32\,t{\rm e}^{\frac{-t^2}{4\theta}}\pi^2\theta\right]\times$$

$$\left[\theta\left(\frac{1}{64}\left(64\,\pi^2\theta^2\lambda + {\rm e}^{\frac{-t^2}{8\theta}}\right)\pi^{-2}\theta^{-2}\lambda^{-1}\right)\right]^2\times$$

$$\pi^{-2}\theta^{-4}\lambda^{-1}\left[{\rm e}^{\frac{-t^2}{8\theta}}\left(\frac{1}{64}\left(64\,\pi^2\theta^2\lambda + {\rm e}^{\frac{-t^2}{8\theta}}\right)\pi^{-2}\theta^{-2}\lambda^{-1}\right)\right]^{-1}, \quad (7)$$

which simplifies to $\omega^{\rm eff} \approx -1 + \frac{32}{3}\pi^2\theta\, te^{-t^2/8\theta}$ for the high energy regime ($\rho \gg \lambda$ that λ is the brane tension).

Similarly, the effective speed of sound in the high energy regime will be

$$(c_s^2)^{\rm eff} \approx \frac{16}{3}\pi^2\theta\, te^{-t^2/8\theta} +$$

$$\frac{-3t - 64\theta^2\pi^2 e^{-t^2/8\theta} + 32\theta\pi^2 t^2 e^{-t^2/8\theta}}{3t}. \quad (8)$$

Now, the equation governing on the scalar perturbation is given by [7,8]

$$\frac{d\Phi}{dN} + \left[1 + \frac{(1+w)\kappa^2\rho}{2H^2}\left(1 + \frac{\rho}{\lambda}\right)\right]\Phi =$$

$$\left[\frac{(1+w)\kappa^2\rho}{4H^2}\right]C_o - \left[\frac{3(1+w)a_o^2\rho^2}{\lambda H^2}\right]e^{2N}U \quad (9)$$

where $U = U_0 \exp\left\{\int(3w-1)dN\right\}$, and N is the number of e-folds. We can integrate equation (9) to find

$$\Phi = \frac{1}{2}(1+\omega)\frac{\rho\,\lambda\,\kappa^2 C_0}{2H^2\lambda + (1+\omega)(\kappa^2\rho\lambda + \kappa^2\rho^2)}$$

$$-6(1+\omega)\frac{H^2\rho\,\lambda\,a_0{}^2 U\exp\left(3\,\omega\,a - 3\,\omega\,a_0 - a + a_0\right)}{6H^2\lambda + (1+\omega)(\kappa^2\rho\lambda + \kappa^2\rho^2)}\exp\left(\frac{t^2}{4\theta}\right)$$

$$+\exp\left[\frac{1}{2}\frac{2\,H^2\lambda + (1+\omega)(\kappa^2\rho\,\lambda + \kappa^2\rho^2)}{H^2\lambda}\frac{t^2}{8\theta}\right]. \quad (10)$$

Figure (4) shows the evolution of Φ for both usual braneworld scenario and our noncommutative setup in the high energy inflation regime ($\rho \gg \lambda$). The curvature perturbation defined in the metric-based perturbation theory is $\xi = \mathcal{R} + \frac{\delta\rho}{3(\rho+p)}$, which reduces to $\mathcal{R}$ on uniform density ($\delta\rho = 0$) hypersurfaces. If there is no dark radiation in the background ($\rho^\varepsilon = 0$), we can obtain the time evolution of the curvature perturbation explicitly as follows

$$\xi^{\rm \,eff} = \frac{1}{96}\frac{{\rm Ei}\left(1, \frac{3t^2}{8\theta}\right)}{\pi^2\theta^2\lambda} - \frac{1}{48}\frac{{\rm e}^{-\frac{3t^2}{8\theta}}}{\pi^2\theta^2\lambda} + \frac{1}{3}\,{\rm Ei}\left(1, \frac{t^2}{4\theta}\right) - \frac{2}{3}\,{\rm e}^{-\frac{t^2}{4\theta}}$$

$$-\frac{1}{768}\,{\rm erf}\left(\frac{t}{2\sqrt{\theta}}\right)\lambda^{-1}\pi^{-3}\theta^{-3}\frac{1}{\sqrt{\theta\,\pi}}$$

$$-\frac{1}{24}\,{\rm erf}\left(\frac{1}{4}\frac{\sqrt{2}t}{\sqrt{\theta}}\right)\sqrt{2}\theta^{-1}\pi^{-1}\frac{1}{\sqrt{\theta\,\pi}} \quad (11)$$

Where ${\rm Ei}(a, z)$ is the exponential integral defined as ${\rm Ei}(a, z) = z^{a-1}\Gamma(1-a, z)$.

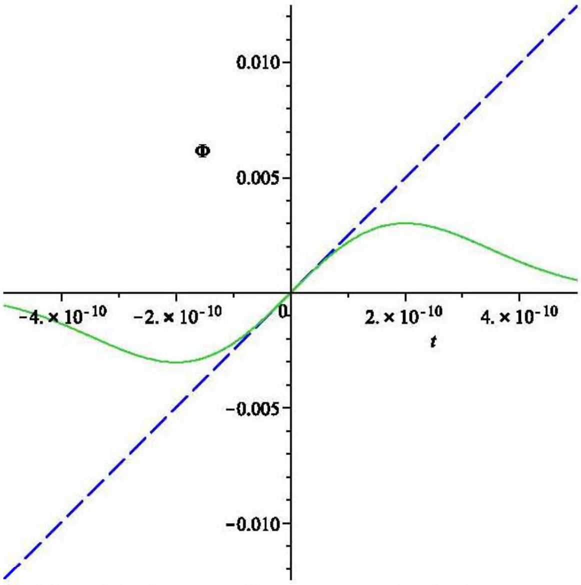

FIG. 4. Evolution of the parameter Φ which is an analog of the Bardeen metric potential as defined in (35) for both usual braneworld scenario (dashed line) and our noncommutative setup (solid line) when $\frac{\rho_0}{\lambda} = 10^{10}$. We assumed that no dark radiation is present in the background geometry.

IV. CONCLUSION

In summary, by adopting the smeared coherent state picture of spacetime noncommutativity, we have generalized the RS II braneworld inflation to noncommutative spaces. This model realizes an inflationary, bouncing solution without recourse to any axillary scalar or vector fields. Due to noncommutative structure of the very spacetime which admits the existence of a fundamental length scale, there is no initial singularity in this model. By treating the scalar perturbations in this setup, we have shown that it is possible essentially to have scale invariant scalar perturbations in this framework. Finally, we have studied the dynamics of cosmological perturbations in this setup.

[1] R. J. Szabo, *Phys. Rept.* **378** (2003) 207
[2] R. Brandenberger and P. M. Ho, *Phys. Rev. D* **66** (2002) 023517.
[3] M. Rinaldi, [arXiv:0908.1949].
[4] P. Nicolini, *Int. J. Mod. Phys. A* **24** (2009) 1229, [arXiv:0807.1939].
[5] L. Randall and R. Sundrum, *Phys. Rev. Lett.* **83** (1999) 4690.
[6] K. Nozari and S. Akhshabi, *Phys. Lett. B* **683** (2010) 186-190, [arXiv:0911.4418].
[7] K. Nozari and S. Akhshabi, Submitted for publication to Phys. Lett. B, April (2010).
[8] D. Langlois, R. Maartens, M. Sasaki and D. Wands, *Phys. Rev. D* **63** (2001) 084009.

Merits of the moiré deflectometry in study of the atmospheric turbulence and wave-front sensing and its potential applications in astronomy

Saifollah Rasouli
Department of Physics, Institute for Advanced Studies in Basic Sciences (IASBS), Zanjan 45137-66731, Iran

Recently, taking advantages of the moiré technique we have developed some different methods with different capabilities to study the atmospheric turbulence and wave-front sensing. In this report we review the moiré based techniques to measuring atmospheric turbulence parameters and we compare the spatial resolutions and precisions of the proposed methods together and with respect to the conventional methods that already have been used for the same purpose. We also review wave-front sensing using the moiré deflectometry. In addition, in this paper we have introduced some potential applications of the moiré deflectometry in astronomy.

PACS numbers: 47.80. v, 42.30. d, 42.25.Dd, 42.81.Pa

I. INTRODUCTION

We have used moiré technique to measure numerous physical quantities such as refractive index gradient, study of atmospheric turbulence, measurement of nonlinear refractive index of materials, wave-front sensing, fiber optics, optical metrology, vibration analysis, and so on. In addition, we have designed and fabricated several devices for measuring different physical quantities. We are very interested in this technique because it has diverse applications and the required instrumentation is usually simple and inexpensive. This is very important in our country. In this paper a brief review of our recent achievements in the study of the atmospheric turbulence and wave-front sensing using moiré deflectometry are presented and some of the potential application in astronomy will be proposed. In this report also comparison of sensitivities and spatial resolutions of different methods are presented.

In the next section moiré technique, Talbot effect, Talbot interferometry, and moiré deflectometry are introduced. In sections 3 we review the moiré based techniques to measuring atmospheric turbulence parameters. In section 4 we introduce a wide dynamic range two channel wave-front sensor that based on the moiré deflectometry. This sensor has many practical applications ranging from wave aberrations of human eyes to adaptive optics in astronomy. In section 5 some of the potential applications of the reviewed methods in astronomy are presented.

II. MOIRE' TECHNIQUE, TALBOT EFFECT, TALBOT INTERFEROMETRY AND MOIRE' DEFLECTOMETRY

Moiré pattern can be created, for example, when two similar straight-line grids (or gratings) are overlaid at a small angle, Fig. 1, or when they have slightly different mesh sizes, Fig. 2. In many applications one of the superimposed gratings is the image of a physical grating or is one of the self-images of the first grating. The former case is named projection moiré technique and the latter case is called moiré deflectometry or Talbot interferometry. When a grating is illuminated with a spatially coherent light source, exact images and many other images can be found at finite distances from the grating. This self-imaging phenomenon is named the Talbot effect. By superimposing another grating on one of the self-images of the first grating, moiré fringes are formed. The Talbot interferometry and the moiré deflectometry are not identical, although they seem quite similar at a first glance. In the Talbot interferometry setup, a collimated light beam passes through a grating and then through a distorting phase object. The distorted shadow of the grating forms a moiré pattern with a second grating located at a Talbot plane (also known as Fourier plane). The moiré deflectometry measures ray deflections in the paraxial approximation, provided that the phase object (or the specular object) is placed in front of the two gratings. The resulting fringe pattern, is a map of ray deflections corresponding to the optical properties of the inspected object. Generally, when the image forming lights propagate in a perturbed medium the image grating is distorted and the distortion is magnified by moiré pattern. When the similar gratings are overlaid at a small angle, the moiré magnification is given by [1]

$$\frac{d_m}{d} = \frac{1}{2sin(\theta/2)} \simeq \frac{1}{\theta}, \tag{1}$$

where d_m, d, and θ stand for moiré fringe spacing, the pitch of the gratings, and gratings' angle.

In case of parallel moiré pattern, when the gratings vectors are parallel together and the resulting moiré fringes are parallel to the gratings lines, the moiré magnification is given by [2]

$$\frac{d_m}{d} = \frac{d}{\delta d}, \tag{2}$$

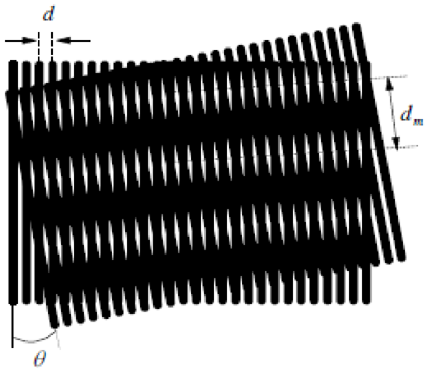

FIG. 1. A moiré pattern, formed by superimposing two sets of parallel lines, one set rotated by angle θ with respect to the other [3].

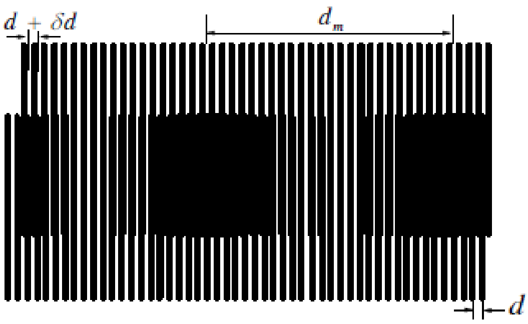

FIG. 2. A moiré pattern, formed by superimposing two sets of parallel lines, when they have slightly different mesh sizes [3].

where δd stands for the difference of mesh sizes of the gratings.

Generally, in the moiré technique displacing one of the gratings by l in a direction normal to its rulings leads to a moiré fringe shift s, given by

$$s = \frac{d}{d_m} l. \tag{3}$$

III. MEASURING ATMOSPHERIC TURBULENCE PARAMETERS BY MEANS OF THE MOIRE' TECHNIQUE

Changes in ground surface temperature create turbulence in the atmosphere. Three physical effects are observed when a light beam propagates through a turbulent atmosphere: optical scintillation, beam wandering, and fluctuations in the angle-of-arrival (AA). These effects are used for measuring turbulence characteristic parameters. Fluctuations of light propagation direction, referred to as the fluctuations of AA, are measured by various methods. In astronomical applications the AA fluctuations measurement is a basic step. Differential image motion monitor [4] and generalized seeing monitor systems [5] are based on AA fluctuations. The edge image waviness effect [6] is also based on AA fluctuations. In some conventional methods the fluctuations of AA are derived from the displacements of one or two image points on the image of a distant object in a telescope. In other techniques the displacements of the image of an edge are exploited. The precisions of these techniques are limited to the pixel size of the recoding CCD. In following we review some of important methods that we have presented recently in measuring the AA fluctuations and the related atmospheric turbulence parameters.

A. Incoherent imaging of a grating in turbulent atmosphere by a telescope

The starting work of the study of atmospheric turbulence was published in Ref. [7]. In this work we have used moiré technique in measuring the refractive-index structure constant, C_n^2, and its profile in the ground level atmosphere. In this method from a low frequency sinusoidal amplitude grating, installed at certain distance from a telescope, successive images are recorded and stored in a computer. By superimposing the recorded images on one of the images, the moiré patterns are formed. We have also used this technique to measure the modulation transfer functions of the ground-level atmosphere [8]. In the present approach after the filed process, by superimposing the images of the grating the moire patterns are formed. Thus observation of the AA fluctuations visually improved by the moiré magnification, but it was not increased precision of the AA fluctuations measurements. Also this method is not a real-time technique. But, compared to the conventional methods [4–6] in this configuration across a rather large cross section of the atmosphere we access to large volume of 2D data.

In this method, when an image point on the focal plane of a telescope objective is displaced by l the AA changes by

$$\alpha = l/f, \tag{4}$$

where f is the objective focal length. Thus order of precision of the method is similar to the order of precision of the conventional methods like differential image motion monitor [4,6]. Meanwhile in this method we are imaging a grating on full size of a CCD's screen, but fro example in the differential image motion monitor two image points are formed on small section of a CCD's screen. Due to this one, in our method measuring the image disablement is accurate.

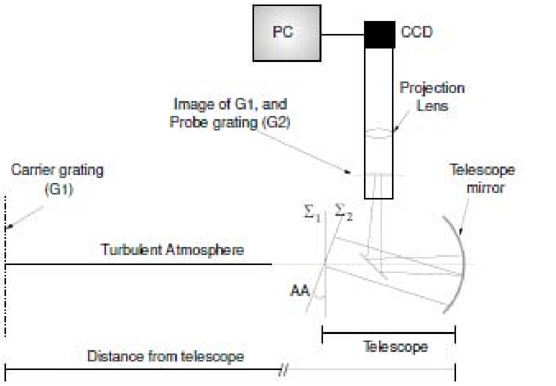

FIG. 3. Schematic diagram of the instrument used for atmosphere turbulence study by moiré technique, incoherent projection of a gratings image on one other grating by a telescope[9].

B. Incoherent imaging of a grating on another grating in turbulent atmosphere by a telescope

In 2006 we have introduced a new technique, based on moiré fringe displacement, for measuring the AA fluctuations [1]. This technique have two main advantages over the previous methods. The displacement of the image grating lines can be magnified about ten times, and many lines of the image grating provide large volume of data which lead to very reliable result. Besides, access to the displacement data over a rather large area is very useful for the evaluation of the turbulence parameters depending on correlations of displacements. The brief description of the technique implementation is as follows. A low frequency grating is installed at a suitable distance from a telescope. The image of the grating, practically forms at the focal plane of the telescope objective. Superimposing a physical grating of the same pitch as the image grating onto the latter forms the moiré pattern. Recording the consecutive moiré patterns with a CCD camera connected to a computer and monitoring the traces of the moiré fringes in each pattern yields the AA fluctuations versus time across the grating image. A schematic diagram of the experimental setup is shown in Fig. 3.

The typical real time moiré fringes obtained by the set-up is shown in Fig. 4(a), and its corresponding low frequency illumination is shown in Fig. 4(b).

In this method, the component α of the AA fluctuation in the direction perpendicular to the lines of the carrier grating (parallel to the moiré fringes) is given by [1]

$$\alpha = \frac{1}{f}\frac{d}{d_m}\, s, \tag{5}$$

where f, d, d_m, and s are the telescope focal length, the pitch of the probe gratings, the moiré fringes spacing, and

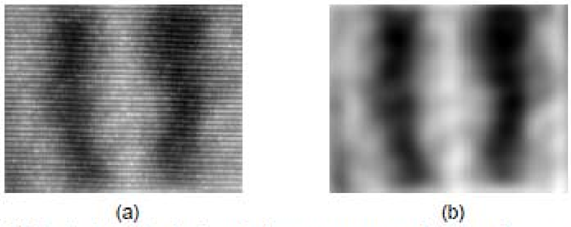

FIG. 4. (a) Typical moiré pattern recorded by the set-up in Fig. 3, (b) the corresponding low frequency illumination [9].

the moiré fringe displacement, respectively. Compared to Eq. (4), here an improving factor $\frac{d}{d_m}$ appears. When the angle between the lines of superimposed gratings is less than 6^o, the magnification is more than ten times. In other word: *"Light-beam deflections due to atmospheric turbulence are one order of magnitude more precise with the aid of moiré patterns [9]."*

C. Application of moire' deflectometry in atmospheric turbulence measurements

Our next scheme, noteworthy both for its simplicity and its cleverness, illustrates the basic idea [2,10]. A monochromatic lightwave from a small and distant source is incident on a finepitch Ronchi ruling. A short distance beyond, a Talbot image of the ruling appears.

With diverging-light illumination of the Ronchi ruling, the Talbot image is slightly larger in scale than the ruling itself. If a duplicate of the ruling is placed in the Talbot image plane, in exactly the same orientation as the original ruling, large fringes result from the moiré effect.

Most importantly, any turbulence-produced local variations in the AA of the incident wave, even if quite small, manifest themselves as easily seen distortions of the moiré fringe pattern. These distortions, captured by a CCD video camera, are analysed by a computer program executing what is, according to our, a computationally efficient algorithm. We have used the technique to determine parameters that characterize the strength of turbulence measured along horizontal paths. A schematic of the experimental setup is shown in Fig. 5.

In this method the componet of the AA fluctuations measurement is given by [2]

$$\alpha = \frac{d}{d_m}\frac{s}{Z_k}, \tag{6}$$

where Z_k denotes the kth Talbot distance of the first grating. The implementation of the technique is straightforward, a telescope is not required, fluctuations can be magnified more than ten times, and the precision of the technique is similar to that reported in our previous work.

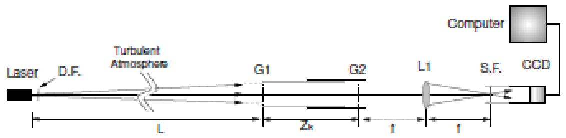

FIG. 5. Schematic diagram of the application of moiré deflectometry in atmospheric turbulence measurements. *D.F.*, *G*1, *G*2, *L*1, and *S.F.*, stand for the neutral density filter, first grating, second grating, Fourier transforming lens, and the spatial filter, respectively [2].

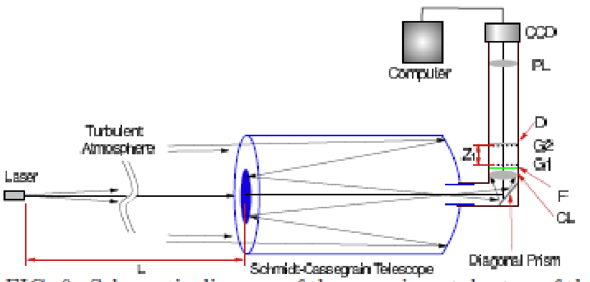

FIG. 6. Schematic diagram of the experimental setup of the moire' deflectometer on a telescope. *CL*, *F*, *G*1, *G*2, and *PL*, stand for the collimating lens, bandpass filter, first grating, second grating, and the lens that projects the moiré pattern produced on the diffuser D on the CCD, respectively.

D. Use of a moire' deflectometer on a telescope for atmospheric turbulence measurements

We have recently presented a high-precision and high-resolution instrument for the study of atmospheric turbulence by measuring the fluctuation of the angle of arrival on the telescope aperture plane [11]. A schematic of the experimental setup is shown in Fig. 6. Compared to our previous methods, because of the large area of the telescope aperture, this instrument is more suitable for studying spatial and temporal properties of wave-fronts. Because of the magnifications of the telescope and moiré deflectometry, the precision of the technique is one order of magnitude more precise than previous methods. In other word we have improved the precision of AA fluctuations for the second time. This instrument has a very good potential for wavefront sensing and adaptive optics applications in astronomy with more sensitivity. Besides, a modified version of this instrument can be used to study other turbulent media such as special fluids and gases. Also this method is a reliable way to investigate turbulence models experimentally.

Here also the component α of the AA fluctuation on the telescope aperture plane is given by [11]:

$$\alpha = \frac{f'}{f}\frac{1}{Z_k}\frac{d}{d_m}s, \qquad (7)$$

where f is the telescope focal length and f' is the focal

Method	α_{min}	Volume of data	Processing way
DIMM	1 arc sec	Two image points	Real-time
IIGT	0.5 arc sec	CCD pixels number	Non real-time
IIGGT	0.06 arc sec	CCD pixels number	Real-time
MD	0.26 arc sec	CCD pixels number	Real-time
MDT	0.01 arc sec	CCD pixels number	Real-time

TABLE I. Comparison of sensitivities and spatial resolutions of different methods, DIMM, IIGT, IIGGT, MD, MDT are stand for the differential image motion monitor, incoherent imaging of a grating by a telescope, incoherent imaging of a grating on another grating by a telescope, moire' deflectometry method, use of a moire' deflectometer on a telescope, respectively. α_{min} stands for the minimum measurable AA fluctuation.

length of the collimating lens. Compared to Eq. (6) here an improving factor f'/f appears. In our work, we have used f=200 cm and $f' = 13.5$ cm, thus the magnification is more than ten times. In other word we have improved the precision of AA fluctuations for second time in this work. As a result of our recent work, now we can claim that: " *Light-beam deflections due to atmospheric turbulence are two orders of magnitude more precise with the aid of moiré deflectometry on a telescope.*

E. Comparison of sensitivities and spatial resolutions of different methods

According to Eqs. (5)-(7), in all of the moiré based methods by increasing the gratings distance, decreasing the pitch of the gratings, or increasing the moiré fringes spacing, the measurement precision is improved. To comparing all of the mentioned methods by considering typical values that we have used in our work namely: d=1/15 mm, f=2 m, f'=10 cm, Zk =0.5 m, s/d_m=1/100, the minimum measurable AA fluctuations are obtained using Eqs. (4)-(7); 2.5×10^{-6}, 3.3×10^{-7}, 1.3×10^{-6}, and 6.6×10^{-8} rad, respectively. More details of the different methods are presented in Table 1.

In comparing the implementation of different methods, I should say that the implementation of the incoherent imaging of a grating by a telescope is not straightforward. On the other hand implementation of the moire' deflectometry method is very straightforward. Also the last method because of its precision and large area of the telescope aperture has potential applications in diverse fields.

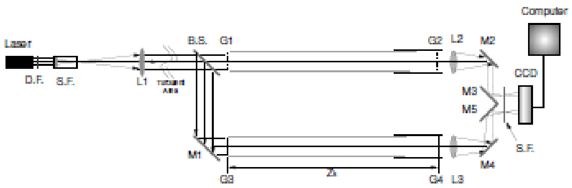

FIG. 7. Schematic diagram of the experimental setup of two channel wave-front sensor [12]. G, L, M, and $S.F.$ stand for the gratings, lenses, mirrors, and spatial filters respectively. $D.F.$, $B.S.$ and Z_k stand for the neutral density filter, beam splitter, and talbot distance, respectively.

IV. WAVE-FRONT SENSING USING THE MOIRE' DEFLECTOMETRY

A wide dynamic range two channel wave-front sensor based on moiré deflectometry has been constructed for measuring atmospheric distortions of wave-front [12,13]. The dynamic range and sensitivity of detection are adjustable by merely changing the distance between two gratings in both moiré deflectometers and relative grating ruling orientation. The spatial resolution of the method is also adjustable by means of bright, dark, and virtual traces for given moiré fringes without paying a toll in the measurement precision. The implementation of the technique is straightforward. The measurement is relatively insensitive to the alignment of the beam into the sensor. This sensor has many practical applications ranging from wave aberrations of human eyes to adaptive optics in astronomy. Implementation of this method on wave-fronts coming from celestial objects are in progress as a research collaboration with Inter-University centre for Astronomy and Astrophysics (IUCCA)'s instrumentation group. First version of set up is shown in Fig. 7. A modified noteworthy both for its simplicity and its cleverness, version of the set up is presented in Ref. [13]. Typical reconstructed wavefront surface using this wavefront sensor, corresponding to distortions generated by air turbulence in a region of $20mm \times 20mm$ are shown in Fig. 8.

V. AVAILABLE APPLICATIONS OF THE MOIRE' DEFLECTOMETRY IN ASTRONOMY

Many of the presented methods by a small modification or even without any change on the arrangement of the set-up can be used for astronomical aims. Implementation of the wave-front sensing and moiré deflectometry on wave-fronts coming from the celestial objects are in progress as a research collaboration with IUCAAs instrumentation group. Also our methods are very suitable in site selection filed work, that need for the large-scale telescopes, as we able to measure seeing or Fried parameter

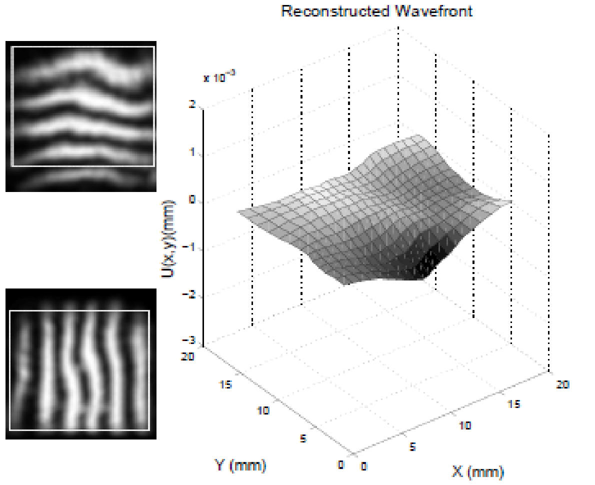

FIG. 8. Reconstructed wavefront, surface plot, corresponding to distortions generated by air turbulence in a region of $20mm \times 20mm$ [13].

and C_n^2 and its vertical profile in a very simple, worthy, and reliable way.

I hope as soon as possible to spend a period of time in IUCCA, Pune, India, to test the performance of the prototype one channel wavefront sensor on the 2 m optical telescope at the centres Garawali Observatory.

VI. CONCLUSION

In brief incorporation of moiré technique in the study of atmospheric turbulence provides the following advantages:

- Access to large volume of data in 2Ds
- Improvement of measurement precision
- Correlations calculations in 2Ds at desired scale
- The required instrumentation is usually simple and inexpensive
- The presented techniques usually are very flexible and can be applied in a wide range of turbulence strengths, by choosing gratings of adequate pitch, size, and separation.
- Finally as a result of our recent work: *Light-beam deflections due to atmospheric turbulence are two orders of magnitude more precise with the aid of moiré deflectometry on a telescope.*

Acknowledgements I would like to express my gratitude to Professor Yousef Sobouti, president of the Institute for Advanced Studies in Basic Sciences (IASBS), for the support he has given me in my scientific work, especially during the last two years. I would also like to thank him for encouraging me to present this paper in the 14^{th} meeting on research in astronomy at IASBS.

Saifollah Rasouli's Email is rasouli@iasbs.ac.ir.

[1] Rasouli S. *et al.*, 2006, Opt. Lett., 31, 3276.
[2] Rasouli S. *et al.*, 2008, Opt. Lett., 33, 980.
[3] Rasouli S., 2007, Ph. D. Thesis.
[4] Sarazin M. *et al.*, 1990, Astron. Astrophys., 227, 294.
[5] Ziad A. *et al.*, 2000, Appl. Opt., 39, 5415.
[6] Belen'kii M. S. *et al.*, 2001, Appl. Opt., 40, 1321.
[7] Rasouli S. *et al.*, 2006, Proc. SPIE, 6364, 63640G.
[8] Rasouli S. *et al.*, 2006, Proc. SPIE, 6364, 63640K.
[9] Rasouli S. *et al.*, 2007, SPIE Newsroom, DOI 10.1117/2.1200702.0569
[10] ICO Newsletter, April 2009 Number 79
[11] Rasouli S., 2010, Opt. Lett., 35, 1470.
[12] Rasouli S. *et al.*, 2009, Proc. SPIE, 6364, 74760K.
[13] Rasouli S. *et al.*, 2010, to be submitted to Opt. Exp.

Chromospheric large cool Jets as the result of Multiple Null Point Reconnections

E. Tavabi[1,2,3] and S. Koutchmy[2,3] and A. Ajabshirzadeh[2]
[1]*Payame Noor University of Zanjan, Zanjan, Iran*
[2]*Research Institute for Astronomy and Astrophysics of Maragha RIAAM, 55134-441 Maragha, Iran*
[3] *Institut d'Astrophysique de Paris, UMR 7095, CNRS and UPMC, 98 Bis Boulevard Arago, F-75014 Paris, France*

Absrract

The study of X-ray jets is an important topic to understand the heating of the solar corona and the origin of the fast wind. The recently launched Hinode mission permitted to observe the cool proxies of these jets with an unprecedented high spatial resolution of 120 km on the Sun. We selected a high cadence sequence of SOT (Hinode) observations taken with both the $HCaII$ and the $H\alpha$ filter to look at the details of the dynamics revealed by a large jet event. Both wavelet and amplitude spectra analysis were used to analyze the observed kink wave and the time variations of intensities during the event. The results are discussed in the frame of different models implying reconnections with the inference of the dynamical phenomena occurring in the vicinity of several null points, including the oscillatory behavior.

Keywords. Chromospheric Jets, Magnetic Null Point, Reconnection.
PACS numbers: 96.60.-j

I. INTRODUCTION

A wide range of dynamic phenomena is occurring in the solar atmosphere, including the upper parts where the magnetic field dominates. For example Soft X-Ray jets and specific flares have been associated with magnetic reconnection occurring in a three dimensional magnetic null point topology consisting of a fan plane located below the null point and a spine field line above it (e.g. Priest and Forbes 2000). In the potential or near-potential magnetic fields, a 3D nullpoint configuration with a fan and a spine naturally occurs if a magnetic bipole is embedded into one polarity region of a large-scale bipolar ambient field (e.g. Antiochos 1998). It is generally accepted that reconnections are appropriate for explaining features such as particle acceleration and plasma heating. The exotic properties of x-type neutral points have played a central role in the development of the X-Ray coronal dynamics. Current sheets accumulate magnetic energy at null points in the plasma, and provide sites for strong magnetic energy release (Priest and Forbes 2000). Craig and Fabling (1996) suggested that current sheets are associated mainly with three-dimensional fan-current reconnection; other reconnection models require quasi-cylindrical spine currents that develop along the exhaust axis of the fluid (Galsgaard et al. 1997). Almost all jets have been classified in two groups, (i) cool chromospheric jet-like structures such as spikes, surges and small scale anemone jets (Sterling 2000; Koutchmy and Stellmacher, 1976; Shibata et al. 1992 and 2007), (ii) and hot magnetic plasma ejection, such as W-L, EUV and X-ray coronal jets (Shibata 1992; Tsuneta1997; Filippov et al. 2009; Koutchmy 1969). Alfven and magnetoacoustic wave modes may exist, though these are normally coupled together. Null-point motions in an axially symmetric system can excite transversal oscillation which was called the kink mode wave, and also this mode can evolve into Alfven wave after its propagation into the more homogeneous medium (Cranmer et al. 2007). Upward propagating waves are generally exploited in theoretical models for heating the chromosphere and the corona (Hollweg and Isenberg 2002). Rickard and Titov (1996) have studied the cold plasma, using linear, resistive, magneto hydrodynamic (MHD) equation to study the dynamics of current accumulation at a three-dimensional magnetic null. Their theoretical analysis shows that the axi-symmetric perturbations for m=0 (where m is the azimuthal wave number) can lead to a current parallel to the spine axis at the null and corresponds to topological reconnection (Craig and Watson 1992), while the m=1 mode produces currents orthogonal to the spine axis at the null (parallel to fan plane), and for $m > 1$ there is never any current at the null. Dynamically, we know that m=0 corresponds to toroidal oscillations propagating along the zero-order field lines and eventually localized parallel to the spine axis with a cylindrical column of current aligned to this axis. The m=1 mode produces motions across both fan and spine axis in single nullpoint events, resulting in a current distribution wholly in the fane plane. One of the most important efficient m=1 mode is concentrating magnetic flux toward the null and produces strong currents in the fan plane. It is possible that for the system of this theoretical study which remains with cold plasma, the evolution of neutral points and currents never see explicitly in hot coronal hole X-ray jets or the whip-like motion which is interpreted as a slingshot-like motion and is the result of reconnections which make some elaborated motions detected as transversal motion of a coronal hole X-ray jets.

II. OBSERVATION

2-1 Data reduction and Image processing.

The Hinode SOT data taken above the solar limb have been used to study the dynamical nature of the cool jets. HCaII data used in this study are from the Broadband Filter Imager (BFI) of SOT and the $H\alpha$ data are from the Narrowband Filter Imager (NFI) (Tsuneta et al. 2007). The observations were performed in continuous fashion over several minute with different cadence of 20 sec at the diffraction limited resolution of or (120km) using a 0.054" pixel size on filtergrams of the HCaII line and approximately two times worse for $H\alpha$, the spatial resolution with the diffraction limit is now (250km) and the scale is 0.08"/pixel (see Figure 1). The Hinode SOT data were calibrated with standard $'fg - prep'$ of the SSW software (Shimizu et al. 2008). A superior spatial image processing for line-like or aligned features is obtained using the mad-max algorithm (Koutchmy and Koutchmy 1989). The mad-max operator acts to enhance the finest scale structure substantially. The mad-max filter is a weakly nonlinear modification of a second derivative spatial filter. Specifically, it is where the second derivative has a maximum when looking along different directions. The behavior of the mad-max qualitatively resembles the second derivative, but the strong selection for the direction of the maximum variation substantially enhances line-like structure. It appears to reduce blending between crossing threads superposed along the line of sight. The algorithm, as originally proposed, samples the second derivative in eight directions, but the directional variation of the second derivative was generalized to a smooth function with a selectable pass band spatial scale for this work (for more details see the November and Koutchmy 1996) . Spatial filtering using "mad-max" algorithms clearly shows relatively bright radial threads in the chromosphere as fine as the resolution limit of about 120 km.

2-2 Event Description

The brightening of several loop system at the edge of a sunspot was observed by SOT for about two-three hours on 2007 July 08, between about 00:34 and 03:11 UT. The dynamic evolution described in the following lasted about one hour, ending at 02:05 UT. Figure 2 and 3 show snapshots outlining the main feature of the jet in both $HCaII$ and $H\alpha$ lines simultaneously, at about 01:14 UT, when the jet spine part becomes visible. The red dashed lines denotes the average axis of the jet (including the interchange space) and the double short blue lines show two different heights with distance of 3 Mm, which henceforth are denoted as layer I and II and indicate the location on

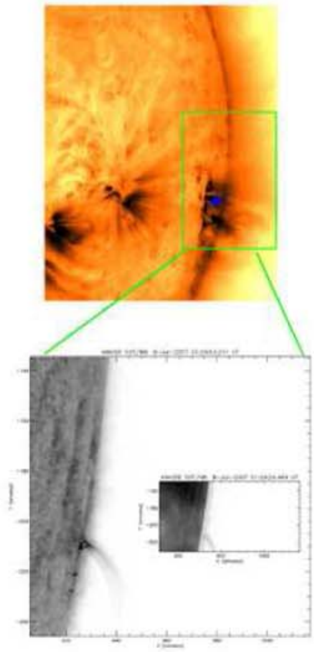

FIG. 1. Top, negative Stereo image in hot EUV line (171 $A°$. Bottom negative $HCaII$ and $H\alpha$ images showing a typical cool jet; the simultaneously obtained $H\alpha$ image is shown inserted in the Ca line Image; times are shown in UT.

the jet where its transversal displacement is further analyzed.

At about 01:25 UT, the jet becomes more dynamic and it seems that two or three null points appear close to each other. They appear to have different brightness and collectively exhibit a small scale anemone jet-like shape as defined by Shibata, or an Eiffel tower shape as defined by others. The observation suggests that the dynamic phenomena were caused by the interaction of newly emerging flux in the arcade like field near the active region. The long-lived phenomenon concentrates in the vicinity of the sunspot, which would have multiple 3D null points during the event. The jet-like event emerged as a brightening propagating along the spine and the slingshot behavior is clearly seen in figure 4; it can be understood by means of models of magnetic reconnection between small emerging bipole. This whip-like motion with brightening also include a small amplitude transversal oscillation which maybe related by means of magneto acoustic wave similar to a propagating kink or an Alfven wave. The propagation of transversal motion across the spine axis is a response of neutrals ions to the collimated magnetic plasma with a specific perturbation along the multiple nullpoint separators (the propagation near the null points and the

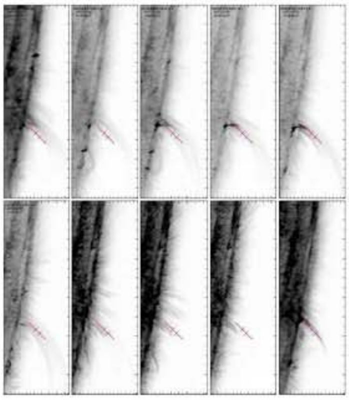

FIG. 2. Selected snapshots of negative and mad-maxed images from the SOT (Hinode) broadband $HCaII$ filter observations (25×65 arcsec^2) at different times (01:14 to 2:14 UT). The spine axis (includes interchange space) are denoted by a red line. Blue lines are plotted at layer-I and II positions in all images to outline the oscillatory transverse motion and displacement of its central part. See the text for details. (An avi animation of this figure is available in the online journal). The animation uses a different intensity scaling, which outlines the jet in more clarity.

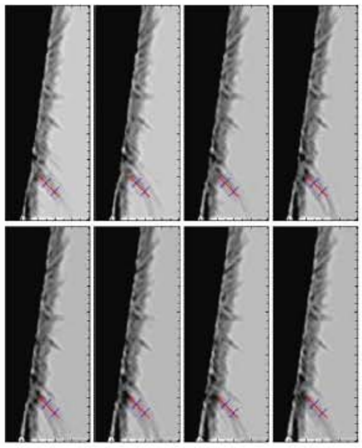

FIG. 3. Selected snapshots of negative and mad-maxed images from the SOT narrowband $H\alpha$ filter observations (35×105 arcsec^2) at different times (01:14 to 2:14 UT). The spine axis (includes interchange space) are denoted by dashed red line. Blue lines are plotted at layer-I and II positions in all images to outline the oscillatory transverse motion and displacement of its central part. See the text for details (an avi animation of this figure is available in the online journal). The animation uses a different intensity scaling, which outlines the jet in more clarity.

propagation of transversal wave along the spine is better visible in the online movie accompanying fig 2 and 3).

III. DATA ANALYSIS

Figure 4 are time/slice diagrams which show two temporal sequences of displacements corresponding to the layer-I and II of the jet. In this figure we find that points on the jet spine axis oscillate transversally with time; in addition the average transverse motion around the central longitudinal spine axis show a whip-like motion from left-to-right in both layers.

Wavelet and fast Fourier transform (FFT) analysis are now used to obtain temporal spectra. In figure 5 the two top plots show the wavelet time frequency analysis power spectra for intensity time fluctuations for layers I and II which were shown in time-slice diagrams of transversal wave oscillations; the bottom plot shows the coherency coefficient (gray plot) and the phase difference (color plot) for the layers corresponding to each other. The horizontal axis is the time in minutes, while the vertical axis is the period in minutes. Darker shades correspond to higher power (95 percent confidence) of the wavelet coefficients. The contours determine the 95 percent confidence level which was calculated by assuming a white noise background spectrum. Wavelet transform suffers from the "wraparound" errors at both edges of a time series (of finite length). The regions in which these effects are important are defined by the cone of influence (COI; see Torrence and Compo, 1998). The COI region, or in other words the region that suffers from edge effects, is chosen as the e-folding time of the Morlet wavelets and it is presented as a cross-hatched in each plot. From the wavelet time/frequency analysis of intensity fluctuation in these layers we obtain a typical period of about 3 min which can be related by the chromospheric 3-min oscillations and from coherency and phase difference diagram we could find a large coherency in the 2-4 min range but for larger period the coherency coefficients decrease. In the observed layers I and II the phase-difference obtained from the wavelet analysis is reassuring in that it is indeed showing a near-zero degree difference in the large part of time between 2-4 min of period and for another time range part it reaches a maximum value of about 120 degree (boundary of blue and red) at 3 min, corresponding to a time delay of 60 Second for these two different layers with a distance between them is about 3 minutes.

FFT analysis is also used to calculate the amplitude spectrum (AS) and it is shown in the middle panels of figure 6. It is found that the AS has a maximum at 5 mHz which corresponds to a period of 180 s and it is confirming the wavelet time/frequency result for both

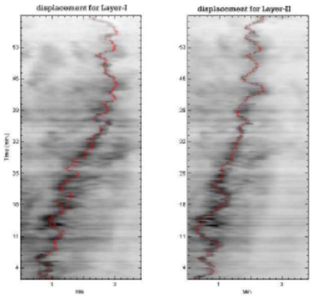

FIG. 4. "Time slice" images in Ca H II line, produced using Hinode observations for layers-I and II, see Fig. 2.

layers. We carry out a cross-correlation analysis of the two oscillation sequences for layers-I and II, in order to evaluate the propagation direction of the oscillation as well as to determine the phase speed. The upper panels of figure 6 display the transversal oscillation sequences for the 2 layers respectively. This oscillation has a maximum cross amplitude spectrum (CAS) at a frequency of 2 mHz. The correlation coefficient between oscillations of different layers as a function of the time lag can be obtained by applying an inverse-FFT method to the CAS profile.

The correlation coefficient has a maximum value for the time lag of 1 min and it is showing that the oscillation for layer-II has a time lag of 1 min relative to the layer-I and indicates a wave propagation upward with a phase speed of 30 to 40 kms-1 along the spine axis. It should be remarked that the phase speed may be much lager than this amount since we could not distinguish a time lag shorter than 40 s, the cadence of image being of about 20 s, so this maximum corresponds to the Nyquist frequency.

IV. SUMMARY AND DISCUSSION

We presented Hinode SOT observations that include high-resolution HCaII and $H\alpha$ lines images taken at solar limb, in the chromospheres, as a first test to study how cool dynamics jets are driven through multiple nulls and how transversal waves are generated. Shibata et al. (2007) analyzed a small scale jet in an active region using SOT data. There events are typically of 3 to 7 arcsec=2 to 5 Mm length and of 0.35 Mm width and their apparent velocity is 10 to 20 kms^{-1}, these small scale jets have a Lambda shape, similar to the shape of X-ray anemone jets in the corona which have been discovered on the coronal hole by the Yohkoh satellite as transitory X-ray enhancement in the solar corona with collimated motion (Shibata et al. 1992). Figure 1 shows that the HCaII large scale jet is typically of more than 20 arcsec length and has a 5 arcsec width; these values are much larger

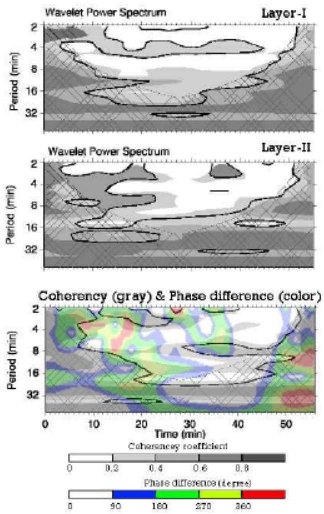

FIG. 5. Upper plots show wavelet powers corresponding to the intensity fluctuations (period vs. time) for layer-I and II. Lower plot shows the coherency (gray) and the phase difference (color)plot simultanously and correspondigly, the color bars for coherency coefficient (gray) and the phase difference at the bottom. Cross-hatched regions indicate the "cone of influence" (COI). The darkest regions mean higher power, and the contours correspond to the 95 percent confidence level (see text and reference for details).

than the physical parameter of HCaII jets reported by Shibata et al. 2007. However the propagating velocity of our HCaII jet is similar and of about 15 kms^{-1}; it is in the range of values which was predicted for cool jets in the low chromosphere and photosphere (Shibata, 1997). We have also provided evidence for jet transversal motions across the spine. We know that the azimuthally symmetric (m=0) modes are the only modes associated with topological reconnection and it is shown that reconnection can only occur in the case of purely radial disturbances and allows a finite current parallel to the spine at the neutral point (Craig and Watson 1992). From the analysis by Rickard and Titov (1996) it is clear that the m=1 mode (current accumulation in separator plane) is the most likely mode to naturally occur for the axisymmetric single null point. There are two ways to generate this mode, tilting and as a result in current accumulation in the separator plane for a time interval that is related to the transient time of the driver, but for the double nullpoint it is only possible to perturb each null with a pure m=1 mode by perturbing the spine axis. Indeed, the separator lies in the fan plane of each null between nulls and when the perturbation is applied to one of the null points of the double null the situation changes. From the theoretical point of view the nature of the fast mag-

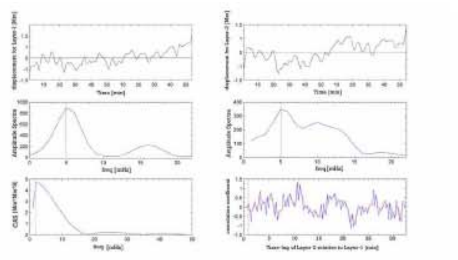

FIG. 6. Upper panels: intensity fluctuations for layer- I and II (black lines). Middel panels show amplitude spectra (AS) for these two layers (blue lines) and red vertcal lines indicate the maximum values for oscillations. In the lower left panel: cross amplitude spectrum (CAS) for the oscillations of layer-I and II; in the lower right panel: correlation coefficient as a function of time lag between the oscillation of layer-I and II (solid blue line) and the fitting using the 5th Fourier harmonic (red dashed line).

netoacoustic or of the Alfven wave propagation in the neighborhood of two nullpoints have been investigated in more detail by McLaughlin and Hood (2005). To our knowledge, the propagation of MHD waves in such cool jets have never been seen; it is similar to what was seen in coronal hole X-ray jet; for such hot events only we see the sling-shot motions of spine axis during their evolution. Our amplitude spectrum analysis also shows a clear transversal wave propagation inside the jet with a phase speed of about 30 to 40 kms^{-1}, which is comparable to the speed of Alfven wave in the low chromosphere plasma. Our results seem to confirm the theoretical predictions quite well.

Acknowledgements We thank B. Filippov for useful discussions and we are very grateful to the Hinode team for providing wonderful observations. Hinode is a Japanese mission developed and launched by ISAS/JAXA, with NAOJ as domestic partner and NASA and STFC (UK) as international partners. Image processing MAD-MAX program was provided by O. Koutchmy, see $http : //www.ann.jussieu.fr/ \quad koutchmy/index_n ewE.html$ and wavelet analysis software was provided by Torrence and Compo (http://atoc.colorado.edu/research/wavelets), This work has been partly supported by RIAAM..

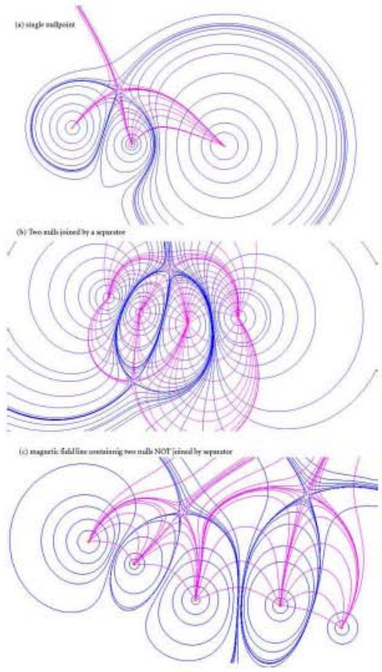

FIG. 7. Magnetic null-point different configurations for one (top) and two (bottoms) neutral magnetic points ($B = 0$) and their separators.

References

Antiochos, S. K., 1998, ApJ., 502, L181
Craig, I. J. D., Fabling, R. B., Henton, S. M., and Rickard, G. J. 1995, ApJ, 455, L197
Craig, I. J. D. and Watson, P. G., 1992, ApJ, 393, 385
Cranmer, S. R., van Ballegooijen, A. A., and Edgar, R. J. 2007, ApJS, 171, 520
Filippov, B., Golub, L. and Koutchmy, S., 2009, Solar Phys., 254, 259
Galsgaard, K. and Nordlund, A. 1997, J. Geophys. Res., 102, 231
Koutchmy, O. and Koutchmy, S., 1989, in Proc. 10th Sacramento Peak Summer Workshop, High Spatial Resolution Solar Observations, ed. O. von der Luhe (Sunspot: NSO), 217
Koutchmy, S. 1969, Astrophysical Letters, 4, 215
Koutchmy, S. and Stellmacher, G. 1976, Solar phys., 49, 253
Hollweg, J. V. and Isenberg, P. A. 2002, J. Geophys. Res., 107, 1147
McLaughlin, J. A. and Hood, A. W., 2005, Astron. and Astrophys., 435, 313
November, L. J. and Koutchmy, S. 1996, ApJ, 466, 512
Priest, E. R., and Forbes, T. G., 2000, Magnetic Reconnection, Cambridge Univ. Press, Cambridge
Rickard, G. J. and Titov, V. S. 1996, ApJ, 472, 840
Shibata, K., Ishido, Y., Acton, L., et al., 1992, PASJ, 44, L173
Shibata, K., et al. 2007, Science, 318, 1591
Shibata, K., in The Corona and Solar Wind Near Minimum Activity, Proc. 5th SOHO Workshop, Oslo, Norway, 17 to 20 June 1997 [European Space Agency (ESA) SP-404, 1997] pp. 103-112.
Shimizu, T., Nagata, S., Tsuneta, S., et al. 2008, Sol. Phys., 249, 221

Sterling, A. C. 1998, ApJ, 508, 916
Tsuneta, S., Ichimoto, K., Katsukawa, Y., et al. 2008, Sol. Phys., 249, 167
Torrence, C., Compo, G.P., 1998. Bull. Amer. Meteor. Soc. 79, 61.

Investigation of Geomagnetic Field effect on Azimuth distribution of Extensive Air shower events

Fazlalizadeh, Maedeh [1] and Khakian Ghomi, Mehdi [1]
[1] *Amirkabir University of Technology, Nuclear engineering and physics Department Tehran, Iran*

In this paper our purpose of research is the investigation of the azimuth anisotropy of cosmic rays via investigation of geomagnetic field effect over secondary particles. This effect deflected both primary and secondary particles. Primary particles are more energetic than secondary particles but their deflection is too less than reported experimental results. In this investigation we calculate the geomagnetic field effect over secondary particles and will compare our results with experimental data and the simulated data made with CORSIKA code and use them for explanation of the experiment.

I. INTRODUCTION

Extensive air showers (EASs) are one of the probes for detection of Cosmic-Rays in the energy range of TeV and more. Cosmic rays come from so farther altitudes. Many factors affect them in this way and deflection them. For reaching correct information about these particles, we should know the factors well. Distribution of the CRs in the Galaxy is homogeneous, but the distribution of air showers on the earth in zenith angle distributions is different. An important effect is the thickness of the atmosphere that is different for CRs during passed through the atmosphere. We expect an isotropic distribution, because the atmospheric thickness is the same in different azimuth directions. But there is a slight North-South anisotropy of the CRs in the energy range of a few TeV to a few hundred TeV which has not been well known yet. There are so many attempts to understand the nature of the anisotropy observed in the EAS arrays [1–3]. Some analysis and calculations is presented for explanations of it, like slope of the ground, time variations of geomagnetic field, and amount and direction of geomagnetic field in the location of CR observation. But still non of the methods couldn't present a complete explanation for the anisotropy. The anisotropy is compared with harmonic functions, usually with the first two harmonics:

$$A = N_0(1 + A_{\mathrm{I}} cos(X - \Phi_{\mathrm{I}}) + A_{\mathrm{II}} cos(2X - \Phi_{\mathrm{II}})) \tag{1}$$

An interesting subject is increasing (decreasing) of AI (AII) with increase of observation latitude, which shows a North-South anisotropy [2,4]. Observations in different points show that the anisotropy is more in higher zenith angle events [2], and also is more in the results of higher latitude observatories. The geomagnetic field changes with changing the altitude and longitude. This guides us to investigate the geomagnetic field as a good candidate for the subject [5]. The investigation of geomagnetic field effect via the primary particles shows that the anisotropy due to the primary particles shows expectable physical behavior. But the amplitude of the anisotropy cannot explain the experimental results [6]. So it seems that this effect is more important over secondary particles than primaries. We investigate this subject now.

II. EXTENSIVE AIR SHOWERS AND SECONDARY PARTICLES

Extensive air showers are cascades initiated by energetic primary particles which develop in the atmosphere. EASs are a category of secondary particles that reach to earth simultaneously. EASs consist of gamma rays, electrons, positrons, negative and positive muons and atomic neuclei. In terms of the number of particles, electrons and positrons constitute the main shower component. Only about 10% of the charged particles in an extensive air shower are muons. For examples a sample of the number of these particles for an EAS with energy of 283.073 TeV is mentioned in table I.

The numbers of the secondary particles are different in different atmospheric depths. They increase initially in a parabolicals fashion and decay exponentially after the maximum of the shower. The longitudinal profile of the secondary particles' number can be parameterized by $N(t) \sim t^{\alpha} exp(-\beta t)$ where $t = x/x_0$ is the

	sea level	300 gr/cm^2
N_{e+}	13131	48004
N_{e-}	18016	73563
$N_{\mu+}$	449	1083
$N_{\mu-}$	452	1107
N_{hs}	158	585

TABLE I. The numbers of some of the secondary particles at sea level and at slant depth of 300 gr/cm^2

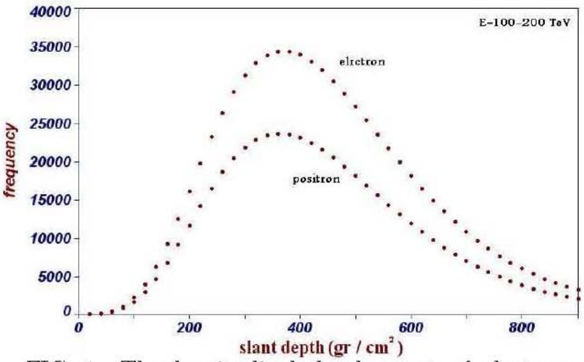

FIG. 1. The longitudinal development of electrons and positrons at different atmospheric depths.

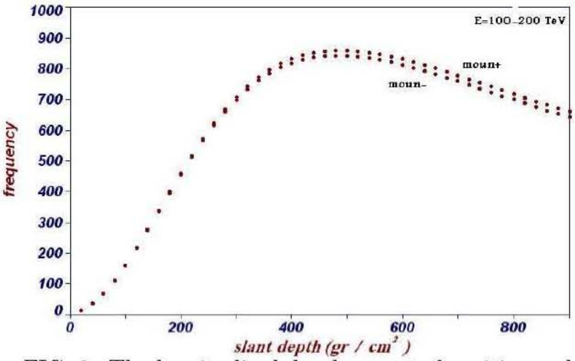

FIG. 2. The longitudinal development of positive and negative muons at different atmospheric depths.

shower depth in units of the radiation length, and α and β are free fit parameters [7]. Figures 1 and 2 show schematically the longitudinal development of some various components of several extensive air showers in the atmosphere for primary energies between 100 to 200 TeV.

Figure 1 shows that electron and positron profiles are similar to each other, and always the number of electrons is more than positrons. In fact the positrons decay into gamma rays. Decreasing of the number of shower particles after reaching to shower maximum occurs due to two important effects: *i*) collision and *ii*) decay. Collision makes particles to go far from the shower axis. The cross section scattering of electrons and positrons is not so small, so they were scattered more than other particles, and they decrease more than other particles until reaching to earth surface. But the number of muons reaches a constant number. Their numbers are hardly reduced to earth surface because of the mean life of muons is not so small, approximately 2.2 μs. This is the known muon ratio of the atmosphere $(\mu_+/\mu_-) \simeq 1.2$ [8]. In figure 2 we can see the negative muons capture in electron orbits and so the number of them is less than positive ones.

III. GEOMAGNETIC FIELD EFFECT ON SECONDARY PARTICLES

Geomagnetic field is approximately a dipole magnetic field which has an angle of 11.5° with the earth rotation axis. Its magnetic moment is $1.8 \times 10^{25} Gs.m^3$ and shifted by 342 km relative to the earth center [9]. The secondary particles are almost relativistic and ultra-relativistic charged particles. The geomagnetic field affects over these charged particles and deflects them. This effect changes with height, latitude and longitude of a place. The energy of the secondary particles and their zenith and azimuth angles are effective factors in amount of their deflection. We are able to compute the energy of the secondary particles in CORSIKA by P_x, P_y, P_z.

To determination the inclination, we used Lorentz Force over the secondary particles from the starting point of the EAS to the observation level (1200 m) and integrated over all of the paths for each particle.

Our reference coordinate (O) is cartesian coordinates at observation point. By knowing the primary particle's momentum (P_x, P_y, P_z) and the geographical position of the location of particle, we can calculate the final momentum in each collision due to the Lorentz Force $\vec{F} = q(\vec{P} \times \vec{B})/\gamma m_0$. In any point of our location $\frac{B_y}{B_x}, \frac{B_y}{B_z} \ll 1$, so

$$\begin{aligned}\vec{F} &= F_x\hat{i} + F_y\hat{j} + F_z\hat{k} \\ &= \tfrac{q}{\gamma m}[(P_yB_z)\hat{i} + (P_zB_x - P_xB_z)\hat{j} + (-P_yB_x)\hat{k}]\end{aligned} \quad (2)$$

The relative energy of each particle is

$$E = \sqrt{m_0^2c^4 + p^2c^2} = \gamma m_0 c^2$$

At the end of the path of each collision, for obtaining final momentum due to Lorentz force, we calculate momentum differential $\Delta\vec{P} = \int \vec{F}dt \cong \vec{F}\Delta t$ where $\Delta t = \Delta h/c$ and Δh is the distance that the particle travels in the atmosphere in the time interval. Therefore $\Delta\vec{P} = \vec{F}\Delta h/c$ and in the next collision we have $\vec{P}(t+\Delta t) = \vec{P}(t)+\Delta\vec{P}$, and obtains new direction. For each point we can use

$$\theta = tan^{-1}(\sqrt{P_x^2 + P_y^2}/P_z) \quad (3)$$

$$\phi = tan^{-1}(P_y/P_x) \quad (4)$$

This process will continue until x becomes smaller than the x of Tehran's height (1200m), and at the end, final angles for each particle (θ_f, ϕ_f) are obtained from $\vec{P}_f$. We need to calculate the effect for all secondary charged particles of a shower.

IV. FIRST STAGE RESULTS

By the process we obtained the final direction of secondary CRs after passing through the geomagnetic field. Then by using a *uniform* random generator for azimuth angles (ϕ_0) of secondary particles and another random generator for zenith directions (θ_0) , we generated many different events. The primary obtained results are presented as follows:

1. The number of the secondary particles reach to the earth respect to zenith angle of the shower is different in the range of $[0, 60°]$. Maximum number of the detected showers at the earth surface is about 30°. (Figure 3)
2. A North-South anisotropy is seen in azimuth (ϕ) angles of the secondary particles in the range of $[0, 360°]$. (Figure 4)
3. Usually the first interaction of primary particles is at higher level of the atmosphere. The interaction rate decreases with decrease of height exponentially. So that we can fit $y = a+bexp(-x/c)$ on it accurately. (Figure 5)
4. The simulation of 100000 particles of a shower with energy of 100 TeV that reach to the earth surface without the geomagnetic field effect, shows that there is a very small difference between the initial angles of the shower (θ_i, ϕ_i) and the final angles (θ_f, ϕ_f) . The results of azimuth and zenith angles distribution was shown in figures 6 and 7 respectively.

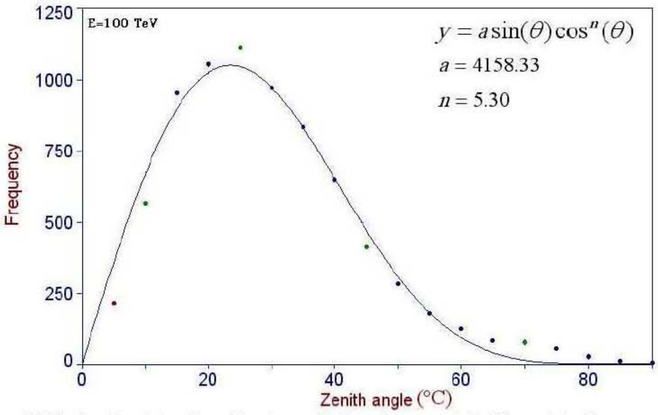

FIG. 3. Zenith distribution of the detected EASs with fitting $y = a\sin(\theta)\cos^n(\theta)$ on it.

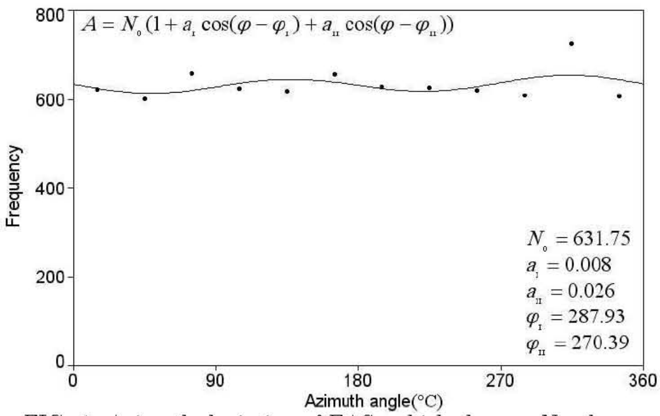

FIG. 4. Azimuth deviation of EASs which shows a North–South anisotropy.

V. DISCUSSION ABOUT THE FUTURE RESULTS

We are doing the above calculations for two situations: *i*) without and *ii*) with the geomagnetic field effect. Then we will compare our simulated results with experimental data and the data made with CORSIKA code. We search for an agreement between our results and the experimental results [2]. A partial agreement shows

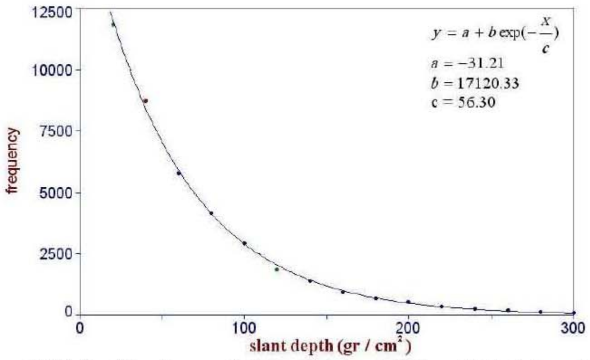

FIG. 5. Numbers of the primary EASs which interact in different heights for 40000 EAS samples.

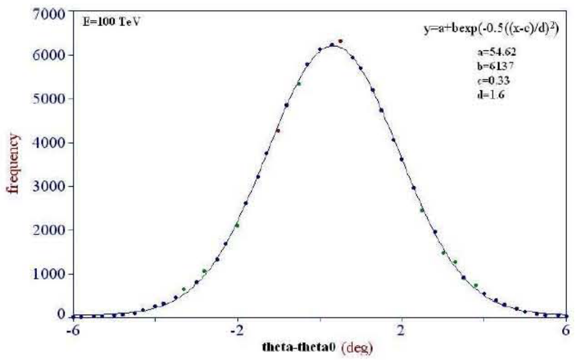

FIG. 6. The distribution of the difference of the initial and the final zenith angles of 100,000 particles in a shower without geomagnetic field effect

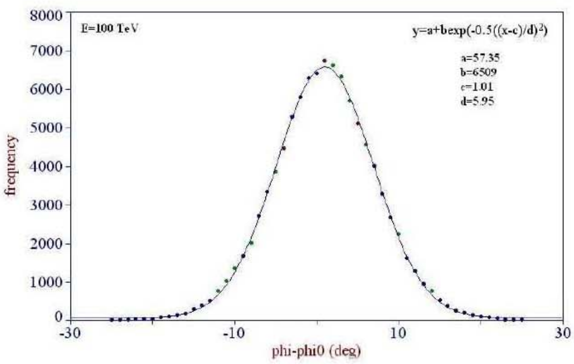

FIG. 7. The distribution of the difference of the initial and the final azimuth angles of 100,000 particles in a shower without geomagnetic field effect

incomplete assumptions, so we need to continue our work by more details.

---

[1] A.A. Ivanov. et al., JETP letters 69,288 (1999)
[2] M. Bahmanabadi, et al., Experimental Astronomy 13, 39 (2002)
[3] H. H. He, et al., Astroparticle Physics 27,528 (2007)
[4] M. Khakian Ghomi, et al., Astronomy and Astrophysics 434,459 (2005)
[5] M. Khakian Ghomi, et al., 30th ICRC Yukatan 0263 (2007)
[6] M. Khakian Ghomi, et al., submitted to JKPS (2010)
[7] C. Grupen, Astroparticle Physics, Springer 157 (2005)
[8] M. Bahmanabadi et al. Astroparticle Physics 24, 183 (2005)
[9] L. I. Dorman, Cosmic Rays in Magnetospheres of the Earth and other Planets, Springer 9 (2008)

Distinguishing between different alternative theories of gravity, using different IMF's in stellar population synthesis scheme

A. Hasani Zonoozi, H. Haghi, and Y. Sobouti
Institute for Advanced Studies in Basic Sciences (IASBS), P. O. Box 45195-1159, Zanjan, Iran

We construct rotation curves of a large sample of galaxies from the distribution of their detectable matter in four known gravitational theory, nonlocal nonlinear gravity model (NLNL), modified Newtonian dynamics (MOND), modified gravity (MOG) and Newtonian gravity plus cold dark matter (CDM) halo to calculate mass-to-light ratios of galaxies. All models were able to explain the rotation curves with nearly the same quality. In order to distinguish between different models, we concern on the implied global stellar mass-to-light (M^*/L) ratios and compare them to the predictions of "stellar population synthesis" (SPS) models. We find out significant disparities in the M^*/L ratios, when we use different gravity theories in rotation curve analyzing. We resort to SPS models and find that through NLNL gravity, M^*/L ratios are in good agreement with those obtained from Kroupa's initial mass function, while MOND is consistence with Salpeter mass function. Furthermore, M^*/L's obtained through MOG and CDM plus Newtonian gravity behave differently. Here is a tool to discriminate a) between different alternative theories of gravity, and b) between different IMF's in SPS contexts.

PACS numbers: 05.10.-a ,05.10.Gg, 98.70.Vc

I. INTRODUCTION

Observable matter in galaxies and in clusters of galaxies cannot produce sufficient gravity to explain their dynamics. To provide the missing gravity some resort to dark matter/dark energy scenarios. Much experimental effort has failed to yield a direct detection of dark matter particles. This lack of direct identification, has encouraged an equally intensive effort to search for alternative theories of gravitation. The pioneering modified Newtonian dynamics (MOND) of Milgrom (1983), the modified gravity (MOG) of Moffat (2005), and varieties of $f(R)$ gravities [5,6,19] fall in this category. In a series of recent papers one of us (YS) incorporates the nonlocality and nonlinearity of the law of gravitation, in that the gravitational acceleration at any one point depends on certain integral properties of the baryonic sources of gravitation in a nonlinear way, into a spacetime formalism and proposes a way to deduce the expected dynamics of the galaxies ([20], hereafter referred to as the nonlocal nonlinear (NLNL) model).

Rotation curves of spiral galaxies provide a valuable body of data to determine the radial dependence of gravitational forces in galactic scales. In the present paper we compare the constructed rotation curves of a large sample of galaxies from the distribution of their detectable matter in different gravity models, MOND, MOG, NLNL, and CDM. We assume that the distribution of the visible light is a reasonable tracer of the stellar matter in the galactic disk, and the distribution of the neutral hydrogen is a tracer of the structure of the gaseous mass. The free adjustable parameter in matching the theoretical rotation curves to data points is the stellar mass-to-light (M^*/L) ratio, assumed to be constant throughout the galaxy.

Seemingly, all models reproduce the observed data with reasonable details. We discover significant disparities in the stellar mass to light ratios (M/L) of the four theories. In order to discriminate between different gravity models we resort to stellar population synthesis (SPS) models. Different galactic initial mass functions predict different color-M/L relation in SPS models. This may also yield an independent consistency test of gravity models. Moreover, it will be a new tool to discriminate between different IMF's in Galaxies.

The paper is organized as follows: In section 2 we give a brief review of different gravity models used in our analysis. Fits to the observed rotation curves are elaborated in section 3. Results and brief concluding remarks are given in sections 4 and 5.

II. ALTERNATIVE GRAVITY MODELS

In this section we give the end formulas of utilized alternative gravity models to construct the rotation curves.

1 - NLNL: The asymptotic speed of a test object orbiting the system is

$$v^2 = \frac{c^2}{2}\left[\lambda\left(\frac{M(r)}{M_\odot}\right)^{1/2}\frac{1}{r} + \frac{2GM(r)}{c^2}\frac{1}{r^2}\right], \qquad (1)$$

where $M(r)$ is the baryonic mass inside the radius r and $\lambda = 2.8\times10^{-12}$ is a dimensionless parameter determined by matching the asymptotic behaviors of Eq. (1) and the observed rotation curves.

2 - MOND: The MONDian and the Newtonian gravitational forces, g and g_N, respectively, are related through the relation $g\mu(g/a_0) = g_N$, where $\mu(x) = x/\sqrt{1+x^2}$ is an interpolating function for the transition from the Newtonian to the MONDian regime and $a_0 \simeq 1.2 \times 10^{-10}\mathrm{ms}^{-2}$. The corresponding rotational velocity of MOND, thus becomes

$$v^2(r) = \frac{GM(r)}{\sqrt{2}r}\left[1+\left(1+\frac{4{a_0}^2r^4}{G^2M^2(r)}\right)^{1/2}\right]^{1/2}. \quad (2)$$

3 - MOG: The resulting modification of the inverse-square Newtons law in the gravitational field of a central mass M is [13]

$$g_M = G_N \times \left\{1+\alpha(r)\left[1-e^{-r/r_0}\left(1+\frac{r}{r_0}\right)\right]\right\}\frac{M(r)}{r^2} \quad (3)$$

M_0 and r_0 are two scaling parameters that vary with distance and determine the coupling strength of the vector field to baryonic matter and the range of the force, respectively. In galactic scales, these parameters $M_0 = 9.6 \times 10^{11} M_\odot$ and $r_0 = 13.9$ kpc [13,8].

Finally we compare the results with those of CDM scenario considering the spherical two-parameter logarithmic halo whose the gravitational potential is

$$\Phi_h(r) = \frac{1}{2}{V_0}^2 \log({R_c}^2 + r^2), \quad (4)$$

where, R_c is the core radius and V_0 is the asymptotic circular velocity of the halo.

III. CONSTRUCTING ROTATION CURVES

We apply different formalism to a wide range of different types of galaxies, a collection of 46 galaxies from [16,17,11,1].

We calculate the rotation speed of a test object circling the galaxy as a function of the distance from the galactic center and the distribution of the detectable matter in the galaxy. We approximate the galaxy by a spherically symmetric system. The error committed in this approximation is of the order of $[R_{gyr}(r)/r]^2$, where $R_{gyr}(r)$ is the gyration radius of the mass enclosed within the radius r. In disk-shape systems this ratio is of the order of few parts in thousand. In considering the accuracy of the observed data, the effects is negligible.

We assume a constant stellar mass-to-light ratio, M^*/L, throughout the galaxy, though this is not strictly the case, because of the color gradient in spiral galaxies.

Given the observed distribution of the baryonic matter (stellar and gaseous disks, plus a spheroidal bulge, if present), the effective radial gravitational force, and subsequently the circular speed, is calculated from Eqs. 1-4. Fitting of the calculated rotation curve to the observed data points is achieved by adjusting the M^*/L ratio, through a least-square χ^2. The best-fit χ^2 and M^*/L values are listed in Table 1. In the case od CDM we have two additional free parameters, R_c and V_0.

IV. COLOR – M/L RELATION

Stellar population synthesis (SPS) models predict a linear relation between colors and M_*/L ratios of galaxies. Redder galaxies should have larger M_*/L [2,3,14]. The slope of this linear relation does not depend on exact details of the history of star formation, i.e. the assumed IMF. Depending on how many stars are present at the low-mass end of the stellar IMF, the color-M/L curve shifts up and down, because those stars contribute significantly to the mass of a population, but insignificant to its luminosity and color.

There is considerable uncertainty in the determinations of the IMF slope for low-mass stars in galaxies. The standard color-M*/L relation assuming a Salpeter IMF ($\alpha = 2.35$) normalization overpredicts the stellar M/L ratios of many of the galaxies. Motivated by recent IMF determinations that suggest a turnover in the IMF at low stellar masses [10], the Salpeter IMF is scaled down by a factor of 0.7 which is equivalent to a Salpeter IMF with a flatter slope ($\alpha = 1$) below 0.35 $M_\odot$ (so-called "scaled Salpeter IMF"), or a Kennikutt (1983) IMF with a brown dwarf fraction of 40% [2]. The scaled Salpeter IMF predicts the lower M*/L ratios for galaxies from the observed color compare to standard Salpeter IMF (table 7 of [3]):

$$\log(M^*/L_B) = 1.737(B-V) - 0.942. \quad (5)$$

To convert from scaled Salpeter IMF to Salpeter (1955), Kroupa (2001), and Kennicutt (1983), we should add roughly (0.15, -0.15, -0.35) dex to the stellar M*/L ratios predicted using the scaled Salpeter IMF (Figure (1)).

In Fig. (1), we contrast M_*/L ratios of the four gravity models against the predictions of SPS. In each frame the solid line is the best fit to the data points obtained from the analysis of the rotation curves. The theoretical SPS prediction of [2,3], for different IMF's are also plotted. The plots of NLNL and MOND have almost the same slopes as the SPS plot. As far as the vertical shift is concerned NLNL is in agreement with Kroupa's IMF, while MOND is somewhere between the standard Salpeter and the scaled Salpeter IMF projections. The cases of MOG and CDM are different. Particularly MOG has much different slope than any of SPS models of varying IMF.

The conclusion is the NLNL and MOND gravity reproduce the color-M/L relation of SPS satisfactorily, thought with different IMF's. Predictions of MOG and CDM are not reconcilable with SPS projections. We maintain that a) the SPS scheme can differentiate between different gravity models and b) the two together can choose between different IMF's. The mere fact that a gravity theory reproduces the observed rotation curves satisfactorily does not tell the whole story.

V. CONCLUDING REMARKS

A number of alternative theories are capable of reproducing the rotation curves of spirals with remarkable details, a nontrivial fact that deserves deliberations. In this paper we use three gravitational theory, modified Newtonian dynamics (MOND), modified gravity (MOG), nonlocal nonlinear gravity model (NLNL), Newtonian gravity plus cold dark matter (CDM) halo to deduce the dynamics of a wide range of high and low brightness galaxy types, and to check the results against observations.

One main feature of the present work is the construction of rotation curves with only one free adjustable parameter, the stellar mass-to-light ratio. This is in contrast to cold dark matter models, where for example, to accommodate an extended halo, one requires two additional parameters, to describe the core size of the halo and its asymptotic circular speed.

Stellar M^*/L ratios play an important role in the mass decomposition of galaxies. Theoretical considerations based on stellar population synthesis (SPS) models impose a constrain on M^*/L ratios: Redder galaxies should have larger M^*/L's. We confirm this finding; NLNL mass-to-light ratios correlate with galaxy colors as projected by SPS models using Kroupa IMF. This is noteworthy, as there is no explicit or implicit connection between the basic tenets of the SPS and NLNL theory. On the other hand, we do not support the no-correlation prediction of MOG and CDM scenarios.

SPS predictions of M^*/L's are sensitive to the adopted initial mass functions (IMF). The M^*/L ratios inferred from the Salpeter IMF are notably greater than those of Kroupa. Our values are in better agreement with those obtained from Kroupa's IMF than with those obtained through Salpeter's [2]. They are lower, in general, and implies lesser disk masses.

Both MOND's and our proposed NLNL gravitation have empirical beginnings and rely heavily on the Tully-Fisher relation, itself an empirical finding. Nonetheless, we think, a) logic-wise, the NLNL approach is a simpler alternative gravitation, and b) prediction-wise, it produces more realistic mass-to-light ratios than MOND.

[1] Begeman, K.G., Broeils, A.H., and Sanders, R.H. 1991 MNRAS, 249, 523
[2] Bell E. F., and de Jong R. S. 2001, ApJ, 550, 212
[3] Bell, E. F., McIntosh, D. H., Katz, N., and Weinberg, M. D. 2003, ApJS, 149, 289
[4] Brownstein, J. R., and Moffat, J. W. 2006, ApJ, 636, 721
[5] Capozziello, S., Cardone, V. F., and Troisi, A. 2007, 375, 1423
[6] Carroll, S., Duvvuri, V., Trodden, M., and Turner, M. 2004, Phys. Rev. D, 70, 2839
[7] Chemin, L., Carignan, C., Foster, T. 2009, ApJ, 705, 1395
[8] Haghi, H., and Rahvar, S. 2010, IJTP, 49, 1004.
[9] Kennicutt, R.C. 1983, ApJ, 272, 54
[10] Kroupa, P., 2001 MNRAS, 322, 231.
[11] McGaugh, S.S., and de Blok, W.J.G. 1998, ApJ, 499: 66-81
[12] Milgrom, M. 1983, ApJ, 270, 365
[13] Moffat, J. W. 2006, JCAP, 2006, 004
[14] Portinari, L., Sommer-Larsen, J., and Tantalo, R. 2004, MNRAS, 347, 691
[15] Salpeter, E. E. 1955, ApJ, 121, 161.
[16] Sanders R. H. 1996, ApJ, 473, 117
[17] Sanders, R.H., andVerheijen M.A.W., 1998, ApJ, 503, 97-108
[18] Sanders R. H., and McGaugh S. S. 2002, ARA&A, 40, 263
[19] Sobouti, Y. 2007, A&A, 464, 921
[20] Sobouti, Y., Hasani Zonoozi, A., and Haghi, H. 2009, A&A, 507, 635, arxiv:0906.0668[gr-qc] (paperI)
[21] Tully, R. B., and Fisher, J. R. 1977, A&A, **54**, 661

Galaxy	Type	B-V	$(\frac{M^*}{L})_{NLNL}$	χ^2_{NLNL}	$(\frac{M^*}{L})_{MOND}$	χ^2_{MOND}	$(\frac{M^*}{L})_{MOG}$	χ^2_{MOG}	$(\frac{M^*}{L})_{CDM}$	χ^2_{CDM}
M 33	Sc	0.55	0.3	*39.25	0.6	30.22	0.8	45	1	152
NGC 300	Sc	0.58	0.4	2.35	0.7	2.26	1.3	2.54	0.57	0.72
NGC 2903	Sc	0.55	1.7	4.79	3.0	6.07	2.4	7.18	1.4	2.3
NGC 3726	SBc	0.45	0.5	4.60	1.0	3.47	0.9	5	1.4	2.66
NGC 3769	SBb	0.64	0.7	0.70	1.2	0.75	1.4	1.06	0.75	0.33
NGC 3877	Sc	0.68	0.9	2.60	1.7	2.66	1.5	3.07	0.35	0.86
NGC 3893	Sc	0.56	1.0	1.88	1.7	4.12	1.6	2.76	0.75	0.7
NGC 3949	Sbc	0.39	0.5	3.97	0.8	5.34	0.8	5	0.25	0.78
NGC 3953	SBbc	0.71	1.5	0.47	2.7	1.13	2.2	0.44	1.55	0.28
NGC 3972	Sbc	0.55	0.8	3.08	1.5	3.22	1.6	2.85	0.4	0.36
NGC 3992	SBbc	0.72	2.7	1.02	4.9	0.65	3.6	2.08	1.98	0.51
NGC 4013	sb	0.83	1.8	2.24	3.1	1.37	2.7	2.05	3.22	1.13
NGC 4051	SBbc	0.62	0.7	0.90	1.2	0.88	1.1	0.76	1	0.54
NGC 4085	Sc	0.47	0.6	*6.03	1.1	6.84	1.1	6.94	0.08	0.8
NGC 4088	Sbc	0.51	0.6	1.75	1.1	1.49	1	1.97	0.64	0.88
NGC 4100	Sbc	0.63	1.3	1.58	2.4	2.07	2.1	2.12	0.75	0.85
NGC 4138	Sa	-	2.0	0.81	3.5	1.61	3.2	1.2	2.37	0.8
NGC 4157	Sb	0.66	1.3	0.87	2.4	0.92	2	0.84	1.2	0.6
NGC 4217	Sb	0.77	1.2	2.90	2.2	3.95	1.9	2.63	0.82	1.1
NGC 4389	SBbc	-	0.2	*5.57	0.4	5.36	0.6	6.33	0.25	0.63
NGC 5585	SBcd	0.46	0.3	*10.46	0.5	10.43	1.1	16.87	0.4	2
NGC 6946	SABcd	0.40	0.3	*21.61	0.5	11.46	0.5	31.75	0.2	1.48
NGC 7793	Scd	0.63	0.6	1.48	1.2	1.48	1.5	1.02	1.08	0.7
UGC 6399	Sm	-	0.6	0.10	1	0.16	1.8	0.04	1.7	0.02
UGC 6973	Sab	-	1.7	*10.57	2.7	20.46	2.6	20.24	1.66	0.2
NGC 801^b	Sc	0.61	0.8	*14.15	1.2	23.14	1.2	23.9	0.64	4.84
NGC 2998^b	SBc	0.45	0.7	2.96	1.2	2.64	1	2.35	1.08	1
NGC 5371^b	S(B)b	0.65	0.9	*6.93	1.6	10.00	1.3	6.65	1.37	2.76
NGC 5533^b	Sab	0.77	2.1	1.11	3.3	2.33	3.8	8.5	2.9	0.7
NGC 5907^b	Sc	0.78	2.1	4.27	4	2.93	3	6.1	1.66	2.48
NGC 6674^b	SBb	0.57	1.6	*6.64	2.7	10.96	2.6	41.06	1.23	5.54
UGC 2885^b	Sbc	0.47	0.9	3.04	1.5	2.80	1.4	6.64	0.26	2.02
DDO 168	SO	0.32	0.1	*21.56	0.2	11.5	1.5	14.64	0.5	3.98
NGC 247	SBc	0.54	0.7	4.16	1.1	3.71	2	3.74	1.63	2.72
NGC 1560	Sd	0.57	0.3	1.52	1.1	3.35	4.6	10.56	4	2.73
NGC 3917	Scd	0.60	0.7	4.58	1.3	4.49	1.4	4.03	0.3	1.17
NGC 4010	SBd	0.54	0.8	1.76	1.4	1.81	1.7	1.16	1.07	0.95
NGC 4183	Sa	0.39	0.4	1.09	0.7	0.98	1	1.54	1.57	0.11
UGC 128	Sdm	0.60	0.6	0.63	1.1	0.48	1.9	0.36	1	0.06
UGC 6446	Sd	0.39	0.3	4.49	0.5	2.30	1.2	2.35	0.8	0.3
UGC 6667	Scd	0.65	0.6	0.69	1	0.94	1.9	0.59	0.9	0.12
UGC 6917	SBd	0.53	0.8	0.72	1.4	0.64	2	0.84	0.78	0.16
UGC 6923	Sdm	-	0.4	1.03	0.8	1.17	1.4	2.28	0.25	0.31
UGC 6930	SBd	0.59	0.4	0.54	0.8	0.28	1.2	0.34	0.37	0.06
UGC 6983	SBcd	0.45	0.9	1.68	1.7	1.30	2.3	1.9	0.53	0.38
UGC 7089	Sdm	-	0.1	0.25	0.2	0.14	0.6	0.11	0.5	0.11

TABLE I. Best-fit χ^2 and M_*/L values of 46 HSB and LSB galaxies in NLNL, MOND, MOG, and CDM models. Hubble types are from NED database. Bulged galaxies are marked by a superscript ^{b}. Surface brightness types are approximate. Starred entries have anomalously large χ^2 and, presumably, are not compatible with the assumption of constant M_*/L ratio.

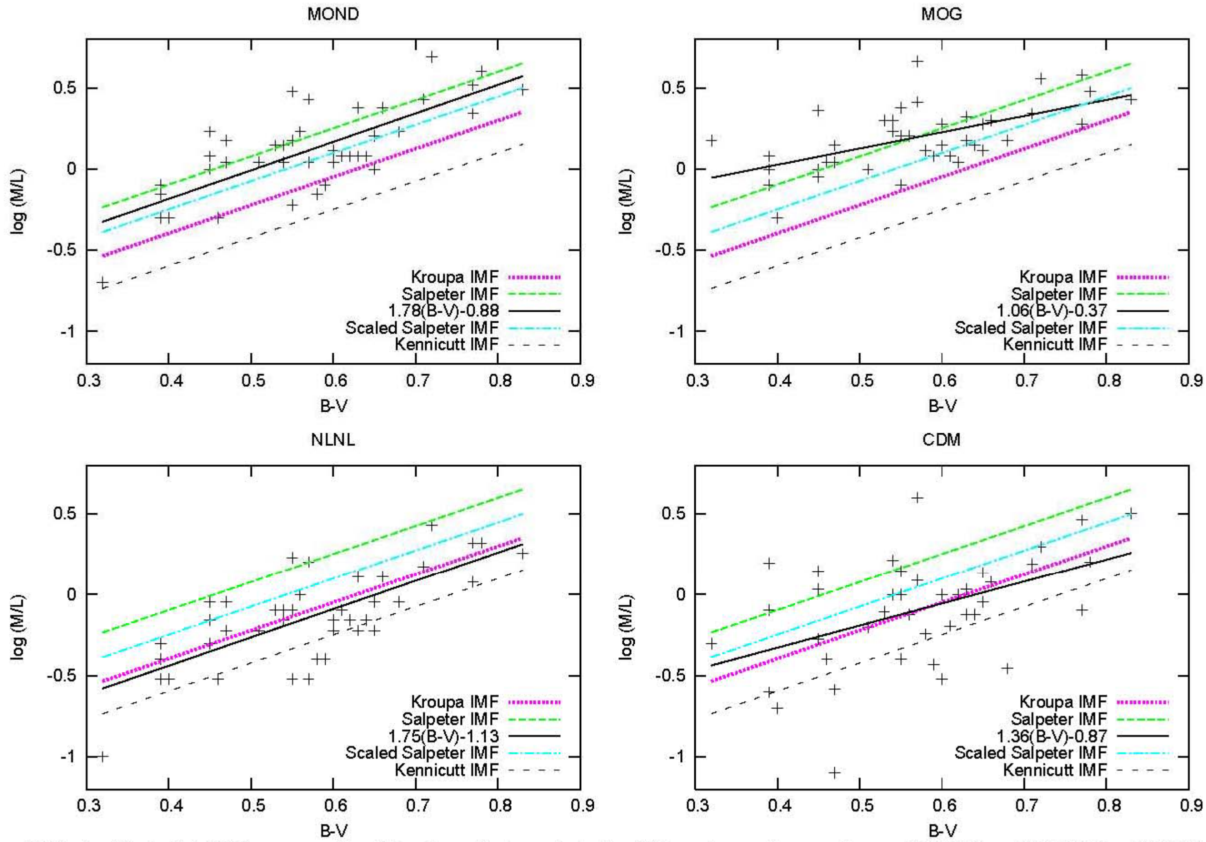

FIG. 1. Plot of M^*/L versus $B-V$ color. Data points in different panels are those of NLNL, of MOND, of MOG, and of CDM plus Newtonian gravity respectively. The solid lines are the best fit lines through the different gravity models predictions. The slopes and the zero-points of best-fitted lines are shown in the legend. The other lines denote the theoretical prediction of stellar population synthesis model with different IMF used and are indicated in the legend. All of the lines have the same slope but have different zero-pint values as represented in bellow eq. 5. Non of the SPS models can reproduce the MOG prediction for the color-M^*/L correlation.

Holographic modified gravity

M.R. Setare *
Department of Science, University of Kurdistan, Pasdaran Ave., Sanandaj, Iran

Abstract

In this paper we study cosmological application of holographic dark energy density in the modified gravity framework. We employ the holographic model of dark energy to obtain the equation of state for the holographic energy density in spatially flat universe. Our calculation show, taking $\Omega_\Lambda = 0.73$ for the present time, it is possible to have w_Λ crossing -1. This implies that one can generate phantom-like equation of state from a holographic dark energy model in flat universe in the modified gravity cosmology framework. Also we develop a reconstruction scheme for the modified gravity with $f(R)$ action.

*E-mail: rezakord@ipm.ir

1 Introduction

Nowadays it is strongly believed that the universe is experiencing an accelerated expansion. Recent observations from type Ia supernovae [1] in associated with Large Scale Structure [2] and Cosmic Microwave Background anisotropies [3] have provided main evidence for this cosmic acceleration. In order to explain why the cosmic acceleration happens, many theories have been proposed. It is the most accepted idea that a mysterious dominant component, dark energy, with negative pressure, leads to this cosmic acceleration, though its nature and cosmological origin still remain enigmatic at present. An alternative proposal for dark energy is the dynamical dark energy scenario. The cosmological constant puzzles may be better interpreted by assuming that the vacuum energy is canceled to exactly zero by some unknown mechanism and introducing a dark energy component with a dynamically variable equation of state. The dynamical dark energy proposal is often realized by some scalar field mechanism which suggests that the energy form with negative pressure is provided by a scalar field evolving down a proper potential. In recent years, many string theorists have devoted to understand and shed light on the cosmological constant or dark energy within the string framework. The famous Kachru-Kallosh-Linde-Trivedi (KKLT) model [4] is a typical example, which tries to construct metastable de Sitter vacua in the light of type IIB string theory. Furthermore, string landscape idea [5] has been proposed for shedding light on the cosmological constant problem based upon the anthropic principle and multiverse speculation. Although we are lacking a quantum gravity theory today, we still can make some attempts to probe the nature of dark energy according to some principles of quantum gravity. The holographic dark energy model is just an appropriate example, which is constructed in the light of the holographic principle of quantum gravity theory. That is to say, the holographic dark energy model possesses some significant features of an underlying theory of dark energy. Currently, an interesting attempt for probing the nature of dark energy within the framework of quantum gravity is the so-called "holographic dark energy" proposal [6, 7, 8, 9]. It is well known that the holographic principle is an important result of the recent researches for exploring the quantum gravity (or string theory) [10]. This principle is enlightened by investigations of the quantum property of black holes. Roughly speaking, in a quantum gravity system, the conventional local quantum field theory will break down. The reason is rather simple: For a quantum gravity system, the conventional local quantum field theory contains too many degrees of freedom, and such many degrees of freedom will lead to the formation of black hole so as to break the effectiveness of the quantum field theory.

For an effective field theory in a box of size L, with UV cut-off Λ the entropy S scales extensively, $S \sim L^3\Lambda^3$. However, the peculiar thermodynamics of black hole [11] has led Bekenstein to postulate that the maximum entropy in a box of volume L^3 behaves nonextensively, growing only as the area of the box, i.e. there is a so-called Bekenstein entropy bound, $S \leq S_{BH} \equiv \pi M_P^2 L^2$. This nonextensive scaling suggests that quantum field theory breaks down in large volume. To reconcile this breakdown with the success of local quantum field theory in describing observed particle phenomenology, Cohen et al. [6] proposed a more restrictive bound – the energy bound. They pointed out that in quantum field theory a short distance (UV) cut-off is related to a long distance (IR) cut-off due to the limit set by forming a black hole. In other words, if the quantum zero-point energy density ρ_Λ is relevant to a UV cut-off Λ, the total energy of the whole system with size L should not exceed the mass of a black hole of the same size, thus we

have $L^3\rho_\Lambda \leq LM_P^2$. This means that the maximum entropy is in order of $S_{BH}^{3/4}$. When we take the whole universe into account, the vacuum energy related to this holographic principle [10] is viewed as dark energy, usually dubbed holographic dark energy. Such a holographic dark energy looks reasonable, since it may provide simultaneously natural solutions to both dark energy problems as demonstrated in Ref.[9]. The holographic dark energy model has been tested and constrained by various astronomical observations [12]. Furthermore, the holographic dark energy model has been extended to include the spatial curvature contribution, i.e. the holographic dark energy model in non-flat space [13]. Because the holographic energy density belongs to a dynamical cosmological constant, we need a dynamical frame to accommodate it instead of general relativity. Therefore it is worthwhile to investigate the holographic energy density in the framework of the Brans-Dicke theory [14, 15, 16, 17]. Einstein's theory of gravity may not describe gravity at very high energy. The simplest alternative to general relativity is Brans-Dicke scalar-tensor theory [18]. Modified gravity provides the natural gravitational alternative for dark energy [19]. Moreover, modified gravity present natural unification of the early-time inflation and late-time acceleration thanks to different role of gravitational terms relevant at small and at large curvature. Also modified gravity may naturally describe the transition from non-phantom phase to phantom one without necessity to introduce the exotic matter. But among the most popular modified gravities which may successfully describe the cosmic speed-up is $F(R)$ gravity. Very simple versions of such theory like $1/R$ [20] and $1/R + R^2$ [21] may lead to the effective quintessence/phantom late-time universe (to see solar system constraints on modified dark energy models refer to [23]). Another theory proposed as gravitational dark energy is scalar-Gauss-Bonnet gravity [22] which is closely related with low-energy string effective action.
In present paper, using the holographic model of dark energy in spatially flat universe, we obtain equation of state for holographic dark energy density in framework of modified gravity for a universe enveloped by R_h as the system's IR cut-off. The current available observational data imply that the holographic vacuum energy behaves as phantom-type dark energy, i.e. the equation-of-state of dark energy crosses the cosmological-constant boundary $w = -1$ during the evolution history. We show this phantomic description of the holographic dark energy in flat universe with $0.21 \leq c \leq 2.1$. Also we develop a reconstruction scheme for the modified gravity with $f(R)$ action, the known holographic energy density is used for this reconstruction.

2 Modified gravity and holographic dark energy

The action of modified gravity is given by

$$S = \int \sqrt{-g}d^4x[f(R) + L_m]. \tag{1}$$

where L_m is the matter Lagrangian density. The equivalent form of above action is [19]

$$S = \int d^4x\sqrt{-g}[P(\phi)R + Q(\phi) + L_m]. \tag{2}$$

where P and Q are proper functions of the scalar field ϕ. By the variation of the action (2) with respect to the ϕ, we obtain

$$P'(\phi)R + Q'(\phi) = 0 \tag{3}$$

which may be solved with respect to ϕ:

$$\phi = \phi(R) \tag{4}$$

By the variation of the action (2) with respect to the metric $g_{\mu\nu}$, one can obtain

$$\frac{-1}{2} g_{\mu\nu}[P(\phi)R + Q(\phi)] - R_{\mu\nu}P(\phi) + \nabla_\mu \nabla_\nu P(\phi) - g_{\mu\nu}\nabla^2 P(\phi) + \frac{1}{2}T_{\mu\nu} = 0 \tag{5}$$

where $T_{\mu\nu}$ is the energy-momentum tensor. The equations corresponding to standard spatially-flat FRW universe are

$$\rho = 6H^2 P(\phi) + Q(\phi) + 6H\frac{dP(\phi)}{dt} \tag{6}$$

$$p = -(4\dot{H} + 6H^2)P(\phi) - Q(\phi) - 2\frac{d^2P(\phi)}{dt^2} - 4H\frac{dP(\phi)}{dt} \tag{7}$$

where, p and ρ are the pressure and energy density due to the scalar field in the modified gravity framework. By combining (6) and (7) and deleting $Q(\phi)$, we find

$$p + \rho = -2\frac{d^2P(\phi)}{dt^2} + 2H\frac{dP(\phi)}{dt} - 4\dot{H}P(\phi) \tag{8}$$

Now we suggest a correspondence between the holographic dark energy scenario and the above modified dark energy model. The holographic energy density ρ_Λ is chosen to be

$$\rho_\Lambda = \frac{3c^2}{R_h^2} \tag{9}$$

where c is a constant, and R_h is the future event horizon given by

$$R_h = a\int_t^\infty \frac{dt}{a} = a\int_a^\infty \frac{da}{Ha^2} \tag{10}$$

The critical energy density, ρ_{cr}, is given by following relation

$$\rho_{cr} = 3H^2 \tag{11}$$

Now we define the dimensionless dark energy as

$$\Omega_\Lambda = \frac{\rho_\Lambda}{\rho_{cr}} = \frac{c^2}{R_h^2 H^2} \tag{12}$$

Using definition Ω_Λ and relation (11), $\dot{R}_h$ gets:

$$\dot{R}_h = R_h H - 1 = \frac{c}{\sqrt{\Omega_\Lambda}} - 1, \tag{13}$$

Let us consider the dark energy dominated universe. In this case the dark energy evolves according to its conservation law

$$\dot{\rho}_\Lambda + 3H(\rho_\Lambda + P_\Lambda) = 0 \tag{14}$$

By considering the definition of holographic energy density ρ_Λ, and using Eq.(13)one can find:

$$\dot{\rho_\Lambda} = \frac{-2}{R_h}\left(\frac{c}{\sqrt{\Omega_\Lambda}} - 1\right)\rho_\Lambda \tag{15}$$

Substitute this relation into Eq.(14) we obtain

$$w_\Lambda = -\left(\frac{1}{3} + \frac{2\sqrt{\Omega_\Lambda}}{3c}\right). \tag{16}$$

A direct fit of the present available SNe Ia data with this holographic model indicates that the best fit result is $c = 0.21$ [25]. Recently, by calculating the average equation of state of the dark energy and the angular scale of the acoustic oscillation from the BOOMERANG and WMAP data on the CMB to constrain the holographic dark energy model, the authors show that the reasonable result is $c \sim 0.7$ [26]. In the other hand, in the study of the constraints on the dark energy from the holographic connection to the small l CMB suppression, an opposite result is derived, i.e. it implies the best fit result is $c = 2.1$ [27]. Thus according to these studies $0.21 \leq c \leq 2.1$. Taking $\Omega_\Lambda = 0.73$ for the present time, in the case of $c = 0.21$, we obtain $w_\Lambda = -3.04$, in the other hand for $c = 2.1$, one can obtain, $w_\Lambda = -0.6$. Using Eq.(16), one can see that by considering $c \leq \sqrt{\Omega_\Lambda}$ we obtain $w_\Lambda \leq -1$. Therefore taking $\Omega_\Lambda = 0.73$ for the present time, it is possible to have w_Λ crossing -1.
As one can redefine the scalar field ϕ properly, we may choose

$$\phi = t. \tag{17}$$

Now using Eqs.(9), (16), one can rewrite Eq.(8) as

$$2\frac{d^2P(t)}{dt^2} - 2H\frac{dP(t)}{dt} + 4\dot{H}P(t) + 2\Omega_\Lambda H^2\left(1 - \frac{\sqrt{\Omega_\Lambda}}{c}\right) = 0 \tag{18}$$

In principle, by solving Eq.(18) we find the form of $P(\phi)$. Using Eqs. (6), (9), we also find the form of $Q(\phi)$ as

$$Q(\phi) = 3\Omega_\Lambda H^2 - 6H^2P(\phi) - 6H\frac{dP(\phi)}{dt} \tag{19}$$

3 Modified gravity and its reconstruction from the holographic dark energy

In this section we consider another approach [24] to realistic cosmology in holographic modified gravity. We start with general $f(R)$-gravity action (1) but without the matter term. For the spatially flat FRW universe we have

$$\rho = f(R) - 6\left(\dot{H} + H^2 - H\frac{d}{dt}\right)f'(R) \tag{20}$$

$$p = f(R) - 2\left(-\dot{H} - 3H^2 + \frac{d^2}{dt^2} + 2H\frac{d}{dt}\right)f'(R) \tag{21}$$

where

$$R = 6\dot{H} + 12H^2 \tag{22}$$

Again we use the holographic dark energy density and substitute Eq.(9) into Eq.(20)

$$3\Omega_\Lambda H^2 = f(R) - 6(\dot{H} + H^2 - H\frac{d}{dt})f'(R) \tag{23}$$

thus

$$f(R) = 3\Omega_\Lambda H^2 + 6(\dot{H} + H^2 - H\frac{d}{dt})f'(R) \tag{24}$$

Using Eqs.(9), (16), and substituting $f(R)$ into Eq.(21) one can obtain

$$2\frac{d^2}{dt^2}f'(R) - 2H\frac{d}{dt}f'(R) + 4\dot{H}f'(R) + 2\Omega_\Lambda H^2(1 - \frac{\sqrt{\Omega_\Lambda}}{c}) = 0 \tag{25}$$

or in another form

$$2(f'''\dot{R}^2 + f''\ddot{R}) - 2Hf''\dot{R} + 4\dot{H}f' + 2\Omega_\Lambda H^2(1 - \frac{\sqrt{\Omega_\Lambda}}{c}) = 0 \tag{26}$$

We shall consider the following simple solution

$$a = a_0(t_s - t)^{h_0}, \tag{27}$$

where a_0, h_0 and t_s are constant. Substituting Eq.(27) into Eq.(22), give us following relation for scalar curvature

$$R = \frac{12h_0^2 - 6h_0}{(t_s - t)^2} \tag{28}$$

Using Eqs.(10, 27) we can write

$$R_h = a_0(t_s - t)^{h_0}\int_t^{t_s}\frac{dt}{a_0(t_s - t)^{h_0}} = \frac{t_s - t}{1 - h_0} \tag{29}$$

Now using definition ρ_Λ and above relation we obtain the time behaviour of holographic dark energy as

$$\rho_\Lambda = \frac{3c^2}{R_h^2} = \frac{3c^2(1 - h_0)^2}{(t_s - t)^2} \tag{30}$$

Substituting the above ρ_Λ into Eq.(20), and using Eqs.(27,28) one can obtain

$$\frac{72h_0^2(1 - 2h_0)}{(t_s - t)^4}f''(R) - \frac{6h_0(h_0 - 1)}{(t_s - t)^2}f'(R) + f(R) = \frac{3c^2(1 - h_0)^2}{(t_s - t)^2} \tag{31}$$

Again we use Eq.(28) and rewrite the above differential equation as following

$$f''(R) + \frac{a}{R}f'(R) + \frac{b}{R^2}f(R) = \frac{d}{R} \tag{32}$$

where

$$a = \frac{h_0 - 1}{2}, \qquad b = \frac{1 - 2h_0}{2}, \qquad d = \frac{c^2(1 - h_0)^2}{4h_0} \tag{33}$$

The solution of differential equation (32) is given by

$$f(R) = C_1 R^{\frac{1}{2}\left(\frac{3-h_0}{2} - \sqrt{\frac{(h_0-3)^2}{4} + 4h_0 - 2}\right)} + C_2 R^{\frac{1}{2}\left(\frac{3-h_0}{2} + \sqrt{\frac{(h_0-3)^2}{4} + 4h_0 - 2}\right)} + \frac{c^2(1 - h_0)^2 R}{2h_0^2} \tag{34}$$

where C_1, C_2 are constant. Therefore, a consistent modified gravity whit holographic dark energy in flat space has the above form. Let us recall the two sufficient conditions which often lead to realistic models [23, 28]

$$\lim_{R\to 0} f(R) = 0, \tag{35}$$

this condition ensures the disappearance of the cosmological constant in the limit of flat space-time. One can see that (34) simply satisfy the above condition. In order that the accelerating expansion in the present universe could be generated, let us consider that $f(R)$ could be a small constant at present universe, that is,

$$f(R_0) = -2R_0, \qquad f'(R_0) \sim 0, \tag{36}$$

where $R_0 \sim (10^{-33}eV)^2$ is current curvature [23]. By impose the conditions (36) on the solution (34) we can obtain the constants C_1 and C_2 as following

$$C_1 = \frac{-R_0^{1-u}}{u+v}[2v + (v+1)\frac{c^2(1-h_0)^2}{2h_0^2}] \tag{37}$$

$$C_2 = \frac{R_0^{1-v}}{u+v}[2u - (1-u)\frac{c^2(1-h_0)^2}{2h_0^2}] \tag{38}$$

where

$$u = \frac{1}{2}\left(\frac{3-h_0}{2} - \sqrt{\frac{(h_0-3)^2}{4} + 4h_0 - 2}\right), \quad v = \frac{1}{2}\left(\frac{3-h_0}{2} + \sqrt{\frac{(h_0-3)^2}{4} + 4h_0 - 2}\right) \tag{39}$$

The model Eq.(34) is similar to the model of Eq.(12) in [29], similarly our model also leads to acceptable cosmic speed-up and is consistent with solar system tests.

4 Conclusions

Within the different candidates to play the role of the dark energy, the modified gravity, has emerged as a possible unification of dark matter and dark energy. In the present paper we have studied cosmological application of holographic dark energy density in the modified gravity framework. By considering the holographic energy density as a dynamical cosmological constant, we have obtained the equation of state for the holographic energy density in the modified gravity framework. We have shown if $c \leq \sqrt{\Omega_\Lambda}$, the holographic dark energy model also will behave like a phantom model of dark energy the amazing feature of which is that the equation of state of dark energy component w_Λ crosses -1. Hence, we see, the determining of the value of c is a key point to the feature of the holographic dark energy and the ultimate fate of the universe as well. Finally we have developed a reconstruction scheme for modified gravity with $f(R)$ action. We have considered the energy density in Eq.(20) in holographic form, then by assumption a simple solution as Eq.(27) we could obtain a differential equation for $f(R)$, the solution of this differential equation give us a modified gravity action which is consistent with holographic dark energy scenario.

References

[1] A. G. Riess *et al.* [Supernova Search Team Collaboration],
Astron. J. **116**, 1009 (1998) [astro-ph/9805201];
S. Perlmutter *et al.* [Supernova Cosmology Project Collaboration],
Astrophys. J. **517**, 565 (1999) [astro-ph/9812133];

P. Astier *et al.*,
Astron. Astrophys. **447**, 31 (2006) [astro-ph/0510447].

[2] M. Tegmark *et al.* [SDSS Collaboration],
Phys. Rev. D **69**, 103501 (2004) [astro-ph/0310723];

K. Abazajian *et al.* [SDSS Collaboration],
Astron. J. **128**, 502 (2004) [astro-ph/0403325];

K. Abazajian *et al.* [SDSS Collaboration],
Astron. J. **129**, 1755 (2005) [astro-ph/0410239].

[3] D. N. Spergel *et al.* [WMAP Collaboration],
Astrophys. J. Suppl. **148**, 175 (2003) [astro-ph/0302209];

D. N. Spergel *et al.*,
astro-ph/0603449.

[4] S. Kachru, R. Kallosh, A. Linde and S. P. Trivedi, Phys. Rev. D **68**, 046005 (2003) [hep-th/0301240].

[5] L. Susskind, hep-th/0302219.

[6] A. G. Cohen, D. B. Kaplan and A. E. Nelson, Phys. Rev. Lett. **82**, 4971 (1999) [hep-th/9803132].

[7] P. Horava and D. Minic, Phys. Rev. Lett. **85**, 1610 (2000) [hep-th/0001145];
S. D. Thomas, Phys. Rev. Lett. **89**, 081301 (2002).

[8] S. D. H. Hsu, Phys. Lett. B **594**, 13 (2004) [hep-th/0403052].

[9] M. Li, Phys. Lett. B **603**, 1 (2004) [hep-th/0403127].

[10] G. 't Hooft, gr-qc/9310026;
L. Susskind, J. Math. Phys. **36**, 6377 (1995) [hep-th/9409089].

[11] J. D. Bekenstein, Phys. Rev. D **7** (1973) 2333;
J. D. Bekenstein, Phys. Rev. D **49** (1994) 1912;
S. W. Hawking, Commun. Math. Phys. **43** (1975) 199;
S. W. Hawking, Phys. Rev. D **13** (1976) 191.

[12] Q. G. Huang and Y. G. Gong, JCAP **0408**, 006 (2004) [astro-ph/0403590];
K. Enqvist, S. Hannestad and M. S. Sloth, JCAP **0502** 004 (2005) [astro-ph/0409275];
J. Shen, B. Wang, E. Abdalla and R. K. Su, Phys. Lett. B **609** 200 (2005) [hep-th/0412227];
H. C. Kao, W. L. Lee and F. L. Lin, Phys. Rev. D **71** 123518 (2005) [astro-ph/0501487].

[13] Q. G. Huang and M. Li, JCAP **0408**, 013 (2004) [astro-ph/0404229].
K. Enqvist and M. S. Sloth, Phys. Rev. Lett. **93**, 221302 (2004) [hep-th/0406019];
K. Ke and M. Li, Phys. Lett. B **606**, 173 (2005) [hep-th/0407056];
Q. G. Huang and M. Li, JCAP **0503**, 001 (2005) [hep-th/0410095];
D. Pavon and W. Zimdahl, Phys. Lett. B **628**, 206 (2005) [gr-qc/0505020];
B. Wang, Y. Gong and E. Abdalla, Phys. Lett. B **624**, 141 (2005) [hep-th/0506069];
H. Kim, H. W. Lee and Y. S. Myung, Phys. Lett. B **632**, 605 (2006) [gr-qc/0509040];
S. Nojiri and S. D. Odintsov, Gen. Rel. Grav. **38**, 1285 (2006) [hep-th/0506212];
E. Elizalde, S. Nojiri, S. D. Odintsov and P. Wang, Phys. Rev. D **71**, 103504 (2005) [hep-th/0502082];
B. Hu and Y. Ling, Phys. Rev. D **73**, 123510 (2006) [hep-th/0601093];
H. Li, Z. K. Guo and Y. Z. Zhang, Int. J. Mod. Phys. D **15**, 869 (2006) [astro-ph/0602521];
M. R. Setare, Phys. Lett. B **642**, 1 (2006) [hep-th/0609069];
M. R. Setare, Phys. Lett. **B642**, 421, (2006) [hep-th/0609104];
M. R. Setare, J. Zhang, X. Zhang, JCAP 0703, 007, (2007);
M. R. Setare, Eur. Phys. J. C **50**, 991, (2007);
M. R. Setare, JCAP, 0701, 023 (2007);
M. R. Setare, Phys. Lett. B **648**, 329, (2007).

[14] Y. Gong, Phys. Rev. D, **70**, 064029, (2004).

[15] H. Kim, H. W. Lee, and Y. S. Myung, Phys. Lett. B **628**, 11, (2005).

[16] D. F. Torres, Phys. Rev. **D66**, 043522, (2002).

[17] M. R. Setare, Phys. Lett. B **644**, 99, (2007).

[18] C. Brans and C. H. Dicke, Phys. Rev. **124**, 925 (1961).

[19] S. Nojiri, S. D. Odintsov, H. Stefancic, Phys. Rev. D **74**, 086009, (2006); S. Nojiri, S. D. Odintsov, J. Phys. A **40**, 6725, (2007); G. Cognola, E. Elizalde, S. Nojiri, S. D. Odintsov and S. Zerbini, Phys. Rev. **D75** , 086002, (2007); S. Nojiri and , S. D. Odintsov, J. Phys. Conf. Ser.66, 012005, (2007).

[20] S. Capozziello, Int. J. Mod. Phys. D 11, 483 (2002); S. Capozziello, S. Carloni and A. Troisi, arXiv:astro-ph/0303041; S. M. Carroll, V. Duvvuri, M. Trodden and S. Turner, Phys. Rev. D 70 (2004) 043528.

[21] S. Nojiri and S. D. Odintsov, Phys. Rev. D 68, 123512 (2003).

[22] S. Nojiri, S. D. Odintsov and M. Sasaki, Phys. Rev. D 71, 123509 (2005); S. Nojiri, S. D. Odintsov and M. Sami, Phys. Rev. **D** 74, 046004, (2006); B. M. N. Carter, I. P. Neupane, Phys. Lett. **B638**, 94, (2006); B. M. N. Carter, and I. P. Neupane, JCAP 0606, 004, (2006); J. W. Moffat, and V. T. Toth . arXiv:0710.0364 [astro-ph].

[23] S. Nojiri, S. D. Odintsov, 0707.1941v2 [hep-th];S. Nojiri, S. D. Odintsov, 0710.1738v2 [hep-th]; G. Cognola, E. Elizalde, S. Nojiri, S. D. Odintsov, L. Sebastiani, S. Zerbini, 0712.4017v1 [hep-th].

[24] S. Capozziello, S. Nojiri, S. D. Odintsov and A. Troisi, Phys. Lett. **B** 639, 135, (2006) ; S. Nojiri and S. D. Odintsov, Phys. Rev. **D74**, 086005, (2006).

[25] Q. G. Huang, Y. Gong, JCAP, 0408, (2004),006.

[26] H. C. Kao, W. L. Lee and F. L. Lin, astro-ph/0501487.

[27] J. Shen, B. Wang, E. Abdalla and R. K. Su, hep-th/0412227.

[28] W. Hu and I. Sawicki, 0705.1158[astro-ph].

[29] S. Nojiri and S. D. Odintsov, Int. J. Geom. Meth. Mod. Phys. 4, 115, (2007).

The effect of twisted magnetic annulus on the period ratio P_1/P_2 of kink MHD waves

K. Karami[1], K. Bahari[2] and S. Nasiri[2,3]
[1] *Department of Physics, University of Kurdistan, Pasdaran Street, Sanandaj, Iran*
[2] *Institute for Advanced Studies in Basic Sciences (IASBS), Gava Zang, Zanjan, Iran*
[3] *Department of Physics, Zanjan University, Zanjan, Iran*

The standing kink magnetohydrodynamic (MHD) modes in a zero-beta cylindrical compressible magnetic flux tube modelled as a twisted core surrounded by a magnetically twisted annulus, both embedded in a straight ambient external field is considered. The dispersion relation is derived and solved analytically and numerically to obtain the frequencies of the kink MHD waves. The main result is that the twisted magnetic annulus does affect the period ratio P_1/P_2 of the kink modes.

I. INTRODUCTION

Transverse coronal loop oscillations triggered by explosive events, such as flares or filament eruptions, were first identified by Aschwanden et al. (1999) and Nakariakov et al. (1999) using the observations of TRACE (the Transition Region And Coronal Explorer). These oscillations have been interpreted as kink MHD modes of a cylindrical coronal flux tube by Nakariakov et al. (1999).

One of important tools in the coronal seismology is determination of the period ratio P_1/P_2 between the period P_1 of the fundamental mode and the period P_2 of its first harmonic. In an homogeneous medium this ratio is exactly 2, but in a more complex configuration it is shifted to lower values. Verwichte et al. (2004), using the observations of TRACE, have identified the fundamental and its first harmonic of the standing transverse kink mode in two coronal loops. The period ratios observed by Verwichte et al. (2004) are 1.81±0.25 and 1.64±0.23. However, these values were corrected with the improvement of the observational error bars to 1.82±0.08 and 1.58±0.06, respectively, by Van Doorsselaere, Nakariakov & Verwichte (2007). Also Verth, Erdélyi & Jess (2008) added some further corrections by considering the effects of loop expansion and estimated a period ratio of 1.54. All these values clearly differ from 2. This may be caused by different factors such as the effects of curvature (see e.g. Van Doorsselaere et al. 2004), leakage (see De Pontieu, Martens & Hudson 2001), density stratification in the loops (see e.g. Andries et al. 2005; Erdélyi & Verth 2007; Karami & Asvar 2007; Safari, Nasiri & Sobouti 2007; Karami, Nasiri & Amiri 2009), magnetic field expansion (see Verth & Erdélyi 2008; Ruderman, Verth & Erdélyi 2008; Verth, Erdélyi & Jess 2008) and magnetic twist (see e.g. Erdélyi & Carter 2006; Erdélyi & Fedun 2006; Karami & Barin 2009).

The twisted magnetic tubes have been investigated in ample detail by Bennett, Roberts & Narain (1999), Klimchuk, Antiochos & Norton (2000), Mikhalyaev & Solov'ev (2005) and Carter & Erdélyi (2007, 2008). For a good review see Karami & Barin (2009).

Ruderman (2007) studied the nonaxisymmetric oscillations of a compressible zero-beta thin twisted magnetic tube surrounded with the straight and homogeneous magnetic field taking the density stratification into account. Using the asymptotic analysis he showed that the eigenmodes and eigenfrequencies of the kink and fluting oscillations are described by a classical Sturm–Liouville problem. The main result of Ruderman (2007), which also has been already obtained by Goossens, Hollweg & Sakurai (1992), was that the twist does not affect the kink mode.

Karami & Barin (2009) studied both the oscillations and damping of standing MHD surface and hybrid waves in coronal loops in presence of twisted magnetic field. They considered a straight cylindrical incompressible flux tube with magnetic twist just in the annulus and straight magnetic field in the internal and external regions. They showed that both the frequencies and damping rates of both the kink and fluting modes increase when the twist parameter increases. They obtained that the period ratio P_1/P_2 of the fundamental and first-overtone for both the kink and fluting surface modes are lower than 2 (for untwisted loop) in presence of the twisted magnetic field.

In the present work, our aim is to investigate the effect of the twisted magnetic annulus on the frequencies of the kink MHD waves in the coronal loops to justify the deviation of the period ratio P_1/P_2 from 2 observed by the TRACE. This paper is organized as follows. In Section II we use the asymptotic analysis obtained by Ruderman (2007) to derive the equations of motion. In Section III, using the relevant boundary conditions, we obtain the dispersion relation. In Section IV, we give numerical results. Section V is devoted to conclusions.

II. EQUATIONS OF MOTION

The linearized MHD equations for a zero-beta plasma are

$$\frac{\partial \delta \mathbf{v}}{\partial t} = \frac{1}{4\pi\rho}[(\nabla \times \delta \mathbf{B}) \times \mathbf{B} + (\nabla \times \mathbf{B}) \times \delta \mathbf{B}], \tag{1}$$

$$\frac{\partial \delta \mathbf{B}}{\partial t} = \nabla \times (\delta \mathbf{v} \times \mathbf{B}), \tag{2}$$

- The background magnetic field is assumed to be

$$\mathbf{B} = \begin{cases} \mathbf{B}_{\rm i} = (0, A_{\rm i} r, B_{z\rm i}(r)), & r < a, \\ \mathbf{B}_0 = (0, A_0 r, B_{z0}(r)), & a < r < R, \\ \mathbf{B}_{\rm e} = (0, 0, B_{z\rm e}), & r > R, \end{cases} \tag{3}$$

where $A_{\rm i}$, A_0, $B_{z\rm e}$ are constant and a, R are radii of the core and tube, respectively. From both the equilibrium equation, i.e. $\frac{dB^2}{dr} = -\frac{2B_\phi^2}{r}$, and the continuity condition of the magnetic pressure across the boundaries of the tube, i.e. $B_{\rm i}^2(a) = B_0^2(a)$, $B_0^2(R) = B_{\rm e}^2(R)$, the z-component of the equilibrium magnetic field can be obtained as

$$\begin{aligned} B_{z\rm i}^2(r) &= B_0^2 + A_{\rm i}^2(a^2 - 2r^2), \\ B_{z0}^2(r) &= B_0^2 + A_0^2(a^2 - 2r^2), \\ B_{z\rm e}^2 &= B_0^2 + A_0^2(a^2 - R^2), \end{aligned} \tag{4}$$

where B_0 is an integration constant. The above magnetic field configuration in the absence of the annulus is the same as the background magnetic field considered by Ruderman (2007).

- ρ is constant over the loop but different in the interior, annulus and exterior regions and denoted by $\rho_{\rm i}$, ρ_0 and $\rho_{\rm e}$, respectively.
- Tube geometry is a circular with cylindrical coordinates, (r, ϕ, z).
- There is no initial steady flow over the tube.
- t-, ϕ- and z- dependence for any of the components $\delta\mathbf{v}$ and $\delta\mathbf{B}$ is $\exp\{{\rm i}(m\phi + k_z z - \omega t)\}$. Where $k_z = l\pi/L$, L is length of the tube, and $l = (1, 2, \cdots)$, $m = (0, 1, 2, \cdots)$ are the longitudinal and azimuthal mode numbers, respectively.

Here like Ruderman (2007), we consider $\epsilon := \frac{Aa}{B_0} \sim k_z a \ll 1$ which is in good agreement with the observations and also look for low frequency eigenmodes. Following the second order perturbation method in terms of ϵ given by Ruderman (2007), solutions of Eqs. (1)-(2) in terms of $\delta P = \frac{\mathbf{B}\cdot\delta\mathbf{B}}{4\pi}$, the Eulerian perturbation in the magnetic pressure, and $\xi_r = -\delta v_r/{\rm i}\omega$, the Lagrangian perturbation in the radial displacement, for the interior and annulus regions yield

$$\delta P(r) = \frac{r}{m^2}\Big(\rho\omega^2 - \frac{B_0^2}{4\pi}F^2\Big)\frac{{\rm d}(r\xi_r)}{{\rm d}r} + \Big(\frac{B_0 A F}{2\pi m}\Big) r\xi_r, \tag{5}$$

$$\frac{\rm d}{{\rm d}r}\Big(r\frac{{\rm d}(r\xi_r)}{{\rm d}r}\Big) - m^2\xi_r = 0, \tag{6}$$

where $F = k_z + m\frac{A}{B_0}$. Equations (5) and (6) are same as Eqs. (19) and (21), respectively, in Ruderman (2007).

In the interior and annulus regions, solutions of Eq. (6) are

$$\xi_r(r) = \begin{cases} \alpha r^{m-1}, & r < a, \\ \beta r^{m-1} + \gamma r^{-m-1}, & a < r < R, \end{cases} \tag{7}$$

and solutions for $\delta P(r)$ are obtained from substituting Eq. (7) in (5) as

$$\delta P(r) = \Big(\rho_{\rm i}\omega^2 - \frac{B_0^2 F_{\rm i}^2}{4\pi} + \frac{B_0 A_{\rm i} F_{\rm i}}{2\pi}\Big)\frac{\alpha r^m}{m}, r < a, \tag{8}$$

$$\delta P(r) = \Big(\rho_0\omega^2 - \frac{B_0^2 F_0^2}{4\pi} + \frac{B_0 A_0 F_0}{2\pi}\Big)\frac{\beta r^m}{m} - \Big(\rho_0\omega^2 - \frac{B_0^2 F_0^2}{4\pi} - \frac{B_0 A_0 F_0}{2\pi}\Big)\frac{\gamma r^{-m}}{m}, a < r < R. \tag{9}$$

For the exterior region, $r > R$, we obtain

$$\frac{{\rm d}^2\delta P}{{\rm d}r^2} + \frac{1}{r}\frac{{\rm d}\delta P}{{\rm d}r} - \Big(k'^2 + \frac{m^2}{r^2}\Big)\delta P = 0, \tag{10}$$

$$\xi_r(r) = -\frac{4\pi}{k'^2 B_0^2}\frac{{\rm d}\delta P}{{\rm d}r}, \tag{11}$$

where

$$k'^2 = k_z^2 - \frac{4\pi\rho_e\omega^2}{B_0^2}. \tag{12}$$

Equations (10) and (11) are same as Eqs. (26) and (25a), respectively, in Ruderman (2007). In the exterior region, $r > R$, the waves should be evanescent. Solutions are

$$\delta P(r) = \varepsilon K_m(k'r), \qquad k'^2 > 0, \tag{13}$$

$$\xi_r(r) = -\varepsilon\frac{4\pi}{k' B_0^2}K'_m(k'r), \tag{14}$$

where K_m is the modified Bessel function of the second kind and a prime on K_m indicates a derivative with respect to its appropriate argument. The coefficients α, β, γ and ε in Eqs. (7), (8), (9), (13) and (14) are determined by the boundary conditions.

III. BOUNDARY CONDITIONS AND DISPERSION RELATION

Following Ruderman (2007), at the perturbed tube boundary the plasma displacement in the radial direction and the magnetic pressure have to be continuous as

$$\xi_{r\mathrm{i}}\Big|_{r=a} = \xi_{r0}\Big|_{r=a}, \qquad \xi_{r0}\Big|_{r=R} = \xi_{r\mathrm{e}}\Big|_{r=R}, \tag{15}$$

$$\begin{aligned} \delta P_\mathrm{i} - \frac{B_{\phi\mathrm{i}}^2}{4\pi a}\xi_{r\mathrm{i}}\Big|_{r=a} &= \delta P_0 - \frac{B_{\phi 0}^2}{4\pi a}\xi_{r0}\Big|_{r=a}, \\ \delta P_0 - \frac{B_{\phi 0}^2}{4\pi R}\xi_{r0}\Big|_{r=R} &= \delta P_\mathrm{e}\Big|_{r=R}. \end{aligned} \tag{16}$$

Using the above boundary conditions and the solutions given by Eqs. (7), (8), (9) for the internal and annulus regions and Eqs. (13), (14) for the exterior region, the dispersion relation is derived as

$$\begin{aligned} &\Big[\frac{4\pi}{B_0^2}\frac{R}{k'}\frac{K_m'(k'R)}{K_m(k'R)}\Xi_m^0\Xi_m - \Xi_m^\mathrm{i}\Big]\Big[1-\Big(\frac{a}{R}\Big)^{2m}\Big] \\ &-\frac{4\pi}{B_0^2}\frac{R}{k'}\frac{K_m'(k'R)}{K_m(k'R)}\Xi_m^\mathrm{i}\Big[\Xi_m^0 - \Big(\frac{a}{R}\Big)^{2m}\Xi_m\Big] \\ &+\Big[\Xi_m - \Big(\frac{a}{R}\Big)^{2m}\Xi_m^0\Big] = 0, \end{aligned} \tag{17}$$

with

$$\begin{aligned} \Xi_m^j = &\frac{1}{m}\Big(\rho_j\omega^2 - \frac{B_0^2k_z^2}{4\pi}\Big) \\ &+\frac{A_j}{4\pi m}(2B_0k_z + mA_j)(1-m), \end{aligned} \tag{18}$$

$$\begin{aligned} \Xi_m = &-\frac{1}{m}\Big(\rho_0\omega^2 - \frac{B_0^2k_z^2}{4\pi}\Big) \\ &+\frac{A_0}{4\pi m}(2B_0k_z + mA_0)(1+m), \end{aligned} \tag{19}$$

where in Ξ_m^j, the superscript j stands for i and 0 corresponding to the interior and annulus regions, respectively.

Note that if we remove the annulus region, i.e. setting $a = R$, then the four boundary conditions, Eqs. (15)-(16), reduce to two boundary conditions and finally the dispersion relation, using the thin flux tube approximation for $K_m(x) \propto x^{-m}$ at small x, yields

$$\omega^2 = C_k^2\Big\{k_z^2 + \frac{A_\mathrm{i}(m-1)}{2B_0^2}(2B_0k_z + A_\mathrm{i}m)\Big\}, \tag{20}$$

where $C_k^2 = \frac{B_0^2}{2\pi(\rho_\mathrm{i}+\rho_\mathrm{e})}$. Equation (20) is same as Eq. (40) in Ruderman (2007). The main result of Ruderman (2007) is that the twist does not affect the kink modes and Eq. (20) shows that we get the same frequencies as in the case that $A_\mathrm{i} = 0$. This result also has been already obtained by Goossens, Hollweg & Sakurai (1992). Note that Eq. (17) shows that even in the presence of annulus, the internal twist does not affect the kink ($m = 1$) modes. Because the internal twist, A_i, only appears in Eq. (18) and when $m = 1$ then it has no contribution.

In Section IV, using the numerical solution of the dispersion relation, Eq. (17), we show that the twisted annulus region, which adds a new boundary to the system, does affect the frequencies of the kink modes.

IV. NUMERICAL RESULTS

The effect of twisted magnetic annulus on the frequencies is calculated by the numerical solution of the dispersion relation, Eq. (17). The results show that the frequencies of the fundamental and first-overtone ($l = 1, 2$) kink ($m = 1$) surface modes increase with increasing the twist parameter. The period ratio of the fundamental and first-overtone, ($l = 1, 2$) modes of the kink ($m = 1$) surface waves with $n = 1$ versus the twist parameter of the annulus is plotted in Fig. 1. Figure 1 shows that the period ratio with increasing the twist parameter of the annulus, for $n = 1$ decreases from 2 (for untwisted loop) down to a minimum and then increases. The period ratio for kink surface modes ($m = 1, n = 1$) with $a/R = 0.5$, for both B_ϕ/B_z=0.011 and 0.015 the ratio P_1/P_2 is 1.82. This is in good agreement with the period ratio observed by Van Doorsslaere, Nakariakov & Verwichte (2007), 1.82±0.08, deduced from the observations of TRACE.

V. CONCLUSIONS

Oscillations of standing kink MHD surface waves in coronal loops in the presence of the twisted magnetic annulus is studied. Using the perturbation method given by Ruderman (2007), the dispersion relation is obtained and solved numerically for obtaining the frequencies of the kink modes. Our dispersion relation confirms the results of other people for the different cases, for example in the absence of annulus region, the twist does not affect the kink modes which is same as the result obtained by Ruderman (2007). The main result of our work is that the twisted magnetic annulus does affect the period ratio of the kink modes. The period ratio for kink surface modes ($m = 1, n = 1$) with $a/R = 0.5$, for both twist parameters 0.011 and 0.015 is in accordance with the TRACE observations.

[1] Andries, J., Goossens, M., Hollweg, J. V., Arregui, I. & Van Doorsselaere, T., 2005, A&A, 430, 1109.
[2] Aschwanden, M. J., Fletcher, L., Schrijver, C. J. & Alexander, D., 1999, ApJ, 520, 880.
[3] Bennett, K., Roberts, B. & Narain, U., 1999, Sol. Phys., 185, 41.
[4] Carter, B. K. & Erdélyi, R., 2007, A&A, 475, 323.
[5] Carter, B. K. & Erdélyi, R., 2008, A&A, 481, 239.
[6] De Pontieu, B., Martens, P. C. H. & Hudson, H. S., 2001, ApJ, 558, 859.
[7] Erdélyi, R. & Carter, B. K., 2006, A&A, 455, 361.
[8] Erdélyi, R. & Fedun, V., 2006, Sol. Phys., 238, 41.

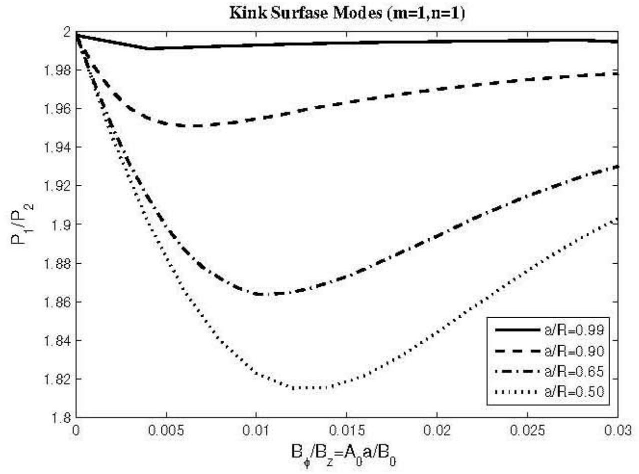

FIG. 1. The period ratio P_1/P_2 of the fundamental and its first-overtone kink ($m = 1$) surface modes with radial mode number $n = 1$ versus the twist parameter of the annulus for different relative core width $a/R = 0.5$ (dotted), 0.65 (dash–dotted), 0.9 (dashed) and 0.99 (solid).

[9] Erdélyi, R. & Fedun, V., 2007, Sol. Phys., 246, 101.
[10] Erdélyi, R. & Verth, G., 2007, A&A, 462, 743.
[11] Goossens, M., Hollweg, J. V. & Sakurai, T., 1992, Sol. Phys., 138, 233.
[12] Goossens, M., Terradas, J., Andries, J., Arregui, I. & Ballester, J. L., 2009, A&A, 503, 213.
[13] Karami, K. & Asvar, A., 2007, MNRAS, 381, 97.
[14] Karami, K. & Barin, M., 2009, MNRAS, 394, 521.
[15] Karami, K., Nasiri, S. & Amiri, S., 2009, MNRAS, 394, 1973.
[16] Klimchuk, J. A., Antiochos, S. K. & Norton, D., 2000, ApJ, 542, 504.
[17] McEwan, M. P., Donnelly, G. R., Díaz, A. J. & Roberts, B., 2006, A&A, 460, 893.
[18] Mikhalyaev, B. B. & Solov'ev, A. A., 2005, Sol. Phys., 227, 249.
[19] Nakariakov, V. M., Ofman, L., DeLuca, E. E., Roberts, B. & Davila, J. M., 1999, Science, 285, 862.
[20] Ruderman, M. S., 2007, Sol. Phys., 246, 119.
[21] Ruderman, M. S., Verth, G. & Erdélyi, R., 2008, ApJ, 686, 694.
[22] Safari, H., Nasiri, S. & Sobouti, Y., 2007, A&A, 470, 1111.
[23] Van Doorsselaere, T., Debosscher, A., Andries, J. & Poedts, S., 2004, A&A, 424, 1065.
[24] Van Doorsslaere, T., Nakariakov, V. M. & Verwichte, E., 2007, A&A, 473, 959.
[25] Verth, G. & Erdélyi, R., 2008, A&A, 486, 1015.
[26] Verth, G., Erdélyi, R. & Jess, D. B., 2008, ApJ, 687, L45.
[27] Verwichte, E., Nakariakov, V. M., Ofman, L. & Deluca, E. E., 2004, Sol. Phys., 223, 77.

The generalized second law in irreversible thermodynamics for the interacting dark energy in a non-flat FRW universe enclosed by the apparent horizon

K. Karami, S. Ghaffari, M.M. Soltanzadeh
Department of Physics, University of Kurdistan, Pasdaran Street, Sanandaj, Iran

We investigate the validity of the generalized second law in irreversible thermodynamics in a non-flat FRW universe containing the interacting dark energy with cold dark matter. The boundary of the universe is assumed to be enclosed by the dynamical apparent horizon. We show that for the present time, the generalized second law in nonequilibrium thermodynamics is satisfied for the special range of the energy transfer constants.

I. INTRODUCTION

Type Ia supernovae observational data suggest that the universe is dominated by two dark components: dark matter and dark energy. Dark matter (DM), a matter without pressure, is mainly used to explain galactic curves and large-scale structure formation, while dark energy (DE), an exotic energy with negative pressure, is used to explain the present cosmic accelerating expansion [1]. One of interesting issue in the cosmological context is the study of the generalized second law of thermodynamics for the different DE models like generalized Chaplygin gas [2], the holographic DE [3] and the new agegraphic DE [4], and so forth. Here our aim is to extend to work of Zhou et al. [5] and investigate the validity of the generalized second law in irreversible thermodynamics for the interacting DE with DM in a non-flat FRW universe enclosed by the dynamical apparent horizon [6].

II. INTERACTING DE AND DM

We consider the Friedmann-Robertson-Walker (FRW) metric for the non-flat universe as

$$\mathrm{d}s^2 = -\mathrm{d}t^2 + a^2(t)\left(\frac{\mathrm{d}r^2}{1-kr^2} + r^2\mathrm{d}\Omega^2\right), \quad (1)$$

where $k = 0, 1, -1$ represent a flat, closed and open FRW universe, respectively. The first Friedmann equation for the non-flat FRW universe takes the form

$$H^2 + \frac{k}{a^2} = \frac{8\pi}{3}\,(\rho_\Lambda + \rho_\mathrm{m}), \quad (2)$$

where we take $G = 1$. Also ρ_Λ and ρ_m are the energy density of DE and DM, respectively. Let us define, as usual, the fractional energy densities as

$$\Omega_\mathrm{m} = \frac{8\pi\rho_\mathrm{m}}{3H^2}, \quad \Omega_\Lambda = \frac{8\pi\rho_\Lambda}{3H^2}, \quad \Omega_k = \frac{k}{a^2H^2}, \quad (3)$$

then, the first Friedmann equation can be written as

$$\Omega_\mathrm{m} + \Omega_\Lambda = 1 + \Omega_k. \quad (4)$$

We consider a universe containing an interacting DE density ρ_Λ and the cold dark matter (CDM), with $\omega_\mathrm{m} = 0$. The energy equations for DE and CDM are

$$\dot{\rho}_\Lambda + 3H(1+\omega_\Lambda)\rho_\Lambda = -\Gamma, \quad (5)$$

$$\dot{\rho}_\mathrm{m} + 3H\rho_\mathrm{m} = \Gamma, \quad (6)$$

where following [5], we choose $\Gamma = 3H\lambda\rho_\Lambda$ as an interaction term with λ a small, dimensionless, positive quantity. For $\Gamma > 0$ the energy proceeds from DE to DM. The deceleration parameter is given by

$$q = -\left(1 + \frac{\dot{H}}{H^2}\right). \quad (7)$$

Taking the time derivative in both sides of Eq. (2), and using Eqs. (3), (4), (5) and (6), we get

$$q = \frac{1}{2}\left(1 + \Omega_k + 3\Omega_x\omega_x\right). \quad (8)$$

III. GENERALIZED SECOND LAW IN IRREVERSIBLE THERMODYNAMICS

The generalized second law (GSL) of thermodynamics was initially formulated be Bekenstein (1973) for black holes. It state that the sum of the ordinary entropy plus on quartet of the area, A, of holes event horizon cannot decrease with time [7]. In equilibrium thermodynamics, irreversible fluxes such as energy transfers play no part and they do not enter the entropy function which is defined for equilibrium state only. However, in non equilibrium extended thermodynamics such fluxes enter the entropy function [5].
The entropy of the DE and CDM which are in interacting with each other are given by Gibb's equation [8]

$$T_\Lambda\mathrm{d}S_\Lambda = \mathrm{d}Q_\Lambda = \mathrm{d}E_\Lambda + P_\Lambda\mathrm{d}V, \quad (9)$$

$$T_m \mathrm{d}S_m = \mathrm{d}Q_m = \mathrm{d}E_m, \tag{10}$$

where, $\mathrm{V} = 4\pi R_{\mathrm{h}}^3/3$ is the volume containing the DE and CDM with the radius of the horizon R_{h}. And

$$E_\Lambda = \rho_\Lambda V, \quad E_m = \rho_{\mathrm{m}} V, \tag{11}$$

$$P_\Lambda = \omega_\Lambda \rho_\Lambda = \frac{3H^2}{8\pi}\omega_\Lambda \Omega_\Lambda. \tag{12}$$

Also T_Λ and T_m are the temperatures of DE and CDM, respectively, and following [5] are given by

$$T_\Lambda = T_{eq} e^{-3(\omega_x+\lambda)(x-x_{eq})}, \tag{13}$$

$$T_m = T_{eq}\frac{r}{r_{eq}} e^{-[2+3(\omega_x+\lambda)](x-x_{eq})}, \tag{14}$$

where $r = \Omega_m/\Omega_\Lambda$ and $x = \ln a$. The subscript 'eq' indicates the value taken by the corresponding quantity when DE and DM are in thermal equilibrium. Note that in Eqs. (13) and (14), λ and ω_Λ are constants. This requires that the temperature of the both DE and CDM inside the horizon in the absence of interaction should be in equilibrium with the Hawking temperature associated with the horizon, so we have

$$T_{eq} = T_h = \frac{1}{2\pi R_h} \tag{15}$$

Taking the derivative in both sides of (9) and (10) with respect to cosmic time t, and using Eqs. (2), (3), (4), (5), (6), (11) and (12), we obtain

$$\dot{Q}_\Lambda = 4\pi R_h^2(\dot{R}_h - HR_h)(1+\omega_\Lambda)\rho_\Lambda - 4\pi R_h^3 H\lambda\rho_\Lambda, \tag{16}$$

$$\dot{Q}_m = 4\pi R_h^2(\dot{R}_h - HR_h)\rho_m + 4\pi R_h^3 H\lambda\rho_\Lambda. \tag{17}$$

Also, there is a geometric entropy on the horizon $S_h = \pi r_h^2$ [8]. The evolution of this horizon entropy is obtained as

$$\dot{S}_h = 2\pi R_h \dot{R}_h. \tag{18}$$

In the presence of interaction between DE and CDM inside the universe enveloped by the horizon, the GSL in irreversible thermodynamics can be obtained by extending Eq. (13) in [5] as

$$\dot{S}^* = \frac{\dot{Q}_m}{T_m} + \frac{\dot{Q}_\Lambda}{T_\Lambda} - A_\Lambda \dot{Q}_\Lambda \ddot{Q}_\Lambda - A_h \dot{Q}_h \ddot{Q}_h + \dot{S}_h, \tag{19}$$

where A_Λ and A_h are the energy transfer constants between DE and DM inside the universe and between the universe and the horizon, respectively. Since the overall system containing the universe and the horizon is isolated, one has $\dot{Q}_h = -(\dot{Q}_m + \dot{Q}_\Lambda)$. Here we assumed the boundary of the universe to be enveloped by the dynamical apparent horizon, as

$$R_h = H^{-1}(1+\Omega_k)^{-1/2}, \tag{20}$$

if we take the derivative in both sides of (20) with respect to cosmic time t, then we obtain

$$\dot{R}_h = \frac{3(1+\Omega_k+\Omega_\Lambda\omega_\Lambda)}{2(1+\Omega_k)^{3/2}}. \tag{21}$$

Taking the time derivative of Eq. (16), (17) and Using Eqs. (13), (14), (20), and (21), we obtain

$$\begin{aligned}\frac{\dot{Q}_m}{T_m} + \frac{\dot{Q}_\Lambda}{T_\Lambda} &= \frac{3\pi}{H(1+\Omega_k)^3}\Big(\frac{1+z_{eq}}{1+z}\Big)^{3(\omega_\Lambda+\lambda)}\Big\{\frac{r_{eq}}{r}\Big(\frac{1+z_{eq}}{1+z}\Big)^2 \\ &\times\Big[\lambda(1+\Omega_k)\Omega_\Lambda + q(1+\Omega_k-\Omega_\Lambda)\Big] \\ &+\Big[q(1+\omega_\Lambda) - \lambda(1+\Omega_k)\Big]\Omega_\Lambda\Big\}.\end{aligned} \tag{22}$$

Where $x - x_{eq} = \ln a/a_{eq} = \ln(\frac{1+z_{eq}}{1+z})$

$$\begin{aligned}\dot{Q}_\Lambda \ddot{Q}_\Lambda &= \frac{9H\Omega_\Lambda^2}{4(1+\Omega_k)^5}\Big\{\Big[2(q+1) - \frac{3q\Omega_k}{(1+\Omega_k)} \\ &- 3(1+\omega_\Lambda+\lambda)\Big]\Big(q(1+\omega_\Lambda) - \lambda(1+\Omega_k)\Big)^2 \\ &+\Big[\frac{\dot{q}}{H} - \frac{2q^2\Omega_k}{(1+\Omega_k)}\Big](1+\omega_\Lambda)\Big(q(1+\omega_\Lambda) \\ &- \lambda(1+\Omega_k)\Big)\Big\},\end{aligned} \tag{23}$$

$$\begin{aligned}\dot{Q}_h \ddot{Q}_h &= \frac{9Hq}{4(1+\Omega_k)^5}\Big\{\Big[\frac{(2-3\Omega_k)}{(1+\Omega_k)}q^2 + \frac{\dot{q}}{H} - q\Big] \\ &\times(1+\Omega_k+\Omega_\Lambda\omega_\Lambda)^2 \\ &- 3q\Omega_\Lambda\omega_\Lambda(1+\omega_\Lambda+\lambda)(1+\Omega_k+\Omega_\Lambda\omega_\Lambda)\Big\},\end{aligned} \tag{24}$$

Where

$$\dot{q} = Hq\Omega_k + \frac{3}{2}H\Omega_\Lambda\omega_\Lambda\Big[2(q+1) - 3(1+\omega_\Lambda+\lambda)\Big]. \tag{25}$$

Taking $\omega_\Lambda = -1$, $\lambda = 0.3$, $z_{eq} = 5.56\times10^7$, $r_{eq} = 1.09\times10^5$ [5] and $\Omega_\Lambda = 0.72$, and $\Omega_k = 0.02$ [9] for the present time, i.e. $z = 0$, we get

$$q = -0.57,$$

$$\dot{q} = 0.03H,$$

and

$$\frac{\dot{Q}_m}{T_m} + \frac{\dot{Q}_x}{T_x} = 1.91\times10^4 H^{-1}, \tag{26}$$

$$\dot{Q}_x \ddot{Q}_x = -6.40\times10^{-4} H, \tag{27}$$

$$\dot{Q}_h\ddot{Q}_h = 11.76 \times 10^{-4}H, \tag{28}$$

$$\dot{S}_h = 2.72H^{-1} \tag{29}$$

herefore, the GSL in irreversible thermodynamics, i.e. Eq. (19), for the present time yields

$$\dot{S}^* = H^{-1}\Big(1.91 \times 10^4 + 6.40 \times 10^{-4}\bar{A}_\Lambda - 11.76 \times 10^{-4}\bar{A}_h + 2.72\Big), \tag{30}$$

here we define $\bar{A} := AH^2$. If we set $\bar{A}_\Lambda = \bar{A}_h$, then Eq. (30) shows that when $\bar{A}_\Lambda = \bar{A}_h \leq 3.56 \times 10^7$, the GSL in nonequilibrium thermodynamics is respected, i.e. $\dot{S}^* \geq 0$, for the present time [6].

IV. CONCLUSION

Here the GSL in nonequilibrium thermodynamics for the interacting DE with CDM in a non-flat FRW universe is investigated. The boundary of the universe is assumed to be enveloped by the dynamical apparent horizon. The dynamical apparent horizon in comparison with the cosmological event horizon, is a good boundary for studying cosmology, since on the apparent horizon there is the well known correspondence between the first law of thermodynamics and the Einstein equation [2]. In the other words, the Friedmann equations describe local properties of spacetimes and the apparent horizon is determined locally, while the cosmological event horizon is determined by global properties of spacetimes [10]. We assumed that when the DE and DM evolve separately, each of them remain in thermal equilibrium with the Hawking temperature on the dynamical apparent horizon. We found that for the present time, the GSL in irreversible thermodynamics is respected for the special range of the energy transfer constants.

[1] Riess A.G. *et al.*, Astron. J. **116**, 1009 (1998);
Perlmutter S. *et al.*, Astrophys. J. **517**, 565 (1999);
de Bernardis P. *et al.*, Nature **404**, 955 (2000);
Perlmutter S. *et al.*, Astrophys. J. **598**, 102 (2003).

[2] Gong Y., Wang B., Wang A., Phys. Rev. D **75**, 123516 (2007).

[3] Wang B., Gong Y., Abdalla E., Phys. Rev. D **74**, 083520 (2006);
Sheykhi A., Class. Quant. Grav. **27**, 025007 (2010);
Karami K., J. Cosmol. Astropart. Phys. **01**, 015 (2010);
Karami K., arXiv:1002.0431.

[4] Karami K., Abdolmaleki A., arXiv:0909.2427.

[5] Zhou J., Wang B., Pavón D., Abdalla E., Mod. Phys. Lett. A **24**, 1689 (2009).

[6] Karami K., Ghaffari S., Phys. Lett. B **685**, 115 (2010).

[7] Bekenstein J.D., Phys. Rev. D **7**, 2333 (1973).

[8] Izquierdo G., Pavon D., Phys. Lett. B **633**, 420 (2006);
Zhou J., Wang B., Gong Y., Abdalla E., Phys. Lett. B **652**, 86 (2007);
Karami K., Ghaffari S., Phys. Lett. B **688**, 125 (2010).

[9] Bennett C.L. *et al.*, Astrophys. J. Suppl. **148**, 1 (2003);
Spergel D.N., Astrophys. J. Suppl. **148**, 175 (2003).

[10] Cai R.-G., Kim S.P., J. High Energy Phys. **02**, 050 (2005).

Thermodynamics of interacting entropy-corrected new agegraphic dark energy

K. Karami[1], A. Sheykhi[2], M. Jamil[3], F. Felegary[1], M.M. Soltanzadeh[1]
[1] *Department of Physics, University of Kurdistan, Pasdaran St., Sanandaj, Iran*
[2] *Department of Physics, Shahid Bahonar University, Kerman, Iran*
[3] *Center for Advanced Mathematics and Physics, National University of Sciences and Technology, Rawalpindi, 46000, Pakistan*

Abstract. Motivated by the recent works [1], we describe the thermodynamical interpretation of the interaction between entropy-corrected version of the new agegraphic dark energy and dark matter in a non-flat universe. When entropy-corrected new agegraphic dark energy and dark matter evolve separately, each of them remains in thermodynamic equilibrium. As soon as an interaction between them is taken into account, their thermodynamical interpretation changes by a stable thermal fluctuation. We obtain a relation between the interaction term of the dark components and this thermal fluctuation.

I. INTRODUCTION

The dark energy puzzle is one of the biggest challenges of the modern cosmology in the past decade. There is ample evidence on the observational side that our universe is currently experiencing a phase of accelerated expansion [2]. Among the various candidates to explain the accelerated expansion, the new agegraphic dark energy (NADE) models condensate in a class of quantum gravity may have interesting cosmological consequences [3]. The main purpose of this work is to study the thermodynamical interpretation of the interaction between dark matter and the entropy-corrected NADE (ECNADE) model for a universe enveloped by the apparent horizon. It was shown that for an accelerating universe the apparent horizon is a physical boundary from the thermodynamical point of view [4]. In particular, it was argued that for an accelerating universe inside the event horizon the generalized second law does not satisfy, while the accelerating universe enveloped by the apparent horizon satisfies the generalized second law of thermodynamics [4,5].

II. THERMODYNAMICAL DESCRIPTION OF THE NON-INTERACTING ECNADE

We consider the Friedmann-Robertson-Walker (FRW) metric for the non-flat universe as

$$ds^2 = -dt^2 + a^2(t)\left(\frac{dr^2}{1-kr^2} + r^2 d\Omega^2\right), \qquad (1)$$

where k = 0, 1,-1 represent a flat, closed and open FRW universe, respectively. For the nonflat FRW universe containing the DE and DM, the first Friedmann equation has the following form

$$H^2 + \frac{k}{a^2} = \frac{1}{3M_P^2}\,(\rho_\Lambda + \rho_{\rm m}), \qquad (2)$$

where ρ_Λ and ρ_m are the energy density of DE and DM, respectively. Let us define the dimensionless energy densities as

$$\Omega_{\rm m} = \frac{\rho_{\rm m}}{3M_P^2H^2}, \quad \Omega_\Lambda = \frac{\rho_\Lambda}{3M_P^2H^2}, \quad \Omega_k = \frac{k}{a^2H^2}, \qquad (3)$$

then, the first Friedmann equation yields

$$\Omega_{\rm m} + \Omega_\Lambda = 1 + \Omega_k. \qquad (4)$$

Following [3], the energy density of the NADE is given by

$$\rho_\Lambda = \frac{3n^2M_P^2}{\eta^2}, \qquad (5)$$

$$\eta = \int \frac{dt}{a} = \int \frac{da}{Ha^2}. \qquad (6)$$

and the energy density of the ECNADE is given by [6]

$$\rho_\Lambda = \frac{3n^2M_P^2}{\eta^2} + \frac{\alpha}{\eta^4}\ln(M_P^2\eta^2) + \frac{\beta}{\eta^4}, \qquad (7)$$

Here and are dimensionless constants of order unity. Consider the FRW universe filled with dark energy and dust (dark matter) which evolve according to their conservation laws

$$\dot\rho_\Lambda + 3H(1+\omega_\Lambda^0)\rho_\Lambda = 0, \qquad (8)$$

$$\dot\rho_{\rm m} + 3H\rho_{\rm m} = 0, \qquad (9)$$

From definition $\rho_\Lambda = 3M_P^2H^2\Omega_\Lambda$, we get

$$\Omega_\Lambda = \frac{n^2}{H^2\eta^2}\gamma_n, \qquad (10)$$

where

$$\gamma_n = 1 + \frac{1}{3n^2M_P^2\eta^2}\Big[\alpha\ln(M_P^2\eta^2) + \beta\Big]. \qquad (11)$$

we obtain the equation of state parameter of the entropy-corrected new agegraphic

$$w_\Lambda^0 = -1 + \frac{2}{3na\gamma_n}\Big(\frac{\Omega_\Lambda}{\gamma_n}\Big)^{1/2}\Big(2\gamma_n - 1 - \frac{\alpha}{3M_P^2 n^2\eta^2}\Big), \quad (12)$$

Therefore, the entropy of the entropy-corrected new agegraphic dark energy is connected with its energy and pressure through the first law of thermodynamics

$$TdS_\Lambda = dE_\Lambda + P_\Lambda dV, \quad (13)$$

where the volume enveloped by the apparent horizon and A_r is the apparent horizon radius

$$V = \frac{4\pi}{3} r_A^3, \quad (14)$$

$$r_A = \frac{1}{\sqrt{H^2 + k/a^2}}, \quad (15)$$

The total energy of the entropy-corrected new agegraphic dark energy inside the apparent horizon is

$$E_\Lambda = \rho_\Lambda V = \Big[3n^2 M_P^2 \eta^{-2} + \alpha\eta^{-4}\ln(M_P^2\eta^2) + \beta\eta^{-4}\Big] \times \Big[\frac{4\pi}{3} r_A^3\Big], \quad (16)$$

Taking the differential form of Eq. (16), we find

$$dE_\Lambda = -12\pi r_A^{0^3} M_P^2 H^2 \Omega_\Lambda \Big[(1+\omega_\Lambda^0)dx - \frac{dr_A^0}{r_A^0}\Big], \quad (17)$$

The associated temperature on the apparent horizon can be written as

$$T = \frac{1}{2\pi r_A}, \quad (18)$$

Inserting Eqs. (17), (18) and (14) into (13), we obtain

$$dS_\Lambda^0 = -24\pi^2 r_A^{0^4} M_P^2 H^{0^2} \Omega_\Lambda^0 (1+\omega_\Lambda^0)\Big[dx^0 - \frac{dr_A^0}{r_A^0}\Big], \quad (19)$$

III. THERMODYNAMICAL DESCRIPTION OF THE INTERACTING ECNADE

We consider a universe containing an interacting ECNADE density ρ_Λ and the cold dark matter (CDM), with $\omega_m = 0$. The energy equations for ECNADE and CDM are

$$\dot\rho_\Lambda + 3H(1+\omega_\Lambda)\rho_\Lambda = -Q, \quad (20)$$

$$\dot\rho_m + 3H\rho_m = Q, \quad (21)$$

where following [7], we choose $Q = \Gamma\rho_\Lambda$ as an interaction term and $\Gamma = 3b^2 H(\frac{1+\Omega_k}{\Omega_\Lambda})$ the decay rate of the ECNADE component into CDM with a coupling constant b^2. The equation of state (EoS) parameter of the interacting ECNADE as

$$w_\Lambda = -1 + \frac{2}{3na\gamma_n}\Big(\frac{\Omega_\Lambda}{\gamma_n}\Big)^{1/2}\Big(2\gamma_n - 1 - \frac{\alpha}{3M_P^2 n^2\eta^2}\Big) - \frac{Q}{9M_p^2 H^3\Omega_\Lambda}, \quad (22)$$

Therefore, the entropy of the entropy-corrected new agegraphic dark energy is connected with its energy and pressure through the first law of thermodynamics

$$TdS_\Lambda = dE_\Lambda + P_\Lambda dV, \quad (23)$$

where now the entropy has been assigned an extra logarithmic correction [8]

$$S_\Lambda = S_\Lambda^{(0)} + S_\Lambda^{(1)}, \quad (24)$$

$$S_\Lambda^{(1)} = -\frac{1}{2}\ln(CT^2), \quad (25)$$

$$C = T\frac{\partial S_\Lambda^{(0)}}{\partial T}, \quad (26)$$

It is a matter of calculation to show that

$$C = -24\pi^2 r_A^{(0)^4} M_P^2 H^{(0)^2}\Omega_\Lambda^{(0)}(1+\omega_\Lambda^{(0)}), \quad (27)$$

$$S_\Lambda^{(1)} = -\frac{1}{2}\ln\Big(-6 r_A^{0^2} M_P^2 H^{0^2}\Omega_\Lambda^0(1+\omega_\Lambda^0)\Big), \quad (28)$$

$$dS_\Lambda = -24\pi^2 r_A^4 M_P^2 H^2 \Omega_\Lambda\Big[(1+\omega_\Lambda)(dx - \frac{dr_A}{r_A}) + \frac{Q}{9M_P^2 H^3\Omega_\Lambda}dx\Big], \quad (29)$$

and thus one gets

$$1+\omega_\Lambda = \Big[-\frac{1}{24\pi^2 r_A^4 M_P^2 H^2\Omega_\Lambda}\frac{dS_\Lambda}{dr_A} - \frac{Q}{9M_P^2 H^3\Omega_\Lambda}\frac{dx}{dr_A}\Big](\frac{dx}{dr_A} - \frac{1}{r_A})^{-1}, \quad (30)$$

$$1+\omega_\Lambda = \Big[-\frac{1}{24\pi^2 r_A^4 M_P^2 H^2\Omega_\Lambda}\Big[\frac{dS_\Lambda^{(0)}}{dr_A} + \frac{dS_\Lambda^{(1)}}{dr_A}\Big] - \frac{Q}{9M_P^2 H^3\Omega_\Lambda}\frac{dx}{dr_A}\Big](\frac{dx}{dr_A} - \frac{1}{r_A})^{-1}, \quad (31)$$

we can easily find

$$\frac{dS_\Lambda^{(0)}}{dr_A} = \frac{\partial S_\Lambda^{(0)}}{\partial r_A^0}\frac{dr_A^0}{dr_A} + \frac{\partial S_\Lambda^{(0)}}{\partial x^0}\frac{dx^0}{dr_A}, \tag{32}$$

$$\frac{dS_\Lambda^{(0)}}{dr_A} = 24\pi^2 r_A^{0^3} M_P^2 H^{0^2}\Omega_\Lambda^0\Big[\frac{(1+\omega_\Lambda^0)(1+\Omega_k)^{\frac{3}{2}}}{1+q+\Omega_k}\Big] \times\Big[\frac{1+q^0+\Omega_k^0}{(1+\Omega_k^0)^{\frac{3}{2}}} - H^0 r_A^0\Big], \tag{33}$$

$$\frac{dS_\Lambda^{(1)}}{dr_A} = \frac{dS_\Lambda^{(1)}}{dx}\frac{dx}{dr_A}, \tag{34}$$

$$\frac{dS_\Lambda^{(1)}}{dr_A} = \Big[\frac{(1+\Omega_k)^{\frac{3}{2}}}{1+q+\Omega_k}\Big]\Big[\frac{\frac{d}{dt}\Big(-6r_A^{0^2}M_P^2H^{0^2}\Omega_\Lambda^0(1+\omega_\Lambda^0)\Big)}{12r_A^{0^2}M_P^2H^{0^2}\Omega_\Lambda^0(1+\omega_\Lambda^0)}\Big], \tag{35}$$

one gets an expression for the interaction term

$$\frac{Q}{9M_P^2H^3\Omega_\Lambda} = (1+\omega_\Lambda)\left(\frac{1}{r_A}\frac{\mathrm{d}r_A}{\mathrm{d}x} - 1\right) - \left(\frac{\frac{\mathrm{d}r_A}{\mathrm{d}x}}{24\pi^2 r_A^4 M_P^2 H^2\Omega_\Lambda}\right)\left(\frac{\mathrm{d}S_\Lambda^{(0)}}{\mathrm{d}r_A} + \frac{\mathrm{d}S_\Lambda^{(1)}}{\mathrm{d}r_A}\right), \tag{36}$$

$$\frac{Q}{9M_P^2H^3\Omega_\Lambda} = \frac{q(1+\omega_\Lambda)}{1+\Omega_k} - \frac{(r_A^0)^3H_0^2\Omega_\Lambda^0(1+\omega_\Lambda^0)q^0}{r_A^4H^3\Omega_\Lambda(1+\Omega_k^0)^{3/2}} + \frac{1}{48\pi^2r_A^4H^3\Omega_\Lambda}\frac{\mathrm{d}}{\mathrm{d}t}\ln\Big[(r_A^0)^2M_P^2H_0^2\Omega_\Lambda^0(1+\omega_\Lambda^0)\Big]. \tag{37}$$

In this way we provide the relation between the interaction term of the dark components and the thermal fluctuation.

IV. CONCLUSION

Here, we provided a thermodynamical description for the ECNADE model in a universe with spatial curvature. It was shown that for an accelerating universe the apparent horizon is a physical boundary from the thermodynamical point of view. We explored the thermodynamical picture of the interacting ECNADE model for a FRW universe enveloped by the apparent horizon. We assumed that in the absence of a coupling, the two dark components remain in separate thermal equilibrium and that the presence of a small coupling between them can be described as stable fluctuations around equilibrium. Finally, resorting to the logarithmic correction to the equilibrium entropy we derived an expression for the interaction term in terms of a thermal fluctuation.

[1] M. Jamil, A. Sheykhi, M.U. Farooq, arXiv:1003.2093; A. Sheykhi, M.R. Setare, arXiv:0912.1408.
[2] A. G. Riess, et al., Astron. J. 116 (1998) 1009.
[3] H. Wei, R.G. Cai, Phys. Lett. B 660 (2008) 113; A. Sheykhi, Phys. Lett. B 680, (2009) 113; K. Karami, M.S. Khaledian, F. Felegary, Z. Azarmi, Phys. Lett. B 686, (2010) 216.
[4] J. Zhou, B. Wang, Y. Gong, E. Abdalla, Phys. Lett. B 652 (2007) 86.
[5] A. Sheykhi, B. Wang, Phys. Lett. B 678 (2009) 434.
[6] H. Wei, Commun. Theor. Phys. 52, (2009) 743.
[7] H. Kim, H.W. Lee, Y.S. Myung, Phys. Lett. B 632 (2006) 605.
[8] S. Das, P. Majumdar, R.K. Bhaduri, Class. Quantum Grav. 19 (2002) 2355.

Photometric study the LMC eclipsing binary OGLE051649.51-693246.1

A. Abedi and S. Mohammadi
Physics Department and Mojtahedi Observatory, Birjand University, Birjand, Iran.

In this work, eclipsing binary OGLE051649.51-693246 have been studied and analysed. The Photometry data have been selected form EROS, OGLE, and MACHO projects in four B, V, R and I filters. These data have been converted to the wavelength of jonson filters by a specific transformation. This method describes the relative and absolute parameters of the system such as mass ratio q, radius ratio, and absolute components magnitude, eccentricity e, and longitude of periastron ω. Finally, using these parameters, LC and DC programs of Wilson- deviney code were run and physical and geometrical parameters ratio have been declaration for components of this system. The results show that this system is a detached binary with component of giant type.

I. INTRODUCTION

In recent years, gravitational micro-lensing projects like EROS, OGLE and MACHO have led to the discovery of many eclipsing binaries in the Magellanic Clouds (Alcock et al., 1997). Ground-based photometries have also been done for variable stars in LMC and SMC. Little attention has been paid to the other eclipsing binaries, and many such light curves have not been analyzed. This has been partly due to the un-availability of spectroscopic data and accurate light curves. Despite this, analyses of the light curves of such systems are important for a better understanding of the eclipsing binaries in these nearby galaxies.

II. DATA PROCESSING

The data are available in I filter in magnitudes from the OGLE-II survey, and in B_M, R_M filters in MACHO, in B_E, R_E filters in EROS projects. Whereas for analyses purpose, we need these data in Johnson filters. Thus, we used the transformations in Grison et al. 1995, and MACHO to convert the data to standard photometric systems. Before analyzing the photometric data, we take the following steps:

1. First item We converted heliocentric Julian date to phase, using the linear ephemeris Grison et al., (1995).

$$JD_{min}(pri) = (2448660.064 \pm 0.002) + (3.628 \pm 0.004)E \tag{1}$$

2. Second item In order to decrease scattering, we used the binned photometry data, to reduce the number of points for any light curve to 200 points.

III. AN INITIAL EVALUATION

Light curve analysis of our target could not be performed completely without spectroscopic observations to constrain spectral types and masses. In order to have exact approximations, we have done as follows: The following formula

$$\frac{T_1}{T_2} = (\frac{1 - l_P}{1 - l_S})^{1/4} \tag{2}$$

was used to estimate the temperature ratio, where T_1 and T_2 are surface temperature of the primary and secondary stars, and l_p and l_s are bolometric deep of the primary and secondary eclipses. We approximate the eclipses deep using the following formula:

$$l_p = \frac{L_p}{L_0} \quad , \quad l_s = \frac{L_s}{L_0} \tag{3}$$

$$L_0 = L_{0B} + L_{0V} + L_{0I} + L_{0R} \tag{4}$$

$$L_S = L_{SB} + L_{SV} + L_{SI} + L_{SR}, \qquad L_P = L_{PB} + L_{PV} + L_{PI} + L_{PR} \tag{5}$$

where L_{PB}, L_{SB}, L_{0B}, L_{PV}, L_{SV}, L_{0V}, L_{PI}, L_{SI}, L_{0I}, L_{PR}, L_{SR} and L_{0R} are the primary and secondary minima deeps and the intensity maximum of light curve in B, V, I, and R filters. The temperature ratio of the primary and secondary stars is obtained as follows:

$$\frac{T_1}{T_2} = 1.077 \tag{6}$$

In this step the intensity light curve without normalization has been used. Since, the OGLE051649.51-693246.1 system has total eclipsing, we could calculate the magnitude of the primary star in V and B filters in the secondary eclipse. According to Fabrizio et al., (2005)

$$\mu_{LMC} = 18.515 \pm 0.085 \tag{7}$$

Therefore, we calculated the absolute magnitude of the primary star as follows:

$$M_V - \overline{m}_V = -3.2 \pm 0.085 \quad , \quad B - V = -0.17 \tag{8}$$

By referring to the standard stellar tables, the III luminosity class and the B3, B4 spectral type were obtained for the primary and secondary stars, respectively, using the temperature ratio. In order to calculate the eccentricity and the longitude of periastron, we utilized the following equation:

$$\frac{2\pi(t_{sec}-t_{pri})}{P} = \pi + 2\tan^{-1}\frac{e\cos\omega}{(1-e^2)^{1/2}} + \frac{2e\cos\omega(1-e^2)^{1/2}}{(1-e^2\sin^2\omega)} \quad (9)$$

In this equation, e and ω are the eccentricity and the longitude of periastron and t_{pri} and t_{sec} are times of primary minimum and secondary minimum, respectively. The left side of this equation can be obtained from direct observations. To calculate the right side of the relation, we rewrite it as follow:

$$X = \pi + 2\tan^{-1}\frac{e\cos\omega}{(1-e^2)^{1/2}} \quad (10)$$

Thus,

$$\frac{2\pi(t_{sec}-t_{pri})}{P} = X - \sin X \quad (11)$$

This equation is solvable using the numerical methods. The value of X for this system is 3.149, obtained from Newton- Raphson iteration.

Moreover, to calculate e and ω, we should use another equation:

$$e\sin\omega = \frac{(d_{sec}-d_{pri})}{(d_{sec}+d_{pri})} \quad (12)$$

where ,d_{pri} and d_{sec} are the times between initial and fourth contacts in the primary and secondary eclipses. We obtained $e \approx 0.055$, and $\omega \approx 270.0°$.

IV. LIGHT CURVE ANALYSIS

In order to determine the photometric elements of OGLE051649.51-693246.1 from the light curve, we used the Wilson and Devinney's (1985) code which is based on Roche model. By estimating quantities such as the mass ratio, q, the primary temperature ,T_1, the secondary temperature ,T_2, the eccentricity, e, and the longitude of the periastron ,ω, we used the initial linear limb darkening coefficients for the primary and secondary components, adopted from the values in van Hamme (1993). The gravity darkening exponents were assumed to be $g_1 = g_2 = 1.0$ (von Zeipel's low), because the primary and secondary stars both have radiative envelopes. In the WD runs, we used mode 2 (detached system). The resulting fit to the light curve observations can be seen in Fig 1. The resulting orbital and physical properties of the system are listed in Table 1.

TABLE I. Photometric solution for of the LMC eclipsing binary OGLE051649.51-693246.1

parameter	filter B	filter V	filter I	filter R	B+V+I+R
i (deg)	88.2	88.2	88.2	88.2	88.2
$T_1(K)$	1720	1720	1720	1780	1720
$T_2(K)$	1520	1520	1520	1510	1520
Ω_1	4.27	4.80	4.65	5.27	4.427
Ω_2	9.90	10.2	10.0	15.252	10.140
q	0.48	0.48	0.47	0.45	0.48
l_3	0	0	0	0	0
e	0.055	0.050	0.070	0.050	0.055
ω	271.0	271.0	271.0	271.0	271.880
x_1	0.59	0.52	0.41	0.49	$\leftarrow$
y_1	0.29	0.27	0.25	0.27	$\leftarrow$
x_2	0.56	0.48	0.32	0.38	$\leftarrow$
y_2	0.29	0.25	0.18	0.20	$\leftarrow$
g_1	1	1	1	1	1
g_2	1	1	1	1	1
A_1	1	1	1	1	1
A_2	1	1	1	1	1
$L_1/(L_1+L_2)$	0.96	0.96	0.96	0.98	-
$L_2/(L_1+L_2)$	0.03	0.03	0.03	0.01	-
r_1 (pole)	0.25	0.22	0.24	0.20	0.25240
r_1 (point)	0.26	0.23	0.24	0.21	0.26169
r_1 (side)	0.26	0.23	0.24	0.20	0.25673
r_1 (bake)	0.26	0.23	0.24	0.21	0.26002
r_2 (pole)	0.05	0.05	0.05	0.03	0.05440
r_2 (point)	0.05	0.05	0.05	0.03	0.05463
r_2 (side)	0.05	0.05	0.05	0.03	0.05460
r_2 (bake)	0.05	0.05	0.05	0.03	0.05462
$\sum(o-c)^2$	0.01	0.00	0.00	0.00	0.027

V. DISCUSSION OF THE RESULTS AND CONCLUSIONS

In the LC program run in mode 2, we never got the "roch lobes are full" message, so we did the fitting in the same mode. Thus, OGLE051649.51-693246.1 close binary system is a detached binary.

In order to correct the initial estimation of the physical properties of the system components, we used a method useful for eclipsing binaries systems with total eclipse. Therefore, this method can be used in light curve analysis of eclipsing binary systems in the LMC where spectroscopic observation in not available.

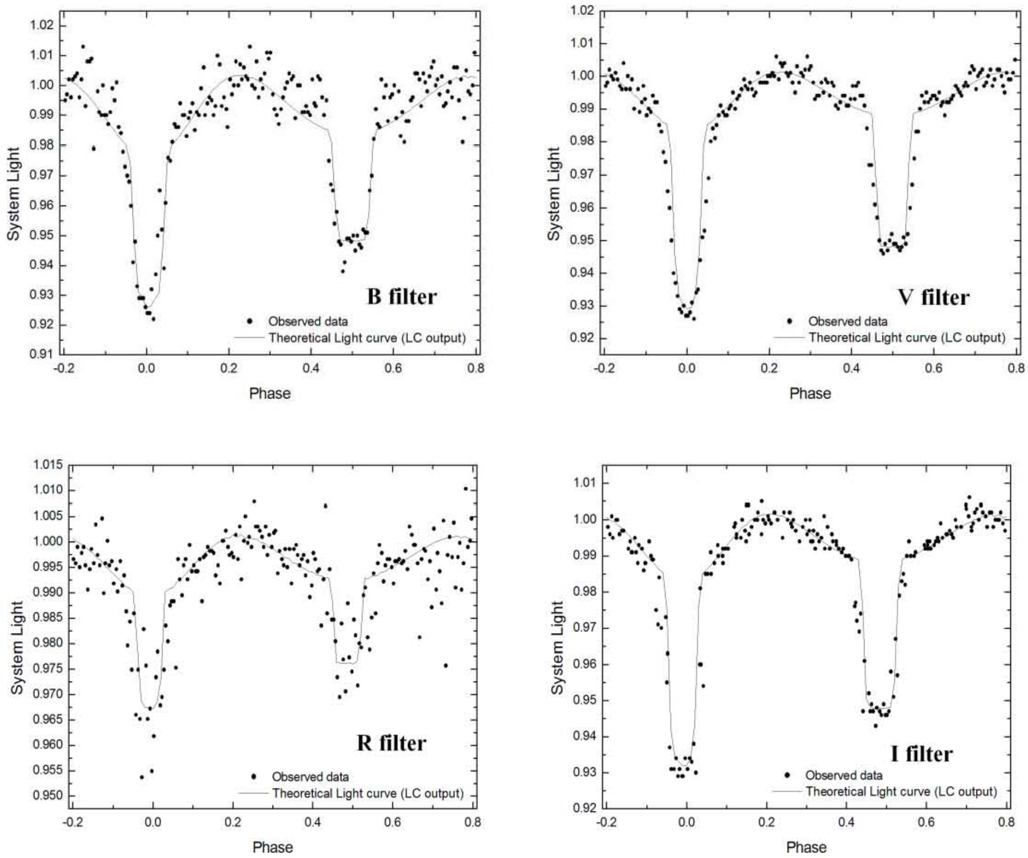

FIG. 1. Normal points of OGLE051649.51-693246.1 in the B, V, R, and I filters together with the computed light curves (solid lines) corresponding to the parameters from solutions of the B, V, R, andI filters.

[1] Alcock et al., Astron. J, 114, 326, (1997).
[2] Di Fabrizio, L., et al., Astronomy and Astrophysics, 430, 603-628 (2005).
[3] Grison, P., et al., Asron. Astrophys. Suple. Ser, 109, 447-469 (1995).
[4] Hilditch, R. W., Cambridge university press, UK (2001).
[5] www macho.anu.edu.au/.
[6] Ostlie, D.A. and Carroll, B.W., New York: Addison- Wesley, Bristol, (1996).
[7] Van Hamme, W., 1993.AJ 106, 2096.

Evolution of Galactic Globular Clusters

Akram Hasani Zonoozi, Zahra Hassani, Zeinab khorrami, and Hosein haghi
Department of Physics, Institute for Advanced Studies in Basic Sciences (IASBS), Zanjan, Iran

We present our results of a large set of N-body simulation to study the evolution of single-mass star clusters. Our main focus is to study the dissolution time of clusters to obtain the effect of different initial properties of a cluster. This permit us to estimate the lifetime of clusters as a function of the initial conditions. Throughout the investigated parameter-space nearly all clusters show a constant half-mass radius for the time after core collapse until dissolution.

PACS numbers: 05.10.-a ,05.10.Gg, 98.70.Vc

I. INTRODUCTION

We have performed a series of N-body simulations to study the dynamical evolution of star clusters in external fields. Our simulations include stellar mass loss, tow-body relaxation and external tidal field effect by neglecting stellar evolution in this step.

The velocity distribution of stars in a cluster established through two-body encounters and supposed to be Maxwellian. This implies that the stars in high velocity tail of Maxwllian distribution are unbound to the cluster. As this hot stars evaporate from the cluster, the remained stars re-establish a new velocity dispersion with a lower mean value. We investigated the single mass clusters evolution in different initial conditions. We vary the particle number of clusters such as half mass radius and Galactic distance, to see how these parameters affect the dynamical evolution and time dissolution of clusters. Galactic distance and half mass radius influence on dissolution time are investigated. Also the behavior of half mass radius, tidal radius and their ratio are investigated in context of different initial mass and different galactic distance.

II. N-BODY MODEL

We performed a series of N-body simulations with the collisional N-body code NBODY6 (Aarseth 2003) to study the globular clusters evolution. The simulations are performed in N-body units, in which the constant of gravitation, initial cluster mass and energy are given by $G = 1$, $M = 1$ and $E_c = -0.25$ respectively. This scaling is useful since the total mass of the cluster together with the radius of the cluster orbit defines the tidal radius and the crossing time in physical units.

The clusters are set up as Plummer profile in virial equilibrium.

$$\rho = \frac{3M}{4\Pi a^3}(1+\frac{r^2}{a^2})^{-\frac{5}{2}}, \quad R_h = 1.35a \tag{1}$$

We also take into account the external tidal filed of the host galaxy also accelerates the dynamical evolution (Baumgardt & Makino 2003). The clusters move on a circular orbit through logarithmic potential of the Milky Way $\phi(R_G) = V_G^2 \ln R_G$ at different Galactocentric radius from 8.5 kpc until 32 kpc with circular velocity $V_G = 220$ km/sec.

Clusters with stars of a single mass evolve through dynamical evolution and loss a certain fraction of their stars through escape. Stars over the two tidal radii distance from the center of the cluster removed from the simulation and assumed are escaped from the cluster.

When 95 per cent of the mass was lost from a cluster, the cluster is dissolved.

Our clusters containing between $N = 1000$ and 5000 single stars with half mass radius in the range of 0.5-4 pc. The distance from the galactic center vary from 8.5 kpc to 32 kpc.

III. RESULTS

A. Dissolution time

We take a cluster with 3000 stars $M = 3000M_\odot$ moving on circular orbit with $R_G = 8.5kpc$, and let half mass radius to vary from $0.5pc$ to $4pc$ to obtain a relation between the dissolution time and the half-mass radius. Fig 1 shows the dissolution time of each cluster versus its initial half-mass radius in logarithmic scales. The best fit line is:

$$\log(T_{diss}) = 0.12\log(R_h) + 3.57, \tag{2}$$

T_{diss} depends on Galactocentric distances, R_G, of cluster. In Fig 2. we have shown T_{diss} in term of R_h for different choose of R_G. The clusters at further Galactocentric distance have larger lifetime.

$$R_G = 8.5kpc : \log(T_{diss}) = 0.12\log(R_h) + 3.38, \tag{3}$$

$$R_G = 15kpc : \log(T_{diss}) = 0.19\log(R_h) + 3.56, \tag{4}$$

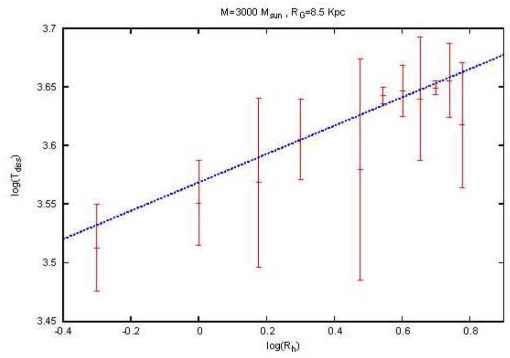

FIG. 1. The dissolution time as a function of the initial half-mass radius for a cluster with $3000M_{\odot}$ moving on at $R_G = 8.5kpc$ from the Galactic center.

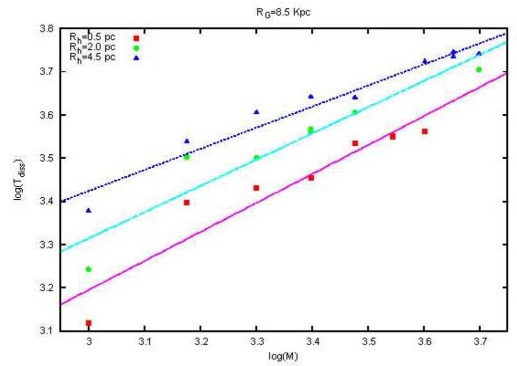

FIG. 3. The dissolution time as a function of the initial cluster mass and half-mass radius. Different lines corresponds to different R_h

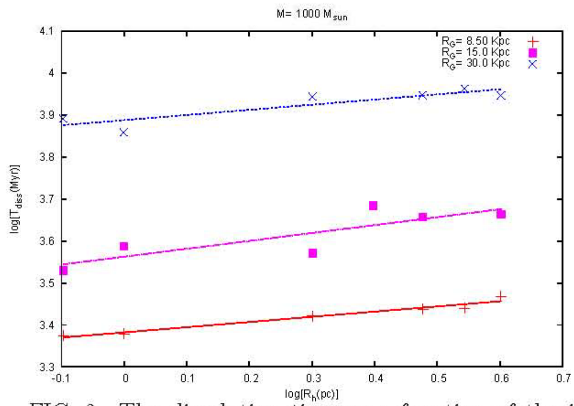

FIG. 2. The dissolution time as a function of the initial half-mass radius for a cluster with $1000M_{\odot}$ moving on at moving at different Galactic distance.

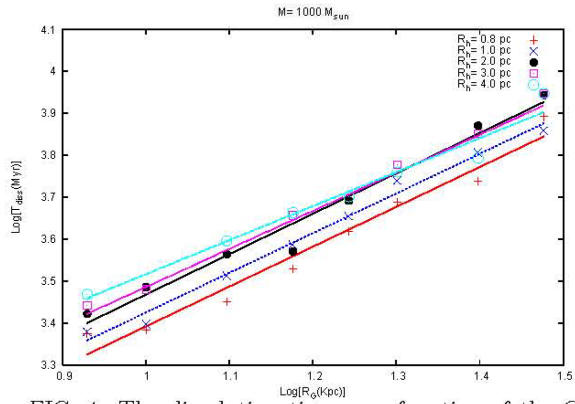

FIG. 4. The dissolution time as a function of the Galactic distance and initial half-mass radius for a cluster with $1000M_{\odot}$.

$$R_G = 30kpc : \log(T_{diss}) = 0.12\log(R_h) + 3.89, \quad (5)$$

Moreover the influence of the clusters initial mass on dissolution time is investigated. Fig 3 depicts how the dissolution time of the clusters change as a function of total initial mass.

$$R_h = 0.5pc : \log(T_{diss}) = 0.67\log(M) + 1.18 \quad (6)$$

$$R_h = 2.0pc : \log(T_{diss}) = 0.61\log(M) + 1.49 \quad (7)$$

$$R_h = 4.5pc : \log(T_{diss}) = 0.49\log(M) + 1.96 \quad (8)$$

Also the affect of galactic distance on dissolution time of galaxy are shown in Fig 4. and Fig 5. for $M = 1000M_{\odot}$ and $M = 3000M_{\odot}$ respectively.

The dissolution time of clusters increase with increasing initial half-mass radius, initial mass and galactic distance.

B. Evolution of half-mass radius

The evolution of half-mass and tidal radius of clusters are investigated in details. The half-mass radius of clusters with same mass and different initial half-mass radius settles to the same equilibrium value after core collapse for large fraction of their life time.

The virial equilibrium implies that, reducing the half-mass radius raises the mean velocity dispersion of member stars. A cluster with the half mass radius,which is twice the other, therefore, exhibit a half mean velocity dispersion of that. But since these clusters have the same tidal radius, they redistribute their mass through two-body relaxation such that after core collapse the initially smaller or larger clusters do not differ in their properties, from a cluster with same initial mass. This hold especially for the half-mass radius.

We investigated the influence of initial mass and Galactic distance of cluster on this value.Galactic distance has an important influence on the clusters asymptotic half

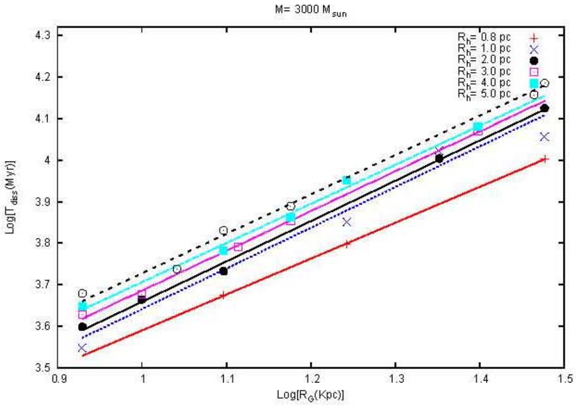

FIG. 5. Same as Fig 4. but for a cluster with $3000M_{\odot}$.

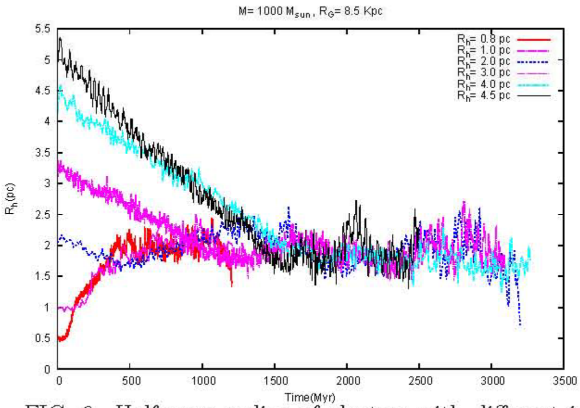

FIG. 6. Half-mass radius of clusters with different initial R_h and $1000M_{\odot}$. All models converge to same value of 2 pc, when they lost 30-50 per cent of their initial mass.

mass radius. By increasing the cluster mass and Galactic distance, the asymptotic value of half-mass radius increase Fig (6-12).

These results indicate that the evolution of half mass radius is strongly dependent on initial density of cluster before core collapse, but independent on it after core collapse.

IV. CONCLUSION

We have done a set of N-body simulation of single mass clusters to model the Galactic star clusters. The clusters are orbiting around the galaxy with logarithmic halo density.

Different initial conditions including mass, half-mass radius of the cluster and galactocentric distance are considered.

1. All simulated clusters dissolve as a result of two-body relaxation and external field effect.

2. Clusters with higher mass would dissolve later, i.e. the lifetime is larger.

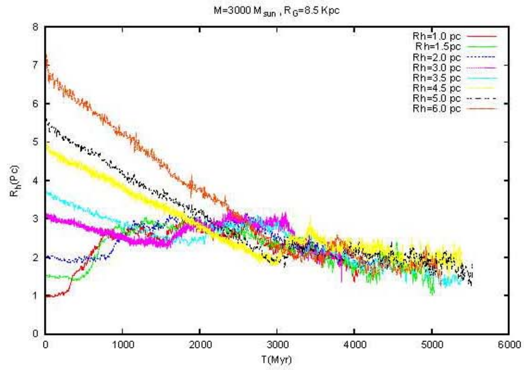

FIG. 7. Same as Fig 7. for clusters with $3000M_{\odot}$, half-mass radius converge to about 2.5 pc.

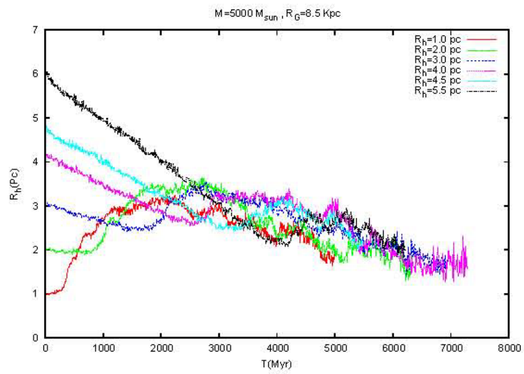

FIG. 8. Same as Fig 7. for clusters with $5000M_{\odot}$, half-mass radius converge to about 3 pc.

3. Clusters with larger Galactocentric distance, can live for a long time, rather than nearby clusters.

4. In agreement with kuepper et al 2008, all clusters with the same mass and different initial half-mass radius, converge to an equilibrium value of half-mass radius, after core collapse. This value depends on the clusters mass and orbital radius. For larger Galoctocentric distance, the equilibrium value is larger.

[1] Aarseth S. J., Gravitational N-Body Simulations, Cambridge University Press
[2] Baumgardt H., Makino J., 2003, MNRAS, 340, 227.
[3] Kuepper, A., 2008, MNRAS, 389, 889.

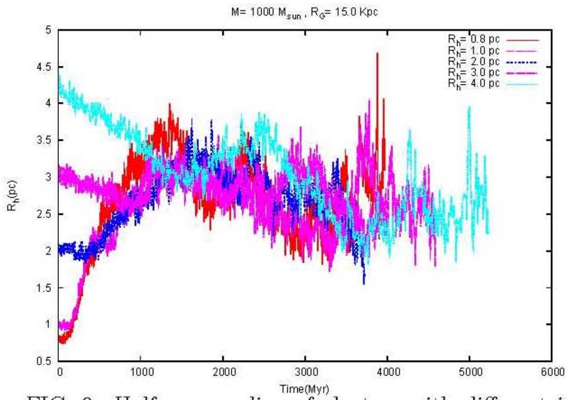

FIG. 9. Half-mass radius of clusters with different initial R_h and $1000 M_\odot$ moving on at $R_G = 15kpc$. All models converge to same value of 3 pc, when they lost 30-50 per cent of their initial mass

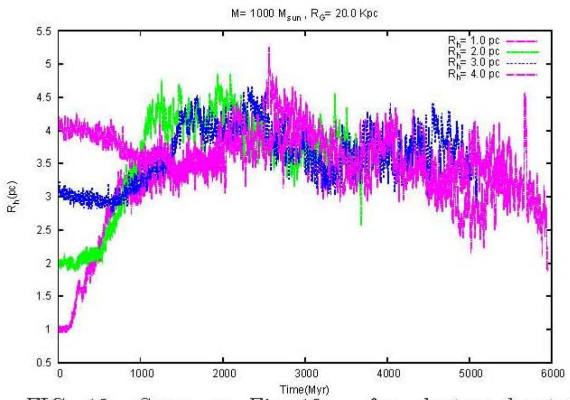

FIG. 10. Same as Fig 10. for clusters located in $R_G = 20kpc$, half-mass radius converge to about 3.5 pc.

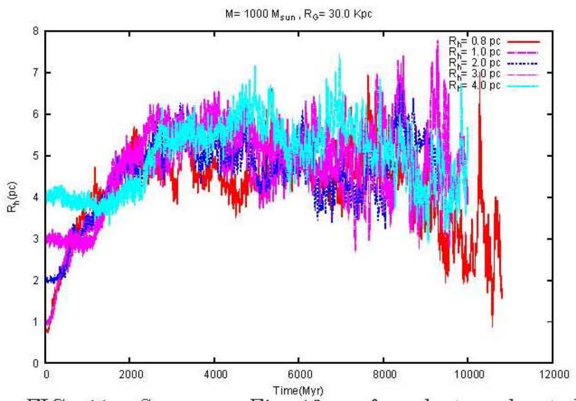

FIG. 11. Same as Fig 10. for clusters located in $R_G = 30kpc$, half-mass radius converge to about 5 pc.

Light Curves Analysis of the New Eclipsing Binary V807 Cas

R. Pazhouhesh[1] and E. G. Melendo[2]
[1] *Physics Department, University of Birjand, Birjand, Iran*
[2] *Esteve Duran Observatory El Montanya - Seva, Barcelona, Spain*

The BV light curves of the new eclipsing binary V807 Cas was analyzed by using the latest version of Wilson Program in order to derive photometric elements of this system. Since no spectroscopic mass ratio is available, the q-search method was applied to yield the preliminary range of mass ratio in order to search for the final solution. The present solution reveals that V807 Cas has a photometric mass ratio q = 0.903 and is a semi-detached binary with the secondary component filling the Rouche lobe.

Keyword: binaries: close-binaries: eclipsing - V807 Cas

I. INTRODUCTION

The new eclipsing binary V807 Cas (HIP 114552=GSC 4010-285, $\alpha_{2000} = 23^h12^m13^s$, $\delta_{2000}= 59°35'\,59.2''$) was discovered as a variable star by the HIPPARCOS mission (ESA, 1997). It was classified as a periodic variable with $1^d.97463$ period, a mean magnitude of $10^m.79$, and average B-V=$0^m.340$ without specifying variability type. V807 Cas is in the center of PK110-0.1, which was initially classified planetary nebula We 1-12.
In 1977, Weinberger published a list of 12 new extended possible planetary nebula. Whereas, because of their characteristic morphology and the presence of a blue central star, almost all of them could easily be suspected to be genuine planetary nebulae, one object (No. 12) captivated because of its unusually bright central star. But the real nature of We 1-12 remain unsolved.
Recent spectroscopic data by Kimeswenger (1998) indicate that V807 Cas has a B1V spectral type, and We 1-12 is not a planetary nebula but isolated HII region and this star is the only source of extinction of the HII region. He found the color excess E(B-V) resulting from interstellar extinction towards the object is 0.6-0.8 mag.

The first photometric observation of V807 Cas was done with collaboration program between Esteve Duran Observatory and the U.s. Naval Observatory Flagstaff station in 1997. Observation showed that V807 Cas is in fact an EB eclipsing binary system with a period close to two days. The phased light curve presented a primary minimum with depth of 0.18 magnitude of 10.80±0.01. It was found an avarage B-V=0.319±0.003. Finally, they compined their data with HIPPARCOS photometry and the following ephemeris was computed:

$$MinI = HJD2450652.428 + 1^d.949189 \times E \qquad (1)$$

New photometric observations of V807 Cas were obtained through BV filters during 2003 and 2004. The observations were made with the 0.6 meter Cassegrain telescope of Esteve Duran Observatory. The stars GSC 4010-463 and GSC 4010-1201 were used for comparison and check stars respectively. Based on ephemeris (1), light curves are shown in Figure1.

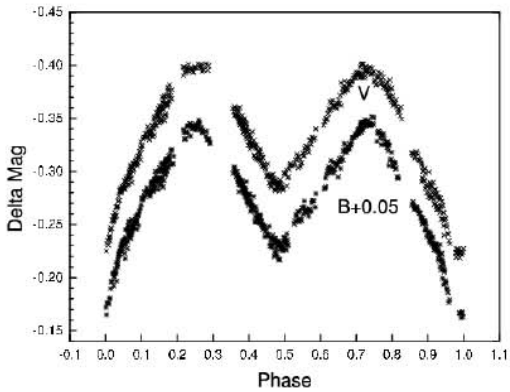

FIG. 1. The BV light curves of V807 Cas obtained at Esteve Duran Observatory.

II. LIGHT CURVES ANALYSIS

Based on photometric data individual observations the magnitude differences were converted to intensities and used as a photometric input data. Photometric solution of the V807 Cas was obtained by employing of the Wilson Program (2003).

Two light curves were employed simultaneously for determination of the geometric and physical elements of the system. Since no spectroscopic mass-ratio was known, a search for solution was made for mass ratio q. The lowest values of the sum of the weighted squared residuals, $\sum(\mathrm{res})^2$, occurred around q=0.9 in mode 5 and q=3.9 in mode 4 (both in semi-detached configuration). Figure 2 and Figure 3 show the fit parameters $\sum(\mathrm{res})^2$ as a

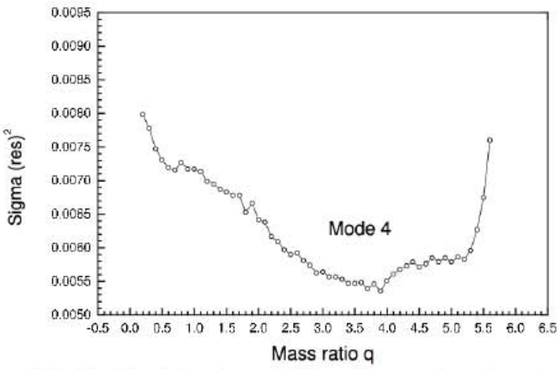

FIG. 2. The behavior of $\sum(\text{res})^2$ as a function of mass-ratio q in mode 4.

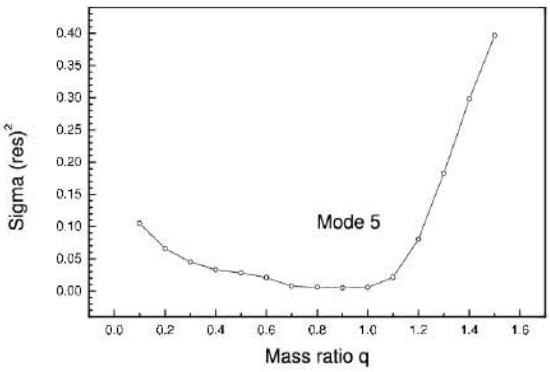

FIG. 3. The behavior of $\sum(\text{res})^2$ as a function of mass-ratio q in mode 5.

Parameter	Value
i	$54^{\circ}.476 \pm 0.168$
x_1	0.814^*
x_2	0.213^*
l_3	0.00^*
$T_1(K)$	7000^*
$T_2(K)$	5103 ± 28
Ω_1	3.855 ± 0.008
q	0.903 ± 0.005
A_1	1.00^*
A_2	0.50^*
g_1	1.000^*
g_2	0.320^*
$r_1(pole)$	0.333 ± 0.001
$r_1(side)$	0.346 ± 0.001
$r_1(back)$	0.365 ± 0.002
$r_2(pole)$	0.348 ± 0.001
$r_2(side)$	0.365 ± 0.001
$r_2(back)$	0.396 ± 0.001
$L_{1V}/(L_1+L_2)$	0.782 ± 0.005
$L_{2V}/(L_1+L_2)$	0.218 ± 0.005
$L_{1B}/(L_1+L_2)$	0.834 ± 0.005
$L_{2B}/(L_1+L_2)$	0.166 ± 0.005
$\sum(\text{res})^2$	0.0045
*assumed	

TABLE I. Physical and geometrical solutions of V807 Cas

function of mass-ratio q in modes 4 and 5 respectively.

We finally adopted the solution in mode 5 (with 0.903 ± 0.005) by taking into account the better fit of the solution.
We made use of the color index (B-V)=0.340 and tables of popper (1980), Flower (1996) to determine the temperature of the primary component (star eclipsed at Min.I). As a result, the temperature of the primary component proved to be $T_1 = 7000^{\circ}K$ and the corresponding spectral class was the type B1V, which is a generally accepted spectral type for the primary component of Algol stars.

The gravity-darkening coefficients were adopted to be $g_1 = g_2 = 0.32$ (Lucy 1967), and bolometric albedo to be $A_1 = A_2 = 0.50$ (Rucinski 1969) in accordance with the assumed stellar convective envelope. Stellar rotation was assumed to be synchronized for both components. For both components, we used bolometric linear, logarithmic and square root laws in Wilson program and the best result was obtained for bolometric linear limb darkening law in Wilson Program and $x_1 = x_2$ parameters of the two components were fixed to their theoretical values, interpolated from Vhlimb Program of Van Hamme(1993). The grid resolution values ere taken as 20, 20, 15, 15 for N1, N2, N1L and N2L, respectively and we used the simple reflection model (Wilson, 1990), with a single reflection ($MREF = 1$, $NREF = 1$). We also assumed that the stars had no spots and nor third light, $l_3 = 0.0$.

The following parameters were free to be adjusted: the orbital inclination i, the mass ratio $q = m_2/m_1$, the mean surface temperature of secondary component T_2, the non-dimensional surface potential of primary component Ω_1, the monochromatic luminosity of primary component L_1. These parameters were varied until the solution converged. That is, the convergent solution was obtained with the adjustable parameters by iterating, until the corrections on the parameters became smaller than corresponding mean errors.

The physical and geometrical elemnts of this system given in Table 1 and theoretical light curve calculated with the final elements is shown in Figure.3. Accordingly, the eclipsing binary V807 Cas is semi-detached binary.

III. CONCLUSION

In the present work, the results from light curves analysis of V807 Cas, based on photoelectric data of Garcia-

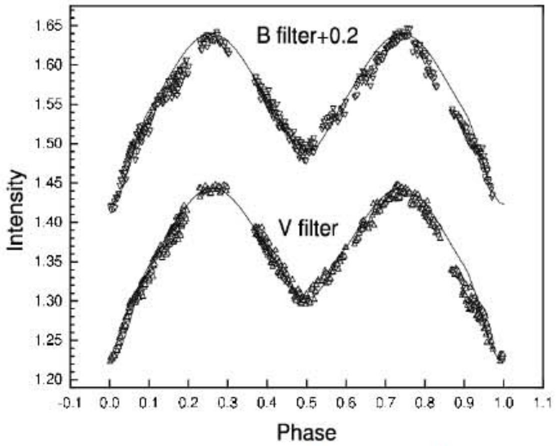

FIG. 4. Open circles show the observed points of V807 Cas and the model fit is shown by continuos lines.

Melendo & Henden, Arne A.(2000) and our photometric data are presented and discussed. We used the latest version of Wilson program for eclipsing binary stars and light curves were employed simultaneously for determination of the geometric and physical elements of the system. The photoelectric light curves of V807 Cas has a normal shape and we supposed there are neither a third light, $l_3 = 0.0$, nor any spots. The spectral type of system is B1V and the temperature of primary component was adopted to be $T_1 = 7000\,(\mathrm{K})$. The surface temperature difference between the two components is computed to be about $\Delta T = 1897\,(K)$ and the temperature of the secondary is derived as $T_1 = 5103\,(\mathrm{K})$. We have used linear limb darkening law and x parameter of both components were fixed to their theoretical values, interpolated from Vhlimb program of Van Hamme (1993). The photometric mass-ratio is estimated about 0.903 ± 0.005 and radial velocity curves are necessary for more reliable estimation of mass-ratio.
we couldn't calculate the O−C of V807 Cas, because there is no times of minimum in the literature. So, we suggest to do more photometric observations to get more times of minima and also obtain more accurate physical and geometrical elements of this system.
The values of the system's parameters are given in Table I.

[1] ESA, 1997, The HIPPARCOS and Tycho Catalogues, ESA-1200.
[2] Ferrellad, G and Melendo, E. G., 1997, IBVS 5009, 501.
[3] Flower, P. J., 1996, APJ 469, 355.
[4] Kaler, J. B and Feibelman, W. A., 1985, MNRAS, 294, 312.
[5] Kimeswenger, S., 1998, MNRAS, 312.
[6] Landolt, A. U., 1992, AJ, 104, 340
[7] Lucy, L. B., 1967, Z. Astrohys, 65, 89.
[8] Poper, D. M., 1980, Ann. Rev. Astrophys, 18, 115.
[9] Rucinski, S. M., 1969, Acta Astron, 19, 245.
[10] Van Hamme, W., 1993, AJ, 108, 2096.
[11] Wilson, R. E., 1990, APJ, 256, 613.
[12] Zijlstra, A. *et al.*, 1990, A& AS, 82, 273.

A CCD Photometric Study and Search for Pulsation in RZ Dra and EG Ceo

R. Pazhouhesh[1], A. Liakos[2] and P. Niarchos[2]
[1] *Physics Department, University of Birjand, Birjand, Iran*
[2] *Department of Astrophysics, Astronomy and Mechanics, Faculty of Physics, National and Kapodistrian University of Athens, Athens, Greece*

This paper presents CCD observations carried out during July and August 2007 on the Algol-type eclipsing binaries system RZ Dra and EG Cep at the Gerostathopoulion Observatory of the University of Athens. All light curves have been analyzed with the PHOEBE program and Wilson-Devinney code (2003 version). A detailed photometric analysis, based on these observations, is presented for both binarity and pulsation. The results indicate RZ Dra and EG Cep are semidetached system where the secondary components fill their Roche lobe. After removing the binary light curves, the pulsation of the primary components can be analyzed using the remaining residuals. The frequency analysis was made with PERIOD 04 program.

I. INTRODUCTION

Eclipsing Binaries are important and several binary systems are known which contain a pulsating component. It is interesting to study such systems, since extra information can be extracted from both their pulsation and eclipsing properties, leading to a more reliable determination of system parameters.
Soudugan et al. (2006) in a paper entitled: "A catalogue of close binaries located in the δ Scuti region of the Cepheid instability strip" have listed the detached and semidetached eclipsing binary system for which one or both components are most plausibly candidates for a δ Scuti type pulsation. we have chosen two eclipsing binary EG Cep and RZ Dra for study and observations.

II. OBSERVATIONS

The photometric observations were carried out at the Gerostathopoulion Observatory of the University of Athens during 8 nights in July and August 2007, using the 0.4m Cassegrain telescope equipped with the ST-8XMEI CCD camera and BVRI Bessel photometric filters. The comparison and check stars used for each system are presented in Table 1 and the calculated times of minima using the method of Kwee & van Woerden (1956), obtained from our observations, are given in Table 2. Light curves of both system are shown in Figure 1 and Figure 2.

TABLE I. The photometric observations log

System	Night spent	Filter used	Comparison Star	Check star
EG Ceo	7	BVRI	GSC 4589:2757	GSC 4589:2842
RZ Dra	5	RI	GSC 3916:1889	GSC 3916:1825

TABLE II. The times of minima from our observations

System	HJD	Error	Filters
EG Ceo	2454264.55370	0.00006	RI
EG Ceo	2454265.37058	0.00015	RI
EG Ceo	2454334.53760	0.00025	BVRI
RZ Dra	2454201.57645	0.00010	R
RZ Dra	2454229.39446	0.00009	RI
RZ Dra	2454232.42467	0.00017	RI

III. O-C ANALYSIS

In order to analyze the O-C diagram of each system, the least squares method has been used. The construction of the O-C diagrams of EG Cep and RZ Dra, are based on a total of 255 and 88 times of minima taken from literature respectively. The computation of the parameters of the third-body orbit is a classical inverse problem with 5 parameters to be found, namely the period of the third body P_3, the HJD of the periastron passage T_0, the semi-amplitude A of the LITE, the argument of periastron Ω and the eccentricity of the third body e_3. The mass function of the third body f(m_3) and the minimal mass of the third component $M_{3,min}$=$M_3 sini_3$ (for i_3=90°) could be computed from this set of parameters. In the cases where the distance of the EB has been measured, the maximum angular separation α of the third body from the eclipsing pair can be also calculated. The weights assigned to individual observations were set as w=1 for visual observations, 5 for photographic and 10

TABLE III. The results of the O-C diagram analysis of EG Cep and RZ Dra

Parameters of the EB	EG Ceo	RZ Dra
$M_1 + M_2(M_\odot)$	1.0 + 0.84	1.9 + 0.78
$Min.\ I$ [HJD]	2400000 + 35956.5430(3)	2400000 + 37181.4353(2)
P (days)	0.5446213(3)	0.5508763(1)
$c_2(days/cycle) \times 10^{-10}$	0.1307(1)	0.0349(1)
$\dot{P}(days/year) \times 10^{-8}$	1.753(1)	0.463(1)
$M_{3,min}(M_\odot)$	0.150(2)	0.226(3)
Parameters of the 3^{rd} body		
P_3[yrs]	74.4(9)	118.1(1)
e_3	0.59(4)	0.72(2)
$M_{3,min}[M_\odot]$	0.15(2)	0.226(3)
χ^2	0.1538	0.0050

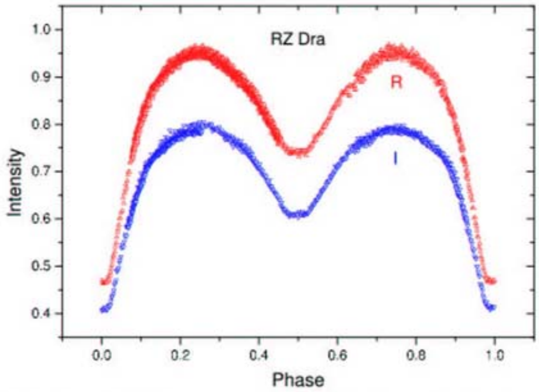

FIG. 2. RI light curves of RZ dra obtained at the Gerostathopoulion Observatory.

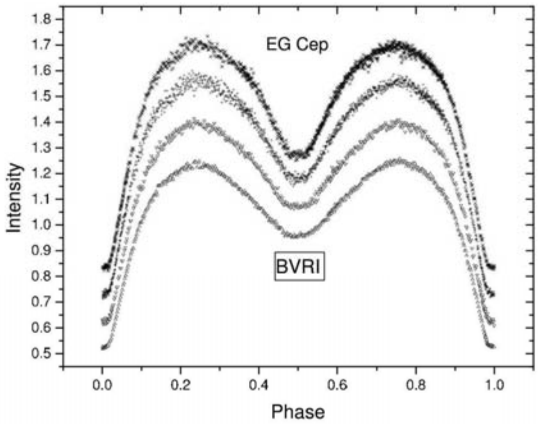

FIG. 1. BVRI light curves of EG Cep obtained at the Gerostathopoulion Observatory.

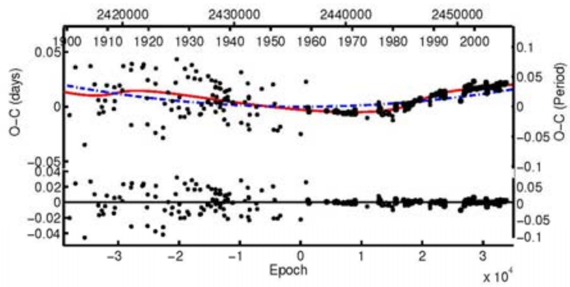

FIG. 3. The O-C diagram of EG Cep fitted by a LITE curve and a parabola (upper part) and total residuals after the subtraction of the whole solution (lower part). The solid line indicates the sum of solution, while the dashed line correspond to the parabola. The bigger the symbol the bigger the weight assigned.

for CCD and photoelectric observations. The derived values of the parameters are listed in Table 3, while the new parabolic ephemeris are presented here for EG Cep and RZ Dra respectively:

$$MinI = HJD2435956.5430(3) + 0^d.5446213(1) \times E \quad (1)$$

$$MinI = HJD2437181.4353(2) + 0^d.5508763(1) \times E \quad (2)$$

In Figure 3. and Figure 4. are shown the sum of the solutions assumed and the total residuals after both solutions have been subtracted.

IV. LIGHT CURVE ANALYSIS

The light curves have been analyzed with the Wilson Program (version 2003)(Wilson & Devinney 1971, Wilson 1979, Wilson 1990) and PHOEBE software (Prsa & Zewitt 2005). We applied the code in MODE 5, which solves the light curves of semi-detached eclipsing binaries, where the secondary (cooler) component fills its Roche lobe, while the primary (hotter) one is well inside its Roche lobe. For radial velocity analysis of RZ Dra, we used 64 points data given by Rucinscki et al. (2005). For detailed analysis we used some constrains for gravity-darkening exponents $g_1 = 1$ and $g_2 = 0.32$, the bolometric albedos $A_1 = 1.0$ and $A_2 = 0.50$. Stellar rotation was assumed to be synchronized for both components.
We used bolometric linear, logarithmic and square root laws in Wilson program and the best result was obtained for bolometric logarithmic limb darkening law of Klinlesmith and Sobieski (1970) of the form:

$$I = I_0\left(1 - x + x\cos\theta - y\cos\theta\ln(\cos\theta)\right) \quad (3)$$

and both x and y parameters of both components were fixed to their theoretical values, interpolated from Vh-

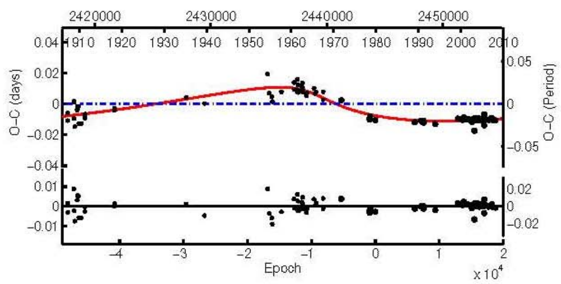

FIG. 4. The O-C diagram of RZ Dra explained same as a figure.2.

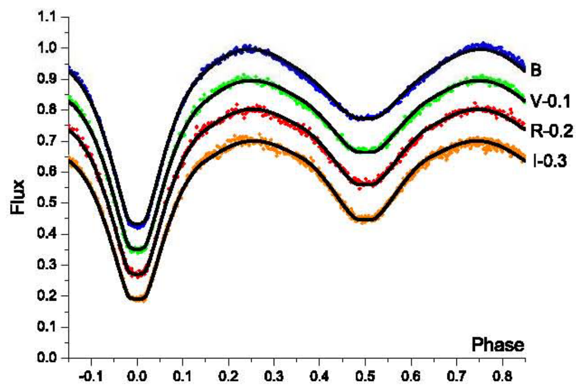

FIG. 5. Observed points and theoretical (solid lines) light curves of EG Cep.

limb program of Van Hamme (1993).
The grid resolution values were taken as 20, 20, 15, 15 for N1, N2, N1L and N2L, respectively and we used the simple reflection model (Wilson, 1990), with a single reflection ($MREF = 1$, $NREF = 1$). We also assumed that the stars had no spots and nor third light, $l_3 = 0.0$. The BVRI light curves of EG Cep, and the radial velocity and the RI light curves of RZ Dra were used simultaneously for determination of the geometric and physical elements of each system.

The light curves solution are summarized in Tables 4 and 5 for EG Cep and RZ Dra, respectively, and the theoretical and observed Light curves are illustrated in Figure.5 and Figure.6.

V. SEARCH FOR PULSATIONS

In order to reveal any possible pulsation nature of RZ Dra and EG Cep we subtracted the theoretical light curves from the observed ones in order to remove the

TABLE IV. Physical and geometrical parameters of EG Ceo

Parameter	Value
i [deg]	87.5 (2)
q (m_2/m_1)	0.449 (1)
a $[R_\odot]$	2.982 (5)
V_γ	6.110 (4)
T_1^* [K]	8500
T_2 [K]	5792 (9)
$L_{1V}/(L_1+L_2)$	0.650 (4)
$L_{2V}/(L_1+L_2)$	0.350 (4)
$r_{1(pole)}$	0.4092 (4)
$r_{2(pole)}$	0.2914 (2)
$r_{1(side)}$	0.4326 (5)
$r_{2(side)}$	0.3039 (2)
$r_{1(back)}$	0.4553 (6)
$r_{2(back)}$	0.3365 (2)
$period$	$0^d.4806547$ (53)
dp/dt	0.133×10^{-5}
Ω_1	2.859 (2)
$(\sum(\text{res})^2)$	0.071
$^*assumed$	

TABLE V. Physical and geometrical parameters of RZ Dra

Parameter	Value
$a(R_\odot)$	2.982 (5)
V_γ	6.110 (4)
R_1 $[R_\odot]$	1.62
R_2 $[R_\odot]$	1.13
M_1 $[M_\odot]$	1.617
M_2 $[M_\odot]$	0.656
$M_{bol,1}$	2.84
$M_{bol,2}$	3.52
α $[R_\odot]$	3.71 (2)
V_γ [km/sec]	14.9 (3)
i [deg]	87 (1)
q (m_2/m_1)	0.406(2)
T_1^* [K]	8150
T_2 $[K]$	5531 (10)
$r_{1(pole)}$	0.4157 (6)
$r_{2(pole)}$	0.2837 (3)
$r_{1(side)}$	0.4399 (7)
$r_{2(side)}$	0.2957 (3)
$r_{1(back)}$	0.4618 (3)
$r_{2(back)}$	0.3284 (3)
Ω_1	2.781 (3)
$(\sum(\text{res})^2)$	0.077
$^*assumed$	

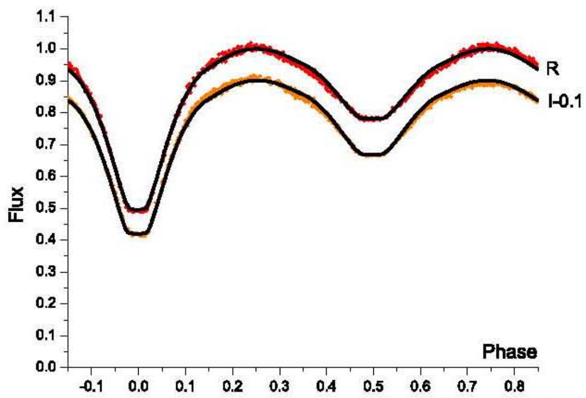

FIG. 6. Observed points and theoretical (solid lines) light curves of RZ Dra.

proximity effects (reflection and eclipticity). The frequency analysis was made with PERIOD 04 software (Lenz & Berger 2005) on the LC residuals, and we found no evidence of pulsational behavior either in EG Cep nor RZ Dra.

VI. DISCUSSION AND CONCLUSIONS

The LC analysis of EG Cep and RZ Dra showed that both of them are semi-detached systems with the secondary component filling its Roche Lobe. The periodic variations of the orbital periods of these systems could be explained by adopting the existence of a tertiary component, while the steady increase of their period is probably due to the mass transfer procedure. In contrast with the O-C diagram solution, the LC analysis for both systems showed that there is not a third light contribution in the total luminosity of the system. This disagreement can be explained by taking into account the small values of mass of the third body found in each case. Finally, we could not detect any pulsation nature of the primary components of both systems. So, high accuracy observations (by using larger telescope and better CCD) will make it possible to look for pulsation and pulsational behavior.

ACKNOWLEDGMENTS

This work has been financially supported by the Special Account for Research Grants No 70/4/5806 of the National & Kapodistrian University of Athens, Greece. The present work was made using minima database: http://var.astro.cz/ocgate/. We thank P. Zasche for providing the Matlab code to compute the results of the O-C analysis.

[1] Klinglesmith, D.A. , Sobieski, S. 1970, AJ 75, 175
[2] Kwee, K., van Woerden, H. 1956, Bulletin of the astronomical institutes of the Netherlands, 12, 464
[3] Lenz, P. & Breger, M. 2005, CoAst, 146, 53
[4] Prša, A., & Zwitter, T. 2005, ApJ, 628, 426
[5] Rucinski, S. M., Lu, W., & Mochnacki, S. W. 2000, AJ, 120, 1133
[6] Soydugan, E., Soydugan, F., Demircan, O. & İbanoğlu, C. 2006, MNRAS, 370, 2013
[7] Van Hamme, W.: 1993, AJ 106, 2096
[8] Wilson, R. E., & Devinney, E. J. 1971, ApJ, 166, 605
[9] Wilson, R. E. 1979, ApJ, 234, 1054
[10] Wilson, R. E. 1990, ApJ, 356, 613
[11] Zombeck, M. V. 1990, Handbook of Space Astronomy and Astrophysics, Cambridge University Press.

The consequence of recent supernova type Ia observations on the Adiabatic Matter Creation model

Hajar Vakili [1], Razieh Emami[1], M. Sadegh Movahed[1,2]
[1] Department of Physics, Shahid Beheshti University, G.C., Evin, Tehran 19839, Iran
[2] School of astronomy, Institute for research in fundamental sciences (IPM), P.O. Box 19395-5531, Tehran, Iran

Adiabatic matter creation has been proposed to describe positive accelerating universe. In this paper we construct the most relevant observable quantity, namely distance modulus in this cosmological model. We use the most recent supernova type Ia data sets as a standard candles containing Union, Constitution, Gold06, HST, Nearby, SNLS, MLCS2k2, Gold and Essence to constrain the free parameters of mentioned model. Based on likelihood statistics, we conclude that, the consistency of adiabatic matter creation with the ESSENCE data set is more than other supernova type Ia used in this paper.

I. INTRODUCTION

A wide range of cosmological data has indicated that the universe is in the positive accelerating phase. Combining the recent observation of cosmic microwave background radiation by WMAP 7-year, Baryonic acoustic oscillation, linear structure formation from SDSS and distance modulus of standard candle, supernova type Ia, have demonstrated that the geometry of universe is flat at 2σ confidence interval and indicated almost 2/3 of total energy density equates to so-called dark energy with equation of state equal to one in the context of ΛCDM model. This type of energy is known as cosmological constant which can explain the acceleration of universe. In spite of well consistency of this model with various type of observations ranging from high redshifts to low radshifts, there exist at least two following problem concerning to cosmological constant, namely the *fine-tuning* and the *cosmic coincidence*. In the framework of quantum field theory, the vacuum expected value is 123 order of magnitude larger than the observed value of 10^{-47} GeV^4. The non-existence of a well-known fundamental mechanism which sets the cosmological constant zero or very small value is so-called the cosmological constant problem. The second problem as the cosmic coincidence, demonstrates that why are the energy densities of dark energy and dark matter nearly equal today? On the other hand, the age of universe calculated in this model has contradicted with the age the oldest stars in globular clusters [1,2].

Such mentioned problems inspired cosmologists to propose models with no cosmological constant or a time varying one. An adiabatic matter creation process instead of cosmological constant generates an accelerating universe. The age of the universe in this model may be large enough to agree with the observations. Lima et. al. in 1996 proposed this process [3] and imposed kinematic constraints on closed, open and flat universes driven by adiabatic matter creation [4,5].

As discussed before, currently the most sensitive probe of this expansion are supernova type Ia (SNIa). In this paper we study the consistency of this model with the latest available SNIa data sets in the wide redshift range using marginalized likelihood statistics to confine the space of model free parameters. The Constitution [6], Union [7], Gold, Essence [8], MLCS2k2 [9], Nearby, SNLS [10], HST [11] and Gold06 [12], data sets are used in this paper.

This paper is organized as follows: in section II, we give a brief explanation regarding to adiabatic matter creation cosmological model. The Hubble parameter which is the key-equation to make a relation between theoretical model and observations describes in this section. The Bayesian analysis and data description will be introduced in section III. Observational constraints on the model free parameters using various SNIa catalogs and discussion regarding to our results will be given in Section IV.

II. ADIABATIC MATTER CREATION MODEL

We start with the homogeneous and isotropic FRW line element ($c = 1$)

$$ds^2 = dt^2 - a^2(t)\left(\frac{dr^2}{1-kr^2} + r^2 d\theta^2 + r^2\sin^2\theta d\phi^2\right) \quad , \tag{1}$$

where r, θ, and ϕ are dimensionless comoving coordinates, $k = 0, \pm 1$ is the curvature parameter of the spatial sections and $a(t)$ is the scale factor.

In models with "adiabatic" creation, the dynamic behavior is determined by the Einstein field equations together the balance equation for the particle number density [13].

$$8\pi G\rho = 3\frac{\dot{a}^2}{a^2} + 3\frac{k}{a^2} \quad , \tag{2}$$

$$8\pi G(p+p_c) = -2\frac{\ddot{a}}{a} - \frac{\dot{a}^2}{a^2} - \frac{k}{a^2} \quad , \tag{3}$$

$$\frac{\dot{n}}{n} + 3\frac{\dot{a}}{a} = \frac{\psi}{n} \quad , \tag{4}$$

where an overdot means time derivative and ρ, p, n and ψ are the energy density, thermostatic pressure, particle number density and matter creation rate, respectively. The creation pressure ,p_c ,depends on the matter creation rate, and for "adiabatic" creation, it takes the following form

$$p_c = -\frac{\rho+p}{3nH}\psi \quad , \tag{5}$$

where $H = \dot{a}/a$ is the Hubble parameter. To give a complete description, the set (2-5) must be supplemented by an equation of state, which in the cosmological domain is usually given by

$$p = (\gamma-1)\rho \tag{6}$$

where the γ parameter specifies if the universe is radiation ($\gamma = \frac{4}{3}$) or dust ($\gamma = 1$) dominated.

Now, according to paper [4], we assume that the matter creation rate is

$$\psi = 3\beta nH \quad . \tag{7}$$

it is straightforward to show that the above equation can be written as

$$\left(\frac{\dot{a}}{a}\right)^2 = H_0^2\left[1-\Omega_0+\Omega_0\left(\frac{1}{a}\right)^{1-3\beta}\right] \quad . \tag{8}$$

where $\Omega_0 = \frac{\rho}{\rho_o}|_{t=t_0}$ and $H_0 = \frac{\dot{a}}{a}|_{t=t_0}$ are the present values of the density and Hubble parameters. For $\beta = 0$ the above equation reproduces the standard cold dark matter FRW result [14].

Some observable quantities in the standard FRW model are easily determined expressing the radial dimensionless coordinate r of a source light as a function of the redshift .

Comoving distance for flat and closed universes may be written as

$$r_{\rm closed}(z) = \frac{\sin[\delta\sin^{-1}\alpha_2 - \delta\sin^{-1}\alpha_1]}{H_0(\Omega_0-1)^{\frac{1}{2}}} \quad , \tag{9}$$

where $\delta = \frac{2}{(1-3\beta)}$, $\alpha_2 = (\frac{\Omega_0-1}{\Omega_0})^{\frac{1}{2}}$, and $\alpha_1 = \alpha_2(1+z)^{-\frac{(1-3\beta)}{2}}$. In particular, the limit for a flat Universe ($\Omega_o = 1$) yields [4]

$$r_{\rm flat}(z) = \frac{2}{(1-3\beta)H_o}\{1-(1+z)^{\frac{2}{1-3\beta}}\} \quad , \tag{10}$$

For an open universe we find the relation as

$$r_{\rm open}(z) = \frac{\sinh[\delta\log(\alpha_2+\sqrt{1+\alpha_2^2}) - \delta\log(\alpha_1+\sqrt{1+\alpha_1^2})]}{H_0(1-\Omega_0)^{\frac{1}{2}}} \quad . \tag{11}$$

The comoving distance relates to the (dimensionless) luminosity distance ,D_L, through

$$D_L(z;\Omega_0,\beta) = \frac{H_0 r(z)(1+z)}{c} \tag{12}$$

apparent magnitude of supernovas m includes the reddening, K correction, is related to the (dimensionless) luminosity distance of a an object at redshift z through:

$$m = \mathcal{M} + 5\log D_L(z;\Omega_0,\beta), \tag{13}$$

where for a spatially flat universe we have:

$$D_L(z;\Omega_0,\beta) = H_0(1+z)\int_0^z \frac{dz'}{H(z';\Omega_0,\beta)} . \tag{14}$$

Also

$$\mathcal{M} = M + 5\log\left(\frac{c/H_0}{1Mpc}\right) + 25. \tag{15}$$

where M is the absolute magnitude. The distance modulus, μ, is defined as:

$$\mu \equiv m - M = 5\log D_L(z;\Omega_0,\beta) + 5\log\left(\frac{c/H_0}{1Mpc}\right) + 25, \tag{16}$$

To compare the theoretical results with the observational data, we compute the distance modulus, as given by equation (16). We compare the distance modulus in dark energy model with that from the observation using likelihood analysis.

TABLE I. The main characteristics of catalogs used in this paper.

Observation	redshift range	number of SNIa
Gold/Gold06	$0.029 - 1.755$	182
ESSENCE	$0.0050 - 1.5510$	192
HST	$0.216 - 1.175$	41
Constitution	$0.15 - 1.010$	397
MLSC2k2	$0.0104 - 1.755$	164
Union	$0.15 - 0.68$	398
Nearby	$0.016 - 0.125$	44
SNLS	$0.249 - 0.960$	73

III. LIKELIHOOD ANALYSIS AND DATA DESCRIPTION

We use Bayesian statistics [16] to investigate the model consistency with SNIa observation data. We introduce

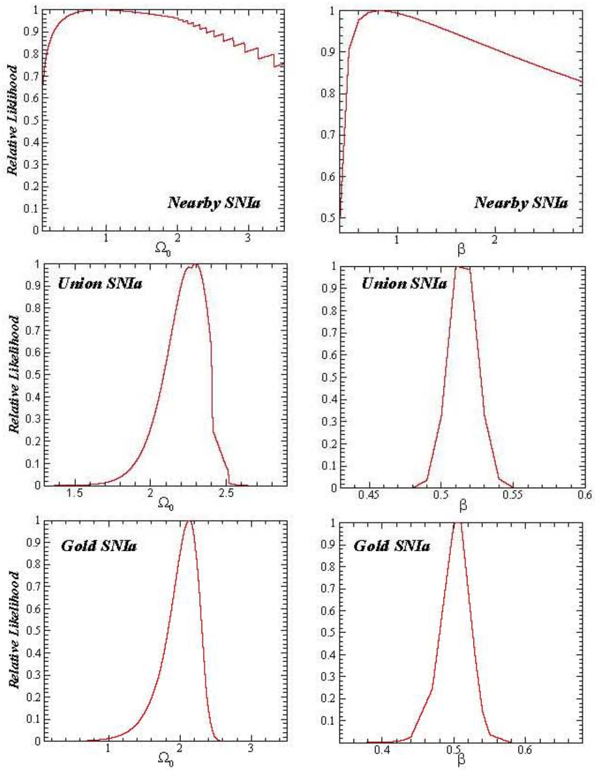

FIG. 1. Relative likelihood functions for β and Ω_0. Upper panel corresponds to Nearby SNIa catalog. Middle panel has been calculated by Union sample. Constraints on the model free parameters by Gold06 has been illustrated in lower panel.

measurements and model parameters as $\{X\}:\{\mu_{\rm obs.}(z)\}$ and $\{\Theta\}:\{\Omega_0,\beta\}$, respectively. Based on the Bayesian theorem, the conditional probability of the model parameters given data set (observation) is so-called posterior probability and is given by:

$$P(\Theta|X)=\frac{\mathcal{L}(X|\Theta)P(\Theta)}{\int\mathcal{L}(X|\Theta)d\Theta}. \tag{17}$$

The first term in the nominator of the right hand side of the above equation is Likelihood and the second terms contains every initial constraint concerning model parameters, so-called prior distribution. This term expresses the degree of belief about the model. In the absence of every prior constraints, the posterior function, $P(\Theta|X)$ is proportional to the Likelihood function. If there is no correlation between various measurements, consequently according to the central limit theorem, Likelihood function is given by a product of Gaussian functions as follows:

$$\mathcal{L}(X|\Theta)=\exp\left(\frac{-\chi^2(\Theta)}{2}\right), \tag{18}$$

where

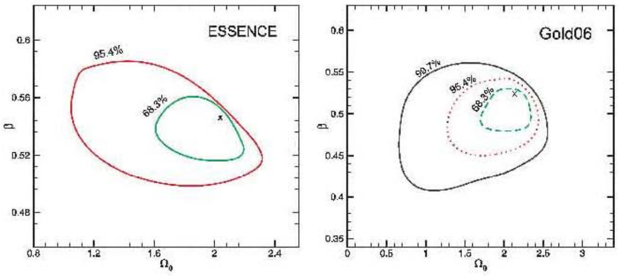

FIG. 2. Joint likelihood analysis for β and Ω_0 determined by Essence (left panel) and Gold (right panel) SNIa catalogs.

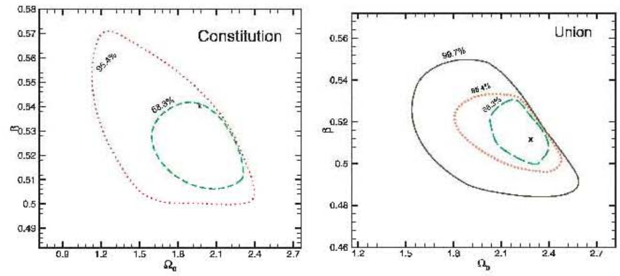

FIG. 3. Joint confidence intervals for β and Ω_0 determined by Constitution (left panel) and Union (right panel) SNIa catalogs.

$$\chi^2(\Theta)=\sum_i^N\frac{[\mu_{\rm obs}(z_i)-\mu_{\rm the}(z_i;\Theta)]^2}{\sigma^2_{\rm obs}(z_i)}. \tag{19}$$

Here $\mu_{\rm obs}(z)$ and $\mu_{\rm the}(z;\Theta)$ are distance modulus given by direct observation of SNIa and determined by equation (16), respectively. Also, $\sigma_{\rm Obs.}(z)$ is the mean standard deviation, associated to $\mu_{Obs.}(z)$ containing systematic and random parts. N represents the number of observations. Apparently, this Likelihood function to be maximum when for a values of the free parameter of cosmological model, Θ, χ^2 reaches to its global minimum. The value of error-bar at 1σ confidence interval of free parameters, Θ are determined by the likelihood function based on the following condition

$$68.3\%=\int_{-\sigma^-}^{+\sigma^+}\mathcal{L}(X|\Theta)d\Theta. \tag{20}$$

Some model parameters represented in χ^2 function introduced in equation (16) are called nuisance parameters, $\bar{M}$. They can decrease the convergency of parameter estimation procedure. One should be marginalized as

$$\bar{\chi}^2=-2\ln\int_{-\infty}^{+\infty}e^{-\chi^2/2}d\bar{M}, \tag{21}$$

where

$$\bar{M}=5\log\left(\frac{c/H_0}{1\quad{\rm Mpc}}\right)+25. \tag{22}$$

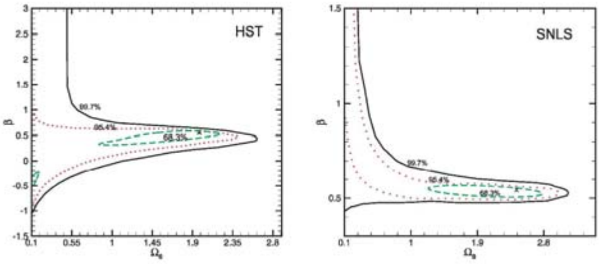

FIG. 4. Contour plots for β and Ω_0 determined by HST (left panel) and SNLS (right panel) SNIa catalogs.

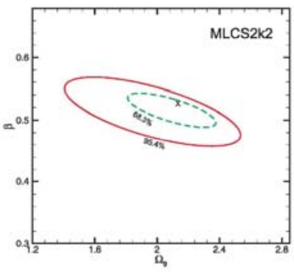

FIG. 5. Joint likelihood analysis for β and Ω_0 determined by MLCS2k2 SNIa catalog.

Using equations (18) and (19), we find:

$$\bar{\chi}^2(X_0) = \chi^2(\bar{M} = 0, \Theta) - \frac{B(X_0)^2}{C} + \ln\left(\frac{C}{2\pi}\right), \quad (23)$$

where

$$B(X_0) = \sum_i^N \frac{[\mu_{\rm obs}(z_i) - \mu_{\rm the}(z_i; \Theta, \bar{M} = 0)]}{\sigma^2_{\rm obs}(z_i)}, \quad (24)$$

$$C = \sum_i^N \frac{1}{\sigma^2_{\rm obs}(z_i)}. \quad (25)$$

Equivalent to marginalization is the minimization of χ^2 with respect to $\bar{M}$ as follows χ^2 can be expanded in terms of $\bar{M}$

$$\bar{\chi}^2_{\rm SNIa}(X_0) = \chi^2(\bar{M} = 0, X_0) - 2\bar{M}B + \bar{M}^2C, \quad (26)$$

which has a minimum value for M = B/C and results in $\bar{M}$

$$\bar{\chi}^2_{\rm SNIa}(X_0) = \chi^2(\bar{M} = 0, X_0) - \frac{B(x_0)^2}{C}. \quad (27)$$

We use some recent of SNIa samples published in literature .Union set, contains a new compilation of Type Ia supernovae, a new data set of low-redshift nearby-Hubble-flow supernovas and new analysis procedures to work with these heterogeneous compilations. It is compiled of 414 SNIa, which reduces to 398 SNIa after selection cuts, includes the recent large samples of SNIa from the Supernova Legacy Survey and ESSENCE Survey, the older data sets, as well as the recently extended data set of distant supernovae observed with HST.

The 192 ESSENCE SNIa data using the four sets of SNIa data: 60 ESSENCE SNIa, 57 Supernova Legacy Survey (SNLS) SNIa, 45 nearby SNIa, and 30 new SNIa recently discovered by the Hubble Space Telescope (HST) and classified as Gold SNIa. The ESSENCE project [16] is a ground-based survey that design to detect about 200 SNIa Ia in the redshift range of 0.2 and 0.8 to measure the equation of state of Dark energy to better than 10 percent. The SNLS and the nearby SNIa data as the complementary cosmological probes have been refitted by [16] with the same light curve fitter used for the ESSENCE data.

The CfA3 sample is added to the Union set (2008) to form the Constitution set. The CfA3 addition makes the cosmologically-useful sample of nearby SNIa between 2.6 and 2.9 times larger than before, reducing the statistical uncertainty to the point where systematics play the largest role. Constitution used four light curve fitters SALT, SALT2, MLCS2k2 (RV = 3.1), and MLCS2k2 (RV = 1.7). SALT produces high-redshift Hubble residuals with systematic trends versus color and larger scatter than MLCS2k2. MLCS2k2 overestimates the intrinsic luminosity of SNIa with $0.7 < z < 1.2$.

To study the early expansion history of the Universe, Riess et. al. [9] initiated the first systematic, space-based search and follow-up effort to collect SNIa at $z > 1$, carried out in conjunction with the Great Observatories Origins Deep Survey (GOODS) Treasury program conducted with the Advanced Camera for Surveys (ACS) aboard HST. A separate piggyback program was utilized to obtain target of opportunity (ToO) follow-up HST observations of the SNe Ia with ACS and NICMOS (the Near-Infrared Camera and Multi-Object Spectrograph). Elsewhere they present a color-based method for discrimination of SNIa at $z > 1$ from other transients and the full harvest of the SNIa survey. This makes MLCS2k2 sample.

We used 71 high redshift type Ia supernovae discovered during the first year of the 5-year Supernova Legacy Survey (SNLS). These events were detected and their multi-color light-curves measured using the MegaPrime/MegaCam instrument at the Canada-France-Hawaii Telescope (CFHT), by repeatedly imaging four one-square degree fields in four bands. Follow-up spectroscopy was performed at the VLT, Gemini and Keck telescopes to confirm the nature of the supernovae and to measure their redshift.

21 newly discovered Type Ia supernovae (SNIa) with the Hubble Space Telescope (HST) make the HST sample. These objects, which include 13 spectroscopically confirmed SNIa at z <1, were discovered during 14 epochs of re-imaging of the GOODS fields North and South over two years with the Advanced Camera for Sur-

veys on HST. Together with a re-calibration of previous HST-discovered SNIa, the full sample of 23 SNIa at $z<1$ provides the highest-redshift sample known.

The Gold06 SNIa data set recently released consists of five distinct subsets defined by the group or instrument that discovered and analyzed the corresponding data. These subsets are: the SNLS subset (47 SNIa), the HST subset (30 SNIa), the HZSST subset (41 SNIa), the SCP subset (26 SNIa) and the Low Redshift (LR) subset (38 SNIa). These subsets sum up to the 182 SNIa of the Gold06 data set.

TABLE II. The best values for the free parameters of the adiabatic matter creation model with the corresponding χ^2_{dof} from the fitting with the different catalogs at 1σ and 2σ confidence levels.

Catalog	χ^2_{dof}	${\Omega_0}^{+1\sigma+2\sigma}_{-1\sigma-2\sigma}$	$\beta^{+1\sigma+2\sigma}_{-1\sigma-2\sigma}$
Gold	0.859	$2.13^{+0.17+0.29}_{-0.25-0.68}$	$0.50^{+0.02+0.04}_{-0.02-0.05}$
ESSENCE	1.006	$2.13^{+0.01+0.13}_{-0.33-0.85}$	$0.53^{+0.03+0.04}_{-0.02-0.05}$
HST	1.108	$1.99^{+0.16+0.36}_{-0.11}$	$0.53^{+0.05+0.09}_{-0.05}$
Constitution	1.167	$2.05^{+0.21+0.35}_{-0.25-0.76}$	$0.51^{+0.02+0.05}_{-0.00-0.02}$
MLCS2k2	1.282	$2.29^{+0.06+0.23}_{-0.25-0.76}$	$0.51^{+0.03+0.06}_{-0.01-0.04}$
Union	3.260	$2.39^{+0.01+0.09}_{-0.27-0.51}$	$0.50^{+0.03+0.04}_{-0.00-0.01}$
Nearby	6.524	0.909	–
SNLS	13.258	$2.45^{+0.35+0.55}_{-0.73}$	$0.51^{+0.03}_{-0.00-0.01}$

IV. DISCUSSION AND CONCLUSION

In this paper we explored one of the alternative scenarios to explain accelerating phase for the Universe which is so-called adiabatic matter creation model. The most recent SNIa data sets, namely, Gold06, Union, Essence, Nearby, HST, MLCS2k2, Constitution and SNLS were used. These catalogs contain supernova distance modulus versus redshift. Table I gives data description for mentioned observations. The confidence interval at 1σ and 2σ as well as the best fit values for β and Ω_0 have been reported in Table II. Figure (1) shows relative likelihood functions based on various data set for model parameters. Joint confidence interval at 1σ and 2σ have been shown in figures (2), (3), (4) and (5). Our results demonstrated that the goodness of fit according to the reduced χ^2 of Essence data set is better than other catalogs. Based on figure (1) one finds that using Nearby catalog to impose constraint on model free parameters leads to no meaningful result. Considering Hubble parameter relation with β, mentioned in equation (8), in addition to containing poor number of data points and being very low redshift sample , we find out that low redshift data sets are not good enough to get conclusion about the model. In HST catalog containing high redshift data points caused a good χ^2_{dof} though lack of enough data points caused the worst consistency at 2σ. SNLS catalogue is suffering from low redshift range too and has the worst goodness of fit subsequently gives an improper 2σ confidence curve. Finally, in spite of the size of Essence and Constitution to be large but they don't give an acceptable 3σ confidence interval. This result is also demonstrated by MLCS2k2. This happens may caused by amassed data point in low redshift part.

[1] J. C. Bueno Sanchez et al., arXiv: astro-ph/0908.2636.
[2] http://lambda.gsfc.nasa.gov/product/map/dr4/params
[3] Lima J.A.S., Germano A.S., Abramo L.R.W.: 1996, Phys. Rev.D53, 4287.
[4] J. A. S. Lima and J. S. Alcaniz, arXiv: astro-ph/9902337.
[5] J. S. Alcaniz and J. A. S. Lima, Astron.Astrophys. 349 (1999) 729-734arXiv: astro-ph/9906410.
[6] M. Hicken et al., Astrophys. J. 700, 1097 (2009) , arXiv: astro-ph/0901.4804.
[7] M. Kowalski et al., Astrophys. J. 686, 749 (2008), arXiv: astro-ph/0804.4142
[8] J. Lu et al., arXiv: astro-ph /0812.3209.
[9] A. G. Riess et al.Astrophys.J.607:665-687 (2004), arXiv: astro-ph/0402512
[10] P. Astier et al. [The SNLS Collaboration], Astron. Astrophys. 447, 31 (2006), arXiv: astro-ph/0510447
[11] A. G. Riess et al., Astrophys. J. 659, 98 (2007), arXiv: astro-ph/0611572.
[12] S. Nesseris et al., arXiv: astro-ph /0612653.
[13] Prigogine I. et al.: 1989, Gen. Rel. Grav. 21, 767
[14] Kolb E.W.: and Turner M.S.: 1990, The Early Universe, Redwood City: Addison-Wesley
[15] S. Baghram et al., arXiv: astro-ph /0904.4390.
[16] W.M. Wood-Vasey et al., [astro-ph/0701041]
[17] Movahed, S. Mohammad Sadegh, PHD thesis, (1385), Cosmology of variable dark energy and statistical analysis of cosmic microwave background radiation, Iran, Tehran, Sharif University of Technology.

The effect of solar gravitational moment on the ephemerid of planets

Zahra Fazel
University of Tabriz, Faculty of Physics, Department of Theoretical and Astrophysics.

Solar gravitational moments (J_n) are the perturbations in the solar gravitational field which appear because of the rotational potential energy. This parameter with different orders of magnitude (n= 2, 4, 6, 8) indicate the distortions in the solar outer shape (as a bulge in the equator and some depression near the poles). These perturbations not only affect the outer solar shape but also the ephemerid of planets in the solar system. Contribution of the solar quadrupole moment is in two ephemerides cases: 1) perturbation of the inclination of planetary orbit, 2) perturbation of the advance of planetary perihelion. Since these quantities are the relativistic phenomena, so the study of gravitational moments will be useful in order to investigate the parameters of the general relativity in Post-Newtonian approach.

Introduction

Historically, a major scientific crisis on the solar oblateness and relativity developed in the middle of the 19 century when LeVerrier found that the planet Mercury apparently was not moving accordance with the laws of Newtonian mechanics and gravitation. At that time, it was not yet understood the role of the solar gravitational moments but the effect of some extra perturbing mass in the solar system was a possible reason for predicted the excess motion of Mercury's perihelion. In 1895, Newcomb recognized the importance of the oblate shape of the Sun and he claimed that some extra mass for example a massive planet near the Sun or a planetoid ring in the elliptical plane could lead to the regression of the node of Mercury's orbit and its perihelion. The great interest is in 1915 when Einstein showed that the excess motion of Mercury's perihelion could be explained as a relativistic effect. In 1965, Brans and Dicke reported an alternative theory in the general relativity consist of the gravitational moments. But this theory was not very successful. In 1979 Moffat used the other version of this theory which he considered relation between the solar oblateness and gravitational moments.

In the present work was applied the value of the solar quadrupole moment (J_2) obtained in our work (Ajabshirizadeh et al. 2008) to determined its contribution in the planetary ephemerid.

Contribution of the solar quadrupole moment in planetary ephemerid

In 1983, Campbell and Moffat represented a relationship which demonstrated the presence of J_2 in two ephemerid quantities, that is, the changing rate of the advance of perihelion (ω) and the inclination (i) of planet's orbit:

$$\langle d\omega/dt\rangle = [(3(GM)^{3/2})/(c^2 a^{5/2}(1-e^2)] + [(3(GM)^{1/2}\mathbf{J_2} R_{sol}^2)/(4a^{7/2}(1-e^2)^2)] \times 3[\cos i \cos i_s + \sin i \sin i_s \cos(\Omega- \Omega_s)]^2 - 1 - 2\,\Omega \sin i \sin i_s \sin(\Omega- \Omega_s) \times [\cos i \cos i_s + \sin i \sin i_s \cos(\Omega- \Omega_s)] - [(3\mathbf{l_{sol}}^4 c^2(1+e^2)^3)/((GM)^{1/2} a^{9/2}(1-e^2)^3)] \quad (1)$$

and

$$\langle di/dt\rangle = [(3(GM)^{1/2}\mathbf{J_2} R_{sol}^2)/(2a^{7/2}(1-e^2)^2)] \times \sin i_s \sin(\Omega- \Omega_s) \times [\cos i \cos i_s + \sin i \sin i_s \cos(\Omega- \Omega_s)] \quad (2)$$

where $G = 6.67 \times 10^{-11}$ $m^3kg^{-1}s^{-1}$; $M = 1.98 \times 10^{30}$ kg; $c = 3 \times 10^8$ ms^{-1}; $R_{sol} = 6.959 \times 10^8$ m; $i_s = 71^\circ 15'$ (inclination of solar equatorial plane with respect to elliptical plane of the epoch 1950); $\Omega_s = 75^\circ 4'$ (right ascension of the ascending node of the Sun). The parameters i and Ω vary from planetary orbit to planetary orbit, and all differ from i_s and Ω_s. Finally $l_{sol} = (3.1 \pm 0.5) \times 10^6$ (a Post-Newtonian parameter is introduced in Campbell et al. 1983 and Moffat and Woolgar, 1988).

Having some information about the planets like as semi-major axis in a elliptical orbit (a) and the eccentricity (e), one can calculate the advance of ω and inclination, i, knowing an exact value of J_2.

It should be noticed that in the calculations the equatorial plane of the Sun is coincident in the orbital plane of the planets.

Post-Newtonian parameters

As it mentioned above in introduction, in order to test the alternative general relativity, one can use the Post-Newtonian parameters. These parameters characterized by α, β and γ refer to the Edington-Roberston parameters of Parameterized Post-Newtonian (PPN) formalism

which describe a fully conservative relativistic theory of gravitation.
The PPN parameters cover particular case of Einstein's theory of gravitation (general relativity) characterized by $\alpha = \beta = \gamma = 1$.
Here, α is the weak equivalence principle with value $(\alpha - 1) < 10^{-14}$, Will (2001) (this parameter is often removed in the fully dynamical theories);
β is the amount of non-linearity in the superposition law of gravity which is obtained from the Nordvelt's effect in Lunar Laser Ranging measurements, $\beta \in [0.999, 1.0003]$; and γ characterizes the amount of space curvature produced by unit rest mass with value $\gamma - 1 = (-2.1 \pm 2.3) \times 10^{-5}$ from the light deflection experiments via the spatial mission CASSINI (Bertotti et al. 1998).
Study of the solar quadrupole moment's effect on the PPN's parameters will be important to determine the ephemerid of planets particularly the advance of perihelion (ω) of Mercury which is a combination of the purely relativistic effect and the Sun's J_2. The formula which I applied them in my calculations is (Pireaux and Rozelot, 2003):

$$\Delta\omega = \Delta\omega_{0GR}\, \delta \quad (\text{rad/ rev}) \qquad (3)$$

with $\Delta\omega_{0GR} = (3 \pi R)/(\alpha\, a\, (1-e^2))$
and $\delta \equiv [\, 1/3\, (2\alpha^2 + 2\alpha\, \gamma - \beta) - (R_s^2)/(R\, \alpha\, a(1-e^2)) * J_2(3\sin^2 i - 1))$
where the following parameters are:
R, the Schwarzschild radius of the Sun, $2GM_s/c^2$;
M_s, solar mass;
R_s, solar radius;
J_2, the quadupole moment of the Sun (our exact value, -2.613×10^{-7});
a, the semi-major axis of Mercury's orbit;
e, the eccentricity of Mercury's orbit;
i, the inclination of Mercury's orbit.
Notice that formula (3) is only valid for fully conservation theories. If it is not case, the complete expression is given in Pireaux and Rozelot, 2001.
I used our J_2's value obtained in Ajabshirizadeh et al (2008) in the above relationships for calculating the $\Delta\omega$ for four near planets and I compared them with the ones of Campbell and Moffat (1983). The results are in following table.

Table 1: The rate of changing of the advance of perihelion for four near planets to the Sun. Left column is the data for J_2 (from the data for the line splitting of the solar oscillations) considered by Campbell & Moffat and the right one is our value of J_2.

	$\Delta\omega$ for $J_2 = (5.5 \pm 1.3) \times 10^{-6}$	$\Delta\omega$ for $J_2 = -2.613 \times 10^{-7}$
Mercury	43.09	43.00
Venus	8.67	8.61
Earth	3.85	3.83

Table 1, shows the difference in calculated $\Delta\omega$ between two different values of the solar quadrupole moment. It indicates the contribution of J_2 in the ephemeris of planets and the role of two different values in changing of $\Delta\omega$. One can conclude that by decreasing of the J_2's value, $\Delta\omega$ is also decrease for three considered planets. Our results indicate a 0.2 % agreement with the ones of Campbell and Moffat. They believe that the general relativity can not explain all of the planetary data; so the anti-symmetric gravitational theory (Moffat and Woolgar, 1988) make it possible to solve all problems in this case by adding other parameter l_{sol}. It seems that exact value of J_2 is useful in the calculations, for this purpose it is needed to program some spatial missions.

Conclusion

Study of the relativistic aspects in the approach of solar dynamical parameters is crucial which open a perspective to the future researches. In this case, obtaining the dynamical value of J_2, i.e. a value independent of the solar models related to rotation and density, will be interested. In order to measure this dynamical value of J_2, there is several important spatial missions, for example:

- BeppiColombo: 2012, precise determinations of the PPN parameters; measuring the precision of the node line of Mercury as a function of J_2 (Milani et al. 2002);
- GAIA: 2012, precise determinations of the PPN parameters; finding the PPN-J_2 relation by applying the relative advance of perihelion of the planets (Hestroffer And Berthier, 2004);
- DynaMICCS: precise determinations of rotation of the Sun's center where approximately whole mass of the Sun is concentrated in there, and indirect determination of J_2 (Turck-chieze et al. 2006);
- Other projects like as ASTROD (Ni, 2002) or LATOR (Turyshev et al. 2005) for precise determination of J_2 and the PPN of γ.

References

1. Ajabshirizadeh, A., Rozelot, J.P. and Fazel, Z., 2008, *Scientica Iranica*, **15**.
2. Bertotti, B. and Giampieri, G., 1998, *Solar Physics*, **178**.
3. Campbell, L. and Moffat, J.W., 1983, *Astrophyisics J.*, **275**

4. Campbell, L., McDow, J.C., Moffat, J.W. and Vincent, D., 1983, *Nature*, **305**.

5. Hestroffer, D. and Berthier, J., 2004, *ESA SP-576*, **297**.

6. LeVerrier, U.J., 1985, *Ann. Obs. Paris*, **5**.

7. Milani,A. Vokrouhlicky,D., Bonanno, C. and Rossi, A., 2002, *Physical Rev. D*., **66**, Issue 8.

8. Moffat, J.W. and Woolgar, E., 1988, *Physical Rev*., **37**.

9. Newcomb, S., 1895-1898, *Tables of Mercury, Astr. Pap. Am. Ephem*., **6**, part 2, Washington.

10. Ni, W.T., 2002, *Intern. J. Mod. Phys. D*., **11**.

11. Pireaux, S. and Rozelot, J.P., 2003, *Astrophys. And Space Sci*., **284**.

12. Turck-chieze, S et al., 2006, *39th ESLAB Symposium, Netherland*, April 2005, gr-qc/0506104.

13. Turyshev, S.G. et al., 2005, *39th ESLAB Symposium, Netherland*, April 2005, gr-qc/0506104.

14. Will, C.M., 2001, *http:www.livingston.org/articles/volume4/2001-4will*.

Flux Tube emergence And MHD Equations

Taheri,Nahid and Ajabshirizadeh,Ali
Tabriz University
[2]Research Institute for Astronomy and Astrophysics of Maragha

A major goal in solar physics has during the last decades been to find how energy flux generated in the solar convection zone is transported and dissipated in the outer solar layers. Here we solve the full MHD equations with non-grey and non-LTE radiative transfer and thermal conduction along the magneticfield lines. The emergence of the magnetic flux tube input at the bottom boundary into a weakly magnetized atmosphere is presented.

Introduction:

One of the stated goals of the newly launched Hinode satellite is to follow the evolution
Of magnetic flux from the moment of emergence through the photosphere and into the
chromosphere and corona. Such observations come at a timely moment as they should prove a fertile testing ground for the 3D numerical models of flux emergence that are
now becoming available due to the technological development of massively parallel computers and algorithms to utilize these. The emergence of magnetic flux tubes has been studied in order to understand not only the dynamics of flux emergence evolution, but also its effects on the solar atmosphere. One of the major questions we are considering is how flux tube emergence changes the energetics and the dynamics of the photosphere, chromosphere and corona. What contribution to atmospheric energetics does the emerging flux represent? Another set of important questions relates to the observational signatures of flux emergence throughout the atmosphere. This paper is rather a first attempt to consider a framework for some of the problems of a magnetic field up through the atmosphere.
The emergence of a magnetic flux tube into such an atmosphere results in varied atmospheric responses. In the last decade more realistic 3D MHD models of active region flux emergence have been developed up to the photosphere. Cheung et al. (2007) consider flux emergence through a convective layer including detailed photospheric radiative transfer,but excluding the layers above the photosphere.

Equations and Numerical Method:

In order to model the rise of magnetic flux tubes through the upper convection layer and their emergence through the photosphere and into the chromosphere and corona we solve the equations of MHD using the Oslo Stagger Code (OSC):

$$\frac{\partial \rho}{\partial t} + \nabla(\rho u) = 0 \quad (1)$$

$$\frac{\partial u}{\partial t} + (u\nabla)u + \frac{1}{\rho}\nabla(P+\tau) = +\frac{J\times \mathrm{B}}{\rho} + g \quad (2)$$

$$\frac{\partial (e)}{\partial t} + \nabla(eu) + u\nabla P = \nabla F_r + \nabla F_c + Q_{joule} + Q_{visc} \quad (3)$$

$$\frac{\partial B}{\partial t} = \nabla\times(u\times B) - \nabla\times(\eta J) \quad (4)$$

Where ρ represents mass density,u fluid velocity, P the gas pressure, J the current density, B the magnetic field, g gravitational acceleration, and e the internal energy. The viscous stress tensor is written τ and the resistivity η. Fr represents the radiative flux, Fc represents the conductive flux, and QJoule and Qvisc are the joule heating and viscous heating respectively.These equations are solved using an extended version of the numerical code described in Dorch & Nordlund (1998); Mackay & Galsgaard (2001) and in more detail by Nordlund& Galsgaard at http://www.astro.ku.dk/□kg and Hansteen et al. (2007)

Initial and boundary conditions:

The five models described here are run on a grid of 256 × 128 × 160 points spanning
8 × 4 × 16 Mm^3 and 16 × 8 × 16 Mm^3. At these resolutions the models have been run for roughly one hour solar time. The average temperature at the bottom boundary is maintained by setting the entropy of the fluid entering the computational domain. The bottom boundary is otherwise open, allowing fluid to enter and leave as required. The upper boundary is set so that the temperature gradient is zero; no conductive heat flux enters or leaves the computational domainthrough the top boundary.Of course, without coronal heating the corona would cool on a time scale of roughly anhour (depending on the magnetic field topology) , when no heat flux enters the model through the upper boundary.

We have therefore seeded the initial model with a magnetic field in which sufficient stresses can be built up to maintain coronal temperatures in the upper part of the computational domain.The initial field was obtained by semi-randomly spreading some 20 − 30 positive and negative patches of vertical field at the bottom boundary, then calculating the potential field that arises from this distribution in the remainder of the domain. Stresses sufficient to maintain a minimal corona are built up by photospheric motions after roughly 20 minutes solar time.
At the top boundary the hydrodynamic variables (aside from the temperature) and the magnetic field are set by characteristic extrapolations. This method hinders most of the reflections that are due to the presence of the upper boundary. No joule Injection of magnetic flux:
We introduce a magnetic sheet or magnetic flux tubes into the lower boundary of the model described above. heating is added in the top five computational zones.

The OSC uses a numerical method that, in principle, does not change ▼.B in time. The solenoidal condition must be enforced on the boundary to ensure that no magnetic monopoles are introduced. This is implemented by applying the boundary condition to the *electric* field, the staggered mesh will then enforce▼. B = 0 to the numerical accuracy of the operators at the boundary. The magnetic field variation at the boundary is defined by:

$$\frac{\partial B}{\partial t} = \nabla \times E \quad (5)$$

Where , for example for the x component of the electric field we have

$$E^n{}_X = E_X + \frac{\Delta(B_y)}{\tau}\Delta z \quad (6)$$

where Enx is the new *x* component of the electric field at the boundary, τ is the time step size, and _z is the vertical cell size, _(By) = Bny −By is the difference between the value of the magnetic field we would like to impose at the boundary, Bny , and the current boundary field By.
We have run models in which a constant horizontal field in the y direction has been injected, and several models where a flux tube is introduced. The flux tube is horizontally rectilinear with twisted magnetic fields lines. The expression for the magnetic field has a structure given by

$$B_{long} = B_O \exp(-\frac{r^2}{R^2})e_z \quad (7)$$

$$B_{trans} = B_{long}\, rqe_\Phi \quad (8)$$

where $r = \sqrt{(x - x_0)^2 + (z - z_0)^2}$

is the radial distance to the center of the tube that has radius R. Blong, Btrans are the longitudinal and transversal magnetic fields in cylindrical coordinates respectively. The parameter q is used by Linton et al. (1996) and Fan et al. (1998) to define the twist of the magnetic field. Following Cheung & Moreno-Insertis (2006), we define a new twist parameter, λ, as
λ ≡ q R. (13)
As the flux tube enters the computational box, the height of the center of the tube (zo) changes in time. The speed of flux tube, (dzo/dt), is set to the average of the velocity of plasma inflow at the boundary in the region where the magnetic flux tube is located each time step.
The field defined by equations 11 and 12 is easily seen to be a horizontal axisymmetric magnetic flux tube in which the longitudinal field has a gaussian profile in the radial direction

Results

We have carried out five simulations with different twist and magnetic field strength in order to study the effects of flux emergence in the photosphere and in th chromosphere.A summary of the runs completed is shown in table 1. In describing the reaction of the atmosphere to the introduction of new magnetic flux we will specifically concentrate on four layers placed at heights of z = 10,235, 450, and 900 km.
We find that all runs show a similar series of events after the emerging magnetic flux pierces the photosphere. These events, that occur at roughly the same time in all models,are summarized in table 2, which shows the processes observed in the simulations ordered in time. These processes are described in the following sections according to where they happen.

Table 1.
Simulation description

Name	Twist λ	B0 [G]	Size	Comment	Time [s]
A1	0.1	4484	8× 4 × 16 Mm3	Flux tube in y direction	2200
A2	0.2	3363	8 × 4 × 16 Mm3	Flux tube in y direction	2100
A3	0.3	4484	8 × 4 ×16 Mm3	Flux tube in y direction	2500
A4	0.6	4484	8 × 4 × 16 Mm3	Flux tube in y direction	3200
B1	0.0 1	121	16 × 8 × 16 Mm3	Flux sheet in y direction.	4500

Table 2.
time evolution

Process	Time[s]
Expansion of granular cells in the photosphere	900
Expansion of the reverse granulation	920
Cooling of the center of granular cells in the photosphere	1160
Tube crosses the photosphere	1300
Tube crosses the chromospheric height forming reverse granulation	1380
Magnetic field moved to the intergranular lanes in the photosphere	1550
Reverse granulation cooling with expansion	1560
Tube crosses the layer z = 450 km	1660
The cells return to “normal” size in the photosphere	2100
Upper chromosphere vertical expansion and cooling	2900

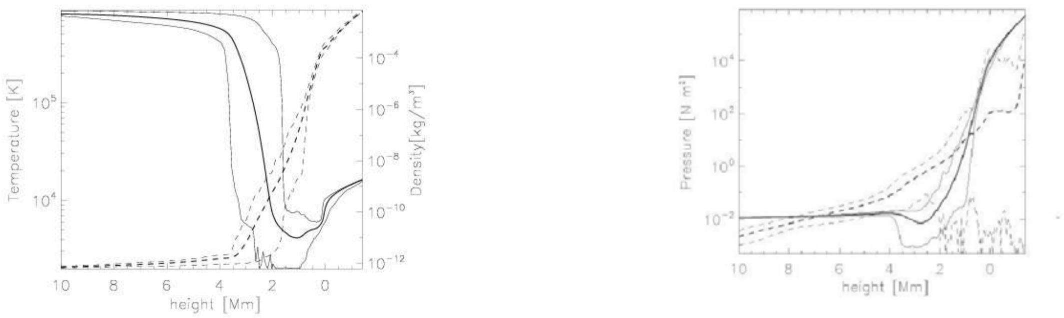

Fig. 1.— Left panel: Temperatures (solid) and densities (dashed). Right panel: Gas (solid) and magnetic (dashed) pressures. All as a function of height in the initial model. Minimum and maximum values are shown in grey, average values are shown in black. The photosphere is situated at z ≈ 0 Mm. The models extent in height is from −1.4 to 14 Mm (top 4 Mm not shown here).

Refrences:
Hansteen V. H., De Pontieu B., Carlsson M., et al., 2007, ArXiv e-prints, 711
Hansteen V. H., 2004, Initial simulations spanning the upper convection zone to the corona, in IAU Symposium, Vol. 223, Stepanov A. V., Benevolenskaya E. E., Kosovichev A. G. (eds.), Multi-Wavelength Investigations of Solar Activity, p. 385
Hansteen V. H., Carlsson M., Gudiksen B., 2007, 3D Numerical Models of the Chromosphere, Transition Region, and Corona, in Astronomical Society of the Pacific Conference Series, Vol. 368, Heinzel P., Dorotovi

Detection of Solar Oscillation (g-modes)

Homayouni Yasaman , Adjabshirizadeh Ali
Faculty of physics, Tabriz University, Tabriz

Abstract
Solar gravity modes are the best probes to study the solar interior and specifically the dynamics of solar core. Here we present an analytical solution to solar gravity modes using relativistic space curvature inside 0.4 fractional radius with the assumption of mass accumulation inside solar core. Furthermore, a modified geometry for the interior regions of the sun is presented. Consequently, a relation of g-mode frequency with fractional radius is calculated. Considering the radial effect of gravitation, in order to calculate the spherical harmonics we have set the value of l to zero.

Introduction

The attempt to observe solar gravity modes have continued since the first observations of helioseismology and the studies on solar g-modes have continued ever since, the classical studies of Christensen Dalsgaard, 1997, and Rogers and Glatzmaier, 2005, have lead to some numerical models and understandings of these waves [1, 2]. However, these modes have yet to be detected due to their small surface amplitudes and the fact that the study on this area is confided mostly to theory.

Solar acoustic modes have their maximum sensitivity in the outer layers, so they are indirect observables of the radiative zone. On the contrary, the maximum sensitivity of the gravity modes is in the solar core, therefore, *g*-modes are capable of providing information about regions that p-modes are incapable of.

Here we try to calculate the frequencies of g-mode oscillations using relativistic metrics. First we present equations of oscillating sun in radial form to obtain the displacement vector in terms of radial component and horizontal component. Using the concept of space-time curvature inside solar the displacement vector along radius is calculated. Consequently, frequencies of oscillation are obtained by replacing the displacement vector with the radial component in equations of oscillating modes.

Expansion of equations of solar linear oscillation

Equations of linear oscillation close to the equilibrium state is derived supposing the spherical symmetric of sun. While the spherical symmetric of perturbations is ignored (l=0) we reach to equations of radial oscillation, these equations are a special solution to non-radial oscillation. For a briefer study of equations of oscillation it is better to use separation of components method so that we would have a radial component and a horizontal component. In case of the displacement vector,

$$\vec{\delta r} = \zeta_r \hat{a}_r + \zeta_\theta \hat{a}_\theta + \zeta_\phi \hat{a}_\phi = \zeta_r \hat{a}_r + \vec{\zeta}_h, \tag{1}$$

where ξ_r is the radial component, ζ_h is the horizontal component and $\hat{a}_\phi, \hat{a}_\theta, \hat{a}_r$ are the unit vectors in directions of ϕ, θ, r. The equation of motion in terms of perturbed quantities [1, 3] is

$$\rho_0 \frac{\partial^2 \vec{\delta r}}{\partial t^2} = -\vec{\nabla} \rho' + \rho_0 g' + \rho' g_0. \tag{2}$$

And the general form of displacement vector $\vec{\delta r}$ is [4]

$$\vec{\delta} r = \sqrt{4\pi}\,\mathrm{Re}\left\{\left[\zeta_r(r)\, y_l^m(\theta,\phi)\hat{a}_r + \zeta_h(r)\left(\frac{\partial y_l^m}{\partial\theta}\hat{a}_\theta + \frac{1}{\sin\theta}\frac{\partial y_l^m}{\partial\varphi}\hat{a}_\phi\right)\right] e^{-i\omega t}\right\}. \tag{3}$$

in this equation ω is the frequency of spherical oscillation modes which is complex, the real part is normally called the alternation frequency and the imaginary part shows the growth of mode.

Relativistic Space

From the viewpoint of relativity, the presence of mass results in curvature of space-time which alters the Euclidean geometry [5].Considering that Schwarzschild metric explains the curvature .Another expression of the space-time curvature is provided by the familiar embedding diagram. For this, z(r) is the displacement ("lift-out") along a radius of the star, viewed as embedded in Euclidean (r, z) space for $r \le R$.

$$z(r) = \sqrt{\frac{3c^2}{8\pi G\rho}}\left(1 - \sqrt{1 - \frac{8\pi G\rho}{3c^2} r^2}\right) \tag{4}$$

is calculated by using the fact that

$$ds^2 = dz^2 + dr^2 \tag{5}$$

for the uniform density model and for the realistic solar interior model.
The evaluated z(r) equation considering the substitution of r with fractional radius

$$z(r) = 0.345\times 10^{11}\left(1 - \sqrt{1 - 4\times 10^{-4} x^2}\right) \tag{6}$$

By replacing the z(r) parameter with radial displacement component $\tilde{\zeta}_r$ from expression (1) and also, using only the radial part from equation δr, this choice was made because of the radial effect of gravitation, for a more explicit approach we limit our choice of m and l to m = l = 0, replacing these conditions in equation (3)we obtain

$$\delta r = z(r)\cos\omega t \tag{7}$$

Previously we mentioned equation of motion in terms of perturbed quantities (2), in this equation the first term on the right hand side of equation is the source of p-mode oscillation, the second term reduces to zero according to Cowling approximation and the last term is the source of g-mode oscillation. Since we chose the radial part for the displacement vector considering the effect of gravitation, here in equation of motion we pick up the term which is the source of g-modes

$$\rho_0 \frac{\partial^2 \delta r}{\partial t^2} = \rho' g_0 \tag{8}$$

Now if we replace the δr from expression (7) in (8) we obtain

$$-\rho_0 \omega^2 z(r)\cos\omega t = \rho' \frac{G\mu_{(r)}}{r^2} = \rho' \frac{G\rho_0 \frac{4}{3}\pi r^3}{r^2} \tag{9}$$

where ρ' is the perturbed density $\rho = \rho_0 + \rho'$,also choosing ρ' as a function of cosines $\rho' = A Cos\,\omega t$ and replacing it in above expression we obtain

$$-\omega^2 z(r)\cos\omega t = -A\cos\omega t G\frac{4}{3}\pi r \tag{10}$$

The reason for this choice of ρ' is

$$\rho = \rho_0 + \rho' = \frac{M}{V} = \frac{M}{V_0 + V'} \tag{11}$$

where V is the perturbed volume $V_0 + V'$

$$(\rho_0 + \rho')(V_0 + V') = M = Const. \tag{12}$$

since the left hand side and the right hand side of the above expression are constant, as a result the term $\rho' V_0 + V'\rho_0$ must also be constant. For simplicity we choose this constant to be zero.

$$\rho' V_0 + V'\rho_0 = 0 \tag{13}$$

$$V' = V_0' \quad \cos\omega t \quad \Rightarrow \rho' = -\frac{\rho_0 V_0'}{V_0}\cos\omega t = -\rho_0'\cos\omega t \tag{14}$$

From expression (10) we have

$$\omega^2 z(r) = \rho_0' G\frac{4}{3}\pi r \Rightarrow \omega^2 = \frac{4\pi G r}{3z(r)} \tag{15}$$

Utilizing equation (15) the frequency for internal oscillation is obtained.

$$\upsilon_{(r)} = \left(\frac{\rho_0' r G}{3\pi z_{(r)}}\right)^{\frac{1}{2}} \tag{16}$$

According to fig. 2 for r = 0.4 R the frequency of oscillation is 690 micro hertz. We could use this data to fit the expression above and calculate ρ_0' ,by which we obtain

$$\rho_0' = 267.65 \quad \left(\frac{kg}{m^3}\right) \tag{17}$$

Using this and the expression for z(r) we obtain the relation for g-mode oscillation frequency

$$\upsilon_{(r)} = \sqrt{\frac{3.81\times10^{-11}x}{(1-\sqrt{1-4\times10^{-4}x^2})}} \tag{18}$$

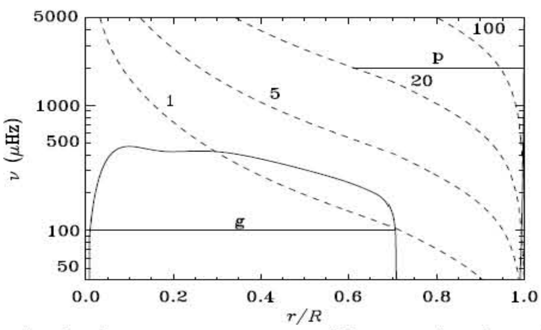

Fig. 1. The frequency in terms of fractional radius [1].

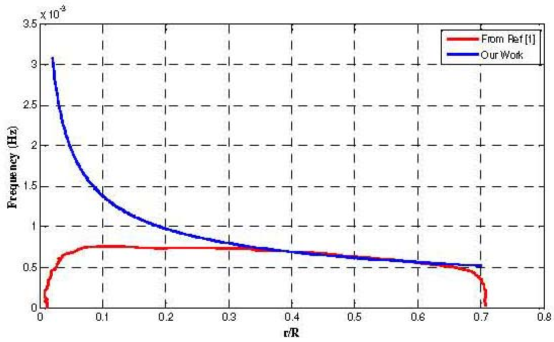

Fig. 2. (Blue) the oscillation frequency from center to surface of sun that was obtained through theoretical methods. The red curve represents the oscillation frequency obtained by Dalsgaard from [1].

Conclusion

In this work the expression for frequency of solar g-modes was estimated by the supposition of concentration of mass under 0.4 radius.
Close to the center of the sun, these frequencies are high and were fitted by the data on 0.4 solar radius. Figure 3 shows the result of our work in comparison with [1] in fig. 2. These two curves show a high degree of conformity from 0.3 to 0.7 fractional radius. However under 0.2 fractional radius the difference between the two curves is large. This could be due to the selection of different type of metric here in contrast to that used by Schwarzschild. Since the Schwarzschild metric is an external solution for curvature, examining other types of metric could solve this singularity for us.
As a final note, the truth about these theories must be achieved through agreement between theory and observation. However, the small surface amplitude of g-modes makes this study difficult.

References

1. Christensen-Dalsgaard, Lecture notes on Stellar Oscillation, Springer, 1997.

2.Tamara M. Roger and Gary A. Glatzmaier, Gravity waves in the Sun, *Mon. Not. R. Astron. Soc* **364**. 1135-1146, 2005.

3. Mohammad Esmailzadeh aghdam, g-mode oscillation, Master thesis, Dept. of Astrophysics, University of Tabriz, Winter 2008.

4. Jean Pierre Rozelot, the Sun's Surface and Subsurface, Springer, 2003.

5. Wm. Robert Johnston, "Calculations on space-time curvature within the Earth and Sun," www.johnstonsarchive.net/relativity, 2008.

Galaxy Luminosity Functions of XMM-LSS Clusters

H. G. Khosroshahi
School of Astronomy, Institute for Research in Fundamental Sciences (IPM), Tehran, Iran
A. Alshino, T. J. Ponman, J. Willis, M. Pierre, F. Pacaud, G. P. Smith

X-ray surveys remain one of the most popular methods of finding galaxy systems. Due to the strong density dependence of X-ray emissivity, X-ray cluster selection is much less vulnerable to contamination along the line-of-sight than optical methods. The XMM-Large Scale Survey (XMM-LSS), a contiguous X-ray survey, has a well-defined selection function which is used to produce a sample of galaxy groups to study their intracluster medium and galaxy properties at medium to high redshift.

We study the galaxy luminosity function of a sample of X-ray selected clusters from the XMM-LSS survey using the Canada-France-Hawaii Telescope Wide Synoptic Legacy Survey (CFHTLS). These are mostly groups and poor clusters, with masses (M500) in the range 0.6 to 19 x 10^{13} $M_{\odot}$ and redshifts between 0.05 and0.61. Hence these are some of the highest redshift X-ray selected groups to have been studied. We derive individual luminosity functions (LFs) for all groups as well as redshift-stacked and temperature-stacked LFs in three filters, g′, r′ and z′, down to $M = -14.5$. All LFs were fitted by Schechter functions which constrained the faint-end slope, α, but did not always fit well to the bright end. Derived values of α ranged from −1.03 to as steep as −2.1. We find no evidence for upturns at faint magnitudes. Evolution in α was apparent in all bands: it becomes shallower with increasing redshift; for example, in the z′ band it flattened from -1.75 at low redshift to -1.22 in the redshift range z =0.43-0.61. Eight of our systems lie at z ~ 0.3, and we combine these to generate a galaxy LF in three colours for X-ray selected groups and poor clusters at redshift 0.3. We find that at z ~ 0.3 α is steeper (-1.67) in the green (g′) band than it is (-1.30) in the red (z′) band. This colour trend disappears at low redshift, which we attribute to reddening of faint blue galaxies from z ~ 0.3 to z ~ 0.

INTRODUCTION

Most of our knowledge of galaxies is based on observations of the local universe, although distant universe observations have also provided a wealth of information. Statistical studies of galaxies at high redshift are mostly limited to rich galaxy clusters mainly due to observational limitations. Galaxy clusters are important cosmological environments where key galaxy transformation such as stripping and strangulation occur. However, in the hierarchical formation of structure rich clusters are the latest structures to be formed. Lower mass systems or galaxy groups may have been the place where galaxies experience a substantial degree of evolution through processes such as mergers and tidal interaction, as a result of the higher efficiency of these processes in the lower velocity dispersion environment of groups.

The Galaxy luminosity function (LF) – the number of galaxies per unit volume in the luminosity interval L to L + dL – has been widely used to study the formation of galaxies and the evolution of galaxy populations with redshift. It is also an excellent statistical tool for describing how different environments influence the properties of galaxies. Both the bright end (Bower et al. (2006), Naab et al. (2007)) and the faint end (Marzke et al. (1994), Khochfar et al. (2007)) of the LF have been the subject of in-depth studies, as they offer strong observational constraints for models of galaxy formation and evolution. While the bright end of the LF is affected by AGN feedback (Bower et al.

(2006)), the faint-end slope is predominantly influenced by feedback from supernovae (Dekel et al. (1986)), and provide a direct indicator of the significance of dwarf galaxies, which are expected to behave differently in rich and poor clusters. Multi-colour LFs, in particular, probe the history of the faint galaxy population, including its star formation history – see for example, Adami et al. (2007). The vast majority of studies of the galaxy LF give faint-end slopes in the range -1 to -2. Most of these have limited magnitude depth ($M > -16$) and recent deep studies are mostly confined to rich local clusters. These studies not only disagree on the value of the faint-end slope, but they also disagree on the exact form of it, as some studies (e.g. Gonz`alez et al. (2006)) found upturns; a single Schechter function was not an adequate fit to the faint end, and a double Schechter function was required to give a reasonable fit. The existence of these upturns is very sensitive to the method used to determine galaxy membership, with some approaches including spurious galaxies or excluding genuine cluster members due to their low surface brightness.

The evolution of the faint-end slope is hard to study, mainly because the number of faint galaxies detected decreases sharply with increasing redshift. Liu et al. (2008) found that the faint-end slope of a field galaxy population became shallower with increasing redshift (up to $z = 0.5$) for all galaxy spectral types. Simulations by Khochfar et al. (2007) show a measurable dependence of the faint-end slope of the galaxy luminosity function on redshift. However, most of this dependence is seen over a relatively large redshift range, $z \geq 2$. Furthermore, it is hard to discriminate galaxy environments in such studies.

OBSERVATIONS AND ANALYSIS

Optical photometry of the XMM-LSS survey was obtained from the Canada-France-Hawaii Telescope Wide Synoptic Legacy Survey 1, referred to as the CFHTLS Wide survey. Data were obtained in five passbands ($u*$, g', r',i' , z') down to a nominal magnitude limit of $i' = 24.5$. Of the 19 deg^2 of CFHTLS Wide data available in the W1 survey area, 4 deg2 overlap with the X-ray selected cluster catalogue presented by Pacaud et al. (2007). Hence our photometric data are drawn from four $1^\circ \times 1^\circ$ catalogues derived from the survey data. The data used in this paper are based upon the reduction procedure outlined in Hoekstra et al. (2006). Source extraction and photometry were performed using SExtractor v2.5.0 (Bertin and Arnouts 1996). Zero point information for sources detected in the CFHTLS Wide field survey W1 area was extrapolated from common sources detected in the Sloan Digital Sky Survey equatorial patch which overlaps the southern edge of the W1 area.

XMM-LSS Class 1 (C1) clusters are a well-controlled X-ray selected and spectroscopically confirmed cluster sample. The criteria used to construct the sample guarantee negligible contamination by point-like sources. The observations of the clusters were performed in a homogeneous way (10-20 ks exposures). 17 out of the 29 XMM-LSS C1 clusters are covered by the CFHTLS Wide field survey. In this paper, we study the luminosity functions of 14 of these 17 clusters – dropping the three with the highest redshifts because their photometric data is too poor to allow useful constraints to be obtained.

Galaxies were detected by SExtractor (Bertin & Arnouts (1996)). Luminosity functions (LFs) were produced in three bands, namely, g', r' and z'. The completeness threshold magnitudes for the three filters g', r' and z' were found to be 24, 23.5 and 23, respectively. These values are also consistent with results based on comparison of the number counts per field to deeper data from the CFHTLS Deep Field and CCCP Megacam observations.

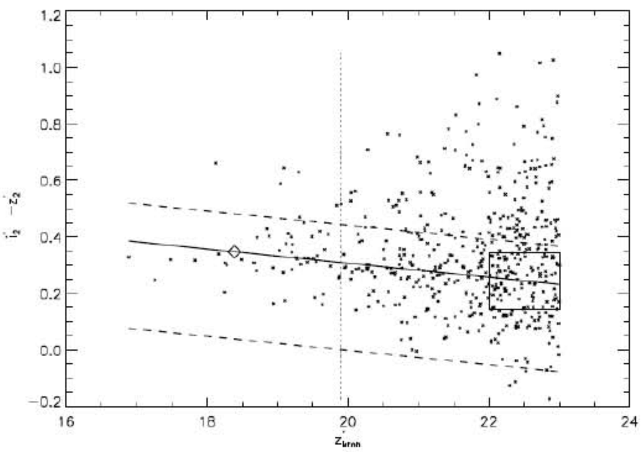

The CMD were used to colour select galaxies which might be cluster members, hence reducing the background due to interlopers. The colours used for this were u^*-g' versus g'_{kron}, g'-r' versus r'_{kron} and i'-z' versus z'_{kron} for the three filters. Colours were measured within 2 arcsec aperture. To define and select cluster members in the CMD, we defined upper and lower colour cuts and only galaxies between these two lines were used to produce the LF, as galaxies outside these limits were most likely not cluster members. To define these two colour cuts, we first defined the red sequence line in the CMD and then pushed this line up and down to allow for statistical errors, and for the likely range of galaxy colours.

RESULTS

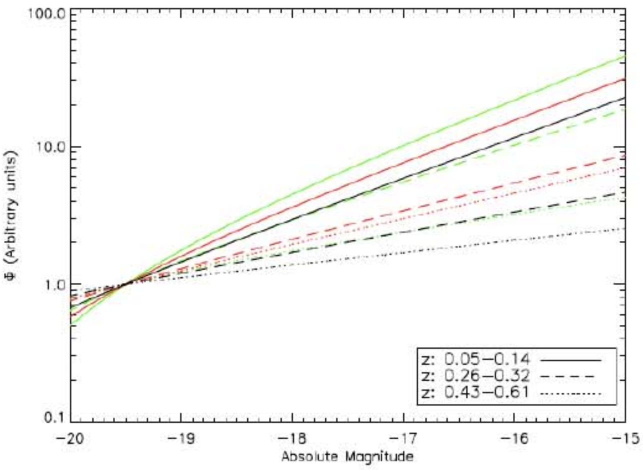

The faint end of the fitted LFs of the C1 sample grouped into three redshift bins: low (0.05-0.14, solid lines), intermediate (0.26-0.32, dashed lines) and high (0.43-0.61, dotted lines). Colours represent the filter bands: green for g', red for r' and black for z'. All LFs were normalised to have Phi = 1 at M=-19.5 for easy comparison. The faint end slopes become shallower with increasing redshifts. Also, at intermediate redshift (dashed lines), the slope shows a trend with colour, becoming steeper towards the blue. This colour trend largely vanishes at low redshifts (solid lines). The values show a trend with colour. The faint-end slope of z-stacked clusters becomes steeper as we move from z' (red side) band to g' (blue side). This trend is very obvious in the second, third and fourth redshift bins ($0.29 \leq z \leq 0.32$) and much less obvious and maybe absent (within the errors) in the first bin ($z \leq 0.14$), see Figure 4 in which we plotted the values of alpha for the three bands for the lower- and intermediate redshift bins. The increase in the faint-end slope of the Schechter function in the bluer bands means that at the faint side of the colour-magnitude diagram the blue galaxies outnumber red ones.

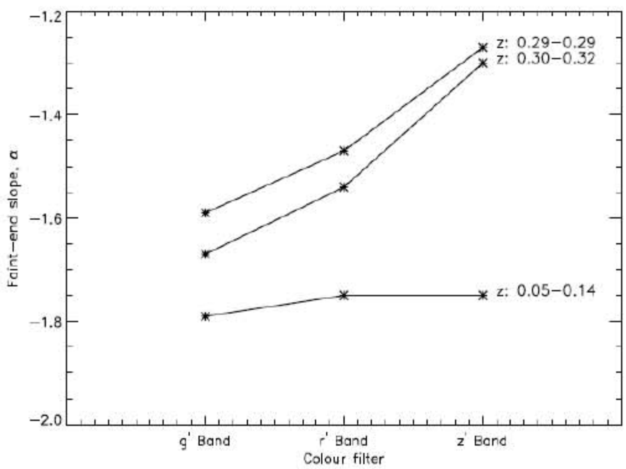

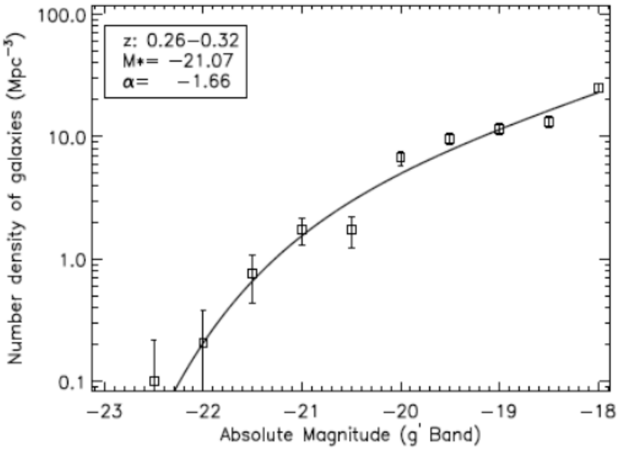

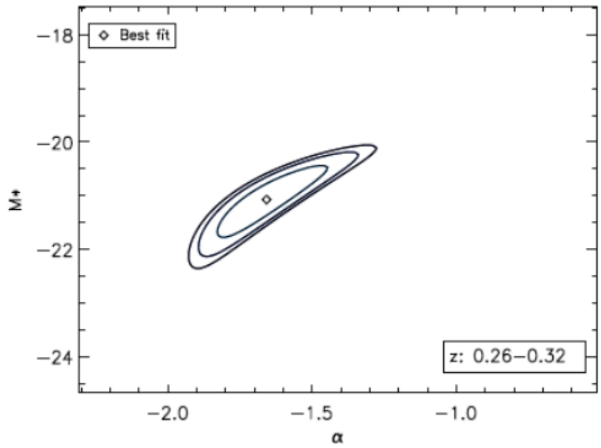

Our results show an evolutionary trend of the faint-end slope, alpha, in all bands used:g′, r′ and z′. Liu et al. (2008) examined the faintend slope of the V-band LF of *field* galaxies with redshifts $z < 0.5$ and found that it becomes shallower with increasing redshift their alpha changed from −1.24 for the lowest redshift bin $0.02 \leq z < 0.1$ to −1.12 for the highest redshift bin $0.4 \leq z < 0.5$. In clusters, a recent study by Lu et al. (2009) of an optically selected cluster sample found steepening of the faint end with decreasing redshift since $z \sim 0.2$, and that the relative number of red-sequence dwarf galaxies had increased by a factor of ~ 3.

It is possible that this LF slope trend with redshift is linked to the finding of Harsono & Propris (2007) that the 'upturn' in the LF faint end (i.e. the excess of galaxies above a single Schechter function) is found only in low redshift clusters. They attributed this to the recent infall of star-forming field galaxies or the whittling down of formerly more massive objects. The impact of recent infall of galaxies into clusters is also supported by the work of Lisker et al. (2007), who showed that dEs in the Virgo cluster fall into two major morphological subclasses: a) dEs with blue centres, thick disks or features reminiscent of late-type galaxies, such as spiral arms or bars; this class showed no central clustering, suggesting that they are an unrelaxed population formed from infalling galaxies. The second subclass is b) nucleated dEs – a fairly relaxed population of spheroidal galaxies indicating that they have resided in the cluster for a long time, or were formed along with it. Lisker et al. (2007) also pointed to other studies deriving similar results, indicating that this subclassification is not specific to the Virgo cluster.

Adami C., Durret F., Mazure A., Pello R., Picat J. P., West M., Meneuk B., 2007, A&A, 462, 411
Bower R. G., Benson A. J., Malbon R., Helly J. C., Frenk C. S., Baugh C. M., Cole S., Lacey C. G., 2006, MNRAS, 370, 645
Bertin, E., Arnouts, S. 1996, A&AS, 117, 393
Gonz´alez R. E., Lares M., Lambas D. G., Valotto C., 2006, A&A, 445, 51
Dekel A., Silm J., 1986, ApJ, 303, 39
Hoekstra H. et al., 2006, ApJ, 647, 116
Khochfar S., Silk J.,Windhorst R. A., Ryan R. E., 2007, ApJ, 668, L115
Lisker T., Grebel E. K., Binggeli B., Glatt K., 2007, ApJ, 660, 1186
Liu, C. T., Capak, P., Mobasher, B., et al. 2008, ApJ, 672, 198
Lu Ting, et al. 2009, MNRAS, Preprint 2009arXiv0905.3392
Marzke R. O., Geller M. J., Huchra J. P., Corwin H. G., 1994, AJ, 108, 437
Naab T., Burkert A., 2003, ApJ, 597, 893
Pacaud, F., et al. 2007, MNRAS, 382, 128

Making a 1M⊙ Model Star by CESAM Code

Naficy, K. Shirzad, M.T.

Birjand University

Abstract

A 1M⊙ model star is made by CESAM code, and some parameters such as radius, temperature, pressure, luminosity, mass, density, opacity, and chemical composition are determined and their evolution are studied. The results of this study are compared with the results of a standard solar model.

Keywords: Methods: numerical. Stars: evolution. Stars: interior

Introduction

Within the limitations due to electronic degeneracy, CESAM allows the computation of the quasi-static evolution of stellar models as long as the assumption of quasi-static equilibrium remains valid, i.e. till the exhaustion of oxygen in the core. The modular structure of CESAM facilitates the choices among several physical formalisms, for equation of state, convection, opacities, diffusion coefficients, etc. Many nuclear networks and initial mixtures are available which allow optimizing the physical description according to the kind of model and evolutionary phase of interest. Mass loss and fall of planetoids are also implemented.

CESAM has been especially designed to facilitate the implementation of various physical constants, opacities, equation of state, atmosphere, nuclear networks etc. So, its overall structure is separated in two spaces:
1) A "*physical space*" where the coefficients of the differential equations are written in a form close to their physical formalism.
2) A "*numerical space*" where the differential equations are formally solved.
Input files, very often only the "*input data file*" is needed. It is read at the onset of the run and collects all the requirements needed for the calculations such as physical parameters (mass, chemical composition, mixing-length parameter, etc.), numerical parameters (maximum number of shells, kind of precision, etc.), criteria for halting the computations (age to be reached, value of the hydrogen abundance at center, etc.), and names and locations of the external data files containing the data of the tabulated EOS and opacity, names for the physical routines to be used, name for the model, for the set of units to be used, etc.
Output files, at the end of each stage, a "*return binary file*" (RBF) is created. It contains all the data needed to initialize or pursue a computation. "*Output data files*" (ODF) are created if necessary. Three ODF are designed for adiabatic, non adiabatic and inversion asteroseismic investigations [1].

Equations of State

In numerical computation methods, a star model is assumed to consist of symmetric layers and uses physical equations of state. In CESAM, equations (1) are used, where Ω is angular velocity, $\nabla=\frac{\partial \ln T}{\partial \ln P}$, ε the rate of nuclear energy per mass unit, U the inner energy per mass unit, χ_i the mass ratio of element i, F_i the flow of χ_i due to diffusion, n_x the number of elements, and ψ_i the velocity of χ_i due to nuclear-thermal reactions.
In addition, we assume that

a) The star is spherical and in hydrostatic equilibrium.
b) There is no macroscopic motion unless in convection state
c) There is no mass loss.
d) We ignore the rotation and magnetic field effects.

$$\frac{\partial T}{\partial M} = \frac{\partial P}{\partial M}\frac{T}{P}\nabla$$
$$\frac{\partial P}{\partial M} = -\frac{GM}{4\pi R^4} + \frac{\Omega^2}{6\pi R}$$
$$\frac{\partial L}{\partial M} = \varepsilon - \frac{\partial U}{\partial t} = \frac{P^2}{\rho^2}\frac{\partial \rho}{\partial t} \qquad (1)$$
$$\frac{\partial R}{\partial M} = \frac{1}{4\pi R^2 \rho}$$
$$\frac{\partial X_i}{\partial t} = -\frac{\partial F_i}{\partial M} + \psi_i \qquad 1 < i < n$$

We have adopted the values of the astronomical and physical constants specified for the calculation of the stellar models compared in the different ESTA tasks [2]. For the solar global parameters, we therefore took $R_\odot = 6.9599 \times 10^{10}$ cm, $L_\odot = 3.846 \times 10^{33}$ erg·s^{-1} and $M_\odot = 1.98919 \times 10^{33}$ g. The value $R_\odot$ refers to the radius of the model layer where $T = T_{\rm eff} = 5777$ K. For solar age, we adopted the value $t_\odot = 4.57$ Gyr [3].

Results and Discussion

1. Element abundance

Figures 1, 2, and 3 show the abundances of ${}^1_1H$, ${}^3_2He$ *and* ${}^4_2He$ as the functions of radius (in units of R$_\odot$) respectively.

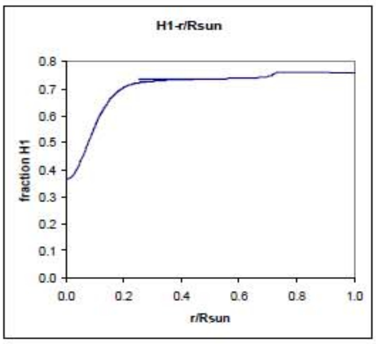

Fig. 1 Abundance of ${}^1_1H$ versus radius

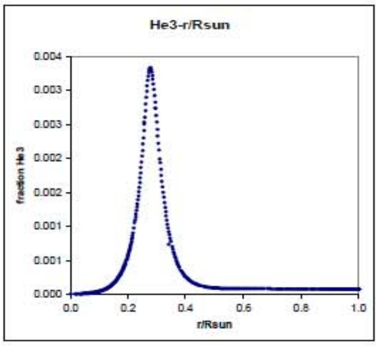

Fig. 2 Abundance of ${}^3_2He$ versus radius

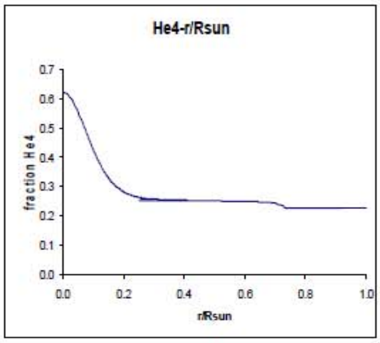

Fig. 3 Abundance of ${}^4_2He$ versus radiu

Since the Sun's primary energy production mechanism is PP chain, ${}^3_2He$ is an intermediate species in the reaction sequence. During the conversion of hydrogen to helium, ${}^3_2He$ is produced and then destroyed again (Eqs. (2) and (3)). At the top of the hydrogen burning region, where the temperature is lower, ${}^3_2He$ is relatively more abundant because it is produced easier than it is destroyed. At greater depths, the higher temperatures allow the helium-helium interaction to proceed more rapidly and the ${}^3_2He$ abundance decreases once again. The slight ramp in the ${}^1_1H$ and ${}^4_2He$ curves near 0.7 $R_\odot$ reflects evolutionary changes in the position of the based of the surface convection zone, combined with the effects of elemental diffusion [5].

$${}^1_1H + {}^1_1H \rightarrow {}^2_1H + e^+ + \nu_e$$
$${}^2_1H + {}^1_1H \rightarrow {}^3_2He + \gamma \qquad (2)$$
$${}^3_2He + {}^3_2He \rightarrow {}^4_2He + 2{}^1_1H \qquad (3)$$

2. Temperature and pressure

We can find temperature and pressure of all layers of stellar interior in the output file of the code. Figures 4 and 5 show these parameters as functions of radius.

Since nuclear energy is produced in the core and is transformed to the surface by convection and radiation, it is expected for temperature to decrease from core to surface.

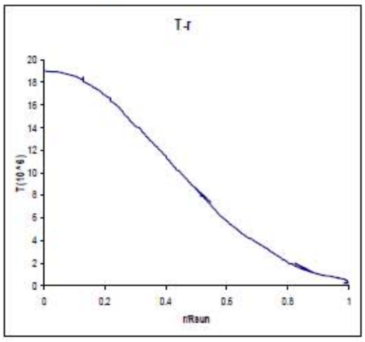

Fig. 4 Change of temperature versus radius

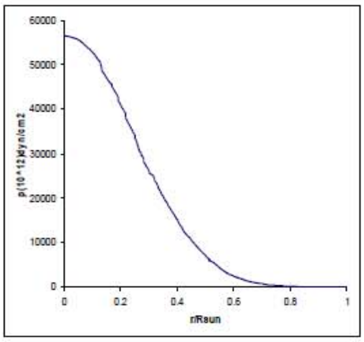

Fig. 5 Change of pressure versus radius

The variation of pressure versus radius is forced by the conditions of hydrostatic equilibrium (the second eq. of (1)), the ideal gas law, and the composition structure of the star [5]. Of course, boundary conditions applied to the stellar structure equations require that T, P, and ρ become negligible at the surface.

3. Interior luminosity and its derivative relative to radius

In figures 6 and 7 we plot the luminosity L and $\frac{dL}{dr}$ as a function of radius. These curves show that the produced energy is higher in mid layers instead of the core. It may not be expected at the first glance, but it's seen in reality because the amount of mass in every layer increases with increasing radius, the fourth equation of (1), thus, although rate of produced energy per unit mass, ε, decreases from center to surface, the most contribution of produced energy is not in the center. It is mostly in layers that have enough mass for producing nuclear energy, the third equation of (1).

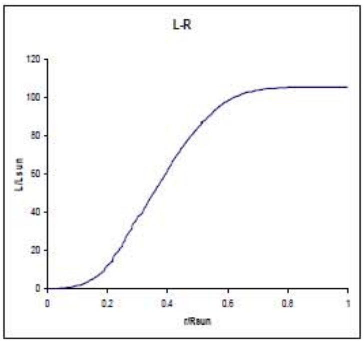

Fig. 6 Luminosity versus radius

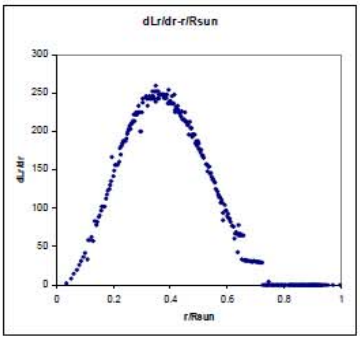

Fig. 7 Gradient of luminosity versus radius

4. Mass, density and opacity

Mass and density as the functions of radius are shown in figures 8 and 9.

In our model of star with the solar mass, opacity as a function of temperature is shown in figure 10. Similar curves with different densities are plotted in figure 11 [5]. In this figure we can see:

- The opacity increases with the increase of density.
- At the left-hand side of figure, we can see each single curve rises steeply with increasing temperature. This reflects the increase in the number of free electrons produced by the ionization of hydrogen and helium.
- The decline of the curve after the peak in the opacity roughly follows a Kramers law, $\bar{\kappa} \propto T^{-3.5}$, and is due to the bound-free and free-free absorption of photons.
- The curve directs flatly at the right-hand side of the figure. Electron scattering dominates at the highest temperatures.

The second and third of above characteristics also exist in our results (figure 10)

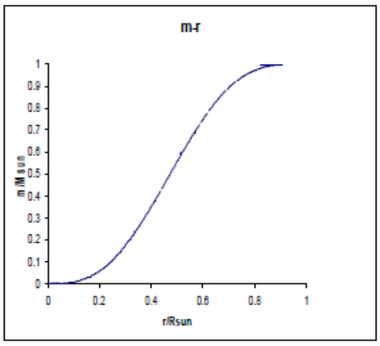

Fig. 8 Mass versus radius

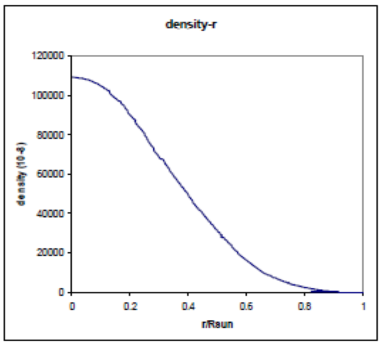

Fig. 9 Density versus radius

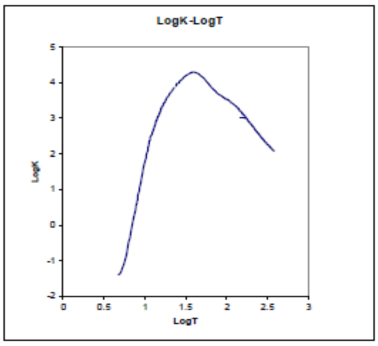

Fig. 10 Opacity versus temperature

6. Evolution

Evolution curve of our model star in H-R diagram is shown in figure 12. It's comparable to 1 M⊙ star evolution curve in figure 13 [5]. The age of star in every stage for our result and standard model of the Sun in [5] are shown in table 1. It's seen that our results are in good agreement with results of standard model star.

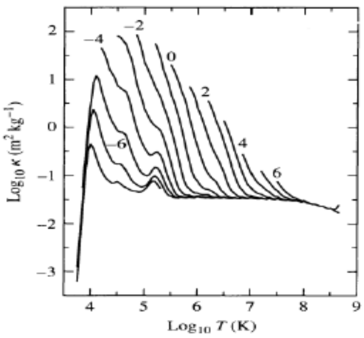

Fig. 11 Opacity versus temperature in the Sun [5]

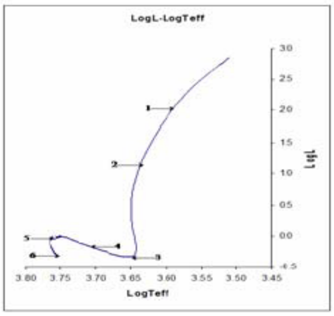

Fig. 12 Evolution curve of our model

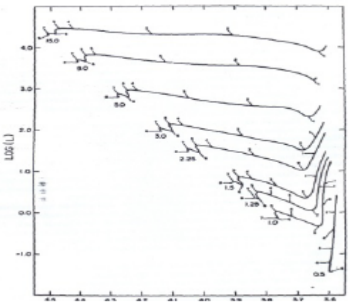

Fig. 13 Evolution curves of stars with different masses [5]

Table 1 The age of star in every stage (million years)

Stage	1	2	3	4	5	6
Our result	0.307	1.901	8.085	23.00	27.50	34.00
Standard model [5]	0.3195	1.786	8.711	30.90	25.19	34.18

References

1. Morel, P. and Lebreton, Y., CESAM: a free code for stellar evolution calculations, Astrophys Space Sci (2007)
2. Lebreton, Y., Monteiro, M.J.P.F.G., Montalbán, J., Baglin, A., Michel, E., The CoRoT evolution and seismic tools activity. , Astrophys. Space Sci. (CoRoT/ESTA Volume). Springer, Berlin (2007)
3. Bahcall, J.N., Pinsonneault, M.H.,Wasserburg, G.J.: Solar models with helium and heavy-element diffusion. Rev. Mod. Phys. **67**, 781(1995)
4. Morel, P., CESAM a code for stellar evolution calculations. Astron. Astrophys. Suppl. Ser. **124**, 597–614 (1997)
5. Ostlie, D.A., Carroll, B.W., "*an introduction to modern stellar astrophysics*", Weber Stat University (1996)

EP Andromedae A double contact Asynchronous Binary

Davood Manzoori[1]
[1] *Department of Physics, University of Mohaghegh Ardabili , P. O.Box. 179, Ardabil, Iran*

In this research the V- band light curve analysis, along with Spot modeling of the EP And system, was carried out using the PHOEBE program. Then absolute dimensions of the system were determined, through which we can discuss the structure and evolution of the system. These analysis indicate, that the system is A double contact binary with nonsynchronous rotation. It is notable that this is the first comprehensive study of the system.

I. INTRODUCTION

EP And (Period= 0.404 d, Vmax=11.45mag. Primary's spectral type F8 V, spectral type of secondary is not known), was discovered by Strohmeier et al. (1955), Eclipsing nature of the system was first found by Filatov (1960). this system was classified as contact binary star by Gettel et al. (2006). It seems that the first photometric BV- light curves (LC) of the system were published by Pribulla et al. (2001), they determined (without giving the errors) only few elements i.e. q, the mass ratio, i, inclination of the orbital plane, and T_2, the effective temperature of secondary star. They found that the secondary component is slightly hotter and the system is probably of W UMa type. Qian and Yuan (2001) studied the period of the system and reported a period increase with the rate dP/dt= $1.16\times10^{-7}d/yr$, without pointing out the factors affecting the period change.

II. LIGHT CURVE SOLUTION AND SPOT ANALYSIS

The present work utilizes the PHOEBE (PHysics Of Eclipsing BinariEs) version 0.3a code (Prsa and Zwitter 2005; Prsa et al. 2008), which is a photometric program based on the Wilson-Devinney code (see Wilson-Devinney 1971, Van Ham and Wilson 2003) and produces corresponding parameters, as well as absolute dimensions, from which we can discuss the evolution of the system. The photometric data were selected in Johnson V passband filter from the website of American Association of Variable Stars Observers (AAVSO). These data were obtained on october 26, 29 and November 25, 2007. The stars HD 70123 and HD 71024 were used as comparison and check, respectively and The following ephemeris given by the fourth edition of the GCVS (Kholopov 1985),

$$T_{minI} = 2442638.5109 + 0.40411057E \qquad (1)$$

was used to convert all the data to phase-magnitude system. The PHOEBE version 0.3a program, was used to obtain the solutions of the LCs in three different modes, namely: over contact, semidetached and double contact modes, separately (See Sec. 3, the discussion). The limb darkening coefficients were taken from Van Hamme (1993) limb darkening tables (for a relative abundance [M/H] =0.1). The other parameters, i.e., q, the mass ratio, Ω_1, the linear functions of true potential of primary, i, the orbital inclination, e, the orbital eccentricity, T_1, T_2, temperatures of primary and secondary components respectively, and L_1, luminosity of the primary component, g_1 The gravity darkening coefficients, $A_1$and F_1, the primary's rotation parameter, were set as free. The free parameters were adjusted sequentially by trial and error method. The calculated parameters for each mode, along with the mean absolute dimensions separately are listed in (column 2 to 7) Table 1. While the normal points and synthetic LCs are illustrated in Fig. 1. [The Synthetic curves and observed points, in the over contact and semi detached modes are not shown here, because of space limitations]. All the parameters with subscription "$\odot$" refer to the relevant quantities of the sun. The errors of parameters listed in Table 1, are mean statistical errors. It was observed that the synthetic LCs in each case could be best fitted to the observed data points by assuming one or two rather large dark spots on the primary and /or secondary, the details of which are given in Table 2. The positions of the spots on the component stars were specified and denoted in Fig. 2 for all the three modes.

III. RESULTS AND DISCUSSION

Since the EP And system was defined as a probable W UMa type star by Pribulla, therefore, the first attempt was made to obtain LC solution and fit in the over contact W UMa mode of the PHOEBE program. But after devoting enough time it was observed that the fitting was not so proper, despite the assumption of two dark spots, one on each component (without spot assumption even rough fitting was not possible). Therefore the mode of the program was changed to double contact. In this mode the fitting of the synthetic curve to the observed data was improved (see Fig. 1). Except the Ω_1 estimated errors of calculated parameters particularly temperatures of the component stars were reduced appreciably (as compared

TABLE I. The results obtained through V light curve analysis using PHOEBE program

Param	*Double contact Sol*		*Over contact Sol.*		*Semidetaced Sol*	
	Value	*Mean Abso. Dimensions*	*Value*	*Mean Abso. Dimensions*	*Value*	*MeanAbso.Dimensions*
i(Deg)	75.50±0.08		80.20 ±0.15		74.50 ±0.11	
e	0.010 ±0.001		0.01±0.001		0.01±0.001	
$T_1(K)$	6700±24	$A(R_\odot)$= 2.10	6600±137	$A(R_\odot)$= 2.20	6700±28	$A(R_\odot)$= 2.10
$T_2(K)$	6700±41	$M_1/M_\odot$=0.571	6450±158	$M_1/M_\odot$=0.655	6600±41	$M_1/M_\odot$=0.571
Ω_1	3.556±0.890	$M_2/M_\odot$=0.192	2.720±0.110	$M_2/M_\odot$=0.223	3.279±0.012	$M_2/M_\odot$=0.192
Ω_2	3.339	$R_1/R_\odot$=0.933	2.724	$R_1/R_\odot$=0.981	3.255	$R_1/R_\odot$=0.735
q	0.337±.003	$R_2/R_\odot$=0.602	0.340±.002	$R_2/R_\odot$=0.552	0.337±0.007	$R_2/R_\odot$=0.602
$(\frac{L_1}{L_1+L_2})_V$	0.62±0.02	$T_1/T_\odot$=0.6700±.0024	0.62±0.02	$T_1/T_\odot$=0.6600±.0137	0.62±0.02	$T_1/T_\odot$=0.6600±.0024
$(\frac{L_2}{L_1+L_2})_V$	0.37	$T_2/T_\odot$=0.6700±.0041	0.38	$T_2/T_\odot$=0.6450±.0158	0.31	
					$T_2/T_\odot$=0.6600±.0041	
X_1	0.515	M_{bol1}=5.244	0.522	M_{bol1}=5.333	0.0.515	M_{bol1}=5.310
X_2	0.526	M_{bol2}=4.294	0.522	M_{bol2}=4.250	0.516	M_{bol2}=4.812
A_1	0.85±0.53		1.00(±0.09		0.78±0.06	
A_2	0.08		0.16		0.55	
g_1	0.58±0.03		1.00±0.06		0.60±0.07	
g_2	0.57		1.00		0.54	
$F1$	1.40±0.02					
	Chi2=0.035		Chi2=0.054		Chi2=0.084	

TABLE II. Spot parameters obtained through PHOEBE Programme for EP And components

Star	*Colat (Deg)*	*Long (Deg)*	*size(Deg)*	*Temp. factor*	*Sol Mode*
1	35.0	190.0	45.0	0.80	Double Contact
2	76.0	170.0	42.0	0.70	Double Contact
2	56.0	230.0	38.0	0.70	Double Contact
1	65.0	200.0	40.0	0.89	Over Contact
2	60.0	195.0	60.0	0.72	Over Contact
1	35.0	185.0	48.5	0.70	Semidetached
2	76.0	180.0	49.4	0.70	Semidetached

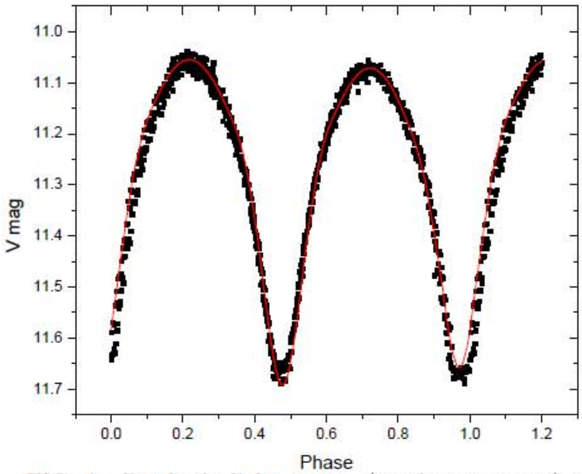

FIG. 1. Synthetic light curve, (continuous curve) using double contact mode of the PHOEBE program, and observed light curve (filled squares) in V filter, fitted based on the calculated parameters in Table 1 and spot parameters of Table 2 for EP And.

to the over contact W UMa mode, see Table 1 col.2), by assuming three dark spots, one on the primary and the other two on the secondary component see the Table 2 and Fig. 2. Moreover in this mode when F1, the synchronicity parameter of the primary, was set as a free, and then its value was changed to higher values, it was observed that the errors of calculations were reduced, while the same was not true in the previous mode. The calculations of the system's parameters and fitting of the curves to the observed data in the semi- detached mode was also performed with the aim of getting more accurate results. But In this mode also despite the assumption of two spots, one on each component, the fitting was poor, our attempts were not so successful (see Tables 1& 2). Therefore we may accept the EP And as a double contact binary system with particulars given in the first three columns of Table 1.

It seems the concept of double contact binaries first was introduced by Wilson (1979), as type of close binary which occurs only for nonsynchronism, the binaries in which both components fill their limiting lobes, naming them as double contact may be misguiding, because they do not have even a single contact point. This can occur, when at least one of the components rotates faster than synchronously, so that its limiting lobe is smaller than the respective Roche lobe (and the limiting lobe would be bigger than Roche lobe, if it rotates slower than synchronously). The situation can occur as a natural consequence of mass transfer, because transfer normally spins -up an accreting star by converting orbital to rotational angular momentum.

One of the main characteristics of semidetached (Algol type) binaries is mass transfer due to Roche lobe filling of late secondary component such mass - exchange will spin

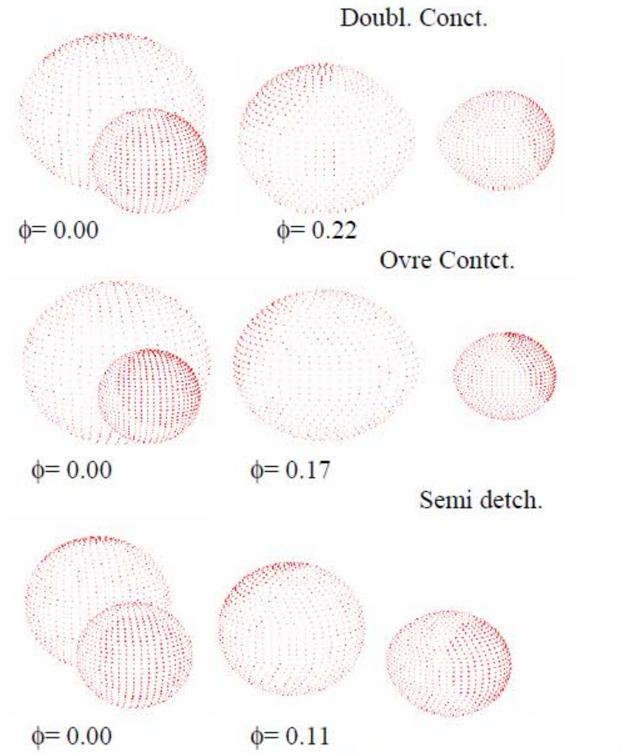

FIG. 2. Representation of spotted regions (darker areas) on the surfaces of the primary and secondary component of EP And.

-up the mass accreting star (most of whose mass is transferred material by the end of rapid phase of mass transfer). But according to Wilson et al. (1985) this rapid rotation will be damped quickly, as soon as mass transfer is stopped. Among semidetached systems there are few members which show asynchronous rotation, (see table 1 of Wilson and Twigg, 1980). Thus, near to or after the end of rapid phase of mass transfer, the mass losing star would normally be found to fill its Roche lobe (rotating synchronously), while the accreting star (or perhaps only its outer envelope) may have accommodated all of its capacity of the angular momentum which can hold, and so fill its limiting "rotational" lobe. According to Wilson and Caldwell (1978) the β Lyrae and V356 Sgr and also U Cep and some of the Algol type systems and now EP And according to present work are most likely candidates of double contact binaries. A main evolutionary consequence of Wilson's finding of double contact is that, since the accreting star after filling the limiting lobe will not be able to accommodate any more of the new high angular momentum material transferred by donor star, therefore such a system must find an alternate way for accommodaing of the transferred matter, as first noted by Wilson and Caldwell (1978); this is a probable explanation for the thick circumstellar disks seen in β Lyr and V356 Sgr, and is perhaps related to numerous strange effects seen is U Cep (see Manzoori 2008). Notice that the

existence of double contact systems introduces a symmetry in to the morphology of close binaries, in that stars may fill lobes exactly not only as a result of mass loss, but also as a result of mass gain.
The disk formed as mentioned(in preceded paragraph), reduces a substantial fraction of the primary's light and therefore the star appears relatively under luminous, therefore it should make primary eclipse shallower than expected. For the same reason it would reduce also the irradiation of the secondary light by the primary, (reduces reflection effect), if the disk emits relatively little light of its own, the effect of its eclipse by the secondary star will be slight, but the eclipse of the secondary by the disk should be appreciable. Thus secondary eclipse should be wider than primary eclipse, and should also be deeper than it would be without an eclipse by the disk. But in case of EP And this is not the case, both the eclipses are almost equal, this indicates that both of the components suffer almost equal amount of light loss which favors a common rather thick envelop surrounding both the stars. In the absence of spectroscopic data to demonstrate this envelope directly, was not possible, an alternate way to show the effect of this gaseous envelope, was by assuming dark spots on the components, to be placed at appropriate longitudes. Referring to Fig. 2 and Table 2, it can be seen that the sizes of the calculated spots are unexpectedly large, moreover their appearances are almost in opposite longitudes on the primary and secondary covering a large areas on the surfaces of the component stars, these unusual sizes of dark spots and their distribution on the surfaces of the stars could be due to absorption effects of light, caused by an envelope of material surrounding the system.
AS stated earlier one of the main conditions of the existence of double contact phase in the evolution of binary stars is nonsynchronous rotation of mass accreting component reaching the centrifugal limit. Naturally a star can not exceed its limiting rotational lobe because its equatorial matter would then be centrifugally unbound (see Wilson, 1985). This later condition is satisfied in EP And system as may be checked from Table 1, the F1= 1.4F2, means the primary is rotating faster than synchronously. The discovery of only very few members of this type of binaries, might be due to relatively brief time scale for binary to spend in double contact phase according to Li et al. (2005).

IV. CONCLUSION

In conclusion we may accept the EP And as a double contact nonsynchronous binary, in which primary is rotating faster than synchronously. Moreover a common envelope of material is surrounding both the components.

Acknowledgements We acknowledge with thanks the variable star observations from the AAVSO International Database contributed by observers worldwide and used in this research.

[1] Gettel, S. J., Geske, M. T., and McKay, T. A., 2006, AJ, 131, 621.
[2] Filatov, G. S., ATsir, 215, 20 K.
[3] Li, L., Han, Z., Zhang, F., 2005, MNRAS, 360, 272
[4] Kholopov, 1985, GCVS, fourth edition
[5] Manzoori, D., APSS, 2008, 318, 57 .
[6] Pribulla, T., Vanko, M., and Parimucha, S., 2001, IBVS, 5184
[7] Prsa, A., and Zwitter, T., 2005, APJ, 628, 426
[8] Prsa, A., Guinan, E. F., Devinney, E. J., De George, M., Bradstreet, D. H. Giammarco, J.M., Alcock, C.R., Engle, S. G., 2008, APJ, 687, 542.
[9] Qian, S., and Ma, Y., 2001, PASP, 113, 754
[10] Strohmeier, W., Geyer, E., Kippenhahn, R., 1955, Kleine Veroff entlichugen der remis sternwate No. 11, Bamberg.
[11] Van Hamme, W. 1993, AJ, 106, 2096.
[12] Van Hamme, W., & Wilson, R. E., 2003, ASP Conf. Ser. 298, GAIA.
[13] Wilson, R.E., APJ, 1979, 234, 1054
[14] Wilson, R.E., ,& Devinny, E.J., 1971, ApJ,166, 605.
[15] Wilson, R.E., & Twigg, L.W., 1980, IAUS, 88, 263.
[16] Wilson, R.E., Van Hamme, W., and Pettera, L.A, 1983, APJ, 289, 748

پارامترهای فیزیکی اصلی باد خورشیدی در هلیوسفر رصدی

علی عجبشیریزاده، آیدا ترابی،نفیسه معصومزاده

دانشگاه تبریز دانشکده فیزیک

مرکز تحقیقات نجوم واخترفیزیک مراغه

چکیده

یکی از موضوعات مهمی که در مبحث تاج خورشیدی مطرح میشودعبارت است از ترازمندی تاج در مقابل جریان باد خورشیدی‌نظر به اینکه دمای تاج بسیار بالااست انرژی جنبشی ذرات در آن به حدی است که جاذبه گرانشی خورشید نمیتواند این ذرات را نگه دارد. از این نظر جریان پیوسته ای از ذرات به نام باد خورشیدی سطح خورشید را دائما ترک میکند. این جریان گاز تقریبا ترکیبی از الکترونهای آزاد،پروتون و یونها میباشد که در مقیاس بزرگ از نظر الکتریکی خنثی است.

در این مقاله با استفاده از داده های ماهواره$ULYSSES$و $SoHo$ منحنی تغییرات پارامترهای اصلی فیزیکی باد خورشیدی نظیر سرعت متوسط پروتون ها ،چگالی پروتونها،میدان مغناطیسی بین سیارهای وهمچنین شار مغناطیسی خروجی$r^2 \Big/ B_r$بر حسب فاصله از مرکز خورشید وزمان رسم و نتایج به دست امده تعبیر فیزیکی شده است.

مقدمه

فضای بین خورشید و ستارگان شامل گاز یونیده وخنثی، میدانهای مغناطیسی وذرات باردارمیباشد. خورشیداز طریق یک حجم بزرگ به نام هلیوسفر مانع ازعبور این مواد از فضای بین ستارهای به داخل منظومه شمسی میشود.

هلیوسفر کاملا منظومه شمسی را احاطه کرده است. تاثیر خورشید تا این فواصل مطرح است زیرا باد خورشیدی تمام هلیوسفر را میپوشاند و یک فشار به سمت خارج به فضای بین ستارهای اعمال میکند. میدان مغناطیسی مربوط به باد خورشیدی مانع از نفوذ پلاسمای بین ستارهای در سطح انرژی پایین به هلیوسفر میشود، با این حال ذرات کیهانی با سطح انرژی بالا، غبار وذرات خنثی نفوذ میکنند و خصوصیات آنها توسط باد خورشیدی،گرانش خورشیدی و تبادل بار تغییر میکند .

بسیاری از ماموریتهای فضایی اکتشافاتی در مورد هلیوسفر نزدیک به استوای خورشید داشتهاند، اما فقط سفینه اولیس از استوا تا بالای قطبهای خورشید را طی کرده و اطلاعات را به سه بعد بسط میدهد .

ULYSSES فضاپیمایی است که توسط NASA وESA به طور مشترک جهت بررسی هلیوسفر خورشیدی در ٦ اکتبر سال ۱۹۹۰ از زمین به فضا پرتاب گردیده است، به طوریکه پس از رسیدن به میدان گرانشی سیاره مشتری در 1992 اولین دور چرخش خود را در این جاذبه شروع کرد.این ماهواره داده هایی از قبیل سرعت باد خورشیدی به خصوص در هنگام گذر از نواحی حفره های تاجی ارسال نموده است. فضاپیما تا به امروز سه بار به گرد قطبهای خورشیدی چرخیده است (18 سال و 8 ماه و 24 روز).تحلیل داده های ارسالی به وسیله این ماهواره دستاوردهای مهمی را در مورد هلیوسفر خورشید و ساختار باد خورشیدی (ترکیب پیچیده ای از گاز داغ یونیزه) می دهد. با توجه به اینکه به علت دیناموی خورشید، شار میدان مغناطیسی از قطب جنوب به سمت قطب شمال خورشید جریان پیدا می کند ، سرعت جریان پروتون ها در باد خورشیدی 800 km/s (دو برابر نواحی استوایی) می باشد.

با در نظر گرفتن داده های مربوط به زمانهای بیشینه و کمینه چرخه های فعالیت خورشیدی و مدارهای چرخش ماهواره در حالتهای اوج و حضیض خورشیدی نمودارها مورد بررسی قرار گرفته است.

نمودار ها برحسب زمان:

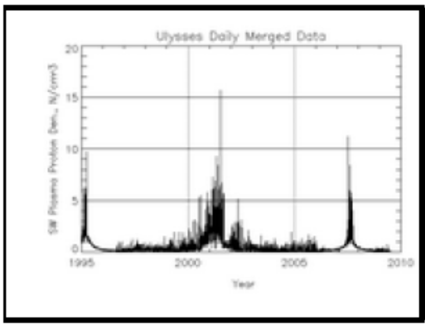

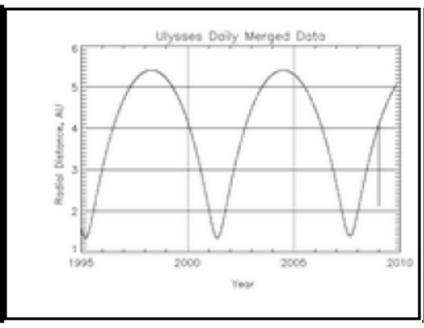

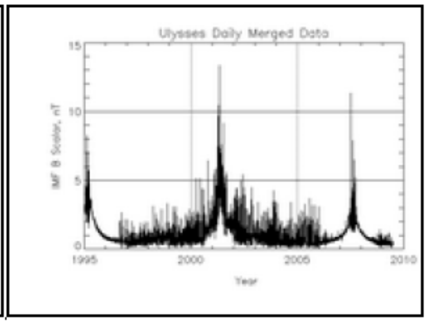

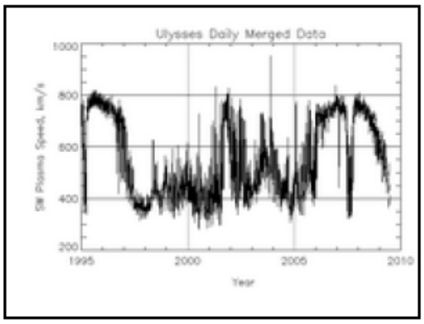

نمودارها برحسب فاصله ماهواره از مرکز خورشید (دور اول):

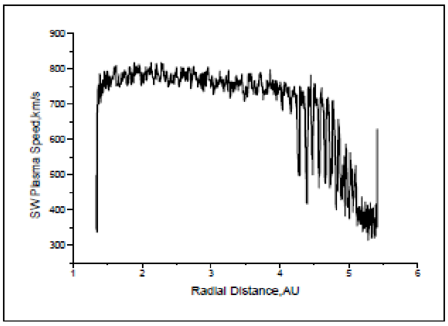

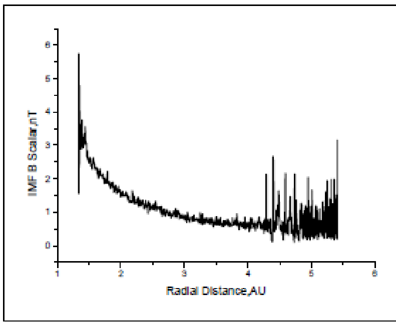

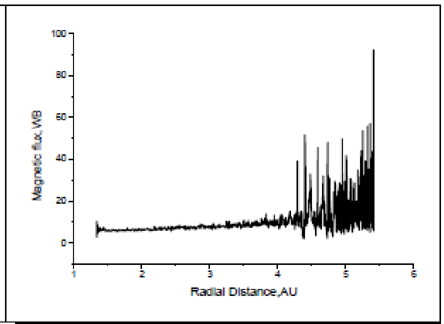

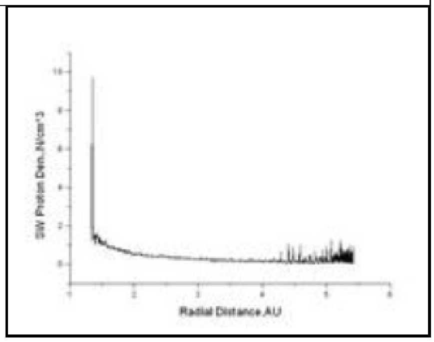

نمودارها برحسب فاصله ماهواره از مرکز خورشید (دور دوم):

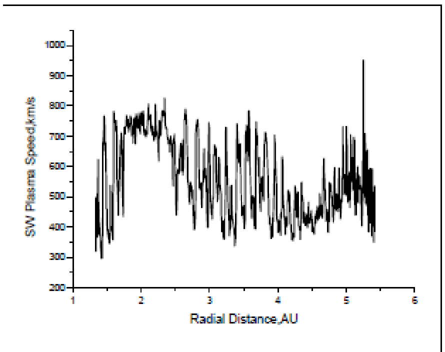

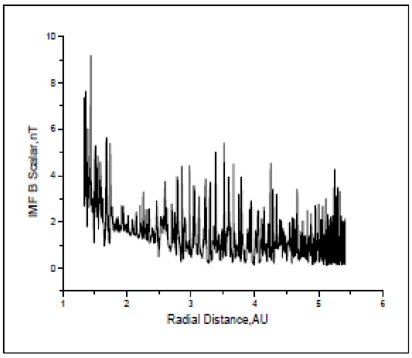

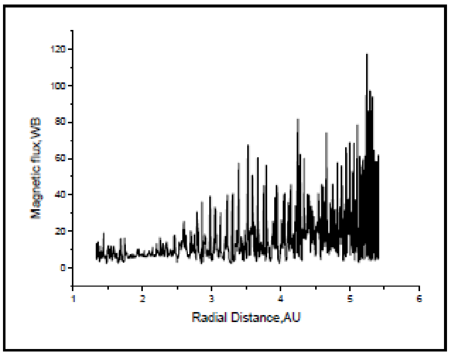

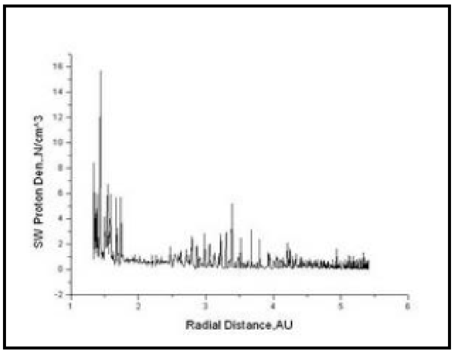

نتیجه گیري:

-مطابق تئوری پارکر (هلیوسفر دینامیک)در محاسبه سرعت باد خورشیدی بر حسب فاصله از مرکز خورشید-حضور میدان مغناطیسی *forcefree* در فاصلههای دور در نظر گرفته نمیشود لذا از این نظر تغییرات سرعت بر حسب فاصله افزایش خطی نشان میدهد. نتایج به دست آمده در محاسبه سرعت باد خورشیدی نسبت به دوری از سطح خورشید نشانگر این مهم است که علت اختلاف سرعت در نواحی استوا و قطب از نظر فیزیکی تنها گرادیان دما نبوده بلکه منشاء مغناطیسی نیز دارد.در بررسی نمودارها با توجه به مدار گردش ماهواره *ulysses* نشان می دهیم که در دور اول در حوالی اوج تغییر شدید در سرعت وجود دارد(به علت تاثیر میدان مغناطیسی مشتری)در حالی که در دور دوم ماهواره تاثیر کمتری از سیاره مشتری داردو لذا نتیجه متفاوت از دور اول میباشد. در حالت اوج، در دور اول ماهواره در نزدیکترین فاصله از سیاره مشتری قرار دارد.دور اول شامل مینیمم فعالیت خورشیدی در چرخه 23 میباشد.(1996) در حالت اوج، در دور دوم در دورترین فاصله از سیاره مشتری قرار دارد.دور دوم شامل ماکزیمم فعالیت چرخه 23(2001) است. همچنین نتیجه میگردد:

-سرعت با (فعالیت خورشیدی) رابطه عکس دارد.

-میدان و فعالیت خورشیدی رابطه مستقیم دارند.

-حضور میدان آشوب در محاسبات ونمودارها و همچنین نقض آشکار اصل بقای شار مغناطیسی حضور میدان اضافی با افزایش فاصله نمایان است.

مرجع‌ها:

1.E.J.Smith,R.G.Marsden,A.Balogh,G.Gloeckler,J.Geiss,D.J.McComas,R.B.Mckibben,R.J.MacDowall,L.J.Lanzerotti,N.Krupp,H.Krueger,M.Landgraf; The sun and H eliosphere at solar Maximum ;VOL.302,PP.1165-1169,2003.

2.نفیسه معصوم زاده:بررسی وپیش بینی چرخه24ام فعالیت خورشیدی ،پایان نامه کارشناسی ارشد،دانشگاه تبریز.

3.NASA WEBSITE.

اندازه گیری زاویه ی ایزوپلانتیک

شمالی، رامین [1] عبدی‌قلعه، رضا [2] افشاری، داود[1]
درودی، احمد [1] نصیری قیداری، سعداله [1]
[1]گروه فیزیک ، دانشکده علوم، دانشگاه زنجان
[2]گروه فیزیک، دانشکده علوم پایه، دانشگاه تربیت معلم آذربایجان

چکیده

عامل اساسی افت کیفیت تصاویر نجومی و دور شدن آن‌ها از حد پراش تلسکوپ، تلاطم جو زمین است. برای تصحیح ابیراهی‌های ناشی از تلاطم جو، از سیستم اپتیک تطبیقی استفاده می‌شود. زاویهٔ ایزوپلانتیک، بیشینهٔ زاویهٔ بین دو ستاره در آسمان است که جبهه‌های موج آنها تلاطم یکسانی را در مسیر انتشار خود در داخل جو تجربه می‌کنند. اندازه‌گیری این زاویه، برای تعیین مکان مناسب برای ساخت رصدخانه و نیز طراحی سیستم اپتیک تطبیقی اهمیت به‌سزایی دارد.

در این مقاله روش اندازه‌گیری زاویهٔ ایزوپلانتیک با استفاده از اندازه‌گیری ضریب چشمک‌زنی ستاره معرفی شده و داده‌های تجربی ثبت شده و نتایج حاصل از آن ارائه می‌شود.

مقدمه

تلاطم جو زمین که ناشی از گرادیان دمایی، افت و خیز رطوبت و جریان باد است، سبب ناهمگنی ضریب شکست جو زمین می‌شود. تلاطم که به صورت فضایی و زمانی تغییر می‌کند، باعث ایجاد ابیراهی روی جبههٔ موج ناشی از یک چشمهٔ نور سماوی شده و در نهایت باعث افت کیفیت تصویر ثبت شده با یک تلسکوپ زمینی و دور شدن آن از حد پراش اپتیکی تلسکوپ می‌شود. در تلسکوپ‌های زمینی، برای جبران ابیراهی‌های ناشی از تلاطم جو، از سیستم اپتیک تطبیقی استفاده می‌شود. تأثیر تلاطم جو زمین را می‌توان در سه مورد خلاصه کرد: چشمک‌زنی، حرکت تصادفی تصویر و تاری تصویر [1].
در یک سیستم اپتیک تطبیقی از یک ستارهٔ پر نور به عنوان مرجع استفاده می‌شود تا با اندازه‌گیری و تصحیح ابیراهی روی این ستاره (ستارهٔ مرجع)، تصویر شئ سماوی هدف به ازای زمان نوردهی بیشتری ثبت شود. ولی از آن‌جایی که تلاطم به صورت فضایی هم تغییر می‌کند، واضح است که فاصلهٔ زاویهٔ فضایی بین ستارهٔ مرجع و شئ هدف نباید از حد معینی بیشتر شود. زاویهٔ ایزوپلانتیک که به عنوان بیشینهٔ زاویهٔ مجاز برای انتخاب ستارهٔ مرجع و شئ هدف معرفی می‌شود، بسته به نقاط جغرافیایی مختلف و شرایط جوی، متغیر است. از این‌رو اندازه‌گیری آن برای تعیین مکان مناسب برای ساختن رصدخانه و طراحی سیستم اپتیک تطبیقی اهمیت به‌سزایی دارد.

زاویهٔ ایزوپلانتیک و ضریب چشمک‌زنی

زاویهٔ ایزوپلانتیک (θ_0) زاویه‌ای است که واریانس اختلاف فاز دو جبههٔ موج ناشی از ستارهٔ مرجع و شئ هدف، یک رادیان باشد. θ_0 با رابطهٔ زیر داده می‌شود [2]:

$$\theta_0^{-5/3} = 114.7\lambda^{-2} Cos(z)^{-8/3} \int dh C_N^2 \left(h\right) h^{5/3}. \qquad (1)$$

k بردار موج، z زاویهٔ سمت‌الرأس، C_N^2 ثابت ساختار جو و h ارتفاع از سطح زمین است.
از طرفی ضریب چشمک‌زنی ستاره را هم می‌توان با رابطهٔ زیر اندازه‌گیری کرد[3]:

$$\sigma_I^2 = 9.62\lambda^{-2}\int dhC_N^2\left(h\right)P\left(h\right) \tag{2}$$

$P\left(h\right)$ تابع وزنی معادله است که به شکل روزنهٔ تلسکوپ بستگی دارد و برای روزنهٔ دایروی به قطر D و نقصان مرکزی ε، به شکل زیر است:

$$P(h) = \frac{1}{\left(1-\varepsilon^2\right)^2}\int_0^\infty dff^{-8/3}Sin^2\left(\pi\lambda hf^2\right) \times\left[\frac{2J_1\left(\pi Df\right)}{\pi Df} - \varepsilon^2\left(\frac{2J_1\left(\varepsilon\pi Df\right)}{\varepsilon\pi Df}\right)\right]^2 \tag{3}$$

که f فرکانس فضایی و J_1 تابع بسل مرتبهٔ اول است. برای روزنه‌های با قطر کوچک، تابع وزنی تقریبا به شکل $P(h) \approx h^{5/6}$ و برای روزنه‌های با قطر بزرگ به صورت $P(h) \approx h^2$ رفتار می‌کند[4].
لوس و همکاران[5] نشان دادند برای یک تلسکوپ با قطر روزنهٔ 10 سانتی‌متر و قطر آینهٔ ثانویهٔ 4 سانتی‌متر، در اندازه گیری ضریب چشمک زنی، رفتار تابع وزنی به شکل $P(h) \approx h^{5/3}$ است. در نتیجه می‌توان با اندازه‌گیری ضریب چشمک‌زنی و استفاده از رابطهٔ زیر زاویه ایزوپلانتیک را اندازه گیری کرد:

$$\theta_0^{-5/3} = K\sigma_I^2 \tag{4}$$

که K به صورت زیر تعریف می‌شود:

$$K = 11.93Cos^{-8/3}\left(z\right)\frac{h_0^{5/3}}{P\left(h_0\right)} \tag{5}$$

که ثابت h_0 در مدل تلاطمی هافناگل[6] 10 کیلومتر است.

اندازه گیری زاویه ایزوپلانتیک در زنجان

وسایل اندازه گیری

برای اندازه گیری ضریب چشمک زنی و در نتیجه زاویه ایزوپلانتیک در زنجان، ما از یک تلسکوپ $Celestron-11''$ با قطر آینه $280mm$ و فاصله کانونی $2800mm$ که دهانه آن با یک روزنه ی حلقه ای با قطر خارجی $10cm$ و قطر داخلی $4cm$ پوشانده شده بود استفاده کردیم، استفاده از این روزنه حلقه ای باعث می شود که در محاسبه ضریب چشمک زنی تابع روزنه رفتاری متناسب با $h^{5/3}$ داشته باشد. جهت ثبت تصاویر از یک

CCD مدل $DMK21AU$ با سرعت تصویربرداری بالا استفاده شد. این CCD تک رنگ، با ابعاد 640×480 پیکسل می باشد که اندازه هر پیکسل $5.6\mu m \times 5.6\mu m$ است. زمان نوردهی آن قابل تنظیم در بازه ی $0.0001\sec$ تا $60\min$ است و بالاترین سرعت تصویربرداری آن $60fps$ است و تصاویر ثبت شده با این CCD از طریق رابط USB به صورت رقومی وارد رایانه می شود. با نصب این دوربین پشت تلسکوپ تصاویری با کیفیت مطلوب برای هدف مورد نظر ما به دست می آید.

داده برداری تجربی

قبل از هرگونه اندازه گیری ابتدا آینه ثانویه تلسکوپ را تنظیم می کنیم و بعد تصاویری با زمان نوردهی $4ms$ از ستاره قطبی ثبت می کنیم، سرعت اندازه گیری ما در داده برداری $60fps$است؛ جامعه آماری ما برای اندازه گیری زاویه ایزو پلانتیک در هر ست 3600 عکس است، یعنی در هر 2 دقیقه از 3600 عکس ثبت شده یک مقدار برای زاویه ایزوپلانتیک بدست می آید که این تعداد از لحاظ آماری مقدار مناسبی است[7]. علیرغم زمان نوردهی کوتاه تصویربرداری، تصاویر ثبت شده از نسبت SN خوبی برخوردار هستند که در شکل 1 نمونه آن نشان داده شده است.

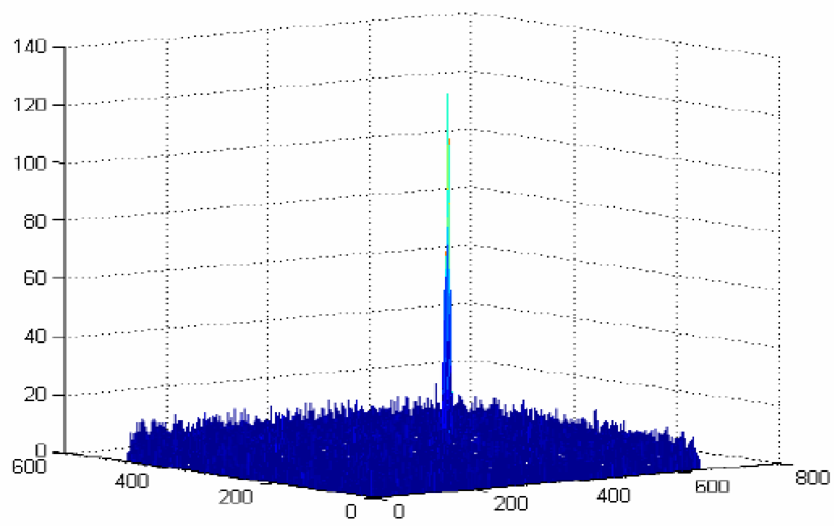

شکل1 : شدت ستاره در تصویربرداری با زمان نوردهی $4ms$ **، برای اندازه گیری ضریب چشمک زنی.**

لازم به ذکر است که CCD پر سرعت $DMK21AU$ تصاویر را صورت 8 بیتی و با فرمت bmp. ذخیره می کند.

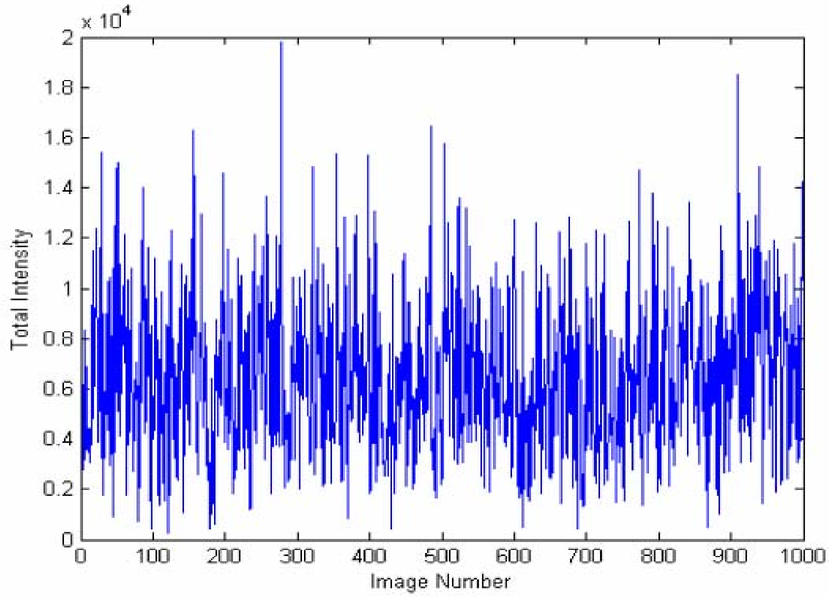

شکل2 : شدت کل محاسبه شده برای 1000 ستاره قطبی در شرایط جوی نامناسب و تلاطم زیاد در لایه های بالای جو.

تحلیل داده ها و نتیجه گیری

برای تحلیل داده ها برنامه ای در نرم افزار $MATLAB$ نوشته شده است که در این برنامه ابتدا محل ستاره تعیین می شود سپس یک پنجره مربعی با ابعاد 30×30 پیکسل که ستاره در مرکز این پنجره قرار دارد جدا می شود، این کار تاثیر بسیار زیادی در افزایش سرعت تحلیل داده ها دارد. بعد از آن نوفه زمینه تصویر ستاره محاسبه شده و با روش حذف آستانه ای [8] شدتهای کمتر از آن در تصویر ستاره صفر می شود. در مرحله بعد از تصویر بدست آمده شدت کل محاسبه می شود و این شدت برای محاسبه ضریب چشمک زنی در هر ست در رایانه ذخیره می شود. برای تک تک تصاویر ذخیره شده در رایانه این کار انجام می شود در پایان با استفاده از این شدتها واریانس نوسانات شدت ستاره محاسبه می شود که همان ضریب چشمک زنی است. سپس با استفاده از ضریب چشمک زنی محاسبه شده و معادله(4) زاویه ایزوپلانتیک برای هر ست تعیین می شود. در شکل زیر زاویه ایزوپلانتیک برای زمان 2 ساعت نشان داده شده است.

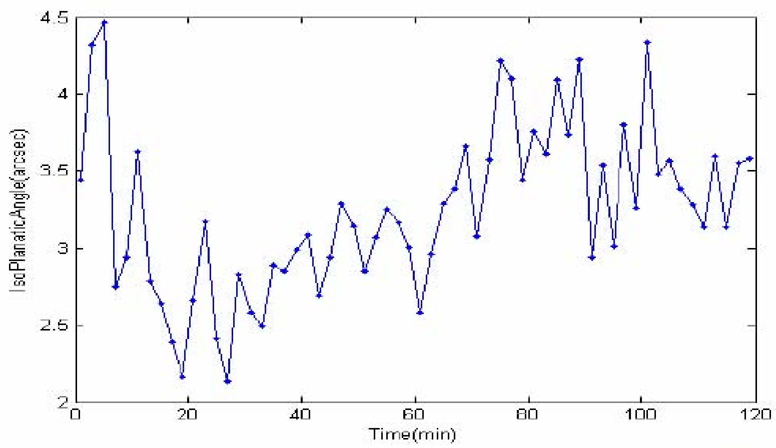

شکل3 : زاویه ایزو پلانتیک در مدت 2 ساعت.

مرجع ها

[1] F. Roddier. "*Adaptive Optics in Astronomy* "; Cambridge University Press, 1999

[2] D. L. Fried; "*Anisoplanatism in adaptive optics*"; *J. Opt. Soc. Am.*72, 52-61 (1982).

[3] F. Roddier, "The effects of atmospheric turbulence in optical astronomy," in *Progress in Optics*,, Vol. **19**, 281–376(1981).

[4] J. Krause-Polstorff, A. Edmund, and L. W. Donald, "Instrument comparison: corrected stellar scintillometer versus isoplanometer," *Appl. Opt.* **32,** 4051–4057 (1993).

[5] G. Loos and C. Hogge, "Turbulence of the upper atmosphere and isoplanatism," *Appl. Opt.* **18,** 2654–2661 (1979).

[6] R. E. Hufnagel, "Propagation through atmospheric turbulence," in *The Infrared Handbook*, W. L. Wolfe and G. J. Zissis, eds. Environmental Research Institute of Michigan, Ann Arbor, Mich., pp. 1–6 (1978).

[7] A. Ziad, R. Conan, A. Tokovinin, F. Martin and J. Borgnino; "*From the Grating Scale Monitor to the Generalized Seeing Monitor*"; *Appl. Opt.* **39**, 5415-5425 (2000).

[8] A. Tokovinin; "*From Differential Image Motion to Seeing*"; *PASP* **114**, 1156-1166 (2002).

بررسی توزیع سمتی و سرسویی میونهای جوی و تعیین ثابت زمانی تابش زمینه و اپاشی با استفاده از تلسکوپ پرتوهای کیهانی

عبدالهی، سهیلا[۱] نجمی، محبوبه[۳] بهمن‌آبادی، محمود[۲] پورمحمد، داود[۱]

[۱] گروه فیزیک، دانشگاه بین المللی امام خمینی (ره)

[۲] دانشکده فیزیک، دانشگاه صنعتی شریف

[۳] گروه فیزیک، دانشگاه سمنان

چکیده

بررسی شار میون‌ها در زوایای سمتی مختلف نشان می‌دهد که شار ذرات ثانویه باردار تحت تاثیر میدان مغناطیسی زمین منحرف شده و یک ناهمسانگردی در راستای شرق و غرب ایجاد می‌شود که این پدیده اثر شرق - غرب نامیده می شود. همچنین بستگی شار میونی به زاویه سرسویی به صورت یک تابع توانی از $\cos(\theta)$ است. برای بررسی شار میون‌ها در زوایای سمتی و سرسویی مختلف، با استفاده از یک تلسکوپ پرتوهای کیهانی، آزمایش‌هایی در رصدخانه دانشگاه صنعتی شریف در تهران $(35°43'N, 51°20'E)$ و در ارتفاع $1200m$ از سطح دریا $(890\,gcm^{-2})$ انجام دادیم. با اندازه‌گیری شار میون‌های جوی در زوایای سمتی مختلف، ناهمسانگردی توزیع میون‌ها در راستای شرق و غرب را مشاهده کردیم. همچنین با اندازه‌گیری شار میون‌ها در زوایای سرسویی $0°-60°$، توزیع سرسویی شار میون‌ها را به صورت $I(\theta) = I(0)cos^n(\theta)$ با $n= 1/98$ بدست آوردیم. از طرف دیگر مقدار ثابت زمانی تابش زمینه در تابع توزیع واپاشی میون را از طریق آزمایش‌های مشابه با واپاشی میون بدست آورده و بستگی آن به شرایط آب وهوایی را بررسی کردیم. این ثابت زمانی برای آزمایش‌های مربوط به واپاشی میون لازم است زیرا تابش زمینه در آن به صورت یک نوفه وارد می‌شود و باید در نظر گرفته شود.

مقدمه

پرتوهای کیهانی اولیه که اساسا پروتون‌ها و هسته‌های اتمی سنگین‌تر هستند، با جو زمین برخورد کرده و منجر به تولید ذرات ثانویه زیادی می‌شوند که بهمن هوایی گسترده نامیده می‌شود. اکثر این ذرات مزون‌های ناپایداری هستند که به سرعت به میون‌ها واپاشیده می‌شوند[۱].

$$\pi^+ \to \mu^+ + \nu_\mu \qquad \pi^- \to \mu^- + \bar{\nu}_\mu$$

میون‌ها به دلیل اثر نسبیتی اتساع زمان می‌توانند به سطح زمین برسند. این ذرات بعد از نوترون (~ ۱۵ min) دارای طولانی‌ترین طول عمر میانگین (۲/۲μs) می‌باشند. میون‌ها با برهم‌کنش‌های ضعیف به صورت زیر واپاشیده می‌شوند.

$$\mu^- \to e^- + \bar{\nu}_e + \nu_\mu \qquad \mu^+ \to e^+ + \bar{\nu}_\mu + \nu_e$$

علی‌رغم آنکه شار پرتوهای کیهانی در بالای جو در راستای شرق و غرب متقارن است، در مشاهدات تجربی شار ذرات ثانویه باردار از جمله میون‌ها در این دو جهت تحت تاثیر میدان مغناطیسی زمین نا-متقارن بدست آمده است، که این پدیده اثر شرق- غرب نامیده می-شود.

در این آزمایش‌ها که در رصدخانه دانشگاه صنعتی شریف در تهران ($۳۵°۴۳'N, ۵۱°۲۰'E$) و در ارتفاع ۱۲۰۰m از سطح دریا ($۸۹۰\,gcm^{-۲}$) انجام گرفت، از یک تلسکوپ قابل چرخش در زاویه‌های سمتی و سرسویی مختلف برای اندازه‌گیری توزیع شار میون‌ها به روش همزمانی استفاده شده است. همچنین بستگی تابش زمینه به شرایط جوی در آزمایش واپاشی میون مورد بررسی قرار گرفته است.
هدف از این آزمایش‌ها، بررسی توزیع سرسویی شار میون‌ها، مشاهده اثر شرق- غرب و تاثیر شرایط جوی بر روی تابش زمینه است.

چیدمان آزمایش

تلسکوپ پرتوهای کیهانی، شامل دو سوسوزن ($۳۰\times۱۰\times۱cm^{۳}$) است که به فاصله ۱ متر از یکدیگر و به صورت موازی باهم قرار گرفته‌اند و برای بررسی همزمانی و واپاشی میون‌ها به کار می‌رود. دهانه این تلسکوپ $۹°$ گشودگی دارد.
از آنجا که بستگی شار میون‌ها به زاویه سرسویی به صورت زیر

$$I(\theta) = I(۰) \cos^{n}(\theta) \qquad (۱)$$

است[۲]، مقدار n را از طریق برازش داده‌های آزمایش همزمانی در زاویه‌های سرسویی مختلف با این تابع بدست می‌آوریم. در این روش از طریق همزمان کردن سوسوزن بالایی و پایینی، شار ذرات باردار ثانویه را در ۲ جهت سمتی غرب ($\varphi = ۹۰°$) و شرق ($\varphi = ۲۷۰°$) و زاویه-های سرسویی $۹۰ \pm ۲۰°, ۹۰ \pm ۴۰°, ۹۰ \pm ۶۰°$ اندازه‌گیری کرده‌ایم. راه‌اندازی الکترونیک مدار آزمایش همزمانی (شکل۱)، به این صورت است که سیگنال ناشی از برخورد ذره به سوسوزن بالایی پس از عبور از تقویت‌کننده($\times۱۰$) و مجزاکننده، وارد مبدل زمان به دامنه (TACبا پنجره زمانی ۲۰۰ ns ، ضریب تقویت ۱) شده و زمان سنج به کار می افتد. سپس سیگنال ناشی از ذره فرودی بر سوسوزن پایینی پس از عبور از تقویت‌کننده ($\times۱۰$) و مجزاکننده، با سیم تأخیری ۱۰ متری به مبدل زمان به دامنه رسیده و زمان‌سنج را متوقف می‌کند.

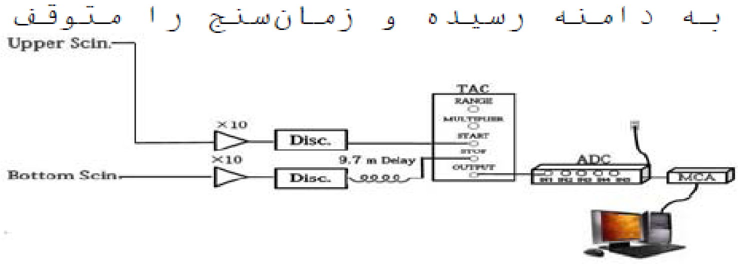

شکل ۱: چیدمان آزمایش همزمانی

بدین ترتیب TAC پالسی با دامنه‌ی متناسب با این بازه‌ی زمانی، تولید و به ADC فرستاده می‌شود و سپس MCA پالس را در کانال مربوطه ذخیره می‌سازد.

تحلیل داده‌ها

ما توزیع میون‌ها را در ۲ جهت سمتی شرق و غرب و زاویه‌های سرسویی $۹۰ \pm ۲۰°, ۹۰ \pm ۴۰°, ۹۰ \pm ۶۰°$ اندازه‌گیری کردیم. هر یک از اندازه-گیری‌ها در بازه زمانی ۸۶٤۰۰ s (۲٤ h) انجام گرفت. شکل۲ برازش داده-های بدست آمده از راستاهای مختلف با رابطه(۱) را نشان می‌دهد. با برازش، n= ۱/۹۸ بدست آمد.

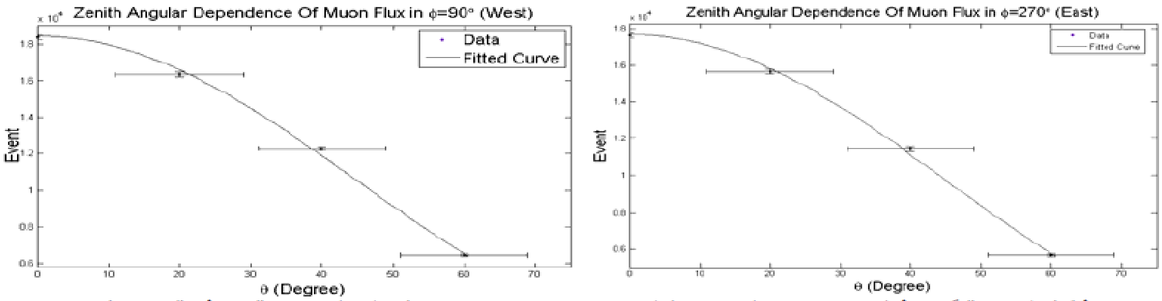

شکل۲:بستگی شار میون‌ها به زاویه سرسویی در زوایای سمتی شرق و غرب

در آزمایش‌های همزمانی، تابش زمینه به صورت یک تابع ثابت از داده ها حذف شده است.

علاوه بر این با مقایسه داده‌ها در دو زاویه سمتی $\varphi = ۹۰°,۲۷۰°$، اثر شرق- غرب را مشاهده کردیم، جدول۱.

زاویه سرسویی / زاویه سمتی	۲۰°	۴۰°	۶۰°
غرب ($\varphi = ۹۰°$)	۱۶۳۵۰	۱۲۲۹۷	۶۴۳۹
شرق ($\varphi = ۲۷۰°$)	۱۵۶۳۶	۱۱۴۲۷	۵۶۵۷

جدول۱: اثر شرق - غرب در زوایای سرسویی مختلف

محاسبه ثابت زمانی تابش زمینه در تابع توزیع واپاشی میون‌ها

میون‌های مثبت و منفی در ماده رفتار متفاوتی دارند،بطوریکه میون‌های مثبت با طول عمری برابر با طول عمر میون آزاد، در ماده واپاشیده می‌شوند اما میون منفی که در مدار اتمی گرفتار می‌شود ممکن است واپاشیده و یا توسط هسته اتمی جذب گردد. این امر سبب کاهش طول عمر میون منفی می‌شود که به نوع ماده‌ی متوقف-کننده‌ی ذره وابسته است. تابع توزیع واپاشی کل میون‌ها در آشکارساز از برهم نهی چندین واپاشی به صورت زیر است[۳]:

$$\frac{dN}{dt} = \frac{N_t}{R+۱}\left(R\,\delta_+ \frac{۱}{\tau_+}\exp\left(-\frac{t}{\tau_+}\right) + \delta_- \frac{۱}{\tau_-}\exp\left(-\frac{t}{\tau_-}\right)\right) + N_b \exp\left(-\frac{t}{\tau_b}\right) \qquad (۲)$$

که در آن τ_+ و τ_- طول‌عمر میون مثبت و منفی، $R = \frac{N_{\mu^+}}{N_{\mu^-}}$ معرف نسبت تعداد میون‌ها، N_t برابر با مجموع کل میون‌ها و τ_b ثابت زمانی تابش زمینه می‌باشد. ضرایب δ_+ و δ_- به احتمال واپاشی میون های مثبت و منفی در ماده وابسته‌اند.

بر خلاف آزمایش‌های همزمانی، طبق رابطه(۲) تابش زمینه در تابع توزیع واپاشی میون‌ها به صورت تابع نمایی می‌باشد. از طریق برازش داده های آزمایش تابش زمینه با رابطه $N_b \exp\left(-\frac{t}{\tau_b}\right)$، ثابت زمانی τ_b را بدست می‌آوریم. بدین منظور مداری با یک سوسوزن مطابق شکل۳ طراحی کردیم.

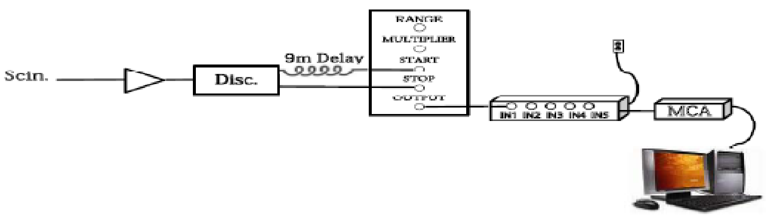

شکل۳:چیدمان آزمایش تابش زمینه (پنجره زمانی TAC ، ۲ ms است.)

شکل٤ نمونه‌ای از تابش زمینه را در مدت ٦۰۰s نشان می‌دهد.

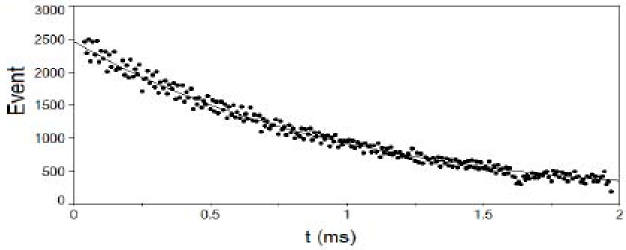

شکل٤:نقاط،منحنی تابش زمینه واپاشی میون‌ها در پنجره زمانی ٢ms و خط، برازش داده‌ها با تابع نمایی را نشان می‌دهد.

این آزمایش‌ها ١٥ بار در شرایط جوی مختلف تکرار شد. جدول٢ داده‌های مربوط به تابش زمینه و مقادیر $\bar{\tau}_b$ در شرایط جوی مختلف و رگراسیون برازش (r^2) را نشان می‌دهد.

Weather	Event(in ٣۰۰۰ s)	$\bar{\tau}_b$ (ms)	r^2
Serene	١١٥٦١١٥	١/١۰١	۰/٩٧٣
Cloudy	١٢٩۰٢٢٥	١/۰٢٣	۰/٩٧٨
Rainy	١٣٨٤٨١٩	۰/٩٦٥	۰/٩٨٢

جدول٢- مقادیر $\bar{\tau}_b$ در شرایط جوی مختلف

تابش زمینه در شرایط بارانی به دلیل میدان الکتریکی ابرها و افزایش تعداد الکترون‌ها نسبت به شرایط ابری و صاف بیشتر است.

نتایج

از آنجایی که نسبت بار میون‌های جوی اطلاعات مفیدی در زمینه‌ی محاسبه‌ی "شار نوترینوهای جوی" فراهم می‌آورد،به مطالعه توزیع میون‌ها پرداختیم. بدین منظور آزمایش‌هایی جهت یافتن شار میون‌ها در زوایای مختلف انجام داده و نشان دادیم که توزیع میون‌ها به زاویه‌ی سرسویی به صورت $\cos^n(\theta)$ با n=١/٩٨ وابسته است.علاوه‌براین، آزمایش‌های انجام شده موید اثر شرق- غرب می‌باشند. در ادامه ثابت زمانی تابش زمینه در تابع توزیع واپاشی میون‌ها را در سه شرایط جوی بارانی،ابری و صاف به ترتیب $\bar{\tau}_b$ = ۰/٩٦٥، $\bar{\tau}_b$ = ١/۰٢٣، $\bar{\tau}_b$ = ١/١۰١ بدست آورده و تأثیر شرایط جوی را بر روی آن بررسی کردیم که نشان می‌دهد در شرایط جوی بارانی تعداد تابش زمینه به حداکثر مقدار خود می‌رسد.بدین ترتیب با مشخص شدن پارامترهای رابطه (٢) در آینده می‌توانیم نسبت میونهای مثبت و منفی را از طریق آزمایش‌های واپاشی تعیین کنیم.

مرجع ها

١. Thomas K. Gaisser, *Cosmic Rays and Particle Physics*(CAMBRIDGE UNIVERSITY PRESS)

٢. M. Bahmanabadi, F. Sheidaei, M. Khakian, and J. Samimi, *Phys.Rev.D*, **volume**٧٤, Issue٨, ٢۰۰٦

٣. شیدایی، فرزانه (پایان نامه‌ی دکتری)، "مطالعه بر روی پرتوهای پرانرژی در سطح تهران"،دانشگاه صنعتی شریف،١٣٨٧.

الگوسازی نواحی فعال خورشید

عجب‌شیری‌زاده،علی

دانشگاه تبریز،دانشکده فیزیک،گروه فیزیک نظری‌واخترفیزیک

مرکز تحقیقات نجوم و اختر فیزیک مراغه

چکیده

ساختار عمومی میدان مغناطیسی خورشید را با برون یابی و تداوم میدان‌های اندازه‌گیری شده فوتوسفر در اتمسفر خارجی خورشید می‌توان تعیین کرد.در حالت کلی ،میدان مغناطیسی با تولد و از بین رفتن نواحی فعال متحول می‌گردد.این تحول را می‌توان از رصدهای Hinode/XRT و Yohkoh/SXT ملاحظه کرد که تاج خورشیدی شامل ساختارهای S شکل بنام Sigmoid می‌باشد.دو S که در ۱۵ ماه می ۱۹۹۸ رصد گردیده است را در نظر می‌گیریم که در تاریخ ۹-۸ ژوئن ۱۹۹۸ حدودا یک ماه بعد نشانگر تحول در میدان‌های تاجی بصورت گسترده و یا پیچشی بعد از هر Eruption می‌باشد. جهت مدل سازی نواحی فعال فرض بر این بوده است که این نواحی به صورت حلقه‌هایی به شکل Ω از میدان‌های ترویئدال که در سطح زیرین ناحیه همرفتی واقع شده‌اند،سرچشمه می‌گیرند.

در شبیه سازی حلقه‌های Ω در ناحیه همرفتی ،صعود شناوری این میدان‌ها در راستای محور دوران که دارای دنباله سمتی (~۹۰°)است،فرض می‌گردد. نتیجه به دست آمده نشان می‌دهد که حرکات همرفتی چرخه‌ای ،نقش بسیار مهمی را در تولد نواحی فعال بازی می‌کند. در واقع بر هم کنش شار مغناطیسی با حباب‌های همرفتی باعث شکل‌گیری حلقه‌های Ω می‌گردد.

MODELING SOLAR ACTIVE REGIONS

ABSTRACT:

The global structure of the sun's magnetic field can be determined by extrapolation of measured photospheric fields. The magnetic field evolves due to the birth and decay of **Active Regions**. One could find this evolution from Yohkoh/SXT and Hinde/XRT observations which show that the corona contains S-shaped structures (sigmoids),indicating coronal magnetic fields are sheared and/or twisted.
Two observed sigmoids of May 15, 1998 which evolved after eruption of June 8-9, 1998 (nearly one month time interval). In simulation, active region are thought to be Ω-shaped loops emerging from a toroidal field located near the base of the convective zone.
Also, the buoyant rise of Ω–loops in the convection zone along rotation axis which has large azimuthal extent(~90°),considered.
The results suggests that *cyclonic convective motions* play an important role in the birth of active region. In fact, considered the interaction of a flux rope with convection, leading to the formation of an Ω–loop.

تعیین حلقه‌های تاج با استفاده از روش بی اسپیلاین

امیرخانلو، فاطمه[1]؛ فتحعلیان، نرگس[1]؛ صفری، حسین[2]
[1] دانشگاه تحصیلات تکمیلی علوم پایه زنجان
[2] دانشگاه زنجان، گروه فیزیک

چکیده
در این مقاله،روش بی اسپیلاین برای شناسایی حلقه‌های تاج خورشید با استفاده از تصاویر فرابنفش ماهواره خورشیدی استرو ، معرفی شده است. بدین منظور، از فیلتر ال‌سی‌تی و مدمکس جهت حذف نویزها و افزایش وضوح تصاویر استفاده شده است. نمایه بردارهای انحنا و عمود استخراج شده است.

مقدمه
منظومه شمسي به وي‍ژه زمين و جو آن تحت تاثير فعالیت دینامیکی خورشید قرار دارد. دانشمندان این پدیده‌ها را متأثر از میدان های مغناطیسی خورشید بیان می‌کنند، بنابراین مطالعه میدان‌های مغناطیسی خورشي د از اهمیت بسزایی برخوردار است. آشکارسازی ساختارهای قوسی شکل، حلقه‌های تاج، نیز می‌توانند کمک خوبی در تحلیل رفتار دینامیکی میدان مغناطیسی خورشید باشند. هر چه قدر مطالعه‌ و تحلیل این ساختارها دقیق‌تر باشند، یقیناً در درک میدان های مغناطیسی خورشید و حل نوسانات حلقه‌های تاج قابل توجه خواهند بود.
فیزیک پیشگان خورشیدی ساختارهای حلقه‌های تاج را با استفاده از برجسته‌سنجی از تصاویر مربوطه استخراج کردند (اشواندن۱۹۹۹، ویگلمن۲۰۰۲). عمده این روش‌ها بر اساس تشخیص چشمی است، اما با افزایش حجم و پیچیدگی داده‌ها از یک طرف و از طرف دیگر زمان‌بر بودن و خطای بالای روش‌های غیرخودکار، محققان را به سمت روش‌های خودکار سوق داده است. از سال ۲۰۰۵ تاکنون چندین روش خودکار برای بخش‌بندی تصاویر تاج‌خورشید (داده‌های ماهواره‌های تریس، سوهو، استرو و ...) مطرح شده است، که هر کدام از آنها مشکلات و معایبی داشتند، از جمله این مشکلات، تمیز ندادن نویزهای زمینه از حلقه‌های تاج بود. ردیابی منحنی‌های با ابعاد بزرگ، (ال-اسی-‌تی)، توسط اشواندن اخیرا انجام شده است. این روش در بسته نرم افزاری IDL/SSW قابل دسترس می باشد[۳].
در این مقاله، بی‌اسپیلاین بر روی تصاویر فرابنفش تاج خورشید برای شناسایی خطوط میدان مغناطیسی اعمال شده است. بی‌اسپیلاین بر اساس یک سری نقاط کنترلی عمل می‌کنند، که توانایی تشخیص شکل انحنائ حلقه را بر عهده دارد و با توجه به نوع حلقه دارای درجات متفاوتی است، که در این مقاله از بی‌اسپیلاین درجه سوم استفاده شده است.

داده ها و تحلیل داده ها
تصاویر فرابنش استرو (STEREO) براي تقليل استفاده شده است. جفت ماهواره هاي زمین مدار گرد استرو (A و B) داراي توان تفکیك فضایی۲/. ثانیه قوسي و با هدف مطالعه تاثیر خورشيد بر دینامیك جو زمین در سال 2006 در مدار قرار گرفته است .

داده‌های به کار برده شده دراین مقاله از روز ۲۰۰۷/۰۶/۰۹ و با بازه هاي زماني 30 ثانيه و در طول موج ۱۷۱ آنگستروم ناحيه فرابنفش مي باشند. داده هاي فرابنفش استرو به صورت قرص كامل خورشيد بوده و ما در اينجا به بررسي چند ناحيه فعال كه داراي حلقه هاي واضحي مي باشند، پرداخته ايم. در شكل 1، نمونه اي از تصويركامل قرص خورشيد و تصور بريده شده از ناحيه فعال نشان داده شده است.

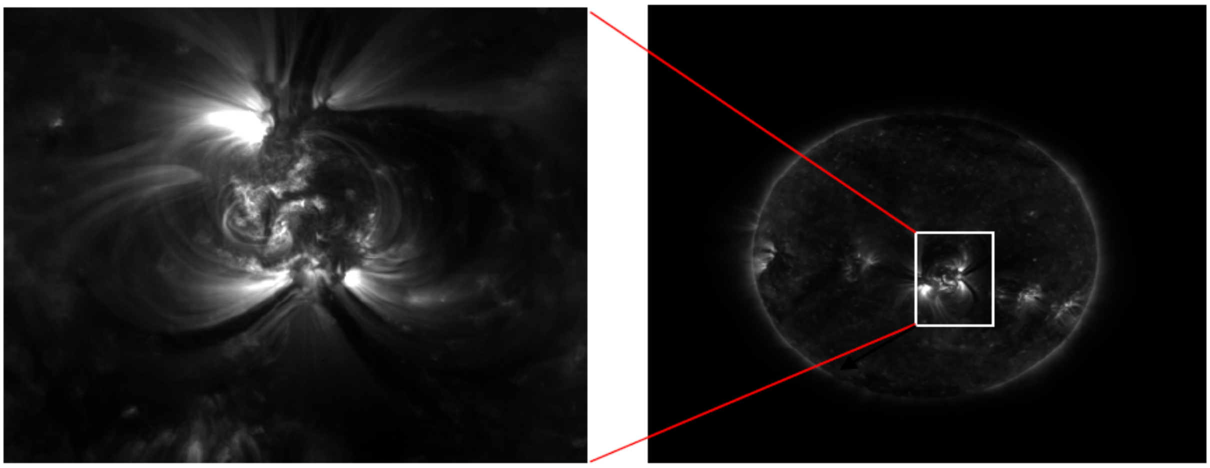

شكل ۱: سمت راست، تصوير قرص كامل خورشيد؛ سمت چپ، تصوير بريده شده
استرو اِی،طول موج ۱۷۱Å
۲۰۰۷/۰۶/۰۹-۰۰۰۹۰۰

برای افزایش کیفیت وضوح تصاویر از فیلترهای ال-اسی-اتی ومدمکس استفاده نمودیم. روش کار فیلتر ال- سی-اتی به این صورت می‌باشد که، در ابتدا یک نقطه را به عنوان پیک در نظر می‌گیرد و سپس آنرا با استفاده از جهت شار ماکزیمم ردیابی می‌کند، در هر دو جهتی که یک حلقه تشکیل می‌شود پیش می‌رود و در هر قسمت از تصویر یک جعبه کار به طول ۳۰ و پهنای ۶ پیکسل در نظر می‌گیرد و شروع به ردیابی حلقه می‌کند. این عمل تا جایی ادامه می‌یابد که شدت روشنایی خیلی کم شود، که در واقع همان نقاط انتهایی حلقه تاج هستند. این ردیابی در دو جهت انجام می‌شود، تا مسیر دقیق یک حلقه مشخص شود.
اصول کار مدمکس به این صورت می‌باشد که در یک تصویر یک نقطه را انتخاب می‌کند و برای این نقطه هشت جهت در همسایگی آن در نظر می‌گیرد. این جهات همان جهت خطوط میدان مغناطیسی هستند. در واقع در اطراف یک پیکسل، هفت پیکسل را شناسایی می کند. این عمل را برای همه همسایگی‌ها تکرار می‌کند و به این ترتیب روشن‌ترین پیکسل را به عنوان حلقه ثبت می‌کند و بقیه را غیرحلقه شناسایی می‌نماید.

روش بی‌اسپیلاین

بی‌اسپیلاین[۴]، یک نوع درون‌یابی است که مسیر یک انحناء را با استفاده از یک مجموعه نقاط تقریب می‌زند، این نقاط به عنوان نقاط کنترلی نامیده می‌شوند که می‌توان به صورت دستی بر روی

تصاویر مشخص نمود. اسپیلاین‌ها درجات متفاوتي دارند. تعداد نقاط کنترلی و درجه بی اسپیلاین با توجه به نوع منحنی تعیین می‌شوند.

خلاصه و نتایج

با اعمال روش‌های بالا بر روی چندین تصویر فرابنفش تاج‌خورشید، در بسته نرم افزاری آی-ادی‌ال و مطلب، توانستیم به نتایج قابل توجهی دست پیدا کنیم که نمونه‌ای از آن در شکل (۲) نشان داده شده است.

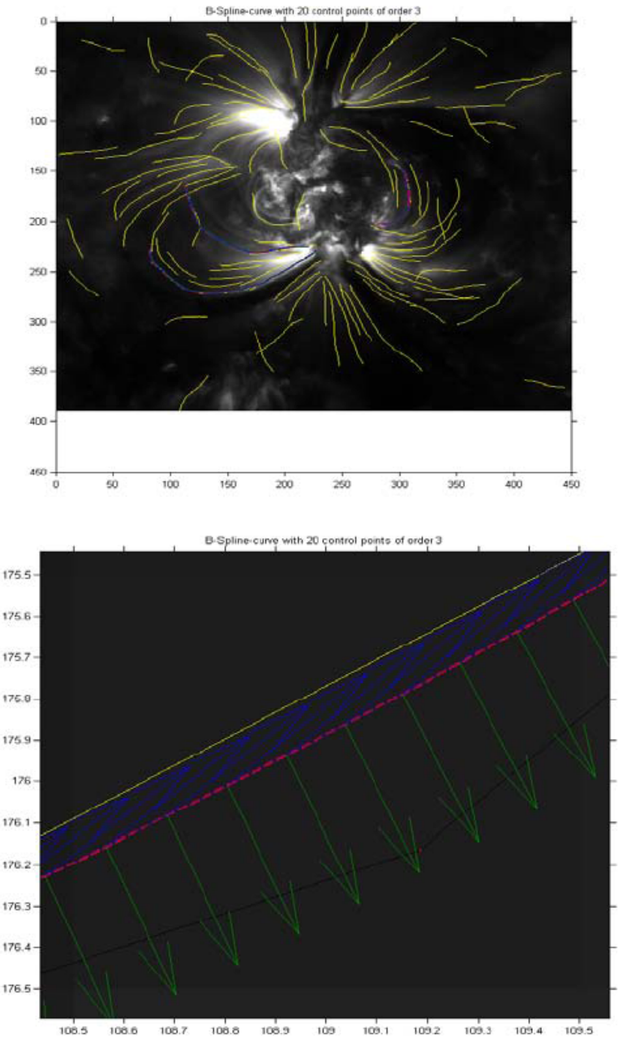

شکل ۲: تصویر بالا، ناحیه بریده شده پس از اعمال فیلترها و بی اسپیلاین
تصویر پایین، نمایش خطوط مماس و عمود بر قسمتی از منحنی
استرو اِی ۰۰۰۹۰۰-۲۰۰۷/۰۶/۰۹

همانطور که در شکل نشان داده شده، در برخی از نواحی ، به دلیل وجود نویزهای زمینه، مسیردقیق حلقه‌ها کاملاً مشخص نیست که

با اعمال این روش و مقایسه همزمان آن با تصویر اصلی توانستیم مسیرهای منقطع شده را تا حدودی کاهش دهیم.
خطوط زرد رنگ، نمایش تصویر پس از اعمال فیلترهای مذکور و نقاط قرمزرنگ، نقاط کنترلی مربوط به اعمال بی اسپیلاین میباشد.
همچنین خطوط مماس و عمود بر آنها را نیز به ترتیب با رنگ های آبی و سبز رسم نمودیم.

مرجع ها

1. Timothy. S. Newman, J. Kwan. Lee and G. Allen. Gary; "Dynamical Aperature-based solar loop Segmentation(DAM)"; *1-4244-0069-04/06/$20.00/2006 IEEE*
2. Bernd. Inhester,"On the smoothing of loops from STEREO reconstructions"; Early draft,stereocurves.tex-*May 14,2009*
3. Marku.s J. Aschwanden; "A code for automated tracing of coronal loops approaching visual perception(LCT)"; Resived *Oct.2009*

بهینه‌سازی ابعاد و سطح داخلی آشکارساز چرنکوف آبی با یک لامپ تکثیر کننده‌ی نوری

مرتضوی مقدم، صبا[1] خلج، پوریا[2] شیدایی، فرزانه[2] پورمحمد، داوود[1] بهمن آبادی، محمود[2]
[1] گروه فیزیک، دانشگاه بین المللی امام خمینی (ره)
[2] دانشکده فیزیک، دانشگاه صنعتی شریف

چکیده

روش های آشکارسازی و تحلیل داده های بهمن های گسترده هوایی روز به روز در حال پیشرفت و گسترش است تا بتوان با این روش دقت اندازه گیری جهت فرود ذره اولیه و تشخیص نوع ذره اولیه را بهینه کرد. در این مقاله ضمن معرفی آشکارساز چرنکوف آبی به عنوان نوعی آشکارساز ذره باردار ثانویه، آزمایش‌هایی برای بهینه سازی یازده هر آشکارساز انجام داده و با انجام یک شبیه سازی همزمان، سعی در بهینه کردن پارامترهای موثر در یازده هر آشکارساز (ابعاد و جنس دیواره داخلی) کرده ایم.

مقدمه

یکی از روش‌های مطالعه روی چشمه های پرتوهای کیهانی پرانرژی ($E>10^{13}$ eV) استفاده از آرایه های سطحی برای آشکار سازی ذرات ثانویه‌ی بهمن‌های هوایی گسترده است. پرتوهای کیهانی پرانرژی وقتی وارد جو زمین می شوند ذرات ثانویه ای تولید می‌کنند که در سطح زمین توسط آرایه ای از آشکارسازهای ذره ای آشکارسازی می‌شوند. با آشکارسازی و مطالعه این ذرات ثانویه می‌توان به جهت و نوع ذره اولیه پی برد[1]. یکی از آشکارسازهایی که در آرایه های سطحی استفاده می‌شود آشکارساز چرنکوف آبی است که در آن ذرات به دلیل داشتن سرعت زیاد (بیشتر از سرعت نور در آب) فوتون گسیل می‌کنند. این تابش به تابش چرنکوف معروف است که به صورت یک مخروط با محوری که مسیر حرکت ذره را مشخص می کند گسیل می شود. زاویه این مخروط به ضریب شکست محیط و سرعت ذره بستگی دارد. برای آب و برای ذرات نسبیتی این زاویه ٤١ درجه است. از مزایای استفاده از این آشکارسازها می‌توان به ارزانی، مقاومت در برابر شرایط سخت وقابلیت آشکارسازی ذرات در زاویه های سرسویی بزرگ اشاره کرد. استفاده از این نوع آشکارساز در تجربه های گذشته موفقیت آمیز گزارش شده است[2]. با توجه به اینکه تعداد ٦٠٠هزار بهمن هوایی گسترده توسط آرایه ای شامل ٤ آشکارساز چرنکوف، که در دانشکده فیزیک دانشگاه صنعتی شریف ساخته شده بود، آشکارسازی شد [3] تصمیم گرفته شد که در این دانشکده برای داشتن آرایه ای با تفکیک زاویه ای بهتر و آهنگ آشکارسازی بیشتر اول یک تک آشکارساز بهینه شود و سپس در آرایه قرار گیرد. در این مقاله شبیه سازی، روش ساخت وبهینه سازی ابعاد و جنس دیواره داخلی یک آشکارساز چرنکوف آبی را قبل از قرار گرفتن در آرایه بررسی می‌کنیم. لازم به ذکر است که شبیه سازی اولیه ای قبلاً انجام شده بود که از نتایج آن برای ساخت مخزن چرنکوف استفاده شد[3].

شبیه سازی

برای شبیه سازی مخزن چرنکوف آبی با هندسه‌ی استوانه ای و دیواره-های داخلی با رنگ سفید (که به صورت پخشی نور را بازمی‌تاباند) و با ضریب پخش ٨٥% درنظرگرفته شده است که در آن تنها یک لامپ تکثیر کننده نوری (PMT) بکار رفته. ذرات باردار هم از سطح

بالایی مخزن و هم از دیواره‌های آن وارد مخزن می‌شود. به دلیل تقارن سمتی، ذرات از سطح بالایی مخزن روی شعاع (محور x) و از دیواره‌ی مخزن روی یک خط قائم (موازی با محور z) وارد می‌شوند. محدوده‌ی تغییرات و تغییر در هر گام در جدول‌های ۱ و ۲ به ترتیب برای سطح بالایی مخزن و دیواره نشان داده شده است که در آنها R شعاع مخزن وH ارتفاع مخزن است.

جدول ۱: محدوده تغییرات و تغییر در هر گام برای ذراتی که از سطح بالایی مخزن وارد می‌شوند

محدوده متغییرها	تغییر در هر گام
$۰ < x < R$	۵ cm
$۰ < \theta < \pi/۲$	$\pi/۱۰$
$۰ < \varphi < \pi$	$\pi/۱۰$

جدول۲: محدوده تغییرات و تغییر در هر گام برای ذراتی که از دیواره‌ی مخزن وارد می‌شوند

محدوده متغییرها	تغییر در هر گام
$۰ < z < H$	۵ cm
$۰ < \theta < \pi/۲$	$\pi/۱۰$
$۰ < \varphi < \pi/۲$	$\pi/۱۰$

با ورود هر ذره در مخزن مخروط نور چرنکوف تشکیل شده و فوتون های چرنکوف تولید شده طبق رابطه

$$N = 2\pi\Delta x\alpha\left(\frac{1}{\lambda_1} - \frac{1}{\lambda_2}\right)\left(1 - \frac{1}{n^2\beta^2}\right)$$

به طور یکنواخت در این مخروط تشکیل و در مخزن حرکت می کنند. در هر گام یک سانتی‌متری از مسیر ذره فوتونهاي چرنکوف تولید می‌شوند و در هر گام انرژی ۲MeV از انرژی ذره کم می‌شود. در هر گام یک سانتی‌متری برای فوتون‌ها شرط جذب و بازتاب به صورت پخشی ازدیواره و کف مخزن و یا رسیدن به سطح PMT که در مرکز سطح فوقاني قرار دارد، بررسی می‌شود. در نهایت تعداد فوتونهاي چرنکوف تولید شده، تعداد فوتون‌های رسیده بهPMT و زمان رسیدن آنها گزارش داده می-شود.

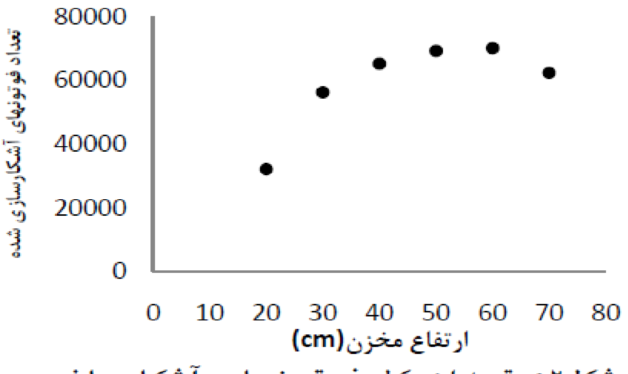

شکل۲: تعداد کل فوتون‌های آشکارسازی شده برحسب ارتفاع مخزن برای مخزن با قطر۴۰cm

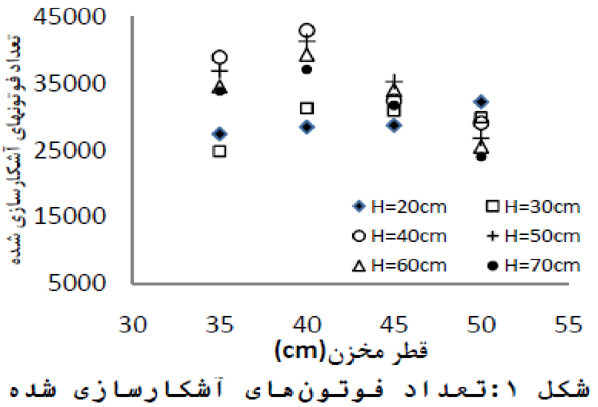

شکل ۱:تعداد فوتون‌های آشکارسازی شده بر حسب قطر مخزن برای ارتفاع‌های متفاوت مخزن

برای بدست آوردن میدان دید PMT که در واقع همان قطر بهینه‌ی مخزن است، ذرات از سطح بالایی در قطرهای متفاوت وارد مخزن با ارتفاع متغییر از ۲۰cm تا ۷۰cm شده و تعداد فوتون‌های آشکارسازی شده بدست آورده شد که در شکل ۱ نشان داده شده است. در این شکل دیده می‌شود که بهترین قطر ۴۰cm است. شکل ۲ تعداد فوتون‌های آشکارسازی شده را بر حسب ارتفاع مخزن برای مخزنی به قطر ۴۰cm را نشان می‌دهد. در این شکل دیده می‌شود که در ارتفاع

٦٠cm بیشترین تعداد فوتون آشکارسازی شده است. این نتایج با شبیه سازی اولیه مطابقت کامل دارد. به دلیل مشکلاتی که در ساخت مخزن با قطر ٤٠cm وجود داشت، از مخزن آماده‌ی موجود در بازار با قطر ٤٥cm استفاده شد و ارتفاع بهینه این مخزن مورد مطالعه قرار گرفت. شکل ٣ نمودار تعداد کل فوتون‌های آشکارسازی شده بر حسب ارتفاع مخزن برای مخزنی باقطر ٤٥cm را نشان می‌دهد. در شکل ٣ دیده می‌شود که ارتفاع بهینه برای مخزن با قطر ٤٥cm، ٦٠cm است.

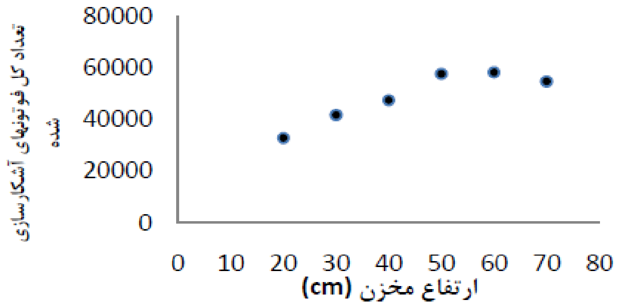

شکل ٣: تعداد کل فوتون‌های آشکارسازی شده برحسب ارتفاع مخزن برای مخزنی به قطر ٤٥cm

چیدمان آزمایش

همانگونه که اشاره شد برپایه اطلاعات بدست آمده از شبیه سازی اولیه برای دستیابی به بهترین ارتفاع آب برای آشکارساز چرنکوف آبی با یک PMT از یک مخزن استوانه ای شکل با ارتفاع ٧٠cm و قطر ٤٥cm استفاده شده که دارای سطح داخلی سفید مات می‌باشد (رنگ سفید مات نور را به صورت پخشی بازتاب می‌کنند) وسطح خارجی آن با رنگ سیاه، برای نور بندی مخزن، پوشیده شده است. برای پیدا کردن آهنگ رخدادها در کل سطح مخزن از یک آشکارساز سوسوزن ($10\times10\times0/5cm^3$) استفاده شده است. برای این منظور فقط نیمی ازسطح زیرین وقسمتی از سطح جانبی مخزن که در شکل٤ نشان داده شده است، بدلیل تقارن سمتی، توسط آشکارساز سوسوزن جاروب می‌شود. برای مقایسه دو دیواره داخلی سفید و آینه‌ای، سطح داخلی را توسط ورقه استنلس استیل آینه‌ای کردیم و آزمایش‌ها را برای سطح داخلی آینه‌ای تکرار کردیم. مدار الکترونیک این آزمایش در شکل٥ نشان داده شده است.

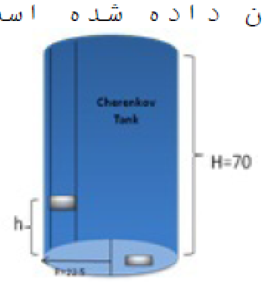

شکل ٤: محل‌هایی که توسط سنتیلاتور جاروب می‌شود.

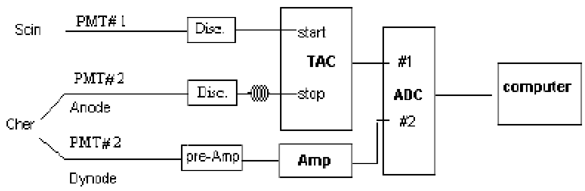

شکل ٥: طرح‌واره‌ای از مدار استفاده شده در آزمایش.

آزمایش

برای هر دو آزمایش (سطح داخلی با خاصیت پخشی و انعکاسی) ارتفاع آب مقطر در مخزن مذکور را از ٢٠cm تا ٧٠cm هر بار به مقدار ١٠cm افزایش دادیم. برای هر عمق از آب، سوسوزن را روی سطح جانبی وسطح زیرین حرکت دادیم. به هر آزمایش ٢٠٠٠

ثانیه زمان اختصاص داده شد تا تعداد ذراتی که هم از مخزن چرنکوف و هم از آشکارساز سوسوزن می‌گذرند در این زمان بدست آید. در تمام طیف‌های همزمانی بدست آمده نوفه‌های محیط حذف شد و در آخر برای هر ارتفاع آب تعداد ذرات گذرنده از کل سطح مخزن محاسبه گردید. آهنگ ثبت کل رخدادها در مخزن به ازای ارتفاع مختلف آب، برای هر دو سطح داخلی، در شکل ٦ آمده است.در این نمودار دیده می‌شود که آزمایش‌ها برای مخزن با دیواره سفید با نتیجه شبیه سازی توافق خوبی دارد. تا ارتفاع آب ٦٠cm آهنگ ثبت رخداد افزایش می‌یابد و پس از آن نمودار تخت می‌شود. همچنین با تغییر جنس دیواره در آهنگ ثبت رخداد تفاوت محسوسی دیده نمی‌شود.

شکل ٧ انرژی به جا مانده از ذراتی که به PMT رسیده‌اند را بر برحسب ارتفاع برای هر دو سطح نمایش می‌دهد.

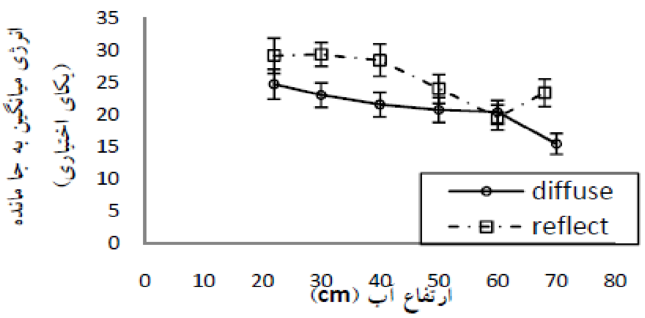

شکل ٧:انرژی میانگین به جا مانده از ذرات بر حسب ارتفاع آب

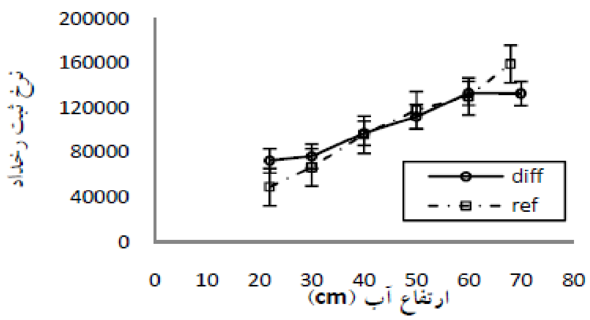

شکل ٦: آهنگ کل ثبت رخداد بر حسب ارتفاع آب.

نتیجه گیري

همانگونه که در شکلهای ٦ و٧ دیده می‌شود در آهنگ ثبت رخداد وانرژیی که از ذره بجا مانده و به PMT رسیده است بین دو مخزن با دیواره سفید و آینه‌ای اختلاف زیادی مشاهده نمی‌شود. با در نظر گرفتن هزینه‌ها و احتمال آلودگی آب در استفاده از سطح داخلی آینه‌ای می‌توان نتیجه گرفت که استفاده از مخزنی که سطح داخلی آن داراي خاصیت پخشي است مقرون به صرفه‌تر است.بادر نظر گرفتن شکل‌های ١و٢ ابعاد بهینه برای مخزن چرنکوف قطر ٤٠cm و ارتفاع ٦٠cm است. همانگونه که اشاره شد به دلیل مشکلات موجود برای تهیه مخزن با قطر٤٠cm از مخزنی با قطر ٤٥cm استفاده شد. با توجه به نمودارهای ٣و٦ مشخص می‌شود ارتفاع بهینه برای آشکارساز چرنکوف آبی با قطر ٤٥cm و سطح داخلی سفید، ارتفاع ٦٠cm است.

مرجع ها

١. T. Stanev, *High Energy Cosmic Rays* (Springer Press)
٢. I. Allekotte et al., *Nuclear Inst. and Methods in Physics Research*, A, Volume٥٨٦, Issue ٣, ١ March ٢٠٠٨, Pages ٤٠٩-٤٢٠ (٢٠٠٧)
٣.شیدایی، فرزانه (پایان نامه‌ی دکتری)، "مطالعه بر روی پرتوهای پرانرژی در سطح تهران"،دانشگاه صنعتی شریف، ١٣٨٧.

آشکارسازی مشتری داغ در گذر سوختیک

سجادیان، صدیقه[1] راهوار، سهراب[1]

[1] دانشگاه صنعتی شریف

چکیده

در سالهای اخیر تعداد زیادی سیارات فراخورشیدی دارای دوره تناوب بسیار کوتاه (که مشتری داغ[1] نامیده شده اند) به کمک روشهای عبور از جلوی ستاره مادر[2] و یا سرعت سنجی شعاعی[3] کشف شده اند. در این مقاله ما سعی می کنیم تا آشکارسازی این سیارات را به روش ریز همگرایی گرانشی برای یک عدسی دوتایی بررسی کنیم. با استفاده از روش پرتوافکنی معکوس[4] و الگوریتم درختی[5] منحنی نوری برای ترکیب سیاره و ستاره مادر را رسم می کنیم و با انجام شبیه سازی مونت کارلو عمق نوری از مرتبه $\bar{\tau} \sim 10^{-8}$ بدست آید. دراین کار نشان مي دهيم كه در ناحيه مادرون قرمز احتمال آشكارسازي بيشتر است.

مقدمه

در سال ۲۰۰۰ مقاله ای (مرجع ۱) به چاپ رسید که در آن پیش بینی شده بود پدیده عبور یک سیاره به اندازه مشتری که در فاصله بسیار نزدیک به ستاره مادر قرار گرفته است، از منحنی سوختیک باعث تقویت نورسیاره می شود. این اختلال در منحنی نوری می تواند با یک تلسکوپ ۱۰ متری رصد شود. بر اساس این مقاله ما نیز سعی کردیم که پدیده عبور یک سیاره شبیه مشتری داغ از سوختیک را شبیه سازی کرده وعمق نوری مربوط به آن را به دست آوریم. در این مورد تابش گرمایی از سطح سیاره سهم بیشتری از تابش های منعکس شده دارد که باعث می شود در ناحیه مادون قرمز احتمال آشکارسازی بیشتر باشد. از طرفی در حین عبور ستاره مادر از منحنی سوختیک، سیاره می تواند چندین بار منحنی سوختیک را قطع کند که این احتمال آشکارسازی را دراطراف قله افزایش می دهد.

در بخش اول روش پرتو افکنی معکوس و الگوریتم درختی که در رسم منحنی نوری استفاده کرده بایک نمونه منحنی نوری رسم شده شرح می دهیم. در بخش دوم ابتدا بر روی مشخصات منحنی نوری بحث کرده و در ادامه به شبیه سازی مونت کارلو در به دست آوردن عمق نوری خواهیم پرداخت. در بخش آخر نیز نتایج را بررسی می کنیم.

---

[1] Hot Jupiter

[2] transit

[3] Radial velocimetery

[4] Inverse ray shooting

[5] Tree code

منحنی نوری

در روش پرتو افکنی معکوس که در مرجع ۲ معرفی شده است ابتدا صفحه عدسی و صفحه منبع به قسمت های ریزی تقسیم می شود. نور به طور معکوس از ناظر به یک سلول در صفحه عدسی می تابد و با در نظر گرفتن میزان انحراف ناشی از وجود عدسی به سلول دیگری در صفحه منبع برخورد می کند. تعداد پرتوهای نوری که به هر سلول در صفحه منبع برخورد می کند نشان دهنده تقویت نوری است که در محل منبع رخ می دهد. به کمک این روش می توان منحنی سوختیک را رسم کرد. اما برای تعیین دقیق میزان تقویت نور در نقا طی که سیاره از سوختیک عبور می کند از الگوریتم درختی استفاده می کنیم که البته این روش با آنچه در مرجع ۳ معرفی شده است، تفاوت دارد. در این روش ابتدا صفحه عدسی را به ٤ قسمت تقسیم می کنیم و در اطراف منبع نیز یک سلول به طوری که در هر مرحله ابعاد این صفحه مساوی با ابعاد سلول در صفحه عدسی باشد، در نظر می گیریم. از هرسلول در صفحه عدسی تعداد زیادی پرتو نور با توجه به اندازه سلول به صفحه منبع می تابانیم. اگر پرتو نور به سلول در صفحه منبع برخورد کند آن سلول برای تقسیم بندی در مرحله بعد روشن می شود و این تقسیم بندی تا جایی ادامه دارد که تعداد زیادی سلول مساحت منبع را به پوشانند. باید توجه کرد که در هر مرحله برخورد تنها یک پرتو به سلول مورد نظر در صفحه منبع، برای روشن شدن آن سلول کافی است. در شکل (۱) سمت چپ نمونه ای از منحنی سوختیک رسم شده به کمک روش پرتو افکنی معکوس، نمایش داده شده است. همانطور که در این شکل مشخص است در حین عبور ستاره مادر از سوختیک سیاره چندین بار سوختیک را قطع می کند.

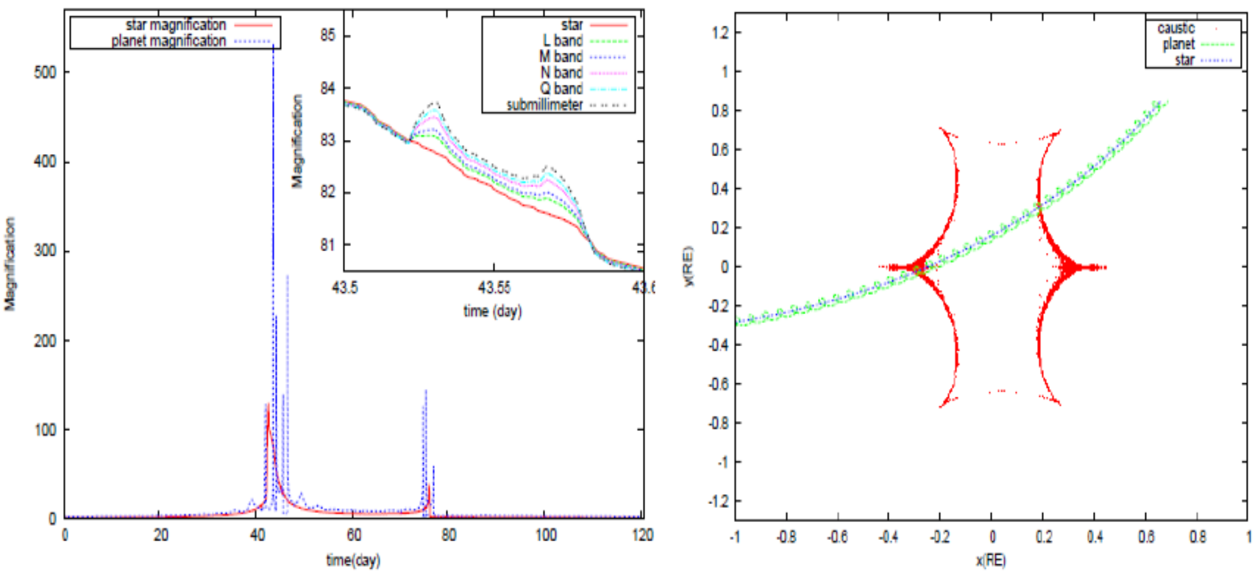

شکل (۱): سمت چپ عبور ستاره منبع وسیاره را از منحنی سوختیک نشان می دهد و سمت راست نیزمنحنی تقویت نورهر دو سیاره و ستاره نمایش داده شده است.

منحنی مربوط به این پیکر بندی نیز در سمت راست همان شکل آمده است. در قسمت بالا سمت راست این نمودار نیز اختلال ایجاد شده توسط سیاره در منحنی نوری ستاره مادر در فیلترهای متفاوتی رسم شده است. همانطور که دیده می شود هر چه به سمت طول موج های بلند تر می رویم این اختلال بیشتر می شود و همچنین به دلیل اینکه در

مورد سیاره اثر سطح مقطع محدود وجود ندارد، هنگامی که سیاره روی خط سوختیک قرار می گیرد نورش به مقدار زیاد تقویت می شود که این موضوع در شکل نشان داده شده است.

مشخصات منحنی نوری و شبیه ساری مونت کارلو

آنچه در آشکارسازی یک سیاره مهم است میزان تقویت نور در حین عبور از سوختیک و نسبت شار ذاتی سیاره به ستاره مادر که به وسیله ناظر در یافت می شود. در زیر راجع به نسبت شار بحث کنیم.

سیارات مشتری داغ دارای شعاع مدار حدود ۰.۰۱ تا ۰.۱ واحد نجومی هستند که در این فاصله سطح سیاره بسیار گرم می شود و در ناحیه مادون قرمز تابش گرمایی دارد که از تابع توزیع پلانک تبعیت می کند (مرجع ۴). این تابش سهم بیشتری نسبت به تابش منعکس شده دارد. شار نسبی در یافتی از سیاره به ستاره که شامل هردو بخش می باشد برابر است با:

$$\frac{I_p(\nu,T_p)}{I_\star(\nu,T_\star)}=[(\frac{R_p}{a})^2\frac{dA_g}{d\nu}+\frac{e^{h\nu/kT_\star}-1}{e^{h\nu/kT_p}-1}(\frac{R_p}{R_\star})^2]g(\Phi) \qquad (۱)$$

که در آن جمله اول شار منعکس شده و جمله دوم نیز نسبت شار گرمایی می باشد. پارامترهای a ، R_p، $R_\star$ و A_g به ترتیب شعاع مدار حرکت سیاره، شعاع سیاره، شعاع ستاره و نیز توان بازتاب هندسی می باشد. برای تعیین وابستگی این رابطه به طول موج این رابطه را در شکل (۲) رسم کرده ایم:

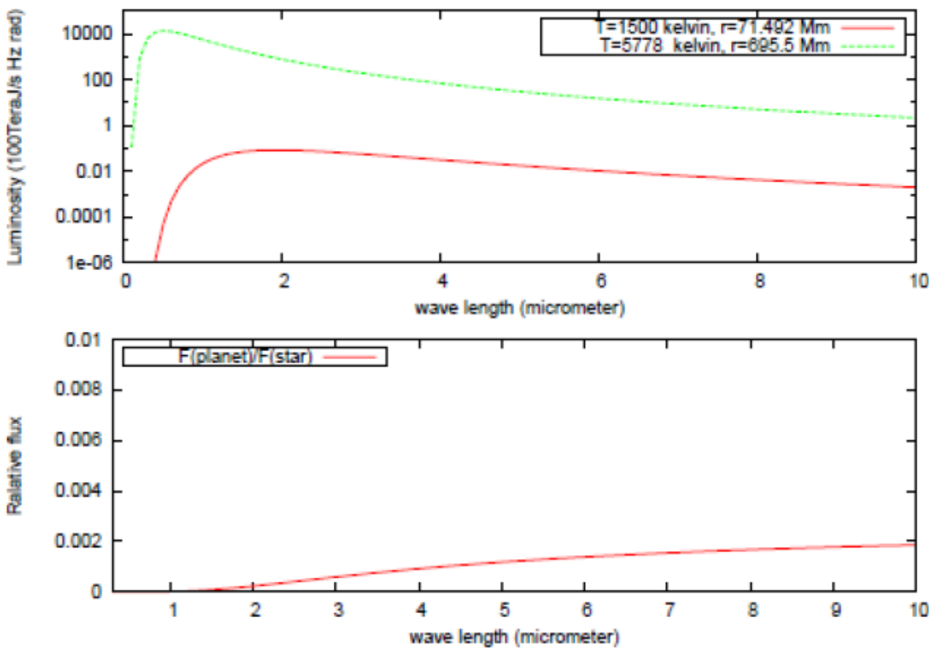

شکل (۲): در شکل بالا نمودار درخشندگی سیاره وستاره بر حسب طول موج رسم شده است و درشکل پایین نسبت شار دریافتی رسم شده که در طول موج های بلند تر این نسبت غالب است.

همانطور که در شکل دیده می شود نسبت این دو شار در ناحیه مادون قرمز غالب است.

در نهایت برای تعیین عمق نوری شبیه سازی مونت کارلوانجام دادیم که در آن برای تعیین پارامترها از تابع توزیع فیزیکی آنها استفاده شده است. حدود ٣٦ درصد از سیاره ها منحنی سوختیک راقطع می کند که از این کسر تعداد آنهایی که دیده می شوند به فیلتر استفاده شده برای رصد و نیز دقت نور سنجی بستگی دارد. برای سه دقت نورسنجی برابر با 10^{-2} و 10^{-3} و 10^{-4} در طول موج حدود ١٠میکرو متر، احتمال رصد $< \epsilon_p >$ ٠.٠٣، ٠.٣٠ و٠.٣٥ درصد بدست آمد. عمق نوری برای آشکارسازی سیاره برابر است با:

$$\tau_p = < \epsilon_p > \times f_p \times \tau \qquad (٢)$$

که در آن τ عمق نوری برای پدیده همگرایی گرانشی است و f_p کسری از ستاره هایی است که مشتری داغ دارند. با جایگذاری مقادیر واقعی کمیت ها $\tau_p \simeq 10^{-8}$ بدست می آید.

نتایج

در این کار ما احتمال آشکارسازی یک مشتری داغ در گذر سوختیک بررسی کرده و به کمک الگوریتم درختی و روش پرتوافکنی معکوس منحنی نوری مورد انتظار را رسم کردیم. در نهایت با شبیه سازی مونت کارلو احتمال آشکارسازی سیاره بدست آوردیم. اگر تنها عبور هندسی سیاره از سوختیک مورد نظر باشد، حدود ٣٦ درصد از سیاره ها از سوختیک عبور می کنند، اما در واقعیت تنها درصد کمی از این سیاره ها با توجه به محدودیت دقت نورسنجی دیده می شوند. در طول موج های بلندتر این درصد افزایش می یابد. نسبت شار سیاره به ستاره تابعی از جرم ستاره مادر نیز می باشد، برای ستاره های کوتوله از نوع M نسبت این شار افزایش می یابد.

مراجع

1) **Graff, D. S., Gaudi, B. S., 2000, ApJ, 538, 133.**
2) **Kayser, R. & Refsdal, S. & Stabell, R., 1986, A&A, 166, 36.**
3) **Wambsganss, J., 1999, J. Comput. Appl. Math., 109, 353.**
4) **Lopez-Morales, M., & Seager, S., 2007, ApJ, 667, 191.**
5) **Mao, S., & Paczynski, B., 1991, ApJ, 374, 3.**
6) **Schneider, P. & Wiess, A., 1986, A&A, 164, 237.**
7) **Schneider, P. & Wiess, A., 1987, A&A, 171, 49.**
8) **Rahvar, S., & Dominik, M., 2009, MNRAS, 392, 1193.**
9) **Sumi, T., et al. 2006, ApJ, 636, 240.**

گرانش اصلاح شده هولوگرافیك

ستاره ، محمد رضا
دانشکده علوم دانشگاه کردستان ، پاسداران ، سنندج

چکیده

در این مقاله مدل انرژي **تاریك هولوگرافیك را در چارچوب گرانش اصلاح شده مطالعه مي کنیم. با اعمال** مدل انرژي **تاریك هولوگرافیك**، معادله حالت را براي چگالي انرژي **هولوگرافیك را در جهان تخت بدست مي آوریم. محاسبات ما نشان مي دهد که با گرفتن** $\Omega_n = 0.73$ براي زمان حال، امکان قطع ۱- براي ω_n وجود دارد. این منجر به معادله حالت فانتوم -گونه براي مدل **انرژي هولوگرافیك در جهان تخت در چارچوب کیهان شناسي گرانش اصلاح** یافته مي گردد. نهایتاً ما شکل کنش(F(R سازگار با مدل **هولوگرافیك را مي یابیم.**

MODIFIED GRAVITATIONAL HOLOGRAFIC

Setare, Mohammad Reza
Department of Science, University of Kurdistan, Sanandaj,

Abstract

In this paper we study cosmological application of holographic dark energy density in the modified gravity framework. We employ the holographic model of dark energy to obtain the equation of state for the holographic energy density in spatially flat universe. Our calculation show, taking $\Omega_n = 0.73$ *for the present time, it is possible to have* ω_n *crossing-1. This implies that one can generate phantom like equation of state from a holographic dark energy model in flat universe in the modified gravity cosmology framework. Also we develop a reconstruction scheme for the modified gravity with f(R) action.*

PACS No. 95.36.+x ، 95.35.+d

مقدمه

امروزه قویاً باور بر اینست که جهان داراي یك انبساط شتابدار است. مشاهدات اخیر مربوط به ابرنواختر هال گونهIa [۱] همراه با ساختار بزرگ مقیاس [۲] وناهمسانگردي تابش زمینه میکروموج کیهاني[۳] همگي گواههاي بر این شتاب انبساط دار جهان هستند. به منظور توضیح انبساط شتابدار جهان ، تعداد زیادي تئوري ارائه گردیده است. بطور گسترده اي باور بر اینست که یك عامل اسرار آمیز، ***انرژي تاریك***،با فشار منفي، منجر به این شتاب کیهاني مي گردد. اگرچه هنوز یك تئوري از گرانش کوانتومي در دسترس نیست ولي مي توان بر مبناي اصول این نظریه به بررسي طبیعت *انرژي تاریك* پرداخت. مدل انرژي تاریك هولوگرافیك از زمره این مدل هاست که بر مبناي اصول اولیه گرانش کوانتومي شکل گرفته است[۴و۵و۶و۷]. از دیگر سوي نسبیت عام اینشتین ممکن است توصیفگر گرانش در انرژي هاي بالا نباشد. تئوریهاي از گرانش اصلاح یافته شق دیگري براي مسئله انرژي تاریك هستند[۸]. از میان مقبول ترین مدل هاي گرانش اصلاح یافته مدل گرانش F(R) شاید موفق ترین آنها در حل مسائل کیهاني مرتبط با انبساط شتابدار جهان باشد.

نسخه هاي ساده تري از اين نظريه، مدل هاي $\frac{1}{R}$[9] و $\frac{1}{R}+R^2$ مي باشند[10].

در اين مقاله با استفاده از مدل انرژي تاريك هولوگرافيك در جهان تحت معادله حالت براي چگالي انرژي هولوگرافيك را در چارچوب گرانش اصلاح يافته مي يابيم. نشان مي دهيم كه انرژي تاريك هولوگرافيك رفتار فانتوم گونه اي از خود بروز ميدهد. وقتي كه پارامتر Cموجود در عبارت چگالي انرژي تاريك در بازه $0.21 \le C \le 2.1$ قرار دارد. در ادامه نشان مي دهيم كه اگر چنانچه گرانش اصلاح يافته بخواهد برحسب مدل انرژي تاريك قابل بيان باشد آنگاه كنش آن بايد چه شكلي داشته باشد.

گرانش اصلاح يافته و انرژي تاريك هولوگرافيك

كنش گرانش اصلاح يافته به صورت زير است:

$$S = \int D^4 x \sqrt{-g}\,[F(R) + Lm] \qquad (۱)$$

كه Lm چگالي لاگرانژين ماده است. شكل معادلي براي كنش بالا به شكل زير مي توان نوشت [8]،

$$S = \int D^4 x \sqrt{-g}\,[P(\phi)R + Q(\phi) + Lm] \qquad (۲)$$

كه در آن توابع P,Qتوابعي از ميدان اسكالر ϕ هستند.

با وردش كنش (۲) نسبت به متريك $g_{\mu\nu}$، خواهيم داشت

$$-\frac{1}{2}g_{\mu\nu}[P(\phi)R + Q(\phi)] - R_{\mu\nu}P(\phi) + \nabla_\mu \nabla_\nu P(\phi) - g_{\mu\nu}\nabla^2 P(\phi) + \frac{1}{2}T_{\mu\nu} = 0 \qquad (۳)$$

كه $T_{\mu\nu}$تانسور تكانه-انرژي است. معادلات متناظر براي جهان FRW تحت بصورت زير است

$$\rho = 6H^2 P(\phi) + Q(\phi) + 6H\frac{dP(\phi)}{dt} \qquad (۴)$$

$$P = -(4\dot{H} + 6H^2)P(\phi) - Q(\phi) - 2\frac{d^2P(\phi)}{dt^2} - 4H\frac{dP(\phi)}{dt} \qquad (۵)$$

كه درآن ρ, Pفشار وچگالي انرژي ميدان اسكالر در چارچوب گرانش اصلاح يافته هستند. با تركيب (۴) و (۵) بدست مي آيد:

$$P + \rho = -2\frac{d^2P(\phi)}{dt^2} + 2H\frac{dP(\phi)}{dt} - 4\dot{H}P(\phi) \qquad (۶)$$

اكنون ما تناظري بين مدل بالا ومدل انرژي تاريك هولوگرافيك را فرض مي كنيم. چگالي انرژي هولوگرافيك بصورت زير است: **(۷)**

$$\rho_n = \frac{3c^2}{R_h^{\,2}}$$

كه در آن Cيك ثابت و R_h افق رويداد آينده است كه به شكل زير مي باشد

$$R_h = a\int_t^\infty \frac{dt}{a} = a\int_a^\infty \frac{da}{Ha^2} \qquad (۸)$$

با تعريف Ω_nبصورت زير

$$\Omega_n = \frac{\rho_n}{\rho_{cr}} = \frac{\rho_n}{3H^2} = \frac{C^2}{R_h^{\,2} H^2} \qquad (۹)$$

مي توان نوشت

$$\dot{R}_h = R_h H - 1 = \frac{C}{\sqrt{\Omega_n}} - 1 \qquad (۱۰)$$

با فرض اينكه انرژي تاريك مولفه غالب در جهان است، قانون بقا را مي توان بصورت زير نوشت

$$\dot{\rho}_n + H(\rho_n + P_n) = 0 \qquad (۱۱)$$

با در نظر گرفتن تعريف چگالي انرژي هولوگرافيك و معادله (۱۰)خواهيم داشت:

$$\dot{\rho}_n = \frac{-2}{R_h}\left(\frac{C}{\sqrt{\Omega_n}} - 1\right)\rho_n \qquad (۱۲)$$

با جايگذاري در معادله (۱۱) و استفاده ز رابطه $\omega_n = \frac{P_n}{\rho_n}$، معادله حالت بصورت زير در مي آيد

$$\omega_n = -\left(\frac{1}{3} + \frac{2\sqrt{\Omega_n}}{3C}\right) \qquad (۱۳)$$

با توجه به نتايج مشاهداتي [۱۲،۱۳، ۱۱] پارامترCدر محدوده $0.21 \le C \le 2.1$ قرار دارد. با فرض0.73=Ω_nبراي زمان حال و در نظر گرفتن محدوده فوق براي

C، پارامتر حالت ω_n در محدوده $-3.04 \le \omega_n \le -0.6$ قرار می گیرد. با استفاده از (۱۳) می توان دیدکه برای اینکه $\omega_n \le -1$ باشد C باید شرط $C \le \sqrt{\Omega}$ را ارضا کند. بنابراین با اتخاذ $\Omega_n = 0.73$ برای زمان حال، امکان قطع -۱ توسط ω_n وجود دارد.

گرانش اصلاح یافته وبازسازی انرژي تاريك هولوگرافيك

اکنون کنش (۱) را بدون جمله ماده در نظر بگیرید. برای جهان FRW تحت داریم:

$$\rho = f(R) - 6(\dot{H} + H^2 + -H\frac{d}{dt})f'(R) \quad (۱۴)$$

$$P = f(R) - 2(-\dot{H} - 3H^2 + \frac{d^2}{dt^2} + 2H\frac{d}{dt})f'(R) \quad (۱۵)$$

$$R = 6\dot{H} + 12H^2 \quad (۱۶)$$

جدداً چگالی انرژی هولوگرافیک را در نظر می گیریم وآنرا در معادله (۱۴) جایگزین می کنیم، بنابراین

$$f(R) = 3\Omega_n H^2 - 6(\dot{H} + H^2 + -H\frac{d}{dt})f'(R) \quad (۱۷)$$

با استفاده از معادلات (۷) و(۱۳) و جایگذاری $f(R)$ فوق در معادله (۱۵) معادله زیر حاصل می آید

$$\frac{d^2}{dt^2}f'(R) - 2H\frac{d}{dt}f'(R) + 4\dot{H}f'(R) + 2\Omega_n H^2(1 - \frac{\sqrt{\Omega_n}}{C}) = 0 \quad (۱۸)$$

ماجواب زیر رابرای a فرض می کنیم

$$a = a_0(t - t_s)^{h_0} \quad (۱۹)$$

که درآن a_0, h_0, t_s ثابت هستند. **جایگذاری** معادله (۱۹) در معادله (۱۶) انحنای اسکالر بصورت زیر در می آید

$$R = \frac{12h_0^{\,2} - 6h_0}{(t_s - t)^2} \quad (۲۰)$$

با استفاده از معادلات (۸) و(۱۹) می توان نوشت

$$R_h = a_0(t_s - t)^{h_0}\int_t^{t_s}\frac{dt}{a_0(t_s - t)^{h_0}} = \frac{t_s - t}{1 - h_0} \quad (۲۱)$$

وبنابراین رفتار چگالی انرژي تاريك هولوگرافيك بر حسب زمان بصورت زير در می آيد

$$\rho_n = \frac{3C^2(1 - h_0)^2}{(t_s - t)^2} \quad (۲۲)$$

با جایگذاری ρ_n فوق در معادله (۱۴) واستفاده از معادلات (۱۹) و(۲۰) داریم

$$\frac{72h_0^{\,2}(1 - 2h_0)}{(t_s - t)^4}f''(R) - \frac{6h_0(h_0 - 1)}{(t_s - t)^2}f'(R) + f(R) = \frac{3C^2(1 - h_0)^2}{(t_s - t)^2} \quad (۲۳)$$

جواب معادله دیفرانسیل بالا بصورت زیرداده می شود

$$f(R) = C_1 R^{1/2(\frac{3-h_0}{2} - \sqrt{\frac{(h_0-3)^2}{4} + 4h_0 - 2})} + C_2 R^{1/2(\frac{3-h_0}{2}) + \sqrt{\frac{(3-h_0)^2}{4} + 4h_0 - 2}} + C^2(1 - h_0)^2 R / 2h_0^{\,2} \quad (۲۴)$$

که در آن C_2, C_1 ثابت هستند. بنابراین یک مدل گرانشی اصلاح یافته سازگار با مدل انرژي تاريك هولوگرافيك در فضای تحت شکل بالاارادارد.مدل بالا شرطی را که معمولاًبر مدل های گرانش اصلاح یافته اعمال می شودیعنی [۱۴، ۱۵]

$$\lim_{R \to 0} f(R) = 0 \quad (۲۵)$$

براورده می کند. برای اینکه انبساط شتابدار جهان در شرایط حاضر رخ دهدباید شرط زیر نیز برآورده شود

$$f(R_0) = -2R_0, f'(R_0) \approx 0 \quad (۲۶)$$

که $R_0 \approx (10^{-33}ev)^2$ انحنای فعلی جهان است [۱۴].

با اعمال شرایط (۲۶)، ثابت های C_2, C_1 بصورت زیر بدست می آیند:

$$C_1 = -\frac{R_0^{\,1-u}}{u + v}[2v + (v + 1)\frac{C^2(1 - h_0)^2}{2h_0^{\,2}}] \quad (۲۷)$$

شبیه‌سازی و آزمایش اثر هدایت کننده نوری سنتیلاتور بر عملکرد آرایه آشکارسازی بهمن‌های گسترده هوایی

عشاق، محمودرضا[۱] بایسته، شیما[۱] بهمن‌آبادی، محمود[۱] شیدایی، فرزانه[۱] صمیمی، جلال[۱]
[۱] دانشکده فیزیک، دانشگاه صنعتی شریف

چکیده

به منظور به کارگیری آرایه‌ای از آشکارسازهای سنتیلاتور که بهترین کارایی را در آشکارسازی بهمن‌های هوایی داشته باشند، یک شبیه‌سازی با هدف یافتن ارتفاع بهینه برای محفظه هدایت کننده نور به تکثیر کننده نوری (PMT) صورت گرفت و نتایج آن توسط آزمایش مورد بررسی قرار گرفت. برای یک سنتیلاتور با ابعاد ($50\times50\times3cm^3$)، ارتفاع بهینه یافته شده ۱۰سانتی‌متر است. همچنین نتایج آزمایش همزمانی، این سنتیلاتورها را مناسبتر از سنتیلاتورهای ($100\times100\times3cm^3$) برای قرارگرفتن در آرایه‌ی آشکارسازی معرفی می‌کند. طیف انرژی تک ذره‌ای و دوذره‌ای به دست آمده از سنتیلاتور برگزیده، توانایی این آشکارساز در ثبت انرژی به جا مانده از ذرات عبوری از ماده سنتیلاتور را نشان می‌دهد.

مقدمه

بهمن‌های گسترده هوایی در اثر ورود ذرات باردار یا فوتون‌های گامای بسیار پرانرژی پرتوی گاما ($E>10^{13}eV$) به جو و برهمکنش آن‌ها با هسته اتم‌های جو به وجود می‌آیند. آشکارسازی ذرات ثانویه‌ی حاصل از این برهمکنش‌ها در سطح زمین توسط آرایه‌ای از آشکارسازهای زمینی صورت می‌گیرد. این آرایه می‌تواند متشکل از تعدادی سنتیلاتور باشد که اختلاف زمانی ورود ذرات ثانویه به این آشکارسازها، جهت فرود ذره‌ی اولیه به جو تعیین می‌کند. نور تولید شده در سنتیلاتورهای مورد استفاده در آزمایشگاه پرتوی کیهانی دانشگاه صنعتی شریف، توسط یک محفظه هدایت کننده به تکثیر کننده نوری می‌رسند. سطح داخلی این محفظه با نور سفید پوشیده شده است؛ بنابراین نور تولید شده یا به طور مستقیم و یا به صورت غیرمستقیم پس از برخورد با دیواره‌ی محفظه و پس از انعکاس از آن سطح، به تکثیر کننده‌ی نوری می‌رسد که همین امر سبب پراکندگی در ثبت همزمانی‌های ذرات مربوط به بهمن‌های هوایی شده و به دنبال آن تعیین دقت زاویه‌ی بهمن هوایی آشکار شده را تحت تأثیر قرار می‌دهد. با افزایش ارتفاع محفظه هدایت کننده، احتمال آشکارسازی ذرات بهمن کاهش می‌یابد، همچنین احتمال آشکارسازی ذرات بهمن با دور شدن عبور آن‌ها از مرکز سنتیلاتور کم می‌شود. از طرف دیگر افزایش ارتفاع محفظه‌ی هدایت کننده، پراکندگی توزیع همزمانی‌ها را کاهش می‌دهد. رنگ سفید سطح داخلی محفظه نوری، سبب هدایت و تجمع تعداد زیادی فوتون به سمت افزونگر فوتونی می‌شود و احتمال آشکارسازی را افزایش می‌دهد. در عین حال رنگ سفید موجب پراکندگی در اندازه‌گیری زمان رسیدن ذرات فرودی می‌شود.

عوامل مذکور بر روی کارایی آشکارساز تأثیر می‌گذارد. بنابراین وابستگی آشکارسازی ذرات، به ارتفاع محفظه‌ی هدایت کننده نور را هم توسط آزمایش و هم شبیه‌سازی مورد بررسی قرار داده‌ایم. علاوه بر آن کارایی دو سنتیلاتور با ابعاد ($50\times50\times3cm^3$) و ($100\times100\times3cm^3$) برای استفاده در یک آرایه از آشکارسازها، با هم مقایسه شده است.

شبیه‌سازی محفظه نوری هدایت کننده

این شبیه‌سازی برای سنتیلاتوری با ابعاد ($۵۰×۵۰×۳cm^۳$) انجام شد که سطح بزرگ بالایی آن ($۵۰×۵۰cm^۲$) با یک محفظه هدایت کننده نوری و بقیه سطوح آن توسط ورق‌های آلومینیوم پوشیده شده است. یک تکثیر کننده نوری بالای سر این مجموعه قرار دارد که کارایی کوانتومی آن η=۲۵% و بهره آن $G=۱۰^۸$ است، بنابراین تعداد الکترون‌های تولید شده در تکثیر کننده نوری قابل محاسبه است $N_e = N_{photon} G\eta$ که N_{photon} تعداد فوتون-های وارد شده به تکثیر کننده نوری است.

برای فوتون‌های تولید شده در سنتیلاتور، دو مسیر برای رسیدن به تکثیر کننده نوری در بالای محفظه هود وجود دارد. اولی به طور مستقیم از کف محفظه و دیگری به طور مستقیم پس از انعکاس از دیواره است. برای هر مسیر سهم فوتون‌های تولید شده را حساب می‌کنیم و با جمع زدن بر روی مسیرها و در نظر گرفتن سهم فوتون‌ها مقدار کارایی آشکارسازی سنتیلاتور را برای هر ارتفاع به دست می‌آوریم. همان‌طور که در شکل دیده می‌شود، در ارتفاع ۱۰ سانتی‌متر بیشترین کارایی را داریم.

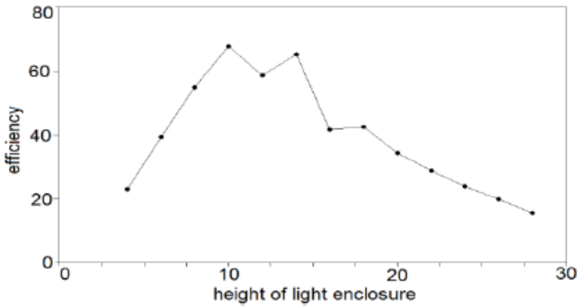

شکل۱: تغییر کارایی آشکارسازی سنتیلاتور با افزایش ارتفاع هدایت کننده نوری.

آزمایش مقایسه کارایی دو محفظه هدایت کننده نوری با ارتفاع‌های مختلف

همان‌طور که نتایج شبیه‌سازی نشان می‌دهد، ارتفاع ۱۰ سانتی‌متر، ارتفاع بهینه برای محفظه هدایت کننده نوری جهت آشکارسازی بهمن‌های هوایی است. در آزمایشی به تحقیق این موضوع می‌پردازیم. در این آزمایش طیف همزمانی میان دو سنتیلاتور با ابعاد ($۱۰×۱۰×۰.۵cm^۳$) و ($۵۰×۵۰×۳cm^۳$) را در دو حالت با هم مقایسه کردیم. حالت اول برای سنتیلاتور ($۵۰×۵۰×۳cm^۳$) یک محفظه نوری با ارتفاع ۱۰ سانتی‌متر انتخاب کردیم و در حالت دوم ارتفاع این محفظه را ۲۰ سانتی‌متر گرفتیم. در هر آزمایش سنتیلاتور کوچکتر زیر سنتیلاتور بزرگتر قرار می‌گیرد. پالس خروجی از دو سنتیلاتور به تفکیک کننده سریع (fast decriminator) که آستانه آن بر روی ۵۰mV قرار دارد می‌رسد. خروجی اولین کانال تفکیک کننده سریع که به تکثیر کننده نوری سنتیلاتور بزرگ متصل است با یک تأخیر زمانی که توسط یک سیم ۱۸متری ایجاد می‌شود، به ورودی توقف واحد تبدیل کننده زمان به دامنه (TAC) می‌رسد. خروجی دومین کانال تفکیک کننده سریع که مربوط به تکثیر کننده نوری سنتیلاتور دوم است، به ورودی شروع واحد تبدیل کننده زمان به دامنه می‌رسد. واحد تبدیل کننده زمان به دامنه بر روی پنجره زمانی ۲۰۰نانوثانیه تنظیم شده است که این پنجره زمانی نیز در واحد دامنه به دیجیتال (ADC) به ۱۰۲٤

قسمت مساوی تقسیم می‌گردد. خروجی این واحد به نرم افزار Mulpar وارد شده و مورد تحلیل قرار می‌گیرد. بدین ترتیب با عبور ذره‌ی ثانویه پرتوی کیهانی از هر دو سنتیلاتور، یک شمارش همزمانی به وجود می‌آیدو طیف اختلاف زمانی‌های عبور ذره از دو سنتیلاتور در پنجره زمانی ۲۰۰نانو ثانیه ثبت می‌شود.

شکل(۲) توزیع اختلاف زمانی‌های ثبت شده از ذرات پرتوی کیهانی برای دو حالت مختلف، اولی با سنتیلاتوری با محفظه نوری به ۱۰cm و دیگری با محفظه نوری به ارتفاع ۲۰cm را نشان می‌دهد. مقایسه نشان می‌دهد که شمارش مفید برای ارتفاع ۱۰cm بیشتر است و پهنای طیف زمانی آن کمی کوچکتر است.

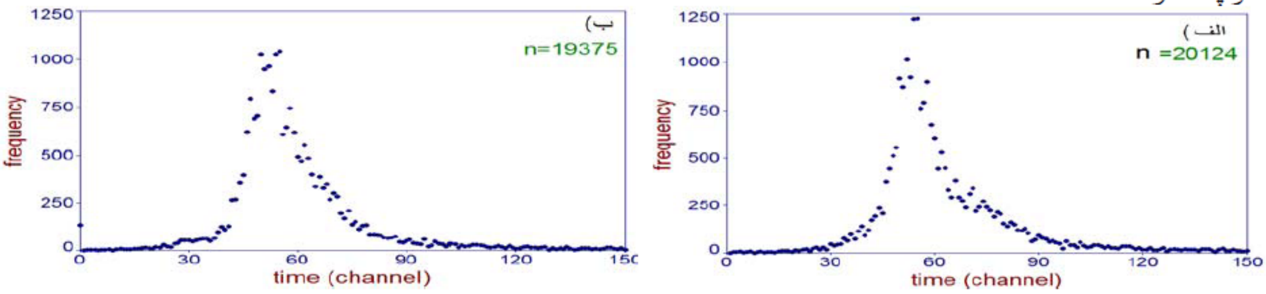

شکل(۲): توزیع اختلاف زمانی‌های ثبت شده بهمن‌های هوایی توسط سنتیلاتورها برای محفظه-های نوری الف)۱۰cm و ب)۲۰cm

مقایسه کارایی دو سنتیلاتور در ابعاد مختلف

آزمایشی چیده شد تا کارایی سنتیلاتور ($۵۰×۵۰×۳cm^۳$) با ارتفاع محفظه ۱۰cm را با سنتیلاتوری به ابعاد ($۱۰۰×۱۰۰×۳cm^۳$) با ارتفاع محفظه‌ی ۱۵cm مقایسه کنیم. بدین منظور با دو آزمایش و آرایش الکترونیکی مشابه با آزمایش قبل، دو طیف همزمانی، میان سنتیلاتور ($۵۰×۵۰×۳cm^۳$) و یک سنتیلاتور ($۱۰×۱۰×۰٫۵cm^۳$) و میان سنتیلاتور ($۱۰۰×۱۰۰×۳cm^۳$) و یک سنتیلاتور ($۱۰۰×۱۵×۱cm^۳$) تشکیل می‌شود. زمان داده‌گیری برای هر دو آزمایش یکسان است. از آنجا که سطح آشکارسازی سنتیلاتور بزرگتر ۴ برابر سنتیلاتور کوچکتر است، در مقایسه کارایی آشکارسازی انتظار می-رود به همین نسبت آشکارسازی بهتری داشته باشیم، ولی مقایسه نشان می-دهد که نسبت شمارش مفید در سنتیلاتور کوچکتر به شمارش مفید در سنتیلاتور بزرگتر تنها ۷۰% می‌باشد، به علاوه با بزرگتر شدن ابعاد آشکارساز در آرایه، عدم قطعیت بزرگتری در زمان رسیدن پرتوهای کیهانی به وجود می‌آید که همین امر باعث ایجاد خطا در جهت بهمن می-شود. مقدار نیم پهنای نیم بیشینه‌ی طیف همزمانی سنتیلاتور بزرگتر و کوچکتر به ترتیب ۱٫۱ns [۱] و ۰٫۹ns است. بنابراین سنتیلاتورهای کوچکتر ($۰٫۲۵m^۲$) برای قرار گرفتن در آرایه مناسبتر به نظر می‌رسد.

کارایی آشکارسازی سنتیلاتور با دور شدن عبور ذره از مرکز و ثبت طیف انرژی تک ذره‌ای و دو ذره‌ای

در این آزمایش سطح زیر سنتیلاتور($۵۰×۵۰×۳cm^۳$)را، به ۲۵ تقسیم کرده و کل آن را توسط سنتیلاتور ($۱۰×۱۰×۰٫۵cm^۳$) جاروب کردیم و در هر مورد طیف همزمانی میان این دو سنتیلاتور را ثبت کردیم. مدار الکترونیکی این آزمایش همانند قسمت‌های قبل می‌باشد با این تفاوت که این بار از خروجی دینود تکثیر کننده نوری سنتیلاتور($۵۰×۵۰×۳cm^۳$)که به یک پیش

تقویت کننده (×۱۰۰) و پس از آن به یک تقویت کننده (×۵۰۰) متصل می‌شود نیز استفاده می‌شود. خروجی این تقویت کننده پس از عبور از تبدیل کننده آنالوگ به دیجیتال توسط نرم افزار Mulpar به صورت پارامتر دوم که به عنوان انرژی تک ذره محسوب می‌شود، ثبت خواهد شد. نمایشی از این مدار در شکل(۳الف) قابل مشاهده است. انتظار داریم که با دور شدن عبور ذره از مرکز سنتیلاتور، شمارش مفید کاهش یابد. همچنین شکل(۳ب) تغییرات شمارش میانگین ذرات بر حسب فاصله از مرکز سنتیلاتور به همراه میله خطای مربوط به هر شمارش را نشان می‌دهد.

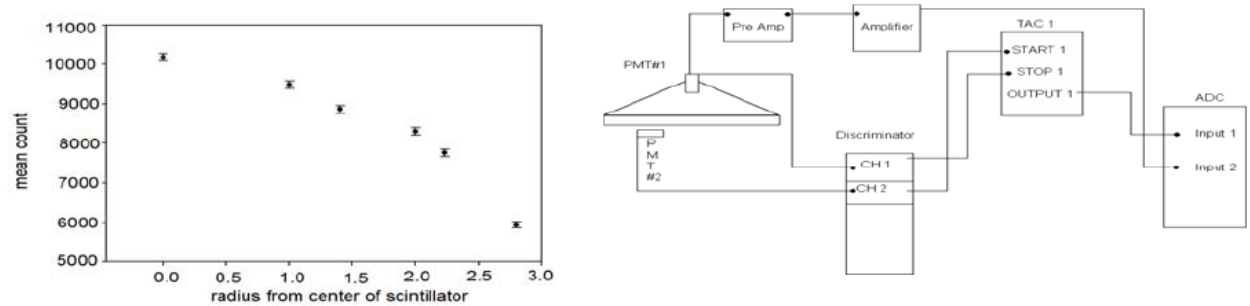

شکل(۳): در طرف راست مدار ثبت شمارش همزمانی دو سنتیلاتور و همچنین اندازه‌گیری انرژی ذره عبوری دیده می‌شود. طرف چپ تغییر شمارش میانگین با دور شدن از مرکز سنتیلاتور است.

در آزمایش دیگری به منظور ثبت انرژی به جا مانده از دو ذره در سنتیلاتور بزرگ، در زیر این سنتیلاتور از دو سنتیلاتور کوچک و مشابه ($۱۰×۱۰×۰٫۵cm^3$) استفاده کردیم. هدف از این آزمایش ثبت همزمانی و انرژی به جا مانده دو ذره بود، که ذره‌ی اول پس از عبور از سنتیلاتور بالایی با یک اختلاف زمانی از یکی از سنتیلاتورهای کوچک پایینی و ذره‌ی دوم پس از عبور از سنتیلاتور بالایی از سنتیلاتور کوچک دیگری عبور می‌کنند. شکل(٤الف) انرژی بهنجار شده مربوط به تک ذره و دو ذره ای نشان داده شده است و در شکل (٤ب) نیز احتمال دیده شدن تک ذره و دوذره بر اساس طیف انرژی تشکیل شده دیده می‌شود.

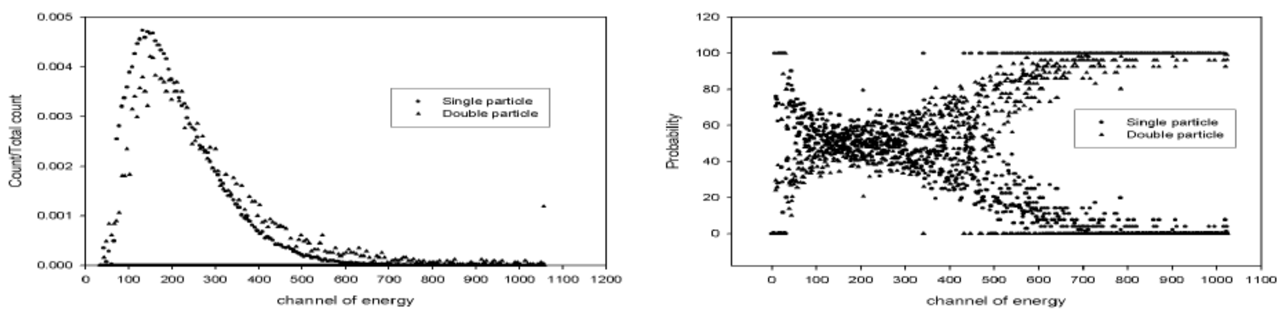

شکل٤: الف) طیف انرژی دو ذره‌ای ب) احتمال دیده شدن تک ذره و دو ذره.

نتیجه‌گیری

به منظور بررسی دقیق پارامترهای بهمن‌های هوایی گسترده (زاویه فرود و انرژی ذرات بهمن)، نیاز است که اجزای آرایه آشکارسازی همچون آشکارسازهای سنتیلاتور عملکردی بهینه داشته باشند. با شبیه‌سازی و آزمایش این آشکارسازها برای بهینه کردن کارایی آن‌ها، سنتیلاتور با ابعاد ($۵۰×۵۰×۳cm^3$) و ارتفاع محفظه هدایت کننده نوری ۱۰cm مناسبتر به نظر می‌رسند. همچنین این سنتیلاتورها از سنتیلاتورهای با ابعاد

($۱۰۰\times۱۰۰\times۳cm^۳$) که در آرایه‌های پیشین [۲] مورد استفاده قرار می‌گرفت، مناسب تر هستند.

مراجع

[۱] Bahmanabadi, M., ۱۹۹۸, *Experimental Astronomy*, ۱۳, ۱۳-۲۷.
[۲] Khakian Ghomi, M., ۲۰۰۵, *Astronomy and astrophysics*, ٤۳٤, ٤٥۹-٤٦۷.

اثر بادهای ستاره‌ای بر قرص‌های برافزایشی خودگراننده

میرترابی، محمد تقی[1] دهقان، سیامک[2] عابدینی، یوسفعلی[2]

[1] دانشگاه الزهرا

[2] دانشگاه زنجان

چکیده

در تحقیق حاضر تحول وابسته به زمان یک قرص برافزایشی خودگراننده با گرانروی نسخه‌ی بتا با حضور بیرون‌ریزی یا باد، مورد بررسی قرار گرفته است. در همین راستا، با استفاده از اعمال معادلات پایه‌ای هیدرودینامیک بر مدل مفروض و بدون بعد کردن آنها، معادلات تحول سامانه‌ی پیش‌ستاره- قرص به‌دست می‌آید. سپس این معادلات بر پایه‌ی روش‌های عددی مناسب مورد حل عددی قرار می‌گیرد. در نهایت با تحلیل داده‌ها و نتایج عددی نشان داده می‌شود که حضور باد، چگالی جرمی در قرص را کاهش داده و موجب کند شدن سرعت سمتی آن می‌شود. همچنین حضور باد موجب افزایش سرعت شعاعی یا برافزایشی در قرص، به‌-خصوص در نواحی بیرونی آن می‌شود. به‌علاوه، نشان داده می‌شود که باد در کنار گران‌روی عامل مهمی در جهت انتقال تکانه‌ی زاویه‌ای به نواحی خارجی‌تر قرص محسوب می‌شود.

مقدمه

قرص‌های برافزایشی اطراف ستارگان پیش‌رشته‌ی اصلی نامزدهای مناسبی جهت ایجاد سامانه‌های سیاره‌ای هستند. ساختار چنین قرص‌هایی که موضوع بسیار مورد علاقه برای بررسی می‌باشد، به کمک دو روش جواب‌های نیمه تحلیلی در حالت ناپایدار[1] و شبیه‌سازی‌های عددی هیدرودینامیکی[2] مورد مطالعه قرار گرفته‌است.
در این تحقیقات، این موضوع مشخص شده است که دو عامل خودگرانندگی و گران‌روی نقش بسیار مهمی در انتقال تکانه‌ی زاویه‌ای در قرص دارند. برافزایی به‌دلیل وجود نوعی اتلاف، که انرژی آزاد شارش بُرشی را به‌صورت گرما آزاد می‌کند، صورت می‌گیرد و در نتیجه به مواد داخل دیسک اجازه می‌دهد به عمق‌های پایین‌تر چاه پتانسیل گرانشی مرکزی سقوط کنند. در یک تصویر ساده لیندن- بل و پرینگل نشان دادند که فرآیند اتلافی می‌بایست به شکل یک نوع تنش باشد که تکانه‌ی زاویه‌ای را به بیرون منتقل کند[3]. این موضوع نقش بسیار مهمی را چنین سامانه‌هایی از کهکشان‌های هسته‌فعال تا پیش‌ستارگان بازی می‌کند.

روابط هیدرودینامیکی حاکم بر سیستم

مدل‌هایی که انتقال تکانه‌ی زاویه‌ای را تحلیل می‌کنند، معمولاً بر نظریه‌های هیدرواستاتیکی استوارند و مبنای آنها تکانه‌ی حرکت، بخاطر وجود گران‌روی در گاز است. به منظور مطالعه‌ی فرآیندهای برافزایی در یک قرص نازک به نیم ضخامت H تحت اثر خودگرانندگی و گران‌روی، با در نظر گرفتن اثر باد یا بیرون‌ریزی، قرصی با تقارن محوری با استفاده از مختصات استوانه‌ای (r,φ,z) در نظر گرفته می‌شود. در این مساله فرض می‌شود که قرص از لحاظ هندسی بسیار نازک و در راستاهایی عمودی و سمتی متقارن است. همچنین فرض می‌شود که اثر باد به‌گونه‌ای است که موجب خروج گاز از دو سطح بالایی و پایینی استوانه می‌شود[4].
با استفاده از اعمال هندسه و شرایط اولیه‌ی مدل بر معادلات نویر- استوکس، معادلات حاکم بر سیستم به‌دست می‌آید. جمله‌ی پایستاری جرم یکی از معادلات حاکم بر سیستم را تشکیل می‌دهد. این رابطه به‌صورت

$$\frac{\delta\sigma}{\delta t}+\frac{1}{r}\frac{\delta}{\delta r}(r\sigma v_r)+\frac{1}{2\pi r}\frac{\delta \dot{M}_W}{\delta r}=0 \qquad (۱)$$

می‌باشد که در آن v_r سرعت برافزایی و $\sigma=2\rho H$ چگالی سطحی در استوانه‌ای به شعاع r می‌باشد. در این رابطه $\dot{M}_W=\int 2\times \dot{m}_W(r')\times 2\pi r' dr'$ نرخ از دست دادن جرم به‌دلیل وجود باد است که در آن $\dot{m}_W$ نرخ از دست دادن جرم در واحد سطح از یک از دو سطح بالایی وپایینی قرص می‌باشد.

معادله‌ی شعاعی تکانه نیز به شکل

$$\frac{\delta v_r}{\delta t}+v_r\frac{\delta v_r}{\delta r}=-\frac{c_s^2}{\sigma}\frac{\delta\sigma}{\delta r}-\frac{GM_r}{r^2}+\frac{v_\varphi^2}{r} \qquad (۲)$$

خواهد بود که در آن v_φ سرعت گردش و c_s سرعت صوت در محیط می‌باشد. در اینجا $-\frac{GM_r}{r^2}$ نشان‌دهنده‌ی اثر خودگرانندگی در قرص می‌باشد. معادله‌ی تکانه‌ی زاویه‌ای نیز به‌شکل

$$\frac{\delta}{\delta t}(rv_\varphi)+v_r\frac{\delta}{\delta r}(rv_\varphi)=\frac{1}{r\sigma}\frac{\delta}{\delta r}\left(r^3\nu\sigma\frac{\delta\Omega}{\delta r}\right)-\frac{r^2\Omega}{2\pi r\sigma}\frac{\delta\dot{M}_W}{\delta r} \qquad (۳)$$

می‌باشد که در آن جمله‌ی آخر نشان‌دهنده‌ی تکانه‌ی زاویه‌ای منتقل شده توسط مواد خروجی از سطح قرص می‌باشد. جمله‌ی ماقبل آخر متناظر با تکانه‌ی زاویه‌ای انتقال یافته بر اثر گران‌روی است که در آن گران‌روی نسخه‌ی بتا[5] با رابطه‌ی $\nu=\beta v_\varphi r$ جایگذاری می‌شود.

حل عددی معادلات حاکم

طراحی الگوریتم برای حل معادلات (۱)، (۲) و (۳)، با بدون بعد سازی و گسسته‌سازی آنها، با در نظر گرفتن شرایط مرزی انجام می‌گیرد. گسسته‌سازی با استفاده از روش مک‌کورمک انجام می‌شود. مراحل کار به این صورت است که برای محاسبه‌ی جملات مشتق زمانیِ پارامترهای فیزیکی، این جملات به‌صورت میانی در زمان گسسته می-شوند. همانند محاسبه‌ی نخستین مرتبه‌ی زمانی پارامترها، برای محاسبه‌ی جملات مشتق مکانی پارامترهای ، این جملات به‌صورت پیش‌رو در مکان در ابتدای مرز، به‌صورت پس‌رو در مکان در انتهای مرز و به‌صورت میانی در سایر نقاط گسسته می‌شوند. طبق آنچه که برای چگونگی گسسته‌سازی روابط بیان شد و با توجه به‌این‌که مش‌بندی مورد استفاده در این الگوریتم با در نظر گرفتن ۱۰۰ نقطه‌ی مکانی و ۱۰۰ نقطه‌ی زمانی انجام گرفته‌است، معادلات حاکم توسط روابط زیر گسسته می‌شود:

$$\Sigma_j^{i+1}=-\frac{1}{R_j}\left(R_{j+1}\Sigma_{j+1}^i V_{R_{j+1}}^i+\dot{M}_{W_{j+1}}^i\right)\frac{\Delta T}{\Delta R}+\frac{1}{R_j}\left(R_{j-1}\Sigma_{j-1}^i V_{R_{j-1}}^i+\dot{M}_{W_{j-1}}^i\right)\frac{\Delta T}{\Delta R}+\Sigma_j^{i-1} \qquad (۴)$$

$$V_{R_j}^{\,i+1}=-A\frac{1}{\Sigma_j^i}\left(\Sigma_{j+1}^i-\Sigma_{j-1}^i\right)\frac{\Delta T}{\Delta R}-B\frac{1}{R_j^2}M_{R_j}^{\,i}2\Delta T+\frac{{V_{\Phi_j}^{\,i}}^2}{R_j}2\Delta T-V_{R_j}^{\,i}\left(V_{R_{j+1}}^{\,i}-V_{R_{j-1}}^{\,i}\right)\frac{\Delta T}{\Delta R}+V_{R_j}^{\,i-1} \qquad (۵)$$

$$V_{\Phi_0}^{\,1}=\beta\frac{1}{R_0^2\Sigma_0^0}\begin{pmatrix} R_1^4 V_{\Phi_1}^{\,0}\Sigma_1^0\left(\frac{V_{\Phi_2}^{\,0}}{R_2}-\frac{V_{\Phi_0}^{\,0}}{R_0}\right)\frac{1}{2\Delta R} \\ -R_0^4 V_{\Phi_0}^{\,0}\Sigma_0^0\left(\frac{V_{\Phi_1}^{\,0}}{R_1}-\frac{V_{\Phi_0}^{\,0}}{R_0}\right)\frac{1}{\Delta R}\end{pmatrix}\frac{\Delta T}{\Delta R}-\frac{V_{R_0}^{\,0}}{R_0}\left(R_1V_{\Phi_1}^{\,0}-R_0V_{\Phi_0}^{\,0}\right)\frac{\Delta T}{\Delta R}-\frac{V_{\Phi_0}^{\,0}}{R_0\Sigma_0^0}\left(\dot{M}_{W_1}^{\,0}-\dot{M}_{W_0}^{\,0}\right)\frac{\Delta T}{\Delta R}+V_{\Phi_0}^{\,0} \qquad (۶)$$

لازم به‌ذکر است که این روابط تنها روابط عمومی الگوریتم نبوده و با در نظر گرفتن شرایط مرزی این روابط مشتمل بر بیش از بیست رابطه خواهند بود.

بررسی تحول زمانی مشخصه‌های فیزیکی سیستم

نمودارهای زیر با تحلیل داده‌های حاصل از حل عددی معادلات (۱)، (۲) و (۳) به‌دست آمده‌است. با توجه به نمودار (۱)، چگالی سطحی به‌مرور زمان به‌دلیل سقوط ماده به‌سمت جرم مرکزی افزایش می‌یابد. همچنین گران‌روی موجب کند شدن سرعت چرخش در قسمت‌های داخلی‌تر قرص برافزایشی می‌شود. اثرات اصطکاکی گران‌روی، موجب کند شدن سرعت سمتی در قسمت‌های داخلی و افزایش آن در قسمت‌های خارجی‌تر قرص برافزایشی می‌شود. همان‌گونه که در این نمودار دیده می‌شود، روند برافزایشی در نواحی داخلی‌تر قرص شدیدتر است و در قسمت‌های خارجی‌تر به‌دلیل کاهش اثر نیروی گرانشی این روند به‌شدت کاهش می‌یابد.

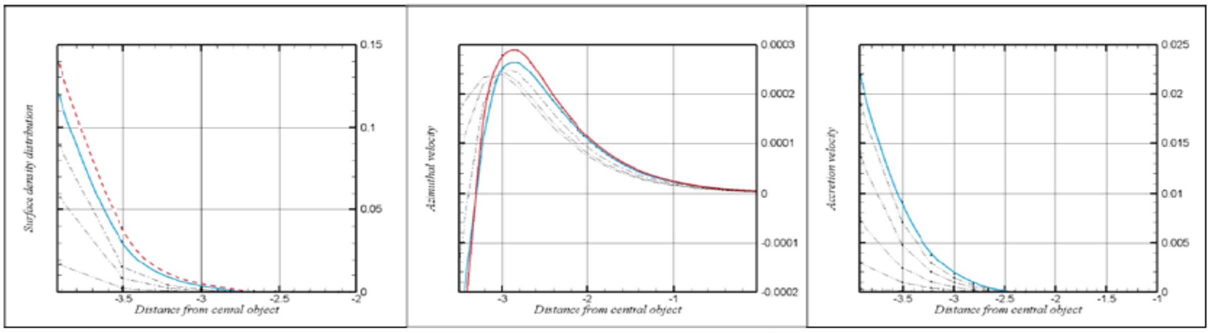

نمودار ۱: به‌ترتیب از چپ به راست تحول زمانی چگالی سطحی جرم، سرعت سمتی و سرعت زمانی، منحنی‌های رنگی قرمز رنگ مربوط به حالت نهایی این مشخصه‌ها بدون حضور باد است.

در نمودار (۲) به‌منظور مقایسه‌ی بهتر اثر باد، اختلاف مشخصه‌های فیزیکی باحضور باد نسبت به مشخصه‌های فیزیکی بدون حضور باد، نسبت به مکان رسم شده است. در این نمودار به‌خوبی مشخص است که اثر باد بر توزیع چگالی جرمی، در نقاط دورتر از جرم مرکزی بیشتر است. عموماً باد یا بیرون‌ریزی باعث کند شدن حرکت چرخشی قرص برافزایشی به‌دور جرم مرکزی، به‌خصوص در قسمت‌های داخلی‌تر آن می‌شود. روند برافزایشی در نواحی داخلی‌تر قرص شدیدتر است و در قسمت‌های خارجی‌تر به‌دلیل کاهش اثر نیروی گرانشی این روند به‌شدت کاهش می‌یابد. وجود باد، تاثیر چندانی در سرعت برافزایشی در قسمت‌های داخلی قرص نداشته ولی در مورد قسمت‌های خارجی‌تر قرص موجب افزایش سرعت برافزایشی می‌شود

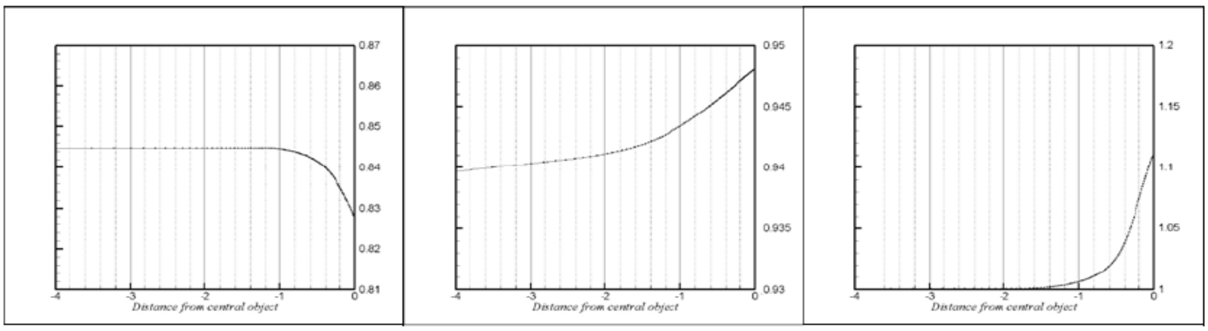

نمودار ۲: به‌ترتیب از چپ به راست نسبت مقادیر نهایی چگالی جرمی، سرعت سمتی و سرعت شعاعی به مقادیر نهایی آنها بدون حضور باد، نسبت به مکان

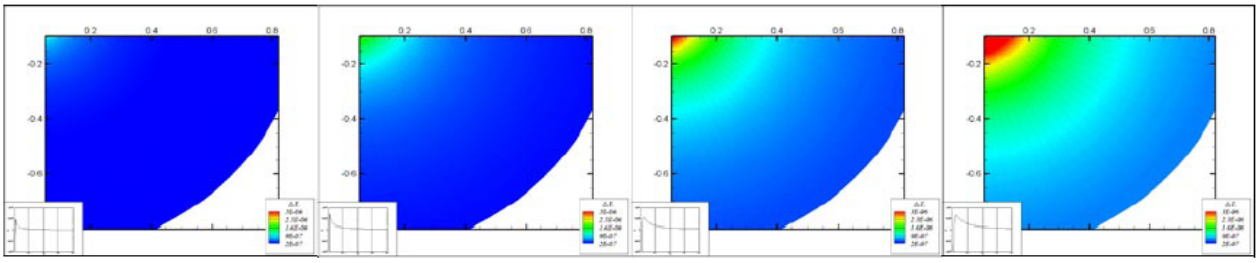

نمودار ۳: به‌ترتیب از چپ به راست نرخ انتقال اندازه‌ی حرکت زاویه‌ای در دیسک به‌مرور زمان

در نمودار (۳) تحول زمانی تغییر اندازه‌حرکت زاویه‌ای نسبت به حالت اولیه (چرخش کپلری) رسم شده است. همان-طور که در این نمودار دیده می‌شود، به مرور زمان تکانه‌ی زاویه‌ای به مناطق خارجی قرص منتقل می‌شود. عوامل خودگرانندگی، گران‌روی و بیرون‌ریزی یا باد، هر سه در انتقال تکانه‌ی زاویه‌ای از نواحی داخلی به نواحی خارجی قرص برافزایشی نقش دارند

نتیجه‌گیری

در روش حاضر، با استفاده از تنظیم مش‌بندی مکانی و زمانی، یک دوره‌ی حدود ۱۲۰۰ ساله از تحول یک قرص برافزایشی با حضور باد مورد شبیه‌سازی و بررسی قرار گرفت. این شبیه‌سازی نشان داد که وجود اثر باد موجب تغییر در چگالی جرمی قرص به‌مرور زمان شده و آن‌را کاهش می‌دهد. همچنین، اثر باد موجب کاهش سرعت سمتی و کند شدن قرص می‌شود. باد تغییر قابل توجهی بر سرعت برافزایشی در نواحی داخلی قرص نداشته، اما موجب افزایش آن در قسمت‌های خارجی قرص می‌شود.

قرص‌های برافزایشی با استفاده از مکانیسم باد یا بیرون‌ریزی، به‌خوبی سرعت سمتی به‌خصوص در لایه‌های داخلی‌تر خود را از دست می‌دهند. این پدیده در نهایت موجب انتقال موثرتر تکانه‌ی زاویه‌ای به قسمت‌های خارجی‌تر قرص می‌شود. بنابراین بادها مکانیسم‌هایی هستند که به روند انتقال تکانه‌ی زاویه‌ای در قرص‌ها کمک می‌کنند.

در مورد قرص‌های برافزایشی واقعی در طبیعت، بسیاری فرآیندهای مهم، به‌غیر از خودگرانندگی، گران‌روی و باد، وجود دارند که در تحقیق حاضر از آنها صرف‌نظر شده‌است. به‌عنوان مثال، میدان‌های مغناطیسی و اثرات آن در این تحقیق در نظر گرفته نشده‌است.. با این وجود نتایج به‌دست آمده در این تحقیق می‌تواند آغازی برای درک فیزیک حاکم بر قرص‌های برافزایشی باشد. همچنین تحقیق حاضر می‌تواند به‌عنوان پایه‌ای برای بررسی مسایل کامل‌تر و پیچیده‌تر بعدی با در نظر گرفتن سایر فرآیندهای موثر در قرص‌های برافزایشی باشد.

مرجع‌ها

1. Mineshige, S., Nakayama, K., & Umemura M., 1997, *Publ.Astron.Soc*, **49**, 439
2. Yokosawa M., 1995, *PASJ*, **47**, 605
3. Lynden-Bell, D., & Pringle, J. E. 1974, *MNRAS*, **168**, 603
4. Shadmehri, M., 2009, *MNRAS*, **395**, 877-88
5. Duschl, W., Strittmatter, P. A., & Biermann P. L. 2000, *A&A*, **357**, 1123

ارتباط بین فعالیتهای خورشیدی و آب و هوای زمین

کامروافر ، وحیده

کارشناسی ارشد فیزیک نجومی

دانشگاه آزاد اسلامی واحد اهواز

چکیده:

خورشید منبع اصلی انرژی برای سطح زمین است و هرگونه تغییری در تشعشع خورشید بر جو زمین و آب و هوا زمین تأثیر می گذارد . از آنجایی که در فعالیتهای خورشید منجمله لک ها، شراره ها و... تغییراتی در روشنایی و میدان مغناطیسی ایجاد می شود انتظار داریم روی آب و هوای زمین تاثیر بگذارد که از بررسی های انجام شده مشخص می شود که این فعالیتها می تواند گرم شدن زمین را به همراه داشته باشد.

Link between solar varation and earth climate

Vahide kamrava

Abstract

The sun is the main source for the earth and any change in sun radiation can affect the climate and earth atmospher.since there are changes in sun activities sunspot, flear,…for stance. We expect it to affeact the clhmate of the earth. The studies which have down show that these activites can make earth warm.

مقدمه:

خورشید به عنوان تنها منبع تولید کننده انرژی برای سیاره ما می تواند روی آب و هوای زمین تـاثیر بگـذارد منجمـان زمانی که لک را به عنوان ناحیه ای فعال روی سطح خورشید مشاهده کردند در صدد یافتن رابطه بین فعالیتها و دمـای زمین بر آمدند نمونه ای از این اثر مربوط به مینیمم ماندر در سال های ۱۷۱۵-۱٦٤٥میلادی است که تقریباً هیچ لکـی بر سطح خورشید مشاهده نشد و همزمان با عصر یخبندان دراروپا بود.

تحقیقات بعدی نشان داد که در بعضی از مناطق رابطه ای مثبت بین چرخه های لک و دما و در بعضی دیگر رابطه ای منفی و یا اصلاً رابطه ای وجود ندارد [۱]از این رو هنوز رابطه این تغییرات مشخص نشده ولی عواملی که مـی توانـد روی آب و هوای زمین تاثیر بگذارد عبارت است از تغییرات در کل تابش خروجی، در تـابش uv و تغییـردر تـابش کیهانی.

تغییرات در تابش خورشید:

آشکار ترین کاندید برای تغییرات در آب و هوای زمین، تغییرات در تابش خورشیدی هماهنگ با فعالیتهای خورشیدی است که با تعداد لک ها در طول دوره ۱۱ ساله همراه است بررسی ها نشان می دهد که تابش در دوره ۱۱ ساله حدود ۰/۱٪ تغییر می کند [۲]این تغییرات در مقیاس کوتاه مدت رخ می دهد اگرچـه لـک هـا نـواحی تاریـک روی سـطح خورشیدند اما اثر آنها با روشنایی فکولاها که نواحی روشن هماهنگ با لک است جبران می شود

تغییرات در تابش uv:

از آنجا که طول موج های uv عامل افزایش یا کاهش ازن در استرتوسفر و تروسفر می باشد هرگونه تغییر در تشعشع uv حاصل از خورشید می تواند ماهیت شیمیایی و دینامیکی جو را تغییر دهد و روی دما تأثیر بگذارد. یکـی از مهـم ترین نتایج، تغییر حرارت اتمسفر است که یکنواخت هم نیست.با افزایش فعالیت های خورشید و در نتیجـه افـزایش

جذب تشعشع uv استراتوسفر گرم می شود[۳] این تغییرات از طریق بادهای استراتوسفر به نواحی پایینی انتقال مـی یابد.

تغییرات در تابش کیهانی:

اگر چه انرژی موجود در باد خورشیدی با تأخیر بیشتری نسبت به تشعشع uv و مرئی به زمین می رسد امـا تـأثیرش بیشتر است. این فرضیه که مربوط است به تغییرات در مقیاس بلند مدت به میدان مغناطیسی باد خورشیدی همـراه بـا تابش کیهانی وابسته است. تشعشع کیهانی عامل اصلی یونیدگی لایه های بالایی اتمسفر است و عامل مهم تغییـر ایـن یونیدگی فعالیت های خورشیدی می باشد. باد خورشیدی و میدان مغناطیسی قوی تابش کیهانی را از جـو زمـین دور می کند در نتیجه مینیمم فعالیتهای خورشید با افزایش تشعشع کیهانی روی زمین و افـزایش هسـته هـای چگـال و در نهایت افزایش پوشش ابر همراه است.ابر نیز نقش موثری در تغییرات آب و هوایی چون افـزایش دمـا و یـا رطوبـت نسبی دارد. افزایش شار تابش کیهانی به افزایش هسته ابرهای چگال و در نتیجه دوام بیشتر ابر ها و آلبدو بیشـتر مـی انجامد که باعث کاهش اشعه آفتاب می شود.[٤]

یکی دیگر از آثار تغییرات مغناطیسی خورشید تولید ایزوتوپ رادیویی ١٤C و ١٠Be در تروپوسفراست که از واکنش پرتوهای کیهانی با مولکولهای جو تحت میدان مغناطیسی قوی باد خورشیدی ایجـاد مـی شـود ١٤Cپـس از ترکیـب سریعاً اکسید می شود و وارد چرخه کربن می شود. ١٠Beنیز به ذرات گرد وغبار معلق در هوا می چسبد و سـرانجام در برف و باران رسوب می کند. از مطالعه مقادیر ١٤C در حلقه های درختان و ١٠Be در یخ های قطبی و رسـوبات اقیانوس ها در ٤ قرن گذشته متوجه شدند که رابطه ای معکوس بین فعالیتهای خورشید و نسبت تولید ایزوتوپ هـای رادیویی وجود دارد[۲]

عامل دیگر ی که تغییر می کند ذرات با انرژی بالایی(شراره ها و طوفانهای خورشیدی) هستند که از خورشید سـاطع می شوند. وقتی این ذرات با اتمسفر برخورد می کنند مولکولهـای گـاز نیتـروژن و بخـار آب را تجزیـه مـی کننـد و مولکول اکسید نیتروژن می سازند اکسید نیتروژن سریع با ازن واکنش می دهد و مقدار آن را کم می کند و از آنجـایی که اکسید نیتروژن می تواند هفته ها تا ماهها دوام داشته باشد می تواند ازن را در تراز پایینی نگه دارد.[٥]

روش بررسی:

در این تحقیق برای بررسی بیشتر دمای سالانه شهرستان اهواز را با تعداد لک های گرفتـه شـده از سـایت soho [٦] مقایسه کرده و مشاهده شد در تمام چرخه تقریباً با افزایش و کاهش تعداد لک ها،دمای هوا نیز افزایش و کاهش مـی یابد. در چرخه ٢١،یعنی ٢٢و ٢٣ این مسئله به خوبی در نمودار١ دیده می شود که با افزایش تعداد لک ها دمای هـوا افزایش و با کاهش آنها دما نیز کاهش یافته است. علاوه بر این با استفاده از نرم افزار spss مقدار p-value =٠/٠٠٩ و ضریب همبستگی r=٠/٣٨ محاسبه شد و این نتیجه حاصل شد که ارتباط مستقیمی بین تعداد لک هـا و دمـای هـوا وجود دارد.

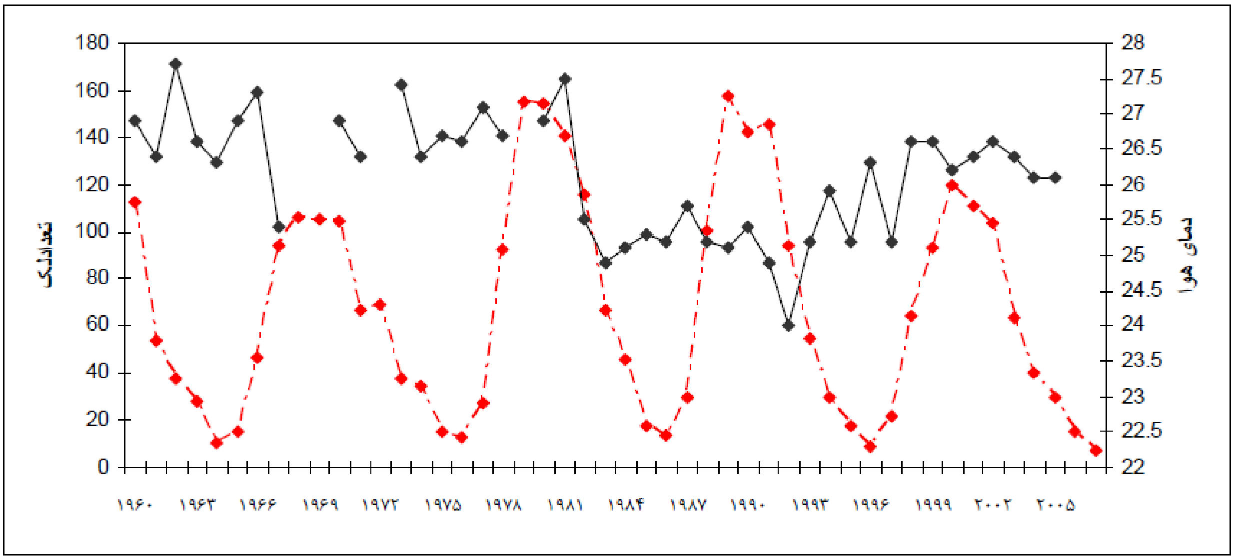

نمودار ۱تعداد لک های خورشید(خط چین) و دمای هوای اهواز از سال ۱۹۶۰ تا کنون را به طور سالیانه نشان می دهد.

نتیجه گیری:

نمودار ها با انطباق نسبتاً خوبی نشان می دهد که رابطه مستقیمی بین فعالیتهای خورشید و دمای هوا وجود دارد به این معنا که با افزایش و کاهش تعداد لک ها (فعالیتها) دمای هوا نیز افزایش و کاهش می یابد. درستی این ارتباط نیز با نرم افزار spssبررسی شده است.

علاوه بر این از مطالعه تغییرات حاصل از فعالیتهای خورشید می توان گفت که اززمان مینیمم ماندر تا کنون تابش خورشید افزایش یافته به دنبال این افزایش، تشعشع uv نیز باعث افزایش ازن جذبی و در نتیجه گرم شدن استراتوسفر می شود. از آنجا که تابش کیهانی نیز روی رطوبت نسبی و آلبدو ناشی از ابر ها تاثیر می گذارد در ماکزیمم فعالیت های خورشیدی تابش کیهانی کاهش و در نتیجه آلبدو کاهش می یابد که گرم شدن زمین را به همراه دارد.

منابع:

1. k. Georgieva.B. kirov and C. Bianchi "longterm variations in the correlation between solar activity and climate"2005, vol.76.965.
2. E. Bard. M.Frank" Clhmate change and solar variability: whats new under the sun?" 2006. Earth and plant science letterers248.
3.D. Shindell, D. Rind, N. Balachandran, J. LeanP. Lonergan." Solar Cycle Variability, Ozone, and Climate"
4. J. Kirkby" Cosmic rays climate "2008
5.p. Brekhe" Closing remarks on the sun influence on climate changes" 2005, vol.76.913
6. sohowww.nascom.nasa.gov/.

بررسی حرکت کشایندی (Apsidal Motion) در سیستمهای دوتایی گرفتی (نظریه و شواهد تجربی)

بهمن حسین زاده[۱]، رضا پژوهش[۲]
۱- دانشجوی دکترای نجوم و اختر فیزیک، دانشگاه بیرجند
۲- استادیار گروه فیزیک، دانشگاه بیرجند

چکیده

همانطور که می دانیم تقریبا ۵۰ در صد ستارگان آسمان را ستارگان دوتایی تشکیل می دهند. لذا سیستمهای دوتایی گرفتی کاندیداهای مناسبی جهت بررسی و محاسبه پارامترهای فیزیکی، هندسی و همچنین تعیین موقعیت تحولی ستارگان می باشند. بنابراین با توجه به مشاهدات تجربی (منحنی نوری، منحنی سرعت شعاعی، کمینه های اول و دوم و ...) می توان حرکت تقدیمی برخی از سیستمهای دوتایی را مورد بررسی قرار داد و با محاسبه آهنگ تغییرات نقطه حضیض در طول سالیان مختلف می توان به اطلاعات جدیدتری دست پیدا کرد. در این مقاله حرکت کشایندی ناشی از اثر مکانیک کلاسیک (تغییر اجرام ستاره ای از حالت نقطه ای)، چرخش محوری ستارگان، اثر وجود جسم سوم (ستاره سوم) و نسبیت عام مورد بررسی قرار گرفته و به کمک آن مقدار آهنگ تغییرات زاویه ای نقطه حضیض $\frac{d\omega}{dt}$ محاسبه می گردد. با مقایسه این مقدار و مقدار تجربی آن که از راه مشاهده به دست می آید، می توان صحت نظریات فیزیکی ساختار داخلی ستارگان و همچنین مدلهای مربوط به سیر تحول ستارگان را بررسی کرد. در این مقاله برای محاسبه آهنگ تغییرات نقطه حضیض $\frac{d\omega}{dt}$ از روش Guinan & Malony (1985) استفاده گردیده است.

مقدمه

بررسی حرکت تقدیمی نقطه حضیض در مدارهای سیستمهای دوتایی گرفتی در مدت زمان طولانی (چندین سال) را حرکت کشایندی(Apsidal Motion) می‌گوییم. حرکت کشایندی از جنبه نظری ناشی از دو جمله کلاسیکی و نسبیتی آهنگ تغییرات زاویه حضیض است که از نظر مقدار عددی بایستی با آهنگ تغییرات مشاهده ای زاویه حضیض برابر باشد. با این توضیحات خواهیم داشت $\dot{\omega}_{obs} = \dot{\omega}_{GR} + \dot{\omega}_{cl}$ که درآن $\dot{\omega}_{cl}$، $\dot{\omega}_{GR}$ و $\dot{\omega}_{obs}$ به ترتیب بیانگر جملات کلاسیکی، نسبیتی و مشاهده ای می باشند. در این مقاله حرکت کشایندی ناشی از اثر مکانیک کلاسیک (تغییر اجرام ستاره ای از حالت نقطه ای) ، چرخش محوری ستارگان، اثر وجود جسم سوم (ستاره سوم) و نسبیت عام را مورد بررسی قرار می دهیم و به کمک آن مقدار آهنگ تغییرات زاویه ای نقطه حضیض را از لحاظ تئوری به دست می آوریم. همچنین از راه مشاهده، مقدار تجربی آهنگ تغییرات نقطه حضیض را برای نمونه ای از دوتایی مورد بررسی قرار می دهیم.

بررسی تئوری آهنگ تغییرات نقطه حضیض

اثرات کلاسیکی

در بررسی اثر جزرومدی حاصل از مولفه های دوتایی که ناشی از تغییر شکل آنها می باشد، دو مولفه اول و دوم را به ترتیب با m_1 و m_2 که لزوما اجرام نقطه ای نبوده نشان داده و مورد تحلیل قرار می دهیم. در این صورت پتانسیل

جذرومدی حاصل از مولفه (ستاره) ۲ بر ۱ به صورت $V_{tidal} = \frac{m_2 G}{R}\sum_{n=2}^{\infty}\left(\frac{r}{R}\right)^n P_n(\cos\theta)$ می باشد که مقدار R در مدار تابعی از زمان است. دینامیک کلی تئوری جذرومدی بیان شده در رابطه مذکور شامل بسط هریک از جملات بر حسب تعدادی از جملات هارمونیکی است. جزرومد جزئی حاصل از ستاره ۲، اطراف ستاره۱ را با دامنه، سرعت و فاز ثابتی جاروب می کند که برآیندشان اغتشاشات کلی در ستاره ۱ را ایجاد می کنند و متقابلا چنین اثراتی در مورد ستاره ۲ تحت اثر ستاره ۱ نیز صادق می باشند. با فرض اینکه مولفه های دوتایی با سرعت زاویه ای یکنواخت ω_1 حول محور عمود بر صفحه دوتایی بچرخند، رابطه کلی V_r حاصل از چرخش ستاره ۱ حول خودش بر حسب هماهنگهای کروی به شکل $V_r = -\frac{1}{3}\omega_1^2 r^2 P_2(\cos\theta')$ تعریف می شود. اکنون با ترکیب پتانسیل چرخشی و جزرومدی، پتانسیل اغتشاشی را به شکل $V_d = V_t + V_r$ تعریف می کنیم حال اگر U را بعنوان پتانسیل گرانشی حاصل از ستاره گازی (مایع) دارای اغتشاش در نظر بگیریم، پتانسیل کل ناشی از این اغتشاشات به صورت $S = U + V_d$ بوده که S خود تا بعی ازعناصرمداری e(خروج از مرکز مداری)، A (نیم قطر اطول مدار نسبی) و ... می باشد. مطابق معادلات لاگرانژی مدار آهنگ حرکت نقطه حضیض را با معادله خطی $\dot{\omega} = (1-e^2)^{\frac{1}{2}}\frac{1}{e}\frac{\partial S}{\partial e}(\mu A)^{\frac{-1}{2}}$ مورد بررسی قرار می دهیم که در آن $\mu = G(m_1 + m_2)$ می باشد. در ادامه با بسط عبارت اغتشاشی S بر حسب ضرایب بسل و با استفاده از رابطه مقدار $\dot{\omega}_s$ را به شکل زیر به دست می آوریم:

$$\dot{\omega}_s = k_{2,1} a_1^5 \frac{1}{m_1}\frac{(m_1+m_2)^{\frac{1}{2}}}{(GA)^{\frac{1}{2}}}\left[15\frac{m_2 G}{A^6} f_2(e) + \frac{\omega_1^2}{A^3} g_2(e)\right] \qquad (1)$$

در این عبارت $f_2(e)$ و $g_2(e)$ برای eهای کمتر از واحد جملاتی همگرا و برابر با عبارات زیرمی باشند:

$$f_2(e) = 1 + \frac{13}{2}e^2 + \frac{181}{8}e^4 + \frac{465}{8}e^6 + \dots \qquad (2)$$
$$g_2(e) = 1 + 2e^2 + 3e^4 + 4e^5 + \dots$$

در حالت کلی در بررسی سیستم دوتایی وبا در نظر گرفتن اثرات هر دو مولفه بر روی یکدیگر مقدار $\frac{\dot{\omega}_s}{\nu}$ که برابر با عبارت $\frac{P}{U}$ می باشد را با استفاده از قانون سوم کپلر و با فرض اینکه مولفه ها در حالت سینکرونومایز می باشند به شکل زیر به دست می آوریم:

$$\frac{P}{U} = k_{2,1}\frac{a_1^5}{A^5}\left[\frac{m_2}{m_1}(15 f_2(e) + g_2(e)) + g_2(e)\right] + k_{2,2}\frac{a_2^5}{A^5}\left[\frac{m_1}{m_2}(15 f_2(e) + g_2(e)) + g_2(e)\right] \qquad (3)$$

دراین رابطه P وU به ترتیب پریود مدار نسبی و پریود حرکت کشایندی می باشند. مقادیر k_{2i} به ساختار داخلی ستارگان وابسته بوده وبرای تعدادی از مدلهای دوتایی توسط Russell جدولبندی شده است. مقدار به دست آمده در رابطه (۳) آهنگ تغییرات کلاسیکی نقطه حضیض می باشد که برای یک سیستم دوتایی با مولفه های یکسان با استفاده از قانون سوم کپلر و با توجه به مقاله (Gimenez 1985) می توان آنرا به شکل زیر نوشت:

$$\dot{\omega}_{cl} = \frac{0.17 f(e,1)}{(mP^2)^{\frac{5}{3}}} k_2 a^5 \qquad (4)$$

در این رابطه تابع $f(e,q)$ را به شکل $f(e,q)=\frac{m_2}{m_1}(15f_2(e)+g_2(e))+g_2(e)$ تعریف می کنیم که در آن q نسبت جرم مولفه ها بوده و در حالت $m_1=m_2$ تبدیل به $f(e,1)$ می شود [2],[3]. علاوه بر اثرات جزرومدی و دورانی وجود جسم سوم نیزآهنگ حرکت کشایندی سیستم را تحت تاثیر قرار داده و سبب اغتشاش در پارامترهای سیستم دوتایی نزدیک می شود. برای اولین بار کار تئوری سیستمهای سه تایی توسط Brown(1936-1937) انجام شد. این تئوری بر اساس نقطه ای بودن جسم سوم تعریف شده و از اثرات جزر و مدی حاصل از آن چشم پوشی نمود. Kopal و Brown رابطه ای برای آهنگ حرکت کشایندی تعریف کردند که تابعی از M_3 (جرم جسم سوم)، P' (پریود مدار سه جسمی)، e' (خروج از مرکز دوتایی عریض) و i' (زاویه میل بین مدار دوتایی و مدار سه جسمی) بوده و به صورت زیر بیان می شود که ثوابت مطابق مرجع مربوطه تعریف شد[4].

$$\dot{\omega}^{Theory}_{3B}(\frac{day}{yr}) = c_1[2-e^2-16\gamma^2-\frac{1}{4}e^4+23e^2\gamma^2-30\gamma^4-\frac{1}{4}e^6 -\frac{37}{4}e^4\gamma^2+\frac{345}{2}e^2\gamma^4-150\gamma^6]+c_2[50-75e^2-168\gamma^2+18e^2\gamma^2 +492\gamma^4+\frac{1425}{4}e^2\gamma^2-\frac{7179}{2}e^2\gamma^4+2430\gamma^6] \quad (5)$$

اثرات نسبیتی

جابجایی نقطه حضیض حاصل از اثرات نسبیتی در یک سیستم دوتایی، در ابتدا توسط لوئی جی ویتا بر حسب جرم کل سیستم و مشخصات مدار بدست آمد. با استفاده از روابط حاکم بر مدار بیضوی در سیستم دوتایی، رابطه پتانسیل اختلالی S به شکل زیر می باشد:

$$S=-\frac{G^2M^2a(1-e^2)}{c^2r^3} \quad (6)$$

که در آن a (نیم قطر اطول مدار بیضوی)، M (مجموع اجرام سیستم دوتایی)، G (ثابت گرانش) وe (خروج از مرکز مداری) می باشند. در این صورت طبق معادلات لاگرانژی مداربه عبارت زیر می رسیم:

$$\dot{\omega}_{GR}=\frac{6\pi GM}{PC^2a(1-e^2)} \quad (7)$$

نهایتا رابطه بدست آمده را با استفاده از قانون سوم کپلر به صورت زیر ساده می کنیم:

$$\dot{\omega}_{GR}=5.45\times10^{-4}\frac{1}{(1-e^2)}(\frac{M}{P})^{\frac{2}{3}} \quad (8)$$

بررسی مشاهده ای آهنگ تغییرات نقطه حضیض

در بررسی مشاهده ای از روش Guinan & Maloney استفاده می کنیم که در آن D را به عنوان جابجایی نقطه min ثانویه از نصف پریود مداری به صورت $D=[(t_2-t_1)-0.5\times P]$ معرفی می نماییم. در این رابطه t_2 به عنوان min

ثانویه مشاهده شده، t_1 min اولیه در همان Epoch و P پریود مداری سیستم مربوطه می باشند. از طرفی طبق این روش رابطه ای بین D و ω (زاویه حضیض) به شکل زیر که در آن e خروج از مرکز مداری و $\pi = 3.1415$ هستند برقرارمی باشند:

$$D = \frac{P}{\pi}[\tan^{-1}(\frac{e\cos\omega}{(1-e^2)^{\frac{1}{2}}}) + \frac{e\cos\omega}{1-e^2\sin^2\omega}(1-e^2)^{\frac{1}{2}}] \quad (9)$$

در ابتدا زمان های کمینه دوم سیستم مربوطه را از مقالات مختلف جمع آوری کرده وبا استفاده از روابط بالا مقادیر D و ω را برای HJD های متفاوت به دست آورده و در نهایت با رسم نمودار ω بر حسب HJD های مربوطه، شیب حاصل از نمودار فیت شده بر نقاط حاصله مقدار $\dot{\omega}_{obs}$ را می دهد. به عنوان مثال داده های رصدی مربوط به DI Her که در مقاله Guinan & Maloney جمع آوری شده را مورد بررسی قرار دادیم و ωهای مربوط به تعدادی ازHJD ها را به دست آوردیم. طبق بررسی، مقاله [6] در حدود ۱۸۰ دوتایی دارای Apsidal Motion را معرفی نموده که برای افرادی که در این زمینه کار می کنند، مرجع بسیار مناسبی می تواند باشد. در مقالات بعدی قصد داریم دو یا چند سیستم پریود کوتاه که دارای Apsidal Motion هستند را با استفاده از رصد خانه دانشگاه بیرجند مورد بررسی و رصد قرار دهیم و با استفاده از همین روش $\dot{\omega}_{obs}$ آنها را محاسبه نموده و با مقدار حاصل از $\dot{\omega}_{Theory}$ مقایسه نموده و اطلاعات مفیدی در مورد این دوتایی ها به دست آوریم[4].[5] .

خلاصه ونتایج

. حرکت کشایندی ناشی از اثر مکانیک کلاسیک، چرخش محوری ستارگان، اثر وجود جسم سوم و نسبیت عام را مورد بررسی قرارداده و به کمک آن مقدار تئوری آهنگ تغییرات زاویه ای نقطه حضیض $\dot{\omega}_{Theory}$ را محاسبه نمودیم. از طرفی با بررسی روش Guinan & Malony (1985) مقدار تجربی آهنگ تغییرات $\dot{\omega}_{obs}$که از راه مشاهده به دست می آید را بیان کرده و با مقایسه آنها صحت نظریات فیزیکی ساختار داخلی ستارگان و همچنین مدلهای مربوط به سیر تحول ستارگان را بررسی نمودیم .

مراجع:

[1]: Gimenez ,A.,1985, Astrophys.J.,**297**,405
[2]: Sterne,T.E.,1339(a),Mon.Not.R.Astron.Soc, **99**,451.
[3]: Sterne,T.E.,1339(b), Mon.Not.R.Astron.Soc.,**99**,662.
[4]: Guinan, E.F.and Maloney, F.P.,1985, Astron.J.,**90**,1519.
[5]: Dariush,A., Riazi, N.,Afroozeh, A.,2004, Apss,**296**,141.
[6]: Petrova,A.V. and Orlov,V.V, 1999,Astronomical Journal,**117**,585

مطالعه ترکیبات جرمی بهمن های هوایی با انرژی های بسیار بالا

رضوی،راضیه[۱] فاطمی، سید جلیل[۱] سومندر، سمیه[۱]

[۱]دانشگاه شهید باهنر کرمان

چکیده:

با اندازه گیری پارامتر عمر هر بهمن وتعیین دقیق تر توزیع سطحی الکترون های آن،پارامترهای ویژه ای از بهمن ها همچون چگالی مرکزی ،زاویه سمت الرأس،α پارامتر چگالی-فاصله وk پارامتر ترقی و تنزل چگالی های بهمن ها جهت تفکیک جرمی شان مورد مطالعه قرارگرفته است که افزایش ترکیب جرمی آنها را با انرژی در گستره مورد نظر نشان می دهد.

مقدمه:

یکی از مطالب مهم در پرتوهای کیهانی ترکیبات جرمی آنها در انرژی های بسیار بالا می باشد.از برخورد این پرتوهای اولیه با جو زمین پدیده بهمن های گسترده هوایی ایجاد می شودکه ساختار چگالی الکترونی آن در سطح زمین توسط تابع **NKG** با پارامتر عمر S به صورت زیر نوشته می شود.[1]

$$F(\frac{r}{r_0}) = c(s) \times (\frac{r}{r_0})^{s-2} \times (\frac{r}{r_0})^{s-4.5} \qquad (۱)$$

که در آن c(s)تابع خاصی از s می باشد که به فرمهای زیر نوشته می شود.

$$c(s) = 0.366 \times s^2 \times (2.07 - s)^{1.25} \quad [2] \qquad (۲)$$

$$c(s) = \frac{\gamma(4.5-s)}{\gamma(s) \times \gamma(4.5-2s)} \qquad (۳)$$

در نمودار زیر برای مقادیر s دو تابع c(s) رسم شده اند. این دو تابع با خطای بسیارکمی همخوانی دارند.

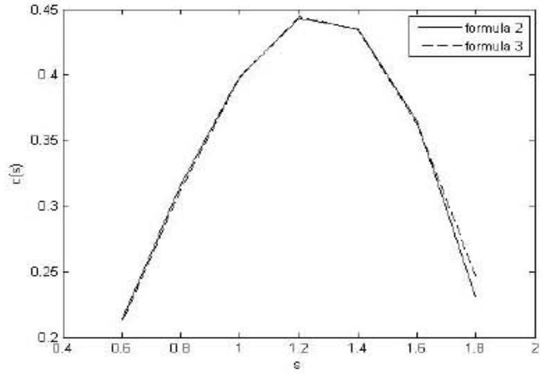

شکل ۱:همخوانی توابع ارائه شده برای توزیع سطحی الکترونهای بهمن ها

با توجه به داده های موجود در کاتالوگ"پرتوهای کیهانی با انرژی بالا مربوط به ایستگاه های Yakutsk,havara park"

که با به کارگیری آشکارسازهای مختلف اطلاعاتی در مورد چندین بهمن هوایی در اختیار ما قرار می دهد [3]که این اطلاعات عبارتند از: شماره هر آشکارساز با چگالی ثبت شده و فاصله هر کدام از مرکز هر بهمن، θ زاویه سمتی، E_p: انرژی اولیه و R: شعاع مولیر بهمن ها

ابتدا ما چگالی های موجود برای هر بهمن را با فرمول NKG، fit کرده ایم.[1]

$$F(\frac{r}{r_0}) = c(s) \times (\frac{r}{r_0})^{s-2} \times (\frac{r}{r_0})^{s-4.5} \qquad (۴)$$

$$\rho(r)_{\mathrm{NKG}} = \frac{\mathrm{N_e}}{\mathrm{r_0}^2} \times \mathrm{F}\left(\frac{\mathrm{r}}{\mathrm{r_0}}\right) \qquad (۵)$$

Ne: تعداد الکترون های هر بهمن و r_0 : شعاع مولیر می باشد.

و برای هر بهمن مقدار S یا پارامتر عمر آن محاسبه می شود.سپس با توجه به اینکه انرژی اولیه برای هر بهمن معین است ، می توان بوسیله فرمول زیر[4] اندازه بهمن را بدست آورد.

$$E = 3.9 \times 10^{15} \times (\frac{N_e}{10^6})^{0.9} \qquad (۶)$$

شکل ۲ رفتار بهمن ها را با پارامتر عمر نشان می دهد.برای بهمن های های مختلف که s های متفاوت دارند به وسیله فرمول NKG در فواصل بین ۰ تا۱۰۰ منحنی $log\rho$ بر حسب $logr$ رسم شده است وشکل ۲ بدست آمده است که هر چه مقدار s بزرگتر می شود منحنی پهنتر می گردد زیرا برای بهمن های های پیرترمنشا آنها سنگین است و عناصر سنگین تر پخش تر می گردند پس برای بهمن هایی با پارامتر عمر بزرگتر احتمال وجود آهن به عنوان منشا بیشتر است.

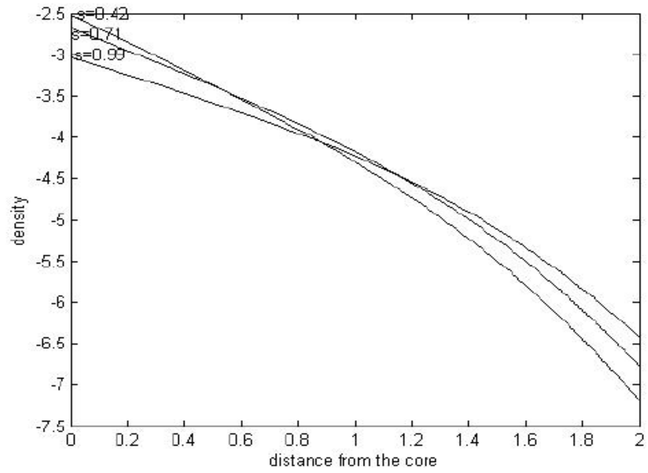

شکل ۲:وابستگی توزیع چگالی بهمن با پارامتر عمر

با توجه به پارامتر عمر محاسبه شده هر بهمن و با استفاده از فرمولNKG چگالی را در ناحیه نزدیک به مرکز بهمن به عنوان چگالی مرکزی میتوان محاسبه نمود و با توجه به این مطلب که چگالی مرکزی هر بهمن مناسب با انرژی بر نوکلئون بوده و انرژی اولیه بهمن مربوط به هسته اولیه مولد بهمن می باشد.در انرژی اولیه خاص با کاهش و افزایش چگالی مرکزی می توان اطلاعاتی در مورد ترکیبات شیمیایی بهمن ها بدست آورد.مسلماً افزایش جرم باعث کاهش چگالی مرکزی می شود.در شکل ۳ کاهش چگالی مرکزی بهمن ها در انرژی بیش از 4×10^{19} ev حاکی از افزایش جرم ذرات در این ناحیه از انرژی است.

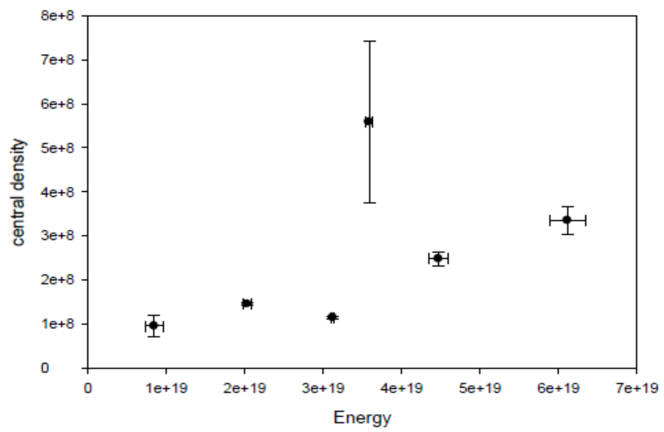

شکل ۳:وابستگی چگالی مرکزی بهمن بر حسب انرژی اولیه آنها

α: پارامتر چگالی – فاصله از مرکز را با استفاده از فرمول زیر بدست می آوریم.

$$\alpha = \frac{\rho_{max}-\rho_{av}}{r_{av}-r_{max}} + \frac{\rho_{av}-\rho_{10}}{r_{10}-r_{av}} \qquad (۷)$$

در این فرمول ρ_{10} و r_{10} به ترتیب چگالی ۱۰ وفاصله از مرکز بهمن می باشد وچگالی میانگین بر طبق رابطه زیر تعریف می شود.

$$\rho_{av} = \frac{\rho_{10} + \rho_{max}}{2}$$

α برای همه بهمن ها محاسبه و بر حسب انرژی در شکل ۴ رسم شده است.

با توجه به شکل زیر تا انرژی تقریباً 4×10^{19}ev افزایش در مقدار α، کاهش جرم ذره اولیه پرتوکیهانی را نشان می دهد و در انرژی های بالاتر از 4×10^{19}ev مقدار α کاهش یافته است که نشان دهنده افزایش جرم ذره اولیه پرتو کیهانی در این ناحیه از انرژی می باشد.

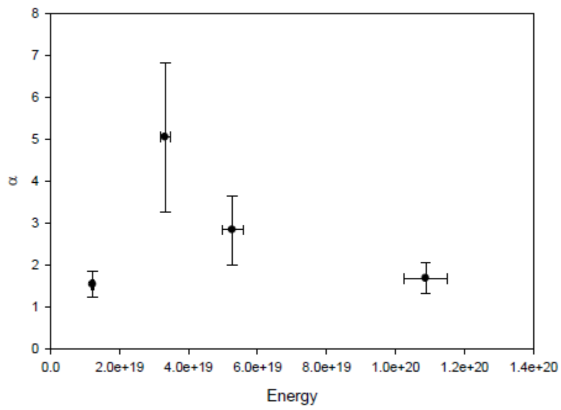

شکل ۴:پارامتر چگالی-فاصله بر حسب انرژی بهمن ها

نتیجه گیری:تجزیه و تحلیل پارامترهای مختلف مؤثر از جرم ذرات اولیه بهمن های گسترده هوایی حاکی از این مطلب است که در انرژی های بالاتر از حدود 4×10^{19}ev نسبت به کمتر از آن افزایش جرم مشاهده می شود که با نتایج کار قبلی Mikhailov همخوانی دارد.

مرجع ها:

[1].J.N.Capdevielle,et al.J.phys.G:Nucl.Part.Phys.**31**(2005) 507-524

[2].G.Hovespyan,et al.29th ICRC.**6**(2005) 97-100

[3].Catalougue of highest energy cosmic rays.No.**3**.Yakutsk.

[4].Hayashida,N.et al.G.Phys:G,**21**,1101,1995

طبقه‌بندی بدون نظارت طیف کهکشان‌ها در داده‌های SDSS/DR7

صداقت‌کیش، آروین[1]

[1] مؤسسه‌ی سپهر اختر شیراز

چکیده

در این مقاله با استفاده از الگوریم داده کاوی PAM طیف ۱۰۰۰۰ کهکشان از داده‌های SDSS/DR7 طبقه‌بندی شده است. روش ارائه شده تضمین می‌کند که کهکشان‌هایی مشابه، به طبقه‌های مشابهی تعلق پیدا می‌کنند. با استفاده از این الگوریتم مشخص شد که ۹۸/۸ درصد از کهکشان‌ها را می‌توان در ۱۶ دسته‌ی مجزا طبقه‌بندی کرد. بر همین اساس ۱/۲ درصد باقی‌مانده نیز در ۹ دسته‌ی فرعی طبقه‌بندی شده است. طبقه‌بندی‌های پیش‌بینی شده یکتا نیستند و تعداد زیادی از کهکشان‌ها در فضای بین این طبقات قرار می‌گیرند. در این روش هر یک از طبقات با یک الگوی طیفی که میانگین طیف همه‌ی داده‌های آن طبقه است نمایش داده می‌شود. بدین ترتیب این الگوریتم کهکشان‌ها را بر اساس رنگ‌شان از یکدیگر مجزا می‌کند. همان‌طور که انتظار آن می‌رفت رابطه‌ای میان طبقه‌بندی این مقاله و رده‌ی هابلی (یا دیگر شاخص‌های ریخت‌شناسانه) مشاهده می‌شود.

مقدمه

تعداد کهکشان‌های ثبت شده امروز به قدری زیاد است که ما را قادر می‌سازد با بررسی گروهی نتایج معتبرتری نسبت به گذشته فراهم کنیم. اطلاعاتی که ما در مورد کهکشان‌ها داریم اغلب از جمع‌بندی دانسته‌ها در مورد گروه بزرگی از اجرام بدست آمده و تعمیم آماری داده شده است؛ از همین رو هر چه تعداد داده‌هایی که برای یک بررسی در نظر می‌گیریم بیشتر باشد احتمالا نتایج قابل اطمینان‌تری بدست می‌آید و به‌عکس بسیار دشوار است از مطالعه‌ی یک کهکشان منفرد بتوان نتیجه‌ای قابل تعمیم بدست آورد (Hubble 1936). SDSS یکی از پیمایش‌های اخیر است که این امکان را فراهم می‌کند. انتشار هفتم داده‌های این پیمایش (SDSS/DR7) حاوی ۹۳۰۰۰۰ طیف کهکشانی است (Abazajian et al. 2009). پیش از این مقاله، گروه دیگری نیز به طبقه‌بندی طیف کهکشان‌ها در SDSS/DR7 پرداخته‌اند (Sanchez Almeida et al. 2010). هم مقاله‌ی حاضر و هم مقاله‌ای که به آن اشاره شد از روش طبقه‌بندی بدون نظارت بهره‌گرفته‌اند تا اثرات تصمیم‌گیری‌های سوبژکتیو به حداقل برسد.

طبقه‌بندی طیفی کهکشان‌ها

روش‌های مختلفی برای طبقه‌بندی طیفی کهکشان‌ها وجود دارد اما معمول‌ترین آن‌ها PCA است (Connolly et al. 1995). در این روش هر طیف به تعدادی از ضرایب تجزیه می‌شود و در آن تعداد اندکی از مقادیر ویژه به طور کامل هر طیف را توصیف می‌کند. در این مقاله برای مقایسه‌ی داده‌های طبقه‌بندی از تحلیل PCA به عنوان مرجع بهره گرفته‌ایم. در انواع تحلیل‌های مشابه انجام شده دو نتیجه عمومیت دارد؛ اول، می‌توان کهکشان‌ها را بر اساس دو یا سه ویژه مقدار اول توصیف و متمایز کرد و دوم، رابطه‌ی بین ضرایب طیفی و گونه‌ی هابلی کهکشان‌ها موجود است. از مشابهت این دو نتیجه‌ی معمول با نتایج الگوریتم مورد استفاده‌ی ما احتمال صحت عمل الگوریتم تقویت می‌شود.

الگوریتم

برخلاف (Sanchez Almeida et al. 2009 & 2010) که از K-Mean بهره گرفته و روش را ASK نام گذاشته‌اند، در اینجا از الگوریتم PAM -که نوعی روش خوشه‌سازی است- برای طبقه‌بندی استفاده شده. در این الگوریتم هر خوشه با یک مقدار میانی مشخص می‌شود. عضویت داده‌ها و کیفیت مقدار میانی تعین شده بر اساس کمینه فاصله‌ی اعضا عادی تا مقدار میانی تعیین می‌گردد. الگوریتم همچنین با سنجش کیفیت مقدار میانی در صورت لزوم آن را با مقداری که بهتر است جایگزین می‌کند (Dunham 2006; Everrit 1995).

برای استفاده از چنین روشی همان‌طور که پیش از این هم اشاره شد، طیف کهکشان‌ها به صورت بردارهایی در یک فضای برداری متناهی بعد، که ابعادش طول موج‌های متمایز کننده هستند، پیاده‌سازی می‌شود.

با اجرای این الگوریتم به سه مسئله‌ی مهم برای منظور این مقاله توجه شود. اول: یافتن تعداد خوشه‌ها، دوم: یافتن مقادیر میانی خوشه‌ها، سوم نسبت دادن هر کهکشان در نمونه‌ی مورد آزمایش به یکی از این مقادیر میانی. مقدار میانی به شکل تصادفی انتخاب می‌شود و سپس هر یک از داده‌ها به عنوان مقدار میانی مورد آزمایش قرار می‌گیرد و بقیه‌ی داده‌ها به نزدیک‌ترین مقدار میانی وابسته می‌شوند. بدین ترتیب بر اساس فاکتور کیفیت بهترین انتخاب صورت می‌گیرد و الگوریتم زمانی که دیگر جانشینی مقادیر میانی به اتمام برسد، متوقف می‌شود. در عمل اگر الگوریتم بخواهد تا زمان تثبیت تمامی مقادیر میانی ادامه پیدا کند مدت زمان زیادی صرف خواهد شد. در حالی که مطالعه‌ی حاضر نشان می‌دهد که اگر الگوریتم با شرط عدم تغییر ۹۸/۸٪ مقادیر میانی بین دو اجرای متوالی متوقف شود عملا تفاوتی در یافتن طبقه‌بندی رده‌های اصلی کهکشانی رخ نمی‌دهد.

قابل پیش‌بینی است که الگوریتم حاضر کند است و برای داده‌های بسیار زیاد منابع پردازشی بزرگی لازم دارد اما در مقایسه با روش K-Mean که در (Sanchez Almeida et al. 2010) پیشنهاد شده، روشی دقیق‌تر است به‌ویژه زمانی که موضوع تعیین مرزهای خارجی یک خوشه‌ی داده باشد. به بیان دیگر با استفاده از این روش می‌توان نسبت داده‌هایی را که میان خوشه‌ها قرار می‌گیرند کاهش داد.

اشکالات

سه مشکل عمده وجود دارد که باید در مورد آن‌ها توضیح داده شود. ۱- آیا طبقه‌بندی انجام شده با تغییر انتخاب‌های تصادفی اولیه تغییر می‌کند؟ با انتخاب یک نمونه کوچکتر از داده‌ی اصلی (در این مورد ۵۰۰) و دو اجرای متفاوت از طبقه‌بندی درصد تکرارپذیری ۸ ± ۷۷٪ به دست آمد. یعنی هر کهکشان با بخت حدود ۷۷ درصدی در هر بار طبقه‌بندی در طبقه‌ای مشابه قرار می‌گیرد، و مقادیر میانی با احتمال حدود ۷۷ درصد فارغ از شرایط اولیه هستند. ۲- ممکن است نویز باعث تشکیل طبقه‌های مصنوعی شود. به همین دلیل روی یک مجموعه از داده‌های مصنوعی که از ٤ طبقه مجزا انتخاب شده‌اند، افزایش نویز امتحان، و مشخص شد که افزایش نقطه به نقطه نسبت سیگنال به نویز تا حدود ۱۰ (مانند SDSS/DR7) باعث افزایش تعداد طبقات می‌شود اما طبقات معین شده حاصل مخلوط شدن ٤ طبقه‌ی اولیه نیستند (الگوریتم در این مورد نویز را طبقه‌بندی کرده)؛ یعنی افزایش نویز تا حد مورد بحث باعث ایجاد تغییرات مصنوعی در طبقه‌بندی نخواهد شد. ۳- الگوریتم کهکشانی را در بیش از یک طبقه قرار می‌دهد؟ برای

مشخص کردن وضعیت کافی است بررسی شود احتمال تعلق طیف کهکشان به هر طبقه چقدر است. اگر $f_c(d)$ تابع چگالی احتمال توزیع خوشه‌ها باشد، آنگاه احتمال بودن یک کهکشان در طبقه‌ای با فاصله‌ی معین برابر است با:

$$P(s,c) = \int_{d(s-c)}^{\infty} f_c(x)dx$$ (۱) s یک طیف و c مرکز یک طبقه است

$$Q(c,s,c_k) = \int_{d(s-c)}^{\infty} f_{c_k}(x)dx$$ (۲) کیفیت طبقه c

بدین ترتیب با استفاده از فاکتور کیفیت مسئله‌ی تعلق طیف یک کهکشان به طبقه مرتفع می‌شود؛ طیف به طبقه‌ای با بیشترین کیفیت تعلق می‌گیرد. رابطه‌ی (۳) نشان می‌دهد که کمترین فاصله از مرکز یک خوشه، با بیشترین کیفیت هم ارز است. از طرف دیگر با استفاده از همین فاکتور می‌توان طیف‌هایی را در هیچ گروهی قرار نمی‌گیرند مشخص ساخت ($Q << 1$) عملا حدود ۰/۰۰۳٪ از طیف کهکشان‌ها در هیچ‌یک از طبقه‌های اصلی و فرعی قرار نمی‌گیرند.

$$Q(c_1,s,c_k) \geq Q(c_2,s,c_k) \Leftrightarrow d(s-c_1) \leq d(s-c_2)$$ (۳)

طبقه‌بندی داده‌های SDSS/DR7

برای این که بتوانیم داده‌ها را به شکل بدون نظارت طبقه‌بندی کنیم باید دامنه و مقیاس طول موج همه‌ی طیف‌ها همانند باشد. از آنجا که در داده‌های SDSS کهکشان‌ها تا انتقال به سرخ ۰/۵ ثبت شده‌اند بنابراین مشکلاتی برای بررسی نواحی فروسرخ نزدیک در طیف‌ها بروز می‌کند به همین دلیل در این بررسی تعدادی از مولفه‌های طیفی را به عنوان مقادیر ویژه در نظر گرفته‌ایم که کار طبقه‌بندی صرفا روی آن‌ها انجام شده است (جدول ۱).

جدول ۱ : باندهای مورد استفاده (بر حسب آنگستروم)

از	تا	شرح
٤٤٥٢	٤٤٧٤	Ca4455
٤٦٣٤	٤٧٢٠	Fe4668
٥١٥٤	٥١٩٦	Mg_2
٥٨٧٦	٥٩٠٩	Na D
٥٣٨٧	٥٤١٥	Fe5406
٥٩٣٦	٥٩٩٤	TiO_1
٦١٨٩	٦٢٧٢	TiO_2

الگوریتم را برای داده‌های مقاله ۱۰۰ بار اجرا می‌کنیم و طبقه‌بندی‌ای را که تعداد طقات کمتر و درصد تکرارپذیری بیشتری داشته باشد انتخاب می‌کنیم. که از میان ۱۰۰ اجرا طبقه‌بندی انتخاب شده ما دارای تکرارپذیری ۷۹٪ و ۲۵ طبقه است که ۹۸/۸٪ طیف‌ها در ۱۶ طبقه‌ی اصلی و ۱/۲٪ درصد باقی‌مانده نیز در ۹ طبقه‌ی فرعی قرار می‌گیرند.

رابطه‌ی طبقه‌بندی انجام شده با PCA و ASK

امروزه بر اساس (Yip et al. 2004) طبقه‌بندی PCA برای حدود ۲۰۰۰۰۰ طیف کهکشانی در SDSS/DR7 انجام شده است. برای اینکه از صحت طبقه‌بندی این مقاله آگاه شویم آن را با PCA محاسبه شده برای SDSS/DR7 مقایسه کرده‌ایم. نتیجه‌ی کلی اینکه؛ دو طبقه‌بندی سازگارند اما دقیقا همسان نیستند؛ طبقه‌بندی ما و

همچنین ASK (Sanchez Almeida et al. 2010) حاوی طبقات بیشتری نسبت به PCA هستند. مابین طبقه‌های ASK و روش ما به جز فقدان یکی از طبقات اصلی (که اعضایش جذب طبقه‌ی قبل و بعد از خود شده) و دو طبقه‌ی فرعی مطابقت کامل از لحاظ مقادیر ویژه وجود دارد، نسبت اعضای هر طبقه نسبت به کل در هر دو روش تقریبا نزدیک به یکدیگر و بیشترین تفاوت مشاهده شده در طبقات اصلی ۰/۲۶۵٪ است. تفاوت در تعداد طبقات ASK و روش حاضر با دقت بیشتر الگوریتم PAM و کوچکتر بودن مجموعه‌ی داده‌های ما ارتباط دارد، میزان مشارکت هر یک از این دو عامل به دقت روشن نیست.

رابطه‌ی طبقه‌بندی انجام شده با گونه‌های هابلی

همان‌طور که می‌دانیم گونه‌ی ریخت‌شناختی یک کهکشان به‌دقت با طیفش بستگی دارد (Connolly et al. 1995; Ferreras et al. 2006; Nair & Abraham 2010). به همین دلیل بر آن شدیم تا نتیجه‌ی این طبقه‌بندی را نیز با رده‌های هابلی مقایسه کنیم. به همین دلیل طیف مجموعه‌ی ۱۰۰ تایی تصادفی از کهکشان‌های بررسی شده در (Nair & Abraham 2010) را با الگوریتم PAM طبقه‌بندی کردیم و سپس رابطه‌ی میان طبقه‌بندی طیفی بدست آمده با رده‌ی هابلی آن‌ها بررسی شد؛ نتیجه اینکه رابطه‌ی یکی به یکی میان ایندو مشاهده نشد. همین نتیجه نیز در (Sanchez Almeida 2010) گزارش شده است.

نتیجه گیری

طبقه‌بندی خودکار انجام شده با الگوریتم PAM برای نمونه‌ی مورد مطالعه‌ی این مقاله که تنها به دلیل محدودیت‌ها انتقال داده و پردازش محدود شده، تعداد طبقات تشخیص داده شده را کاهش می‌دهد و کیفیت طبقات بهبود می‌بخشد. این طبقه‌بندی از لحاظ رابطه‌ی مشاهده شده با PCA و رده‌های هابلی تفاوت چشمگیری با دیگر مطالعه‌ی انجام شده از این دست ندارد.

مرجع‌ها

1. Abazajian, K. N., Adelman-McCarthy, J. K., Ag¨ueros, M. A., et al. 2009, ApJS, 182, 543.
2. Connolly, A. J., Szalay, A. S., Bershady, M. A., Kinney, A. L., & Calzetti, D. 1995, AJ, 110, 1071.
3. Everitt, B. S. 1995, Cluster Analysis (London: Arnold).
4. Ferreras, I., Pasquali, A., de Carvalho, R. R., de la Rosa, I. G., & Lahav, O. 2006, MNRAS, 370, 828.
5. Dunham, Margaret H. 2006, Data Mining (London: Pearson).
6. Nair, P. B., Abraham, R. G. 2010, astroph/1001.2401v1.
7. S´anchez Almeida, J., Aguerri, J. A., Mu˜noz-Tu˜n´on, C., & Vazdekis, A. 2009, ApJ, 698, 1497
8. S´anchez Almeida, J., Aguerri, J. A., Mu˜noz-Tu˜n´on, C., & Vazdekis, A. 2010, astroph/1003.3186v1.
9. Hubble, E. P. 1936, Realm of the Nebulae (New Haven: Yale University Press).